Inorganic products used in the Conservation of Cultural Heritage: interaction with carbonatic substrates and newly-formed crystalline phases

Ph.D. Thesis

Elena Possenti
ID nr. R11205

Ai miei nonni ed alla mia splendida famiglia allargata

Contents:

Abstract

Diammonium hydrogenphosphate (DAP) water solutions are promising inorganic-mineral treatments for the consolidation of ornamental carbonatic stones and, in the last few years, DAP-based treatments are gaining increasing interest by the open literature. The core idea of the treatment is to transform part of the original stone material in insoluble newly-formed phosphate phases, through the reaction of the phosphate ions of the reagent with calcium ions of the substrate. At present, there is a growing quest for a deeper insight on their interaction with carbonatic stone matrixes, as well as the development of analytical protocol to characterize their diffusion and penetration profile within the matrix.

The research project of this PhD thesis aims to define the crystal-chemistry and distribution of reaction products within carbonatic substrates, exploring the effects induced by the crystallization to the stone matrix. Different multi-analytical approaches were used. Case by case, the combination of conventional and innovative analytical techniques allowed exploring the feasibility and potentiality of high resolution ATR-FTIR microspectroscopy, synchrotron radiation (SR) X-ray diffraction in transmittance and grazing geometry, and of SR micro-computed tomography to study inorganic-mineral treatments and their interactions with stone substrates.

Starting from the DAP reaction with calcite of two representative lithotypes, a compact metamorphic stone (*Carrara marble*) and a porous sedimentary one (*Noto limestone*), we investigated the crystallization of newly-formed phosphates, describing the variables that affect the reaction mechanism and the nucleation of the reaction products. The nucleation of different phosphate phases resulted influenced by the availability of free calcium ions, which, in turn, is influenced by several factors mutually interfering. The DAP molarity, the pH and the pH variation during the reaction, the lithotype and the application methods were found crucial factors in the formation of specific crystallites, determining their composition, crystallinity and localization.

The effects induced by the nucleation of phosphates to the stone substrate were evaluated in terms of micro-structural variations, modification of the porosity (pore size distribution, total open porosity, average of pore radius, specific surface area) and penetration depth. The composition and distribution of specific phases in the matrix, as well as the arrangement of the new phases into the voids, were investigated by combining different techniques, including qualitative and quantitative-morphometric imaging analysis.

On the basis of the experimental data collected on laboratory stone specimens, an applicative study was carried out on a decayed carved artefact (*Angera stone*), in order explore the effects of DAP consolidation when complex weathered stone matrixes are involved.

We expect that the experimental findings of this research activity will be transferred to the conservation practice, providing guidelines to restorers in order to perform treatments with improved performances, considering the peculiarity of specific case studies and the conservative history of stone artworks.

1 Introduction

1.1 The importance of consolidating treatments on Cultural Heritage stone artworks

The concept of "conservation, preservation" origins, intimately, from the idea that a culture has toward the conception of art, identity and history. In fact, the intentional conservation of an object is the declaration and the exhibition of a specific feeling, an ethic and aesthetic choice, a sort of need: this object must be preserved, this work of art should be transmitted. The idea of "Cultural Heritage" grows in this context. In fact, an object becomes an artwork with Cultural Heritage relevance because it is, somehow, the witnesses of historical and artistic values, of a past culture and social feelings, but also of a constructive technology and of the executive knowhow to manipulate the matter. Following that, it is possible to consider that the main characteristic of Cultural Heritage objects is that they indissolubly merge material and cultural aspects. This concept is the starting point for the contemporary Conservation Science and for the acknowledgement that the scientific multi-disciplinary insight on artistic materials is as important as the study of their humanistic values.

It derives from here one of the main aim of Conservation Science, namely, preserving as much as possible the original material because it is the portion of matter handled by artists and it is consequently characterized by Cultural Heritage relevance.

In the wide range of materials used to produce artworks, the stone materials are a class particularly employed and one among the most ancient. In fact, magmatic (both intrusive and volcanic), metamorphic and sedimentary stones have been quarried, carved and transformed in artworks since ancient time. These stone materials are susceptible to deterioration and, since their extraction from the quarry, they interact with the surrounding environment, starting their conservative history. To classify the interactions occurring with the environment, the term "weathering" is used to identify a natural process of rock disintegration by external factors [1], the word "alteration" indicates a modification that do not imply a worsening in the conservation state, while "deterioration, degradation or decay" means irreversible loss of characteristic that damage the material and its function, exposing to conservation risk its Cultural value [1–3]. The stones can show many types of damages [4] and each particular deterioration pattern is described by specific terms (in Italy: UNI 11182:2006 [5], internationally: International Council of Monuments and Sites (ICOMOS) - International Scientific Committee for Stone (ISCS) [6]). The same terms can be applied to the wider class of inorganic materials called as "stone materials", expression that in Conservation Science is referred either to natural stones either to artificial inorganic materials, *e.g.,* plasters, mortars, stuccoes. However, in the

following text, the expression will be used to identify natural stones, since this thesis focused only on the treatment of natural lithotypes.

Focusing the discussion on stone deterioration, the causes of decay are several, including the intrinsic properties of the stone, the conservation state, the environmental factors and the degradation mechanisms [7]. In some cases, there is only one active decay phenomenon, but, in many cases, there may be several factors mutually acting at once; some of them can be very sudden and rapid, while in other cases the processes are very slow. In general, the acknowledged decay causes are the air pollution, the growth of salts and the biodeterioration, the differential stress and the intrinsic problems [3]. The aforementioned causes act on the stones toward physical processes (*e.g.,* gravity force), mechanical processes (*e.g.,* thermal cycling, hygric and hydric swelling, crystal growth with molar volume increase inside the voids) and chemical processes (*e.g.,* mineral dissolution reactions and surface recession rates on calcareous stone) and all of them determine changes in the texture, microstructure, mechanical properties and crystal-chemistry composition of the stone matrix.

To stop or to slow the deterioration of stone artworks, the consolidation and the protection are among the most important steps in the conservation practice [8]. The protection acts on the surface of the stone artwork and prevents the development of further weathering processes due to external or environmental decay agents [3,9,10]. The consolidation is an operation addressed to stone materials affected by loss of cohesion and increases the strength of a decayed matrix due to the diffusion by capillarity, inside the pores, of liquid substances able to chemically and/or mechanically bind detached material portions [9,11].

Ideally, a consolidant should restore the stone strength at least as strong as it was originally (consolidating value), providing the treated stone with the same thermal expansion and elastic modulus as the underlying untreated bulk. Important parameters are also the: penetration and depth profile, compatibility of the consolidant with substrate, durability of treatment, effect on liquid water and vapour permeability, biological resistance. Further requirements are that the consolidant should not induce mechanical stresses, it should be reasonably cheap, easy to apply, safe to handle, safe for the environment and completely invisible [9–11].

There are many suitable compounds for stone consolidation and they are conventionally classified in organic polymers or inorganic-mineral products. Traditionally, the problems connected to the stone consolidation were faced with the use of organic polimeric products, both natural (*e.g.,* waxes, siccative oils, natural resins, proteins) and artificial (*e.g.,* epoxies, acrylics, alkoxysilanes), usually in organic solvents or water dispersions. The products set inside the matrix through reactions of polymerization or of hydrolysis and subsequent condensation. These treatments have been widely used in stone conservation as they supply positive performances, potential reversibility and simple use [12,13]. However, when dealing with organic-polymeric products, problems arise in the short-midterm (steric hindrance, colour change, loss of properties, poor chemical affinity, tendency to crack) and they exhibit limitations in terms of compatibility, durability and effectiveness in the long-run [14].

An important issue is that lithotypes need to "breathe". In other words, the stone substrate should remain permeable to water vapour and to liquid water in order to allow the evaporation of moisture arising, for example, from capillarity uptake. In many cases, the use of hydrophobic non-transpiring polymers blocked moisture at the interface between the treated zone and the underlying untreated

stone soluble salts, causing consequent shear stresses, the formation of crypto-efflorescences and a potential biological growth.

The inorganic-mineral treatments overcome this limit of organic products, being water-based products and forming a hydrophilic, transpiring and porous consolidating systems. The reaction mechanism is different as well. In fact, inorganic-mineral products embody the reaction of the treatment with the substrate, involving the dissolution of some minerals and the precipitation of new phases in their place. Several inorganic-mineral products are available for the stone consolidation and there are specific treatments for carbonatic or for silicatic matrixes. Focusing on carbonatic stones, the most studied are: calcium carbonate compounds (calcium hydroxide, slaked lime, biological deposition), magnesium hydroxide, barium hydroxide compounds and artificial calcium oxalates [7].

Even if these treatments present several advantages, they show some cons as well: *e.g.,* too slow or too quick reaction time, low solubility of the reagent, complex chain reactions, low penetration capacity [14].

More recently, the scientific community investigated the potentiality of new products aimed to improve the consolidating performances of more traditional compounds. Within this class of materials, already available on the market and widely tested on stone surfaces, it is possible to annoverate the hybrid products (namely substances characterized by hybrid properties between organic and inorganic products, as calcium alkoxides [15], oxamate salts [16,17], calcium tartrate [18], alkyl sulphates [19], alcoxysilanes [12,13]), nanomaterials-based products (*e.g.*, nanoparticles (NPs) of calcium hydroxide, strontium hydroxide, silicon dioxide, calcium alcoxides and hydroxiapatite [7,20]) and functionalized classical products (*e.g.*, silicon-based hybrid polimer nanocomposites, particle-modified silica consolidants, calcium oxalate-silica nanocomposites, hydroxyapatite-titania nanocomposites, [7,21,22]). These new materials, especially if nanosized, show evidence of an increased chemical reactivity and provide the possibility of a deep penetratation into stone matrixes, due to their reduced particle size. On the other side, it is known that their morphology, size and properties strongly depend on the synthesis route, thus slight variations of the experimental parameters during their synthesis may determine a not negligible variations of the NPs properties [7].

1.2 DAP treatments. The state of art

In 2011, a new inorganic-mineral consolidating treatment for carbonate stones has been introduced in Conservation Science [23,24]. The treatment is based on ammonium phosphate water solutions and it takes inspiration from some historical patinas found on the surface of marbles, limestones, sandstones, dolostones and granites [25–29]. These patinas are composed of calcium phosphates and calcium oxalates [10,25,27] and display a clear consolidating action, since theses phases fill the empty spaces reconnecting detached grain boundaries [30].

From the chemical-mineralogical viewpoint, the ammonium phosphate treatment forms calcium phosphates on carbonatic substrates through a mild reaction of dissolution and recrystallization [31], occurring between phosphate groups in solution of the reagent and calcium ions of the substrate. Afterwards, artificial calcium phosphates nucleate directly inside the stone matrix with a pseudomorphic replacement reaction [32] and form a crystal-network inside the micro-cracks that bind

the detached grains. In comparison with the inorganic consolidating products previously described in §
1.1, the advantages of ammonium phosphate-based treatments are: i) high water solubility of the
reagent, which allows using solutions with a high concentration of the consolidating product; ii)
absence of toxicity for the environment and for the operators; iii) stability and low solubility of the
newly-formed phosphate phases.

As a consequence, the treatment is expected to supply also a protective effect, because the formed
phases have a lower solubility and a slower dissolution rate than calcite. For these reasons, calcium
phosphates act as a thin sacrificial layer that reduces the reactivity of fresh substrates and provides a
passivating barrier toward acid environmental agents. Moreover, a de-sulphating action is also
documented, since gypsum crusts or calcium-bearing soluble salts are an alternative source of calcium
ions required to form calcium phosphates [23,33–37].

In the last years, the potentiality of this new treatment has been widely explored and ammonium
phosphate solutions were tested for the conservation of a huge fan of historical materials: mural
paintings, plasters and frescoes [37–39], gypsum stuccoes [40,41], archaeological bones [42,43].
Actually, in this very rich scenario, the major part of the papers available in the open literature focus
on the conservation of natural stone (mainly marble and porous sedimentary stones). The introduction
of ammonium phosphate treatments in conservation worksites raised immediate enthusiasm from the
restorers and many of them applied the treatment to carbonatic stone materials. However, the use of
this new treatment in pilot worksites shed light on the need of experimental studies to understand the
reaction mechanisms and the reaction products.

In the field of stone conservation with ammonium phosphate, the research activity is nowadays
focused on the use of the product for the *consolidation* [23,24,44–52] or the *protection* [21,53–58] of
natural and artificial carbonatic stones. The main difference between the two aforementioned
utilizations of the treatment (*i.e.*, *consolidation* or *protection*) involve the use of different application
guidelines: a) for stone protection, the artificial growth of a compact homogeneous coating of calcium
phosphates on the surface of a material is developed; b) for stone consolidation, the treatment is aimed
to form a porous crystal network inside the stone bulk.

Regardless the treatment type, the crystallization of calcium phosphates phases can be obtained using
different water soluble reagents and several phosphate precursors were involved in order to promote
the reaction: monocalcium phosphate ($CaH_4P_2O_8$ [53]), ammonium dihydrogen phosphate, ADP,
$NH_4H_2PO_4$; diammonium hydrogenphosphate, DAP, $(NH_4)_2HPO_4$; ammonium phosphate, AP or TAP,
$(NH_4)_3PO_4$ [23,56]. The solutions of these ammonium salts differ in their pH value (ranging from 5 to
11) and in the speciation of phosphate ions (PO_4^{3-}, HPO_4^{2-} and $H_2PO_4^-$ ions) [23,56]; however, since
the speciation depends on the pH, the nature of the phosphate precursor is basically irrelevant, as long
as the pH of the phosphate solution is controlled [59]. During a phosphate-based treatment on
carbonatic substrates, the reaction should occur at basic value and the pH value of reagent solutions
should be adjusted to avoid the acid dissolution of calcite and the formation of acid, metastable
phosphates. At the moment, DAP is the most studied phosphate-precursor in literature.

Focusing to treatments protocols for stone consolidation, several DAP treatment conditions were tested
in the last years: molarity of the phosphate solution (DAP concentration ranging from 0.1 M up to 3
M), use of different solvents in the solution (water, ethanol, iso propanol), reaction time (from 1 hour

to 2 weeks), calcium source (calcite of the substrate or artificially added, *e.g.,* $CaCl_2$, $Ca(NO_3)_2$, $Ca(OH)_2$, calcium gluconate, calcium formate) [31,59–61].

1.3 Open issues and aim of the thesis

Several research paper have been published in the last few years on the consolidation of carbonate stone substrates with phosphate-based treatments and several techniques were used in order to evaluate the consolidating effect and the penetration depth within the stone substrate [59,60]. However, is worth nothing that the performances of a consolidation treatment depend on several factors mutually infereing (as *e.g.,* the product, the stone characteristics, the ambient conditions [14]) and their evaluations is not always straightforward [14,62].

Thus, the core idea of this study is to explore some of the variables that, in the field, might affect the good application of the product and the success of the treatment. Therefore, among the many phosphate-precursors available, DAP is the reagent used in this research because DAP solutions have a natural pH around 8 and it avoids the pH value adjustment.

Ideally, the reaction product of DAP solutions with a single crystal of calcite is stoichiometric hydroxyapatite (HAP, $Ca_{10}(PO_4)_6OH_2$) [32,63] according to the reaction [59]:

$$10CaCO_3 + 5(NH_4)HPO_4 \rightarrow Ca_{10}(PO_4)_6(OH)_2 + 5(NH_4)_2CO_3 + 3CO_2 + 2H_2O \qquad (1.1)$$
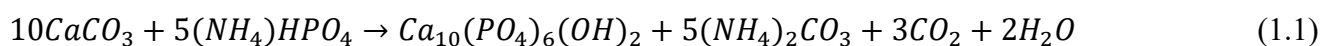
The HAP formation is highly desirable and it is expected to be an effective consolidating agent for carbonate stones because: i) it is an insoluble crystalline phase and it is notably less soluble than calcite (K_{sp} 25 °C: calcite 4.8×10^{-9} mol/L, hydroxyapatite 1.6×10^{-117} mol/L [23]); ii) it is a stable phase even in acid environment, leading to stability and durability of the treatment; iii) it provides a high affinity and compatibility between the treatment products and the stone substrate, arising from the formation of crystalline phases inside a crystalline matrix.

The DAP reaction with carbonatic stones is more complex, because in this case it is non-stoichiometric and it depends on several parameters: *e.g.,* temperature, pH, presence of foreign ions, degree of supersaturation. As a consequence, the treatment can promote the formation of some crystalline phases, inhibiting the precipitation of others, as well as it may induce the formation of a mixture of different calcium phosphates which significantly differ in terms of Ca/P molar ratio [64,65]. The detected phases after DAP treatments on carbonatic polycrystalline substrates are: brushite (DCPD, $CaHPO_4·2H_2O$) [23,31], monocalcium phosphate monohydrate (MCPM, $Ca(HPO_4)_2·H_2O$) [33], amorphous calcium phosphate (ACP, $Ca_xH_y(PO_4)_z·nH_2O$ with n = 3–4.5), monocalcium phosphate anhydrous (MCPA, $Ca(HPO_4)_2$), tricalcium phosphate (TCP, $Ca_3(PO_4)_2$) and octacalcium phosphate (OCP, $Ca_8(HPO_4)_2·5H_2O$) [54]. Moreover, recent findings [31,54] also suggested that the HAP formation after DAP treatments is most probably non-stoichiometric, since in presence of carbonate anions, PO_4^{3-} and OH^- groups can be partially replaced by CO_3^{2-} groups [66]. The higher the Ca/P molar ratio, the lower the solubility of the calcium phosphate phases. Therefore, the characterization of the exact composition of the newly-formed phases becomes crucial as the formation of soluble and metastable phases might be detrimental for the treatment and the crystallization of phosphates should

be driven toward the most stable and insoluble phases. Unfortunately, the characterization of the newly-formed calcium phosphate phases is analytically challenging [45,46] and the previous studies highlight the need of new multi-analytical approaches able to unambiguously describe the different calcium phosphates. The systematic crystal-chemistry investigation of these systems is complex and, in many cases, even the assessment of the actual formation of HAP after DAP application is ambiguous due to the precipitation of complex mixtures of calcium phosphates with similar structure and composition, most likely non-stoichiometric, ionic substituted, calcium-deficient or poorly crystalline. Furthermore, many of these phases are trace phases and/or metastable phosphate phases, which tend to transform into other calcium phosphates. Once verified the formation of a mixture of phases, an additional important task is the definition of their distribution with respect to the substrate. How the newly-formed phases are distributed on the surface of the treated stone and into the micro-cavities of the material? Are the insoluble phases nucleated directly on calcite of the substrate or are they randomly arranged, in mixture with soluble phases? Where is the HAP (if precipitated)? The exhaustive comprehension of similar systems is not merely an analytical goal, but it has a direct and important relapse in conservation field, as the formation of specific insoluble crystalline phases and their distribution on the substrate directly influences the performances of the consolidating treatment with the time.

The formation of specific calcium phosphate phases depends on the interactions occurring between the reagent and the stone material. In the last 2-3 years, several research groups investigated this relationship, testing different treatment methods in order to define the best treatment conditions for the DAP treatments in the field. Nevertheless, there is the quest for further investigations to understand how the characteristics of the lithotype (composition, microstructure) and the treatment protocol (application, molarity, pH) influence the formation of specific phosphate phases on marbles and limestones.

A further open issue, emerging from the survey in literature, is the need of a clear exploration the penetration depth of the treatment inside the stone matrix. Preliminary papers on the diffusion of the DAP solution in a porous sedimentary stone were published at the end of 2017 [69], investigating the distribution of the DAP solution during the treatment. However, as briefly showed, no exhaustive data were available on: i) the crystalline phases nucleated in the stone bulk; ii) their penetration depth and their distribution in the voids; iii) the potential modification of the porosity after the DAP treatment.

In this scenario, it is important to consider two further aspects. The first one is that inorganic-mineral treatments lead to chemical interactions with the minerals of the substrate and, more precisely, with the specific surface of exposed stone grains. Furthermore, as each rock has a specific microstructure and grain size, stone grains have specific surface for any given lithotype. The second aspect is that the weathering and decay mechanisms significantly modify the cohesion of stone materials, increasing the exposed specific surface of lithotypes and modifying the porous structure. Therefore, the increase of the potential reactivity and the exposed reactive surface of stone grains will be different from case study to case study.

It follows that the reaction mechanisms of a consolidating treatment with a given stone material should be investigated considering the complex interplay of the substrate features, the physical-chemical properties of the consolidating product and the treatment conditions (*e.g.,* contact time, application method, product molarity, solvent type, etc.) [47,62]. In addition, it is well known that the capillarity

properties of a lithotype are significantly different in a fresh quarry stones and the same stone of an artwork naturally decayed. Thus, in the view of Conservation Science, it is imperative to characterize the diffusion mechanism and the exposed surface of stone grains on quarry stone specimens as well as on artificially decayed/weathered specimens and naturally deteriorated stone artefacts.

This PhD thesis is focused on the conservation of three carbonatic stones quarried in Italy, widely used in architecture and characterized by different origin, microstructure, porosity or mineralogical composition.

The *Carrara marble* and the *Noto limestone* were selected in order to study the interaction of DAP solutions with calcite-based lithotypes and to evaluate the potentiality of DAP treatments to consolidate highly porous vs compact crystalline substrates. A specific insight is carried out on *Angera stone*, a sedimentary dolostone largely used in Milan and Lombardy for several sculpture masterpieces and building facades. In fact, severe decay damages are documented on carved elements in Angera stone, but no data are available on the potential use of DAP treatments to preserve dolostones.

Summarizing, this research is inserted in the context briefly described and it is focused to:

- characterize the reaction products formed after the DAP treatments on carbonatic stone substrates, defining their crystal-chemistry and their distribution on the substrate;
- define a new multi-analytical approach able to discriminate the calcium phosphate phases with destructive and non-destructive methods;
- understand how the peculiarity of the lithotype (in terms of composition and microstructure) and of the treatment method (application technique, molarity, pH) influence the DAP reaction with the stone substrate and the nucleation of newly-formed phases;
- investigate the diffusion of the newly-formed phases inside the stone matrix, defining their composition, distribution and penetration depth;
- test the application of the DAP solutions to consolidate naturally decayed Angera stone carved artefacts.

The final attempt of this PhD research is to develop scientific guidelines for optimized treatments with improved performances, able to consider the peculiarity of specificity case studies and the conservative history of stone artworks in the field.

2 Crystal-chemistry of calcium phosphates

2.1 Phosphate minerals

Phosphate minerals are abundant in nature, and they have been known since ancient times in the form of gemstones (*e.g.,* turquois) or bone minerals (*e.g.,* apatite). Besides these two phosphate phases, only six other phosphate minerals were known before 1800, including lazulite, pyromorphite (lead apatite), torbenite and vivianite [70].

Geologically, phosphorous is an abundant crustal element and the phosphate minerals are potential accessory minerals in every rock formation. Phosphate minerals, especially apatites, are common accessory minerals in many igneous rocks (deposits of apatites), metamorphic and sedimentary rocks (phosphorites) [71]. Pegmatites are the major host of phosphate minerals, in association to rare elements. The high number of possible structural replacements and the wide number of secondary minerals, which can be derived by the supergene alterations of the so-called primary phosphates, origin a very wide fan of different phosphate phases. Biological systems generate their own important suite of phosphate minerals, since most of the normal and pathological hard tissues of vertebrates are apatitic minerals [64,70,71].

Natural phosphate minerals are generally anisodesmic with other XO_4^{3-} groups. Mutual substitution of P for As are very common, as well as the complete solid solutions between some phosphates and arsenates [70,72,73]. Solid solutions between phosphates and silicates have been observed at high temperature (950-1450 °C) [74] and the extensive replacement of P with Ge, V, S and B has been reported in apatites and other phosphate minerals. Isotypism and isomorphism in phosphate minerals are common.

In general, the minerals of this class are divided in:

- Anhydrous phosphates (*e.g.,* xenotime YPO_4, monazite (Ce, La, Th)PO_4);
- Anhydrous phosphates with additional anions. The ions are usually [OH] and [F], and they can be replaced isomorphically. An example is the apatite series and the pyromorphite series. In the pyromorphite series, the external ion is [Cl] and the end members are the pyromorphite $Pb_5(PO_4)_3Cl$, the mimetite $Pb_5(AsO_4)_3Cl$, and the vanadinite $Pb_5(VO_4)_3Cl$;
- Hydrated phosphates without additional anions. It includes several minerals, among which: the vivianite series (general formula $Me_3^{II}(XO_4)_2 \cdot 8H_2O$, where Me_3^{II} is a bivalent cation, *e.g.,* Mg-isomorphogen and X can be P or As), the group of the "micaceous" uranyl oxysalts (*i.e.,* autunite, uranocircite, torbernite and zeunerite) and brushite $CaHPO_4 \cdot 2H_2O$;
- hydrated phosphates with additional anions (*e.g.,* turquois, $CuAl_6(PO_4)_4(OH)_8 \cdot 4H_2O$). The additional anion is usually [OH], seldom [Cl].

2.2 Calcium phosphate minerals

It is possible to identify four structurally different types of phosphates: the orthophosphates (PO_4^{3-}), the metaphosphates (PO_3^-), the pyrophosphates ($P_2O_7^{4-}$), and the polyphosphate ($PO_3)_n^{n-}$ [64].

This PhD thesis focuses in particular on calcium phosphates, as Ca-phosphates are of great interest in Cultural Heritage and Conservation field. In fact, calcium phosphates have been used as pigments (white and black bone ash), utensils and ornaments (animal bones and teeth) or have been found in historical patinas on ornamental stones and wall paintings, probably as mineralised by-product of bio-decayed organic substance [25,27,75]. More recently, calcium phosphate phases have been proposed as new products for the conservation of decayed stone materials.

In this light, the main crystal-chemistry features of the calcium phosphate phases investigated in this thesis are briefly described in the following section.

2.3 Calcium orthophosphates

The calcium orthophosphates belongs to the "0.8 Strunz class of phosphates, arsenates and vanadates" or to the 37, 39 and 41 Dana classes "Anhydrous Acid Phosphates,Hydrated Acid Phosphates and Anhydrous Phosphates, etc. Containing Hydroxyl or Halogen", respectively. To this mineral class belong more than 400 minerals, with a structure built up with the $[PO_4]^{3-}$ tetrahedron as building block unit. Many of them also include hydrogen, in the form of acid orthophosphate anions ($H_2PO_4^-$, HPO_4^2) and/or structural H_2O molecules.

Minerals, or synthetic inorganic compounds, in the tertiary system $Ca(OH)_2$-H_3PO_4-H_2O are characterized by different calcium to phosphate molar ratio (Ca/P), acidity and solubility. In general, the lower the Ca/P ratio, the more acidic and soluble the calcium phosphate phase; hydrated phases are more soluble than anhydrous ones. The Ca/P molar ratio ranges between 0.5 and 2.0 [65,76]. The processes of nucleation and growth of calcium orthophosphates have been widely reviewed and it is general opinion that the crystallization of many calcium phosphates involve the formation of metastable precursor phases that can transform into more stable phases. Moreover, the presence of organic molecules or inorganic additives have a strong influence of the crystallization pattern and the descending reaction frequently engages the formation of complex mixture of intermediate phases, whose composition is difficult to predict [77].

2.3.1 The apatite series

Apatites form an important series of minerals and have the general formula $Ca_5(PO_4)_3X$, where X can be a F^- (fluorapatite, FAp), OH^- (hydroxyapatite, HAP) or a Cl^- (chlorapatite, ClAp) [78]. The basic apatite structure is hexagonal, with space group $P6_3/m$ and lattice parameter $a \sim 9.4$ and $c \sim 6.9$ Å. Ca^{2+} ions can be partly or completely replaced by Ba^{2+}, Sr^{2+} or Pb^{2+}, and PO_4^{3-} by AsO_4^{3-}ions. Coupled substitutions are very common as well. Carbonate apatites (CO_3Aps) are a complex and common

example of nonstoichiometric substitutions with CO_3^{2-} groups and vacant sites, replacing PO_4^{3-}. Some site substitutions lead to lowering of the symmetry.

Hydroxyapatite (HAP, HAp, HA, OHAp, $Ca_{10}(PO_4)_6(OH)_2$, Ca/P = 1.67)
Hydroxyapatite is the most stable and least soluble calcium orthophosphate after fluorapatite. The word hydroxylapatite is also used, especially in the older literature. Stoichiometric HAP crystals may have either monoclinic (space group $P2_1/b$ with lattice parameters $a \sim 9.42$, $b \sim 2a$, $c \sim 6.88$ Å, $\gamma \sim 120°$ [79]) or hexagonal (space group $P6_3/m$ [80]) symmetry. The most stable is the monoclinic form, while the hexagonal one generally occurs in biological apatites or heating the monoclinic HAP at temperatures above 250 ºC (with a monoclinic-to-hexagonal phase transition [71,76]). The crystal structure of HAP is built up by regular PO_4-tetrahedra and distorted CaO_9- and CaO_5OH-polyhedra. CaO_5OH-polyhedra are hexagonally disposed about a central [001] (Fig. 2.1). The OH ions lie in columns on these hexads at $(0,0,z)$. In hexagonal HAP, the hydroxide ions are more disordered if compared with the monoclinic form, pointing either upward or downward along [001]. Partial substitutions of the hydroxide group, by fluoride or chloride, stabilize the hexagonal structure of HAP at ambient temperature. Therefore, hexagonal HAP is seldom a stoichiometric phase. The surface layers of HAP are usually compositionally different from the bulk and display Ca/P molar ratios from 1.67 for stoichiometric HAP to ~1.5 of fully calcium-deficient HAP [64,80,81].
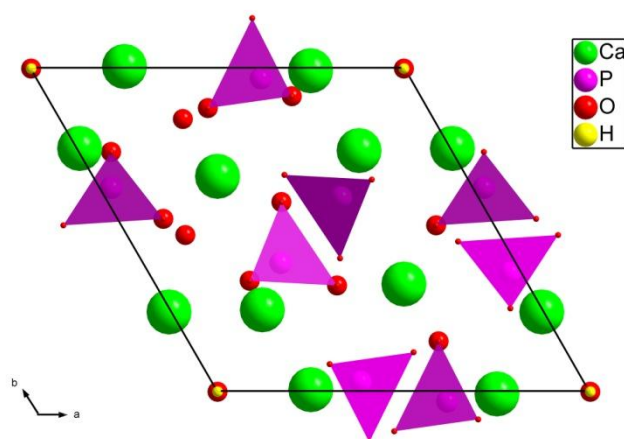

Fig. 2.1 Structure of hydroxyapatite, observed along the *c* axis. PO₄ units are showed as tetrahedra.

Calcium-deficient hydroxyapatite (CDHAP, CDHA or Ca-def HAP, $Ca_{10-x}(HPO_4)_x(PO_4)_{6-x}(OH)_{2-x}$ with $0 < x < 1$)
Calcium-deficient hydroxyapatite crystals are poorly crystalline and of submicron dimensions. The heating above 700 ºC converts CDHAP with Ca/P = 1.5 to β-TCP and that with $1.5 < $ Ca/P $ < 1.67$ into a mixture of HAP and β-TCP. The variability in Ca/P molar ratio of CDHAP has been explained through different models: surface absorption, site substitution and inter-crystalline mixtures of HAP and OCP [82,83]. In CDHAP structure, there are vacancies of Ca^{2+} and OH^- ions; for the orthophosphate ions, a portion of PO_4^{3-} ions is either protonated (as HPO_4^{2-}) or substituted by other ions (e.g., CO_3^{2-}) [84].

Due to a lack of stoichiometry, CDHAP usually contains other ions as well [85]. The refinement of the CDHAP structures are still missing and the unit-cell parameters remain uncertain; however, a study of defects has been published by Zahn and Hochrein [86]. At a first approximation, CDHAP can be considered a HAP with some missing ions [87]. More pronounced is the calcium deficiency, and more disordered and defected is the CDHAP structure [88].

2.3.2 Nonapatitic calcium phosphates

Dicalcium phosphate dihydrate (DCPD, $CaHPO_4 \cdot 2H_2O$, Ca/P=1)

The DCPD crystals are structurally and compositionally identical to the mineral brushite, but the acronym is used only for the synthetic counterpart. DCPD has been described either in the monoclinic non-centrosymmetric space group *Ia* [89] with *Z*=4, or in the centrosymmetric space group *Ia*/2, with lattice parameters $a \sim 5.81$, $b \sim 15.18$, $c \sim 6.24$ and $\beta \sim 116.4°$ [90]. The structure consists of chains made by discrete PO_4 groups, the oxygens of which shared by Ca atoms on each side. These chains lie on (010) and run along a direction parallel to [101]. These chains form corrugated sheets which represent the prominent feature of the structure [90]. The sheets are composed of $CaHPO_4$, are normal to the *b*-axis, and H_2O molecules are inter-layered between the calcium phosphate chains [64]. The structure of DCPD is closely related to that of gypsum, $CaSO_4 \cdot 2H_2O$.

DCPD is formed from solutions at pH < 6.5, it is described as an intermediate in bio-mineralization and, with other phases (*e.g.,* octacalcium phosphate (OCP) and amorphous calcium phosphate phases (ACP)), it is a metastable precursor in the precipitation of hydroxyapatite [64,77].

Dicalcium phosphate anhydrous (DCPA, $CaHPO_4$, Ca/P=1)

The DCPA crystals are structurally and compositionally identical to the mineral monetite, but, likewise DCPD, the short form DCPA identifies the phases artificially synthesised [78]. DCPA can be obtained with different protocols [78] or by dehydration of DCPD crystals at 180 °C [68]. At room temperature, DCPA is triclinic, space group *P*-1 [91] with lattice parameters $a \sim 6.91$, $b \sim 6.6$, $c \sim 6.99$ Å, $\alpha \sim 96.34$, $\beta \sim 103.82$ and $\gamma \sim 88.33°$ [92].

Octacalcium phosphate (OCP, $Ca_8(HPO_4)_2(PO_4)_4 \cdot 5H_2O$, Ca/P=1,33)

The structure of OCP, initially defined by [93] and refined in 1988 [94], has been deeply investigated [93–96]. It is is triclinic, space group *P*-1, with the unit-cell parameters: $a \sim 19.69$, $b \sim 9.52$, $c \sim 6.83$ Å and $\alpha \sim 90.15$, $\beta \sim 92.54$ and $\gamma \sim 108.65°$ [94]. The asymmetric unit is $Ca_8(HPO_4)_2(PO_4)_4 \cdot 5H_2O$, with Z = 2. The structure of OCP is composed of apatitic layers (sheets of phosphate ions interspersed with Ca^{2+} ions) alternated with "hydrated" (phosphate and Ca^{2+} ions less densely packed with a slightly variable number of bonded H_2O molecules) parallel to (100). The structure of OCP shows remarkable similarity to the hexagonal structure of hydroxyapatite [64,65,78], and this can determine the epitaxial growth of these two phases [97] or the inclusion of OCP as "central dark lines" observed in biological apatites [64,71]. Morphologically, OCP crystallizes as {100} blades of triclinic pinacoidal symmetry, elongated along the *a*-axis and bordered by the forms {010}, {001} and {011}. The H_2O content of OCP crystals is about 1/5 of that of DCPD and this is partly responsible for its lower solubility [64,71]. OCP is described as a possible unstable transient intermediate in the formation of carbonated apatite of

hard tissues [64,98] because it nucleates and grows more easily in aqueous solutions than the thermodynamically more stable hydroxyapatite.

β-tricalcium phosphate (β-TCP, β-$Ca_3(PO_4)_2$, Ca/P=1,50)

β-TCP crystallizes in the rhombohedral space group *R*3*c* with unit cell parameters $a \sim 10.44$, $c \sim 37.37$ Å (hexagonal setting) and its unit-cell contains 21 [$Ca_3(PO_4)_2$] formula units [64,97,99]. The crystal structure of β -TCP has been described in terms of a distorted $Ba_3(VO_4)_2$–type structure [78]. β -TCP has three non-equivalent PO_4^{3-} groups, each with specific intra-tetrahedral bond lengths and angles. One of the PO_4^{3-} groups is characterized by positional disorder, with resulting partial site occupancies. The ideal crystal structure of β-TCP has voids that are virtually too small to accommodate calcium sites; however, smaller cations can occupy the voids and stabilize the structure: *e.g.,* whitlockite (β-TCa,MgP, β-$(Ca,Mg)_3(PO_4)_2$ or β-TCMgP, $Ca_9Mg(PO_3OH)(PO_4)_6$), the Mg-substituted natural form of β-TCP, which is stabilized by the accommodation of magnesium ions [99].

Crystalline β-TCP is a high temperature phase (formation above 800 ºC, prepared by thermal decomposition of calcium phosphates or by solid-state interaction of acidic calcium orthophosphates, *e.g.*, DCPD or OCP, with a base, *e.g.*, CaO) and cannot be precipitated from aqueous solutions. The heating above ~ 1125 ºC transforms β-TCP to α-TCP [71].

Amorphous Calcium Phosphates (ACPs)

Amorphous Calcium Phosphates (ACPs) are a particular class of calcium orthophosphates because they are characterized by variable chemical composition and glass-like physical properties, with no translational long-range orders (LRO) of the atomic sites. Until 2010, Amorphous Calcium Phosphate (ACP) has been considered a specific compound. The current approach considers ACPs as amorphous forms of other calcium orthophosphates and divides the ACPs in two groups: low-temperature ACPs (obtained from aqueous-solutions) and high-temperature ACPs. The low-temperature ACPs, described with the chemical formula $Ca_xH_y(PO_4)_z \cdot nH_2O$, with n=3–4.5 and 15-20% H_2O, are often detected as a transient precursor phase during the precipitation of other calcium orthophosphates from aqueous solutions. Low temperature, high solution pH and high concentration of Ca^{2+} and PO_4^{3-} ions increase the amorphization degree of ACPs. Since ACPs are characterised by the lack of LRO, it is complex to describe the structure of similar phases. Their short-range order (SRO) depends, case by case, on several variables, *e.g.,* Ca/P molar ratio, preparation conditions, etc. Two hypothesis were reported in the literature about the potential SRO structure of ACPs: the first considers that ACPs have an apatitic structure in crystals too small to give an X-ray diffraction pattern; the second describes ACPs as roughly spherical cluster of $Ca_9(PO_4)_6$ ions, randomly close-packet to form larger particles with water in the interstices (Posner's clusters). Similar clusters should be the first nuclei in the formation of calcium-deficient hydroxyapatite [76]. The ACPs are thermodynamically unstable phases and spontaneously tend to transform to more stable crystalline calcium orthophosphates, mainly to calcium apatites [100].

3 Materials and Methods

As described in § 1.3, the Ph.D. reserach project focuses on the characterization of crystalline phases formed after stone consolidation with inorganic mineral treatments. The research activity involved the use of reagents to treat different lithotypes with different treatment methods, and pure calcium phosphate powders (commercial or synthesised in the lab) were used as reference materials to characterize the newly-formed phases and their location with respect to the stone matrix. This wide-range fan of materials was characterized by a multi-analytical approach. Specific analytical protocols and measurement setup were *ad hoc* defined to investigate specific issues. In the following, four schemes are shown in order to describe the analytical techniques used for different goals (Fig. 3.1-Fig. 3.4). The same experiments were performed several times in order to check the statistical reproducibility of the acquired data.
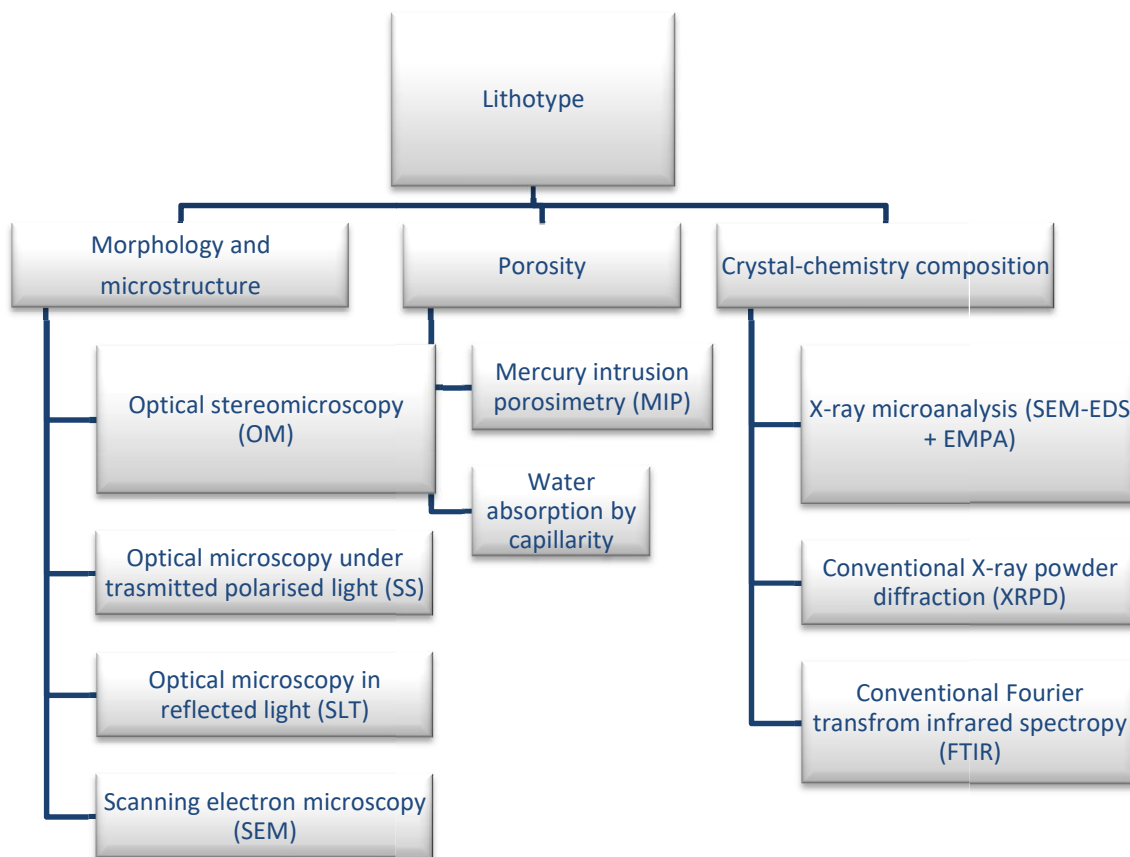
Fig. 3.1 Schematic summary of the analytical techniques used for the characterization of different lithotypes.
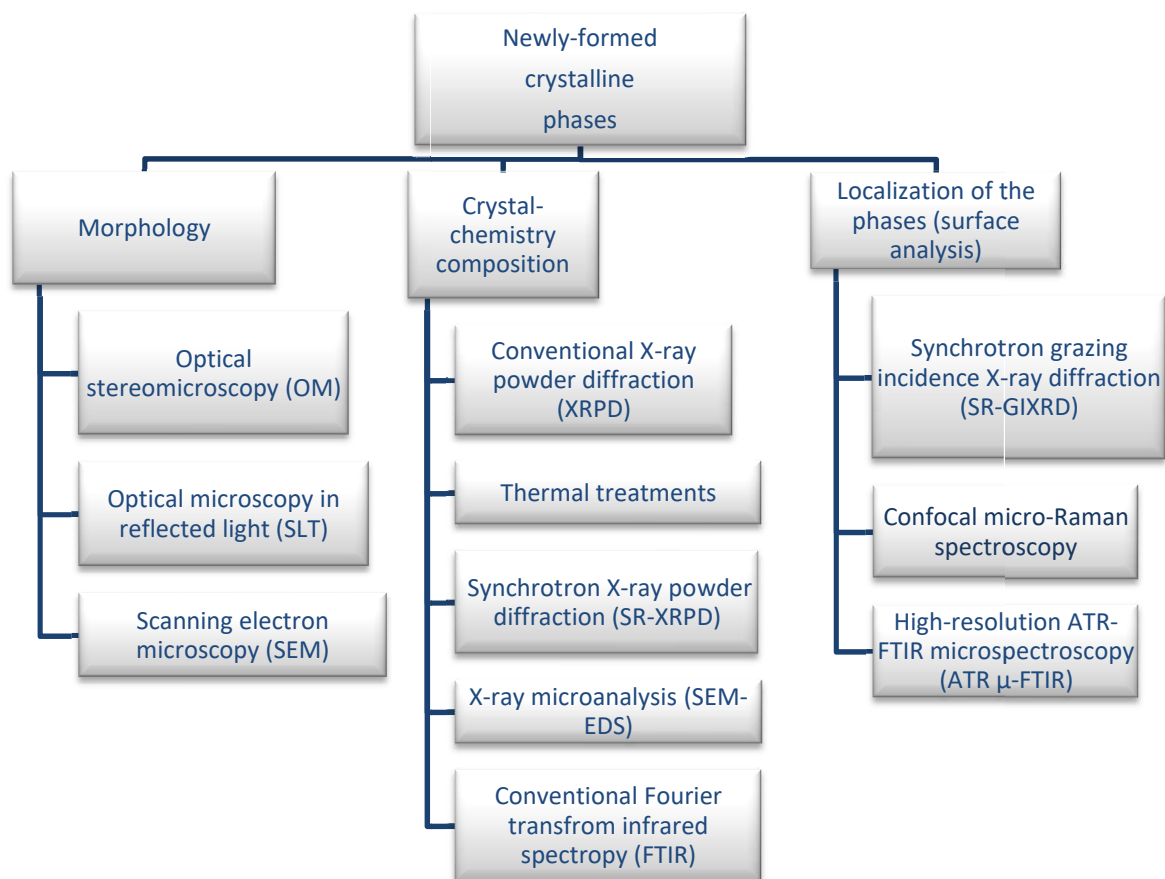
Fig. 3.2 Schematic summary of the analytical techniques used for the characterization of the crystalline phases formed on the stone substrates after the consolidating treatments.
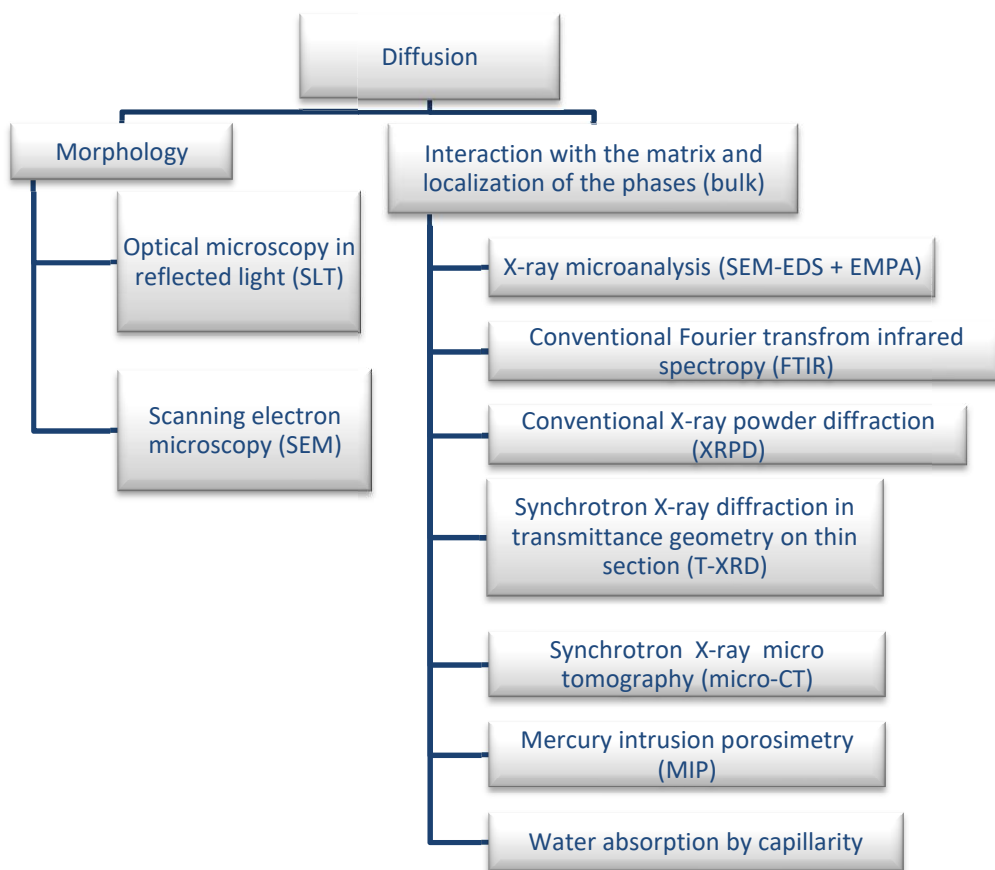
Diffusion

Morphology

Optical microscopy in reflected light (SLT)

Scanning electron microscopy (SEM)

Interaction with the matrix and localization of the phases (bulk)

X-ray microanalysis (SEM-EDS + EMPA)

Conventional Fourier transfrom infrared spectropy (FTIR)

Conventional X-ray powder diffraction (XRPD)

Synchrotron X-ray diffraction in transmittance geometry on thin section (T-XRD)

Synchrotron X-ray micro tomography (micro-CT)

Mercury intrusion porosimetry (MIP)

Water absorption by capillarity

Fig. 3.3 Schematic summary of the analytical techniques used to study the penetration depth of the newly-formed phases in the porous stone substrates.

Treatments to naturally decayed lithotype

Morphology

Optical stereomicroscopy (OM)

Optical microscopy in reflected light (SLT)

Scanning electron microscopy (SEM)

Crystal-chemistry composition of the new phases

X-ray microanalysis (SEM-EDS + EMPA)

Vibrational spectroscopies (FTIR + Raman)

Conventional X-ray powder diffraction (XRPD)

Evaluation of treatment performances

Colour measurement

Water uptake by capillarity with the contact sponge method

Mercury intrusion porosimetry (MIP)

Fig. 3.4 Schematic summary of the analytical techniques used to study the DAP reaction with a carbonate carved lithotype decayed in urban environment.

3.1 Materials

3.1.1 Reagents and powder references of calcium phosphate phases

DAP (CAS Number 7783–28-0, assay $\geq$ 99.0%, reagent grade), DCPD (CAS Number 7789-77-7, assay $\geq$ 98.0%, reagent grade) and HAP (CAS Number 1306-06-5, reagent grade) were purchased by Sigma-Aldrich. $NaH_2PO_4 \cdot H_2O$ (CAS Number 10049-21-5, assay $\geq$ 99.0%, reagent grade), $Ca(CH_3COO)_2 \cdot xH_2O$ (CAS Number 62-54-4, assay $\geq$ 99.0%, reagent grade), HCl were purchased by Merck, Darmstadt Germany.

DCPA (CAS Number 7758-87-4) was obtained by dehydration of DCPD, with a heating treatment at 180 °C in air for 2 h, as reported by Drouet [68].

OCP (CAS Number 13767-12-9), not available on sale, was synthesized in laboratory testing the protocols suggested by C. Drouet in [68], by W. E. Brown in [95] and by R. LeGeros in 1985 [101]. OCP crystallized successfully with the latter protocol [101], even if mixed with plate-like crystal of DCPD that embedded OCP fibres; no OCP was formed with the first two ones [68,95]. Therefore, the reaction conditions suggested by R. LeGeros were modified in order to promote the formation of pure OCP. In particular, 250 mL of 0.04 mol/L $NaH_2PO_4 \cdot H_2O$ were added drop wise with a speed of 1.39 mL/min in quiescent 250 mL of 0.04 mol/L $Ca(CH_3COO)_2 \cdot xH_2O$ at 70 °C (± 1°C). At the beginning of the reaction, the pH of calcium acetate solution was adjusted to 4.50 by the addition of 6.45 mL of 1 mol/L HCl solution. The molarity of the HCl solution was selected in order to regulate the pH without any substantial volume variation of the mother solution, as the use of more diluted acid solutions lead to the formation of impure OCP. At the end of the reaction, the pH was 4.28. The solid precipitated was kept in contact with the mother solution for 20 minutes; after that, it was isolated by filtration, rinsed with deionised water and dried at room temperature. The obtained powders were stocked in a desiccator to avoid any phase transformation.

The synthesised OCP consists of micro-crystals with a platy blade-like or acicular morphology (Fig. 3.5). These crystals are typified by an extreme thinness in one direction and some of them are optically twinned. The nature of the precipitate was checked with a structure refinement by the Rietveld method using the X-ray synchrotron powder diffraction pattern (further details in § 3.2.3.2). The high-quality refinement ($R(F^2)$ = 0.0435, wRp = 0.0588) confirmed the formation of monophasic OCP with a triclinic structure (space group: P-1), with unit-cell parameters: a = 19.677(5) Å, b = 9.533(3) Å, c = 6.835(2) Å, α = 90.14(3) °, β = 92.55(4) °, γ = 108.31(3) °, V = 1215.7(4) Å^3, in good agreement with the data previously reported in the literature [93,94].
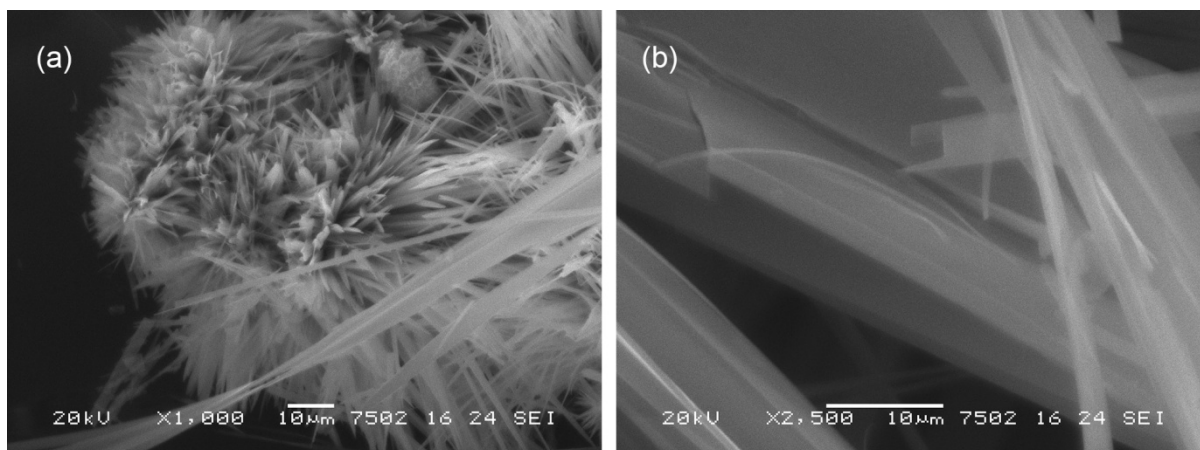
Fig. 3.5 SEM images (secondary electrons) at different magnification of OCP crystals formed by precipitation after the optimized protocol.

3.1.2 Treatment protocol

The DAP treatments were carried out on Carrara marble, Noto limestone and Angera stone. Depending on the specific research goals, the treatments and the investigations were carried out on quarry specimens, on artificially weathered specimens and/or on a naturally decayed carved artwork (details at § 4). The stone substrates were treated by poultice or capillarity with two different molarities (0.76 M and 3.00 M) of DAP aqueous solutions. The 0.76 M concentration was selected on the basis of previous experiments [31,50] and on the *in situ* DAP consolidating practice [102]; the choice of 3 M concentration was driven by previous experimental findings reported in literature [54], to have the formation of a thicker layer of calcium phosphates. To ensure a statistics trend of the data, three similar specimens were prepared for each kind of treatment protocols.

The poultice treatments were performed using a ratio of 520 mL of DAP solution for 100 g of dry cellulose pulp (MH 300 Phase, Italy). The cellulose pulp and the DAP solution were hand blended for about 5 minutes and then a poultice layer of about 1-1.5 cm was spread onto the specimens (Fig. 3.6a). A sheet of Japanese paper was placed between the paper poultice and the stone substrate, to rule the fluid transport and to prevent damages at the specimen surface due to the sticking of the poultice after drying. The specimens were wrapped in a plastic film after poultice application to avoid the evaporation of the solution and left reacting for 24 hours (Carrara marble and Noto limestone) or for 48 hours (Angera stone). After that, the plastic film was removed and the specimens, with the poultice on top, were left drying at room temperature for other 24 hours. The poultice was then removed.

The treatments by capillarity (Fig. 3.6b) were performed putting the specimens in contact with DAP water solution through a multiple layer of filter papers (about 1 cm) inside plastic boxes. The filter papers were inserted dry and they suctioned the consolidating solution by capillarity. Dry specimens were then put in contact to the wet surface of the paper filters. During the treatment, the boxes were kept close to avoid the evaporation of the solution. After 24 hours, the specimens were removed from the paper filters and left to dry for 24 hours.

A set of Noto limestone specimens was treated for 2 hours by poultice and capillarity, in order to compare the effects induced by treatment time on the crystallization and the penetration depth of the

newly-formed phases. The contact time of 2 hours has been selected in order to allow the DAP solution to partially react with the substrate.

After the drying of 24 hours, all the treated specimens were rinsed three times by immersion or by poultice in MilliQ water to remove the possible soluble phases (unreacted DAP and reaction byproducts) and dried again in desiccators. The investigations were carried out after 7 days, at complete drying.
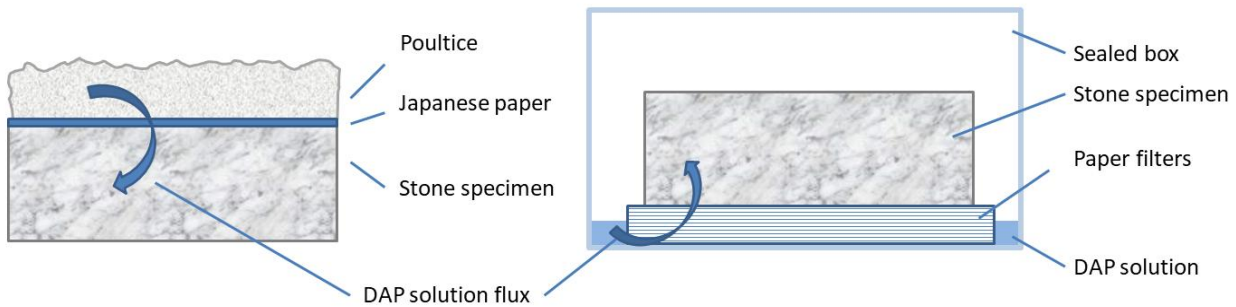

Fig. 3.6 Scheme (not in scale) illustrating the treatments performed by poultice and capillarity on the stone specimens.

3.2 Analytical techniques

3.2.1 Microscopy analyses

3.2.1.1 Optical microscopy (OM)

The morphological feature of the stone materials before and after the consolidating treatments were evaluated by optical stereomicroscopy. In particular, the observations focused to check any potential occurrence of superficial macro- and micro-crystals as well as to understand any possible influence of the treatment method or the reagent molarity on the newly-formed phases and their "consolidating action" (*e.g.,* presence of detachments, micro-cracks, peeling effects, formation of superficial crusts). The optical micro-images were also used to document the morphology of the calcium phosphate phases synthesised in lab and used as references. The observations were performed with a Leitz Wild M420 stereomicroscope (magnifications in the range 4x-64x) connected with a digital camera Nikon DS-5M/USB with; the micro-images were collected and manipulate with the Lucia Image TM software (version 5.0).

3.2.1.2 Optical microscopy under transmitted polarised light (SS)

The microstructure and texture of quarry lithotypes and artificially decayed specimens were investigated on thin sections with a transmitting-light polarizing microscope Nikon Eclipse E400 Pol.

The images were collected by the digital camera 3CCD JVC KY-F55BE and managed by the Lucia Image TM software (version 5.0).

3.2.1.3 Optical microscopy in reflected light (SLT)

The crystallization of phosphate phases on the surface of treated stone materials, their interaction with the surface of stone grains (corrosions, detachments, binding action) and their penetration depth inside the stone matrix was preliminary observed on polished cross sections with the optical microscope in reflected light in dark field. The observations were performed with a Leitz Ortholux microscope (magnifications in the range 6.5x - 44x) coupled with a digital camera Nikon DS-5M/USB and managed by the Lucia Image TM software (version 5.0).

3.2.1.4 Scanning electron microscopy (SEM-EDS)

Scanning Electron Microscopy was extensively used to characterize the morphology of raw materials (*e.g.,* powder references and non-treated lithotypes), of crystalline phases nucleated after the treatments and of cross sections of treated lithotypes. The shape of the newly-formed crystalline phases was investigated by zenithal observations on the surface of treated specimens; the growth of the phases from the surface, the action of the treatment on the minerals of the stone substrate, the arrangement of the new phases on the substrate and their distribution inside the stone matrixes were analysed on polished cross sections.

The observations were carried out with a scanning electron microscopy (SEM) JEOL 5910 LV with tungsten filament source coupled with energy dispersive X-ray spectrometer (EDS) IXRF-2000 (0–20 keV). Morphological and micro-chemical analyses were performed in high and low vacuum mode (HV-SEI, LV-BSE) on carbon-coated samples.

3.2.1.5 Electron microprobe analyses (EMPA)

Electron micro probe analyses were carried out to determine the chemical composition of the stone matrixes and of the newly-formed phases nucleated in the substrate. The investigation were carried out with a JEOL 8200 Super Probe instrument equipped with pre-centred tungsten filament hairpin type coupled with a with wavelength dispersive X-ray spectrometer system (WDS). WDS quantitative analysis and micro-chemical mapping were performed in high vacuum mode on carbon-coated samples.

3.2.2 Mercury intrusion porosimetry (MIP)

The porous microstructure and the pore size distribution is a key feature of specific lithotypes. The decay processes act on the microstructure of the stone materials and modify the porosity of the substrate following different patterns governed by the nature of the lithotype. A third modification might occur during inorganic-mineral treatments, as these products diffuse inside the voids of the stone matrix, react with the surface of the exposed stone grains and nucleate new phases inside the pores. Therefore, the original porous microstructure of quarry stone materials, their modification with

artificial weathering or with the natural decay in polluted environments, along with the effects induced by DAP consolidant treatments, were investigated with a Thermo Scientific mercury intrusion porosimeter Pascal 140 + Pascal 240, in the range of pore radius 50 - 0.0037 μm, with a pressure between 0.02 - 200 MPa, volume resolution of 0.1 mm^3 and accuracy > 0.2 %. MIP measurements provide the total pore volume and the pore size distribution, in the macro- and mesopore IUPAC ranges [103,104].

3.2.3 X-ray diffraction techniques

X-ray diffraction techniques (XRD) were used to characterize the minerals of the quarry lithotypes as well as to investigate the phase composition and the penetration inside the substrate of the newly-formed crystalline phases nucleated after the consolidating treatments. The XRD techniques were widely used over the Ph.D. research project and the XRD measurements were performed with different experimental setup, collecting XRD data using the diffractometers available at the Earth Science Department and at the ICBVC lab, as well as the high-resolution diffractometers available at the beamlines of large-scale facilities (Elettra, Trieste – Italy; E.S.R.F., Grenoble – France).

The synchrotron radiation (SR) provided the advantage of an extremely high number of photons coupled with a very small spot size. The SR source provides continuous radiation in a tunable and wide energy range, allowing the optimization of measurements conditions by selecting the excitation energy. The high brightness and high good signal-to-noise ratio of SR provides high-quality data and high spatial resolution. The experimental setup, the instrumental parameters and the analytical protocol were *ad hoc* refined at each set of measurements, according to the different needs. The different experimental setup and working parameters are described in the following.

A whole pattern profile fitting of the diffraction data acquired with SR was performed by the Rietveld method [105,106], using the GSAS package (http://www.ccp14.ac.uk/solution/gsas/; profile function: pseudo-Voigt, background function: Chebyshev polynomial). The Rietveld refinement on silicon standard was used to determine the experimental wavelengths (and related error) of SR measurements.

3.2.3.1 Conventional X-ray powder diffraction (XRPD)

Preliminary bulk information of the commercial references and of the crystalline phases nucleated on the treated specimens were obtained with a Panalytical X'Pert PRO X-ray powder diffractometer, equipped with a Cu-Kα radiation source (λ ~ 1.54 Å), a PW 3050/60 goniometer, anti-scatter slit and divergence slit (1° and 1/2° respectively), a PW3040/60 generator and a X'Celerator solid state detector PW3015/20 nickel filtered. The newly-formed calcium phosphates were scratched from the whole treated surface, finely ground and spread on zero-background holders. The XRD patterns were collected at room temperature (rT, 25 °C) in Bragg-Brentano geometry in the angular range 3° – 75° of 2ϑ, with a stepsize of 0.017 °, scan-step time of 200 s, accelerating voltage of 40 kV and electric current at the Cu anode of 40 mA.

3.2.3.2 Synchrotron X-ray powder diffraction (SR-XRPD)

The X-ray diffraction patterns of synthesized OCP powder reference and of crystalline phases formed after consolidating treatments were collected at the ELETTRA Synchrotron facility, Trieste (Italy). The newly formed phosphate phases were scratched from the treated stone surface and finely ground. The investigation with a synchrotron radiation was required to: i) perform a structural refinement by the Rietveld method; ii) assess the presence of minor phases in the synthesized OCP, and consequently to validate the synthesis route for OCP reference; iii) investigate the presence of minor phases and to discriminate slight differences between similar crystalline structures for samples scratched from treated stones.

The experiments were performed in transmission geometry, using quartz or boron capillary at the:

- XRD1 beamline [107]. The diffraction data were collected at rT with a monochromatic wavelength of $\lambda = 0.700784(6)$ Å, using a Pilatus 2M hybrid-pixel area detector.

- MCX beamline [108,109]. The diffraction data were collected at rT with focalized monochromatic beam of $\lambda = 0.885227(6)$ Å, using the high-resolution four circles Huber diffractometer and the MarCCD camera on the 2θ arm. Some samples were exposed to heating treatments aimed to investigate the phase transformation induced by heating and detect low fraction of secondary phases as thermal by-products. In-situ heating from rT to 900 °C was performed using a gas blower (Oxford Danfysik DGB-0002) with a heating ramp speed of 5 °C/min. The X-ray diffraction patterns were acquired in real-time at specific temperatures where phase transitions are expected (250 °C, 750 °C, 850 °C). Additional patterns were collected at 100 °C, 500 °C, at 900 °C and after cooling to rT.

For both the measurements, the diffraction patterns were collected in the 2θ angular range of $1.5 - 50°$, with a step size of $0.01°$.

3.2.3.3 Synchrotron grazing incidence X-ray diffraction (SR-GIXRD)

The GIXRD experiments were performed to characterize in a non-destructive way the composition of the crystalline phases nucleated on the surface of the treated stones in order to understand how the: i) composition of the substrate influences the composition of the nucleated phases; ii) possible presence of compositional micro-heterogeneity of the stone substrate might influence the growth of specific calcium phosphates phases.

The GIXRD experiments were carried out at the MCX beamline of the ELETTRA with the high-resolution diffractometer described in § 4.2.3.2. The experiments were performed on the treated specimens without any sampling using a focalized monochromatic beam of $\lambda = 0.88523(6)$ Å (exp. n° 20160183) and of $\lambda = 0.82591(6)$ Å (exp. n°20167062) in the 2ϑ angular range of $1.5 - 50$ °, with a step size of $0.01°$. The X-ray diffraction data were collected in grazing-angle geometry with fixed incident grazing angles (Φ): 0.5, 1.0, 2.5 and 5.0 °. The specimens were investigated also with $\Phi = 7.0$ ° but no significant differences were observed. The acquisition setup and the incidence angles were optimised considering the critical angle, the surface topology and the spatial resolution. The X-ray beam spot size was of 300 μm (vertical) x 500 μm (horizontal), allowing the investigation of a micro-portion of stone surface.

The optimized protocol was subsequently used to investigate in a non-destructive way historical painted stratigraphies or real artworks (§ 6.2).

3.2.3.4 Synchrotron X-ray diffraction in transmittance geometry on thin section (SR-TXRD)

The SR-TXRD analyses were used to investigate the penetration depth of calcium and magnesium phosphates inside DAP-treated stone materials. The SR-TXRD measurements were performed with an X-ray spot size in the range between 10-40 μm, in order to collect compositional information at the microscale. At the same time, the collection of XRD data of a volume of few dozen of cubic micrometres allows to average the possible micro-heterogeneity of the stone matrix, overcoming the limits of punctual analysis. The XRD measurements were performed in transmittance geometry on thin sections (400-900 μm) of treated stone embedded in epoxy resin. SR was necessary to detect weak XRD Bragg peaks emitted from minor phases or from low fractions of phases nucleated in the inner portion of the stone matrixes.

The SR-TXRD measurements were performed at the ID15b beamline of the European Synchrotron Radiation Facility (E.S.R.F., Grenoble – France) [110], with $\lambda = 0.410500$ (3) Å and at the XRD1 beamline of ELETTRA, with $\lambda = 0.688800$ (1) Å. The beamsize was 10×10 μm^2 or 40×40 μm^2 depending on the goal of the experiments.

3.2.4 Vibrational spectroscopies

The infrared and Raman vibrational spectroscopies were used to characterize the spectral feature of the minerals of the stone matrix and the newly-formed crystalline phases. Each technique and experimental setup was selected with specific goals.

3.2.4.1 Conventional Fourier transform infrared spectroscopy (FTIR)

The compositional characterization of the newly formed phases was performed with a Thermo Scientific™ Nicolet™ Nexus spectrophotometer equipped with a DTGS detector (spectral range 4000–400 cm^{-1}) coupled with a Continuμm™ infrared microscope with mercury cadmium telluride detector (MCT/A) cooled with liquid nitrogen (spectral range 4000–650 cm^{-1}). The spectral resolution used was 2 cm^{-1},with accumulations of 64 or 128 scans. Samples were prepared in KBr pellets or mounted in diamond anvil cell.

3.2.4.2 High-resolution ATR-FTIR microspectroscopy (ATR μ-FTIR)

The ATR μ-FTIR measurements were performed in order to investigate the microscale distribution of crystalline phases and to investigate how the variation of the pH value during the DAP reaction influences the formation of specific crystalline phases. The investigations were carried out with a LUMOS standalone FTIR microscope (Bruker Optik GmbH), equipped with a motorized *xyz* sample stage and automated Ge-ATR probe (tip diameter about 100 μm), driven by a piezo, included into the

8x cassegrain objective (NA = 0.6). Considering the Ge refractive index value (4), the theoretical lateral resolution of about 1 μm [23] was obtained collecting the spectra with a 4.0 x 4.0 μm^2 aperture, step size (along x and y) around 3.5 μm, 16 or 32 scans, spectral resolution of 4 cm^{-1} and different ATR pressure (low, medium, high). The data were treated with the OPUS-IR™ software (Bruker Optik GmbH, version 7.5).

3.2.4.3 Confocal micro-Raman spectroscopy

The Raman spectra of specific newly-formed crystals were collected with a Senterra dispersive micro-Raman spectrometer (Bruker). The investigations were carried out with the 532 nm (frequency-doubled Nd-YAG laser, 50 mW) and 785 nm (near-infrared diodes, 100 mW) excitation sources, in order to compare and distinguish the calcium phosphate Raman patterns acquired with different excitation lines. Spectra were colleed with a spectral resolution of 3 – 5 cm^{-1} (1200 grooves/mm gratings) in the range 100–4000 cm^{-1} and 30–1800 s acquisition time (3 – 30 accumulations, 10 – 60 s each). The instrument was equipped with a Peltier-cooled CCD detector (1024 × 256 pixels) and coupled to an Olympus BX51 microscope (50×, 50× LWD and 100× objectives) with motorised *xyz*. The spectrometer was calibrated using the silicon Raman peak at 520.6 cm^{-1}. The raw Raman spectra were elaborated with no background correction and no relative rescaling.

3.2.5 Synchrotron Radiation X-ray micro-Computed Tomography (SRμ-CT)

Synchrotron Radiation X-ray micro-Computed Tomography (SRμ-CT) was used to investigate the pore network, the pores shape and the connectivity of the voids, in order to understand how these features are modified by DAP treatments. SRμ-CT experiments were carried out at the SYRMEP (Synchrotron Radiation for Medical Physics) beamline at the ELETTRA Synchrotron facility, Trieste (Italy) [111–113]. The end-station is based on a Si (111) double-crystal monochromator, working with in Bragg configuration in the energy range 8.3-35 keV [114]. The hard X-ray imaging experiments were carried out using a 25 keV X-ray energy. The samples were mounted onto a high-resolution rotation stage and 1440 X-ray projections were acquired with constant angular step over a 180° rotation by a 12-bit water-cooled CCD camera (4008 × 2672 pixels), with a sample-to-detector distance of 200 mm. For this study, the tomographic images were acquired in edge detection mode (''near field'' Fresnel diffraction region) to take advantage of phase-contrast effects, in order to enhance the smaller features present in the samples and to highlight the interfaces between the different phases compared to the pure absorption mode [114,115].

To reconstruct a 3D image of the specimens, the tomographic projections were elaborated with the *SYRMEP Tomo Project* (STP), an open-source software tool designed for post-beamtime use [113,116]. In order to enhance the reliability of morphological and quantitative analysis, a single-distance phase-retrieval algorithm was used to increase the contrast between solid portion and voids. The 2D reconstructed slices were pre- and post- processed by using the ImageJ freeware software [117,118]. The 3D renderings were obtained using the commercial software VGStudio 3.1.2. The

quantitative analysis of the porosity was carried out with the software library Pore3D [119], written in IDL[©] language.

3.2.6 Physical properties measurements

3.2.6.1 Colour measurement (UNE-EN 15886:2011)

Spectrophotometry was used to measure the colour of the lithotypes before and after application of the DAP consolidant, in order to assess any changes in accordance with the UNE-EN 15886:2011 standard [120]. The measurements were carried pout using a Minolta CM-700d spectrophotometer with a geometry of diffuse reflectance. CIELab Colour Space was chosen and *L** (lightness, form 0 to 100), *a** (green-red chromatism, from -60 to +60) and *b** (blue-yellow chromatism, from -60 to +60) parameters were calculated by means reflectance values [120].

The measurement conditions were the following: measurement diameter of 8 mm; modes Specular Component Included/Specular Component Excluded (SCI/SCE), thus measuring both the light reflected specularly and the light reflected diffusely; D65 standard illuminant (which corresponds to daylight with a colour temperature of 6504 K) and observer 10°; wavelength range from 360 to 740 nm with stepsize of 10 nm.

The colour difference (ΔE) between untreated and treated specimens defined using the CIELab components (L_1*, a_1*, b_1*) and (L_2*, a_2*, b_2*) were calculated as:

$$\Delta E \quad = \sqrt{\Delta L^{*2} + \Delta a^{*2} + \Delta b^{*2}} \qquad\qquad (3.1)$$

Measurements were performed on prismatic laboratory specimens ($5\times5\times2$ or $5\times5\times5$ cm^3) as well as on the historical artefact in Angera stone. For each treatment condition, the colour change was calculated as the average of 25 measurements for laboratory specimens and of 50 measurements for the Angera stone carved artefact.

3.2.6.2 Water uptake by capillarity with the contact sponge method (UNI 11432:2011)

The contact sponge method measures the water absorption behaviour of a porous material, as indicated by the European Standard UNI 1142:2011 (*Beni culturali Materiali lapidei naturali ed artificiali - Misura della capacita di assorbimento di acqua mediante spugna di contatto*, [121]). The method determines the water absorption per unit area using a 1034 Rodac[®] contact-plate (with 5.6 cm diameter) containing a humid sponge *Calypso natural make-up* from Spontex[®]. The sponge, inserted in the contact-plate, is wetted with a known amount of deionised water and pressed against the investigated stone surface for a given time. For the experiments of this Ph.D. research project, the contact time was 60 s. The contact sponge is thicker than the height of the borders of the contact-plate, and this determines that a constant and maximum amount of pressure is applied manually [121,122].

The amount of water absorbed by the material surface under investigation is determined by a balance as the weight difference between the initial and final weight of the contact-plate containing the humid sponge, before and after contact with a surface. The water absorption (*Wa*) is expressed as the mass difference in function of area and time, according to the equation:

$$Wa\left(\frac{g}{m^2 s}\right) = \frac{\Delta m}{A \times t} = \frac{(m_i - m_f)}{A \times t}$$ (3.2)

With:

m_i = initial weight of the wetted sponge inside the contact plate, in g.
m_f = weight of the sponge inside the contact-plate after contact, in g.
A = sponge area (0.002376 m^2)
t = contact time, in s.

3.2.6.3 Water absorption by capillarity (UNI EN 15801:2010)

The effects induced by the treatments on the water transport properties and water sorptivity of the stone matrix were ascertained on untreated and treated samples according to the European Standard UNI EN 15801:2010 (*Conservation of cultural property – test methods – determination of water absorption by capillarity*, [123]). The protocol includes the gravimetric determination of the water absorption of a 50 × 50 × 20 mm specimens in contact with deionized water through a multiple layer of about 1 cm of filter papers. The specimens were dried for 7 days at 60±2 °C before the investigations. The experiment took place at room temperature in sealed boxes and the measurements have been carried out at regular steps (10, 20, 30, 60 min, and 2, 4, 5, 24 h).

The gravimetric increase due to water uptake was elaborated in the form of amount of absorbed water per surface unit (Q), water absorption curves and capillary absorption coefficient (CA) [124].

Q is calculated as

$$Q_i = \frac{(m_i - m_0)}{A} \times 1000$$ (3.3)

With:

m_i = weight, in g, of the wet specimen at the time $t_i(\sqrt{s})$
m_0 = weight, in g, of the dry specimen
A = surface, in cm^2, of the specimen in contact with the paper filters layer

The water absorption curve is expressed as Q (mg/cm^2) for the *y*-axis *vs.* the square root of the absorption time ($\sqrt{\text{seconds}}$) for the *x*-axis.

The slope of the curve is the capillary absorption coefficient, CA (unit = mg/(cm$^2\sqrt{s}$), and it is defined as the angular coefficient of the ideal straight line tangent the curve. CA is calculated as:

$$CA = \frac{Q_i - Q_0}{\sqrt{t_i}}$$ (3.4)

With:

Q_i = amount of water absorbed by capillarity by a surface unit at the time t_i

Q_0 = intercept obtained on the vertical axis of the straight line tangent the curve in the linear initial part of the curve

$\sqrt{t_i}$ = square root of the time t_i, in s.

CA is an important parameter to evaluate the water uptake in the short term as the higher is the slope, the higher is the water absorption rate of the material.

4 The lithotypes

For this PhD research activity, three different carbonatic lithotypes were selected in order to study the interaction of DAP solutions with compact and porous carbonates and to evaluate the potentiality of DAP treatments to preserve decayed matrixes.

The selected stones are Carrara marble, Noto limestone and Angera stone. The three lithotypes differ significantly for origin, microstructure, porosity or mineralogical composition. Literature include many researches dealing with the causes of stone decay and many references are available [125–128]. In general, as they are characterized by a carbonatic matrix, water plays a key role in the stone deterioration acting through the acid dissolution [129,130] and or by the transport of soluble salts [131]. Water, by definition presenting a neutral pH, becomes acidic due to the dissolution of carbon dioxide naturally present in air and to atmospheric urban pollutants, especially sulphur compounds (SO_x and H_2S), nitrogen compounds (NO_x and ammonia), natural and anthropogenic carbon dioxide (CO_2). The deposition of acid water, either in the form of rainwater or condensation, promotes a reaction of acid dissolution of the carbonatic cement of carbonate lithotypes, which basically develops a set of descending problems, *e.g.,* progressive corrosion of the substrate with surface recession, re-crystallization of salts, loss of cohesion. Typically, at drying of acid waters, the dissolved ions re-precipitate on the substrate with the formation of soluble salts (sulphates, nitrates and bicarbonates), often hydrated [1–3]. The phenomenon of salt re-crystallization occurs on the surface of the carved elements, with the formation of black crusts and decohesion, as well as inside the stone bulk, with the development of crypto-efflorescences.

The formation of decay salts in hydrated phases usually occur with a molar volume increase, which also induces noticeable mechanical damages when the precipitation of such phases takes place in the micropores. The decay evolves in decohesions and in the detachment of the crusts, with the exposure of inner layers, deeply pulverised [132,133].

A similar decay pattern, based on the combination of chemical and mechanical damages, also occur in the regions close to the sea, where the atmospheric water (acidified by natural CO_2 and artificial pollution) is also enriched of sodium chloride.

If the mechanisms of acid dissolution are common for all the carbonatic stone, each lithotype is characterized by the development of typical deterioration features [5,6]. Therefore, in the following, three brief sections are devoted to the main geological setting, the composition and microstructure, the typical decay features and the goals of this PhD study for each lithotype.

4.1 Carrara marble

The Apuan marbles, and White Carrara marbles in particular, were used as ornamental materials for historic and modern buildings, façades and sculpture elements since antiquity. A first documented trace of the use of Apuan marbles dates back to the Roman period, but a possible pre-Roman extraction has been hypothesised [134].

The Carrara marble basins are on the Tyrrhenian side of the Apuan Alps, a fundamental geological area belonging to the northern Apennines in the north-western region of Italy. The Apuan marbles are rocks of middle-grade dynamic thermic metamorphism of sedimentary carbonatic protolithos, formed during the Rhaethic-Liassic times [134,135]. The sedimentation occurred in two phases: the Noric-Raethian phase, with the hyperaline shelf of the Grezzoni formation, and the Raethian-Hattangian phase, with the carbonatic shelf. The latter one produced the marbles, with the two tectono-metamorphic events that involved the Massa and Apuane units starting from the Upper Oligocene. Concerning the metamorphic degree, the metamorphic polyphasic and sintectonic mark has typical mineralogical associations of the chlorite-biotite zone of green schists facies. Most likely, the temperature ranged between 300-400 °C and the pressure was between 3-4 kbars, as revealed by the stable association of pyrophillite and quartz. The calcite-dolomite geothermometer suggests the occurrence of different temperatures in various zones: higher temperatures in the western zone (up to 420-460 °C) and lower temperatures in the eastern areas (310-380 °C).

In the sequence, the marbles are massive, compact and homogeneous metacalcars. The colour is white or grey, rarely with darker vein. The mineralogical composition of marbles involves mainly pure calcite, with low amounts of muscovite, quartz, pyrite, albite and rarely chlorite [136].

Fig. 4.1 shows the microstructure of the marble used in this study: a dolomitic marble (labelled in the text as "Carrara marble"). The grain size ranges from 100 to 300 μm, but in some areas the gain size ranges from 300 to 800 μm with crystals showing rhombohedral cleavage. The size decreases in correspondence with some veins or where dolomite crystals are more abundant (Fig. 4.2). The porosity of the quarry sample is very low (about ~1 %), with a pore size distribution centred between 0.20 and 0.05 μm (Fig. 4.3).
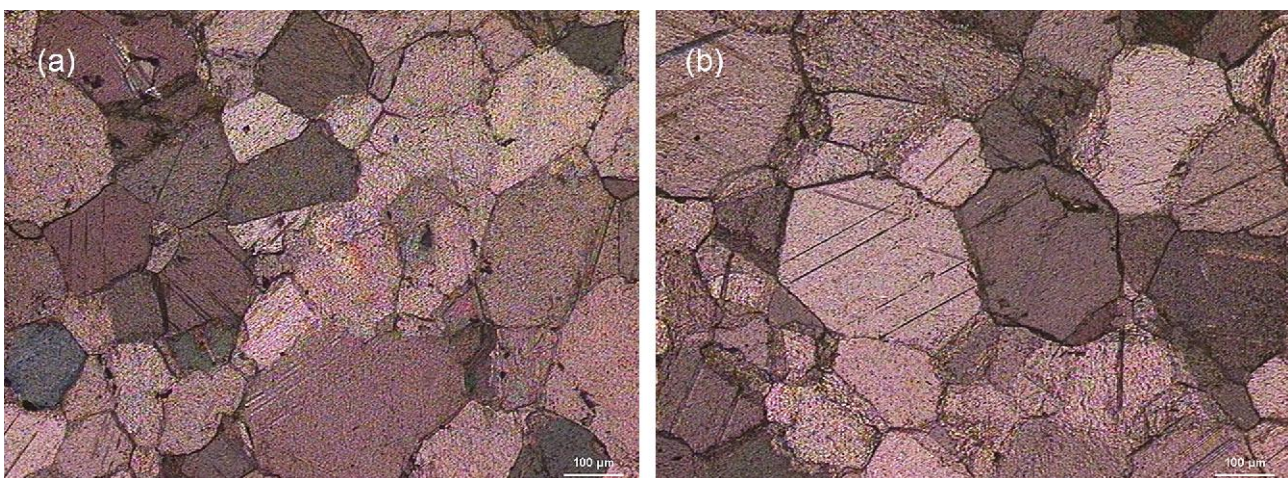
Fig. 4.1 Observation in thin section (polarised transmitting light, parallel Nicols) of the microstructure of Carrara marble. Granoblastic texture of the quarry sample (a) in comparison with the texture of the sample artificially decayed (b) by thermal treatments (heating at 200 °C for 3 hours).
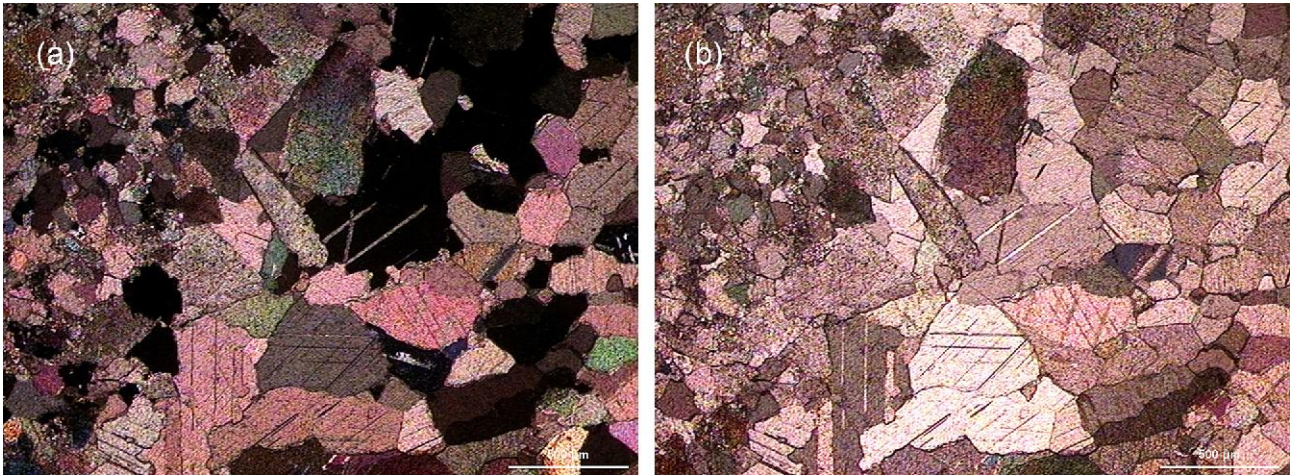
Fig. 4.2 Observation in thin section (polarised transmitting light) with crossed Nicols (a) and plane polarised light (b) of Carrara marble. Very fine grained vein (left) in contact with the granoblastic texture.

A comparison with different samples coming from quarries of the Carrara province allows to consider the features (size, morphology, boundaries) of the marble used for the tests similar to the features of the marble quarried in the Colonnata basic (Gioia quarry), the easternmost basin of the Carrara quarrying area.

In addition to the acid dissolution, the typical deterioration phenomena of marbles involve the thermal cycles. In fact, the thermal excursions (day/night temperature fluctuations, heating/cooling cycles due to solar radiation) determine a mechanical stress among calcite grains boundaries due to the anisotropic thermal behaviour of calcite crystals (parallel expansion and perpendicular contraction to the crystallographic *c*-axis) [137,138]. As a result, the cycled thermal variations develops a system of micro-cracks and decohesions that determine the typical grain detachment called "sugaring". In this thesis, DAP solutions were studied as consolidating agent to hinder the sugaring of Carrara marble. Therefore, for the experiments, a set of prismatic specimens (5x5x2 cm) were obtained from a freshly quarried block (Fig. 4.2a). As heating is an acknowledged method to promote microstructural variations and grain detachment as close as possible to those exhibited by historical naturally decayed marbles [49,139–141], a group of specimens was artificially weathered by thermal treatments with a protocol developed in the ICVBC-CNR laboratory, which slightly modified the procedure suggested in [142] (heating at 200 °C for 3 hours, instead of 400 °C for 1 hour). After the artificial weathering, the stone matrix of the Carrara marble specimens shows grain detachments (Fig. 4.2b) and an increase of the total open porosity from ~1 % to ~2.5 % as well as a variation of the pore size distribution. A comparison of the variation of the pore size distribution before and after the artificial decay, as checked by mercury intrusion porosimetry (MIP), is showed in Fig. 4.3.
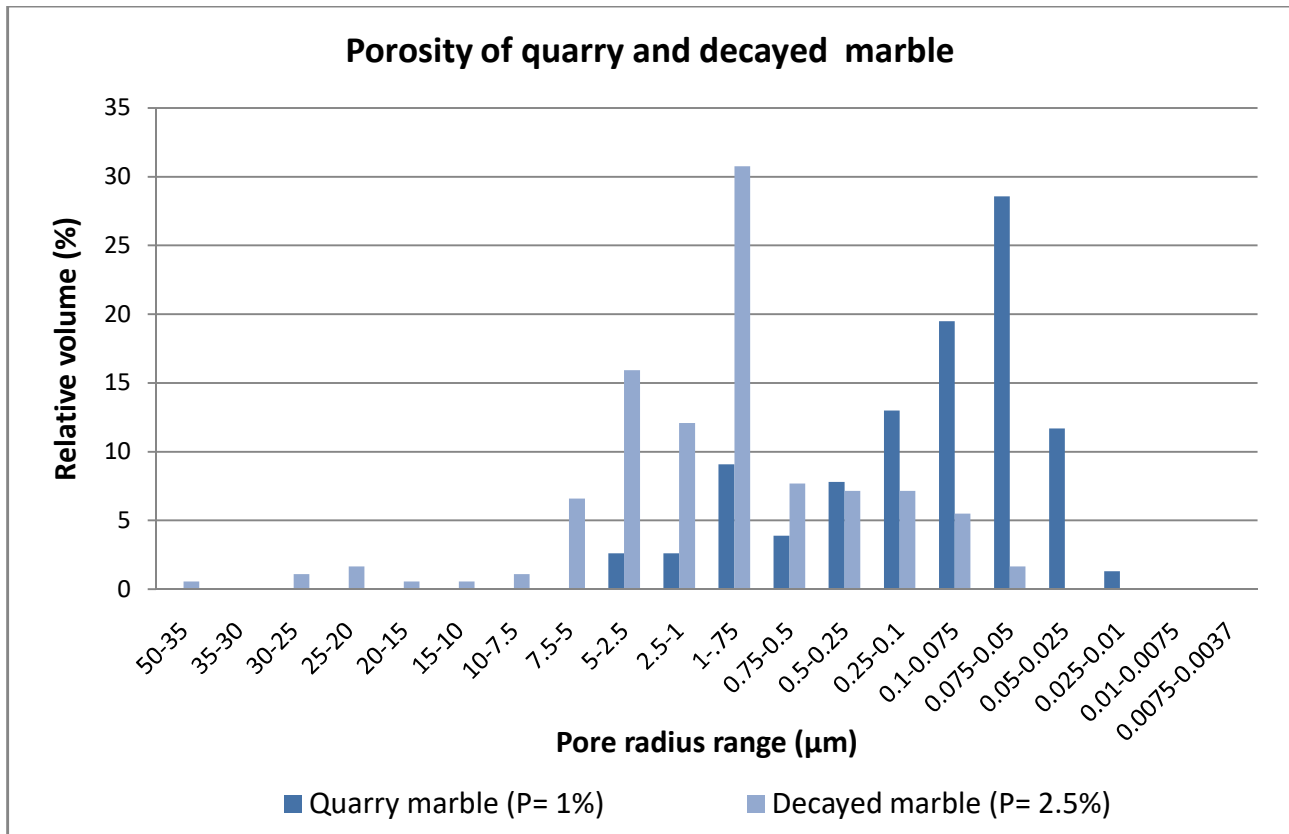
Fig. 4.3 Pore size distribution of quarry Carrara marble ("Quarry marble", blue bars) and of artificially decayed Carrara marble ("Decayed marble", light blue bars). The total open porosity of both the lithotypes in % is showed within the brackets as "P=".

4.2 Noto limestone

The "*Palazzolo Formation limestone*", also recognized as "*Noto limestone*", is a calcarenite widely used as building stone for the architecture and sculpture since ancient time [143]. The Noto limestone it is known to be very easy to sculpt and the lithotype has been extensively carved for the elaborated Baroque monuments of the Val di Noto (Siracuse), an area in the south-eastern Sicily, recently included in the UNESCO's World Heritage List.

The terms "Palazzolo Formation", as established by Rigo and Barbieri [144], describe a series of limestone and bioclastic limestone stacked in accordance with the marls of the Tellaro Formation, that outcrops in the Hyblean Plateau. The Formation is composed by the Gaetanì and the Buscemi Members, the lower and the upper part, as identified by Di Grande et al. [145]. The Gaetanì Member is an alternation of marly and yellowish limestones, while limestones predominate in the Buscemi Member, which shows a yellowish-grey colour. The Palazzolo Formation has two different lithofacies. The first one consists of fine-grained grey limestones and soft marly limestones alternated in layers of 20–40 cm; the second one is a white-yellowish limestones outcropping in massive levels [146,147].

In the quarries (located close to Noto and Palazzolo Acreide), the stone is in irregular sedimented beds interlayered by marly levels. Bioturbations due to living benthic organisms before the diagenesis are

evident in the stone bulk as sedimentary structures with tubular shape, elliptical section (from 0.5 to 4 cm) and variable length [148].

Among the varieties of porous limestones outcropping in the Iblean Plateau, the Noto Yellowish Limestone type was selected for the study. This variety is classified as a biomicrite [131] and it is mainly composed of calcite, with traces of clay minerals, quartz and iron oxides; the microstructure is irregular, and displays an allochemical content of about 30%, mainly consisting of bioclasts and peloids. The matrix is mainly micritic and microsparitic, while sparry cement occurs only within foraminifera. The porosity is high (25-35 %), with diffused cavities in the range of the micro-pores [149].

The heterogeneous deterioration of Noto calcarenite have been deeply studied [131,149–151] and the typical degradation forms are the differential degradation, the alveolization, the detachment and the chromatic alteration.

The main causes of degradation have been related to the textural heterogeneity, the occurrence of expandable clay minerals in the stone matrix (*e.g.* smectite), as well as to salt crystallization (*e.g.* chlorine salts due to the closeness with the sea) and to the tubular sedimentary bioturbations that affects the mechanical behaviour of the stone. The decay of Noto limestone basically leads to the intergranular disintegration and to the increase of the porosity.

In this thesis, DAP solutions are applied to Noto limestone to investigate the diffusion of consolidant solutions in highly porous lithotypes and to characterize the DAP interaction with the stone microstructure and its porosity. Since Noto limestone naturally shows a very high porosity, the experiments were carried out on a set of freshly quarried prismatic specimens (5x5x2 cm and 5x5x5 cm). The microstructure of Noto limestone used in this study is shown in Fig. 4.4 while the porous structure assessed by MIP is plotted in Fig. 4.5.
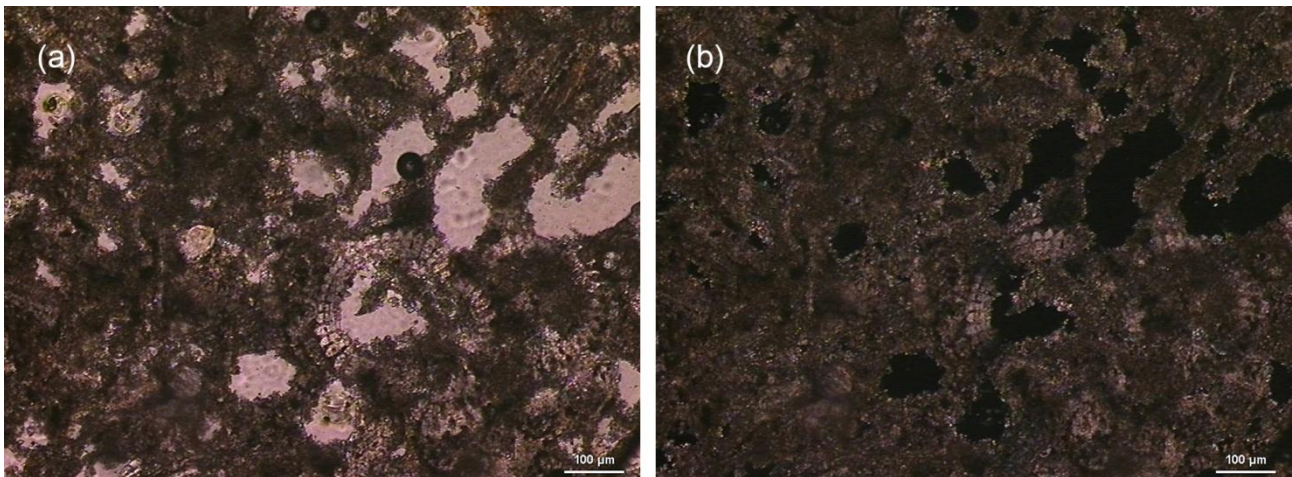
Fig. 4.4 Observation in thin section (polarised transmitting light) with parallel (a) and crossed Nicols (b) of quarry Noto limestone, showing the typical micritic and microsparitic matrix, the presence of micro-fossils and diffused cavities.
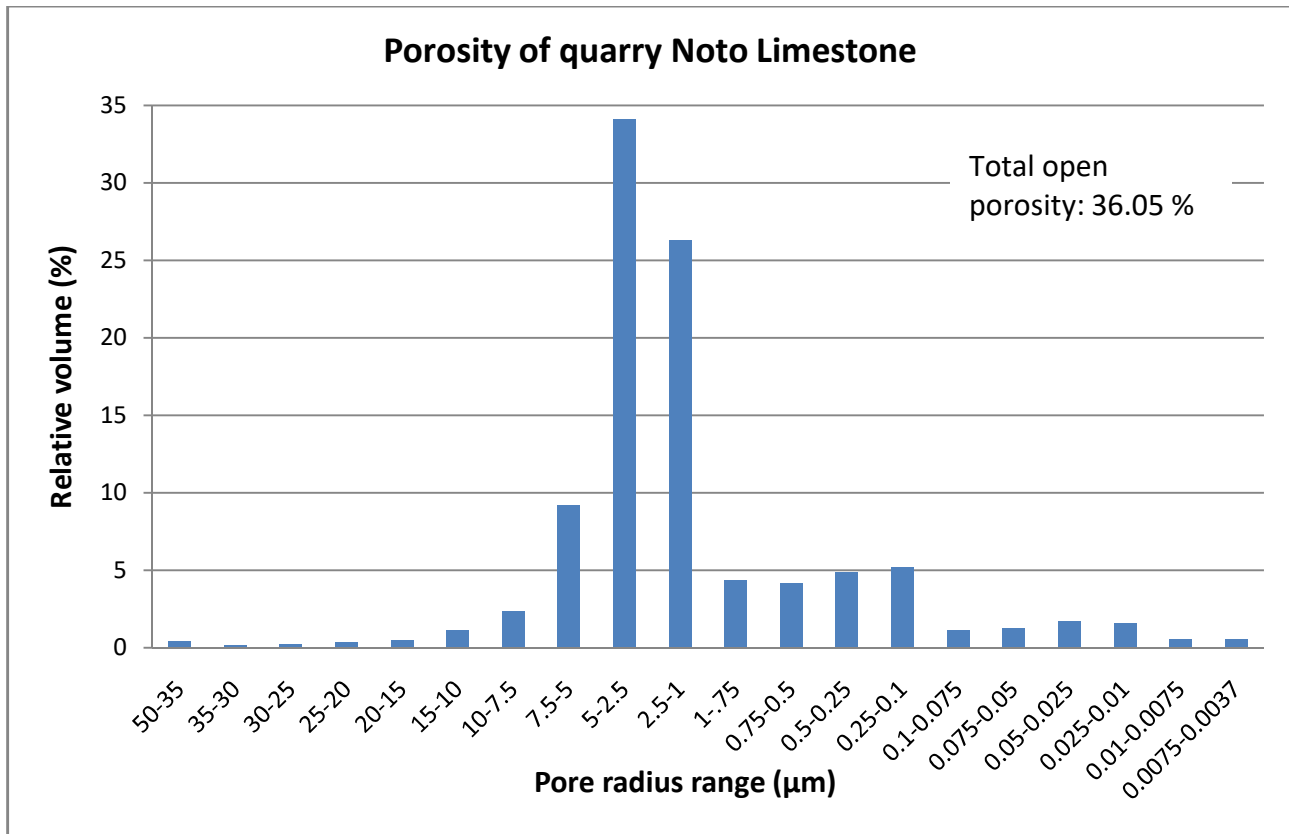
Fig. 4.5. Pore size distribution of quarry Noto limestone.

4.3 Angera stone

The Angera stone, also called "*Travertino di Angera*", is a dolostone widely used in the Lombard architecture as ornamental building material since the Roman age. The lithotype outcrops in the Verbano Cusio Ossola province (VCO), in the northern Italy (Piedmont), where the Southern Alps (Africa verging) and the Alpine nappe system (Europe verging) structural domains are exposed and separated by the Canavese Line [152]. The Angera stone belongs to the stratigraphical succession of the Southern Alps, constituted by a sedimentary cover, the "Serie dei Laghi" in the south-east, and a pre-alpine crystalline basement, represented by the Ivrea-Verbano Zone in the north-west.

In particular, the Angera stone is a massive limestone related to the "Dolomia Principale" formation of the Upper Triassic. The lithotype outcrops on the eastern shore of the Maggiore Lake, close to the namesake city. The Angera stone is characterized by a very fine grain size, typical of carbonatic rocks formed by chemical precipitation, and a high porosity due to the presence of voids. The Angera stone is available in three different colour varieties: white, pink and yellow; in many cases the three varieties show coloured veins. The stone is composed mainly of dolomite ($CaMg(CO_3)_2$) in association with low amounts of clay minerals and iron oxides, acting as chromofores for the yellow and pink varieties [153–157].

The white and yellow Angera stone show a microcrystalline texture with stone grains weakly bonded each other. Close to the pores with bigger diameter, well shaped dolomite crystals are formed and they

size about ten-times the grains of the matrix. The pink variety has bigger grains in the matrix and the stone matrix is more compact.

The typical decay of Angera stone is a strong acid dissolution that involves the stones in outdoor conditions and exposed to deeply polluted urban environment. The deterioration process acts on the carbonate cement of the Angera stone, leading to the formation of soluble Ca- and Mg- sulphates, black crusts and decohesion, efflorescences and crypto-efflorescences, and strong exfoliation. Traditionally, the exfoliation of Angera stone was treated with organic consolidants and water repellents (siliconic resins, acrylic resin); however, these polymers were not porous or transpiring. Therefore, their presence hindered the breathability of the stone matrix, determining the enhancement of the crystallization under the stone surface and, in many cases, worsened the decohesion and exfoliation processes of carved elements.

In this research, the experiments were performed on the white Angera stone because it is the variety which undergoes to the most severe decohesions and exfoliations, due to an initial low intergranular cohesion. The investigations were performed on a carved artwork of the XVII century to investigate the DAP-based consolidating treatments on a dolostone naturally decayed in outdoor urban conditions. The microstructure of Angera stone used in this study is shown in Fig. 4.6.
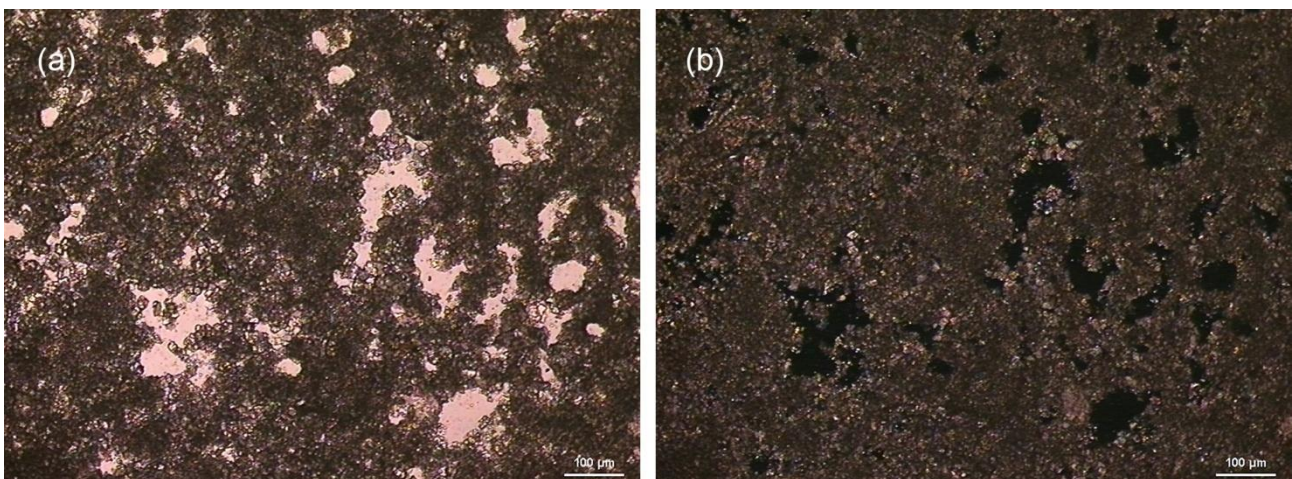
Fig. 4.6 Observation in thin section (polarised transmitting light) with parallel (a) and crossed Nicols (b) of quarry White Angera stone, showing the typical microcrystalline texture.

5 Results and discussion

5.1 Introduction

The reaction of DAP solutions with calcite promotes the formation of calcium phosphates (CaPs) arranged in a *shell* on the surface of calcite grains. This phenomenon takes place either on compact lithotypes as well as on porous substrates. On compact matrixes, the newly-formed phases form mainly an external layer on the surface of the stone. On porous matrixes, the DAP solutions penetrates into the pores and calcium phosphates crystallize mainly inside the voids, whose surfaces are composed of calcite.

Thus, the crystal growth on calcite is investigated on two lithotypes, Carrara marble and Noto limestone, selected because mainly composed of calcite and representative substrates for a compact and a porous matrix.

In the following, the focus of section § 5.1 is the crystallization of CaPs occurring mainly on the surface of treated stones and specific insights will be carried out on Carrara marble to understand the crystallization process on different treatment conditions. The section § 5.2 is devoted to study the penetration depth of CaPs within the porous carbonatic substrate of Noto limestone. The combination of the data collected on § 5.1 and § 5.2 are then used to investigate the DAP-based consolidation on a pilot case study carried out on a naturally decayed stone matrix (section § 5.3).

5.2 DAP reaction on calcite

5.2.1 Nucleation of phosphates on calcite

The reaction of DAP solutions with calcite of Carrara marble and Noto limestone induces a micrometric recession of the substrate followed by the crystallization of a complex mixtures of calcium phosphates (Ca and P clearly detected by EDS) on the reaction profile of carbonate grains. These newly-formed phases form a *shell*, namely a crystal network, which grows on the reaction profile of calcite grains and between grain boundaries. The nucleation of the *shell* occur either on the surface of the treated lithotypes either inside the poroes (natural voids and artificial micro-cracks). Over the *shell*, there is a spotty formation of calcium phosphates, which are arranged in crystal aggregates. These crystal aggregates grow only on the surface of the specimens, which provides room for the crystallization.

Focusing on the morphology, SEM images of Fig. 5.1 clearly show that the newly-formed calcium phosphates have different crystal habit: i) thin rose-like phases (thickness < 100 nm, dimensions ~ 1-2 μm, Fig. 5.1a); ii) spherical units and aggregates of spherical units in elongated arrangement (diameter

~ 300 - 900 nm, Fig. 5.1b); iii) larger and thicker acicular plate-like blades (length up to 100-150 µm, thickness ~ 100-400 nm, Fig. 5.1c and Fig. 5.1d). The *shell* is characterised by thin transversal micro-cracks (Fig. 5.1c).

No differences, in terms of crystal morphology, are detected on specimens treated by capillarity or by poultice.
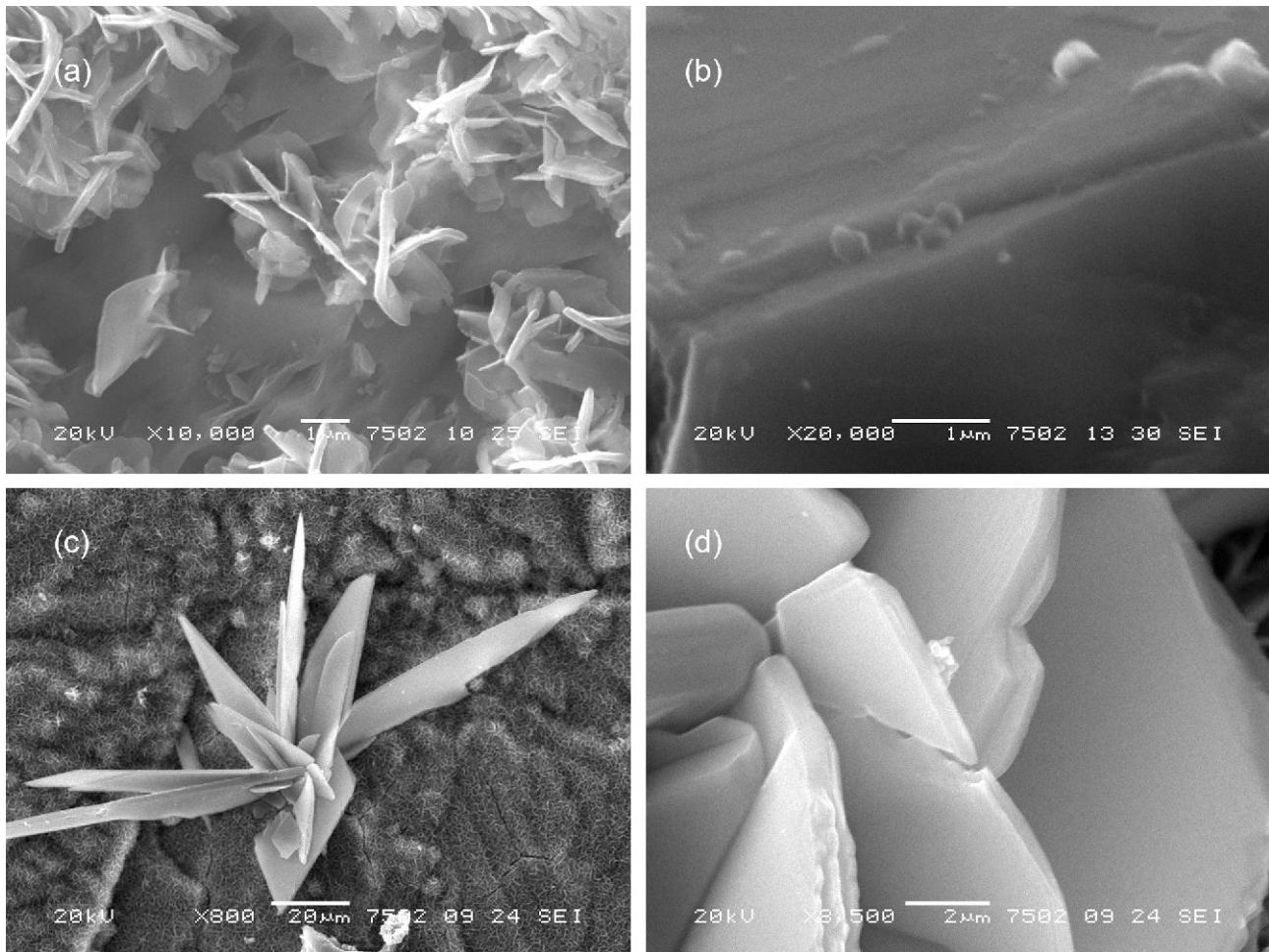
Fig. 5.1 Morphology of calcium phosphates formed on Carrara marble after DAP treatments by capillarity with 0.76 M DAP solution: thin rose-like phases (a), spherical units (b) and acicular plate-like blades (c). (d) is a detail at higher magnification of the acicular blades of (c). Similar crystal morphologies are detected on specimens treated by poultice.

The lithotype controls the crystallization of phosphates in terms of phase morphology (abundance of specific crystal habits) and penetration depth inside the substrate.

More in detail, the rose-like crystals are predominant on the Carrara marble (*e.g.* Fig. 5.2a and Fig. 5.2b), while rounded units are mainly on the Noto limestone (Fig. 5.2c and Fig. 5.2d). Plate-like blades, as those showed in Fig. 5.1c and Fig. 5.1d, are formed only on Carrara marble. These data, in line with some preliminary results collected on Carrara marble and Noto limestone powders [31], give indication that the lithotype has a not negligible influence on the crystal nucleation.

Carrara marble

Surface   Cross section

Noto limestone

Surface   Cross section
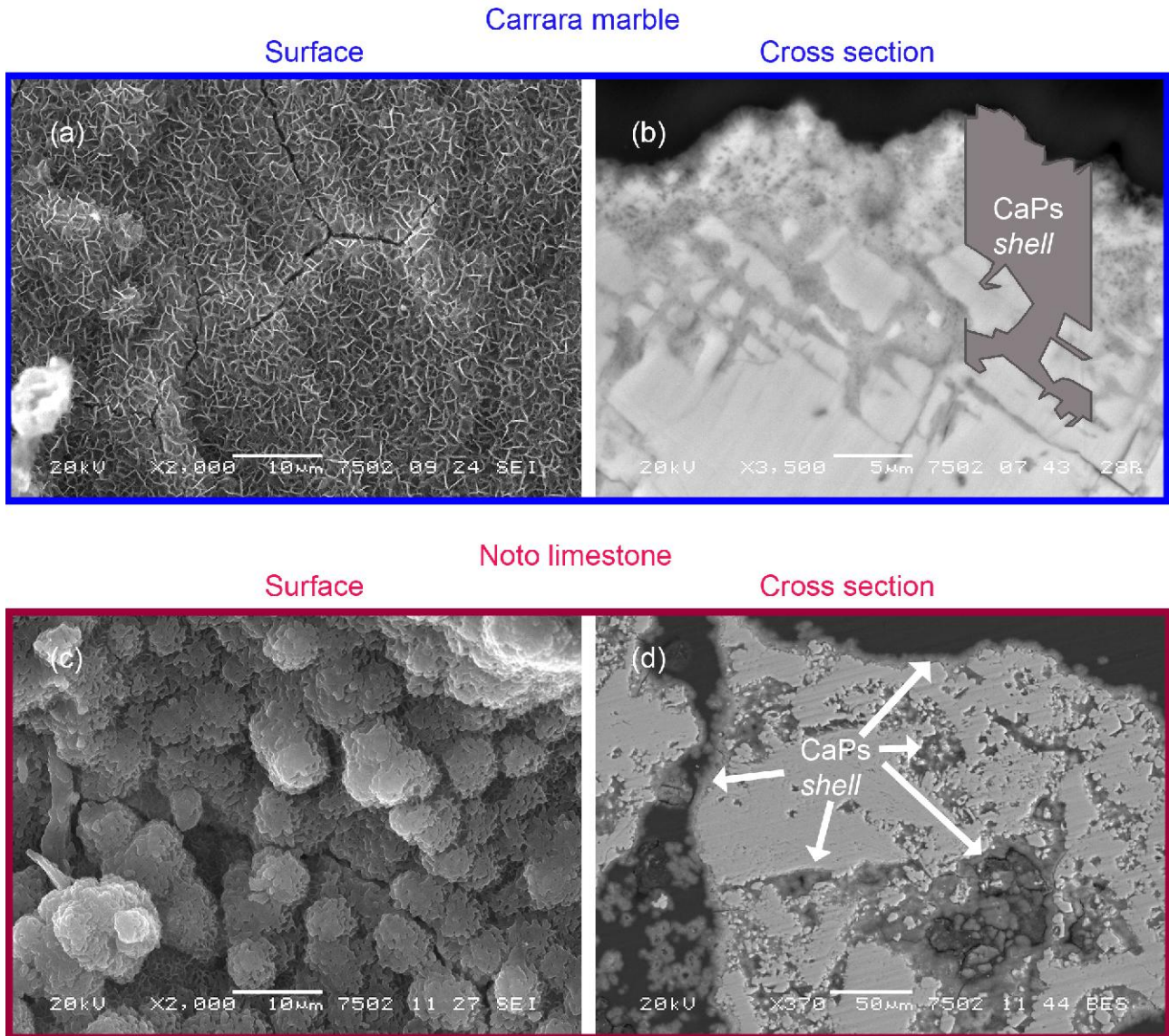
Fig. 5.2 SEM images showing the different morphology of the CaPs *shell* formed on: Carrara marble (a), (b); Noto limestone (c), (d). The SEM images are collected on the surface of treated specimens (a, c) and on polished cross sections (b, d). The treatments were performed by capillarity with a 0.76 M DAP solution. On Carrara marble, crystals have a predominant rose-like morphology and the formation of the phases occur mainly on the surface. On Noto limestone, the newly-formed crystals are mainly rounded and their nucleation is widespread in voids of the stone matrix.

In the case of quarry Carrara marble, the phosphate phases nucleate mainly close to the surface of the specimens, as the low porosity inhibits the diffusion of the reagent. For this reason, the newly-formed phosphates form a *shell* which is almost an external layer. In some cases, the *shell* seems not connected to the underlying substrate and it displays detachments from calcite (Fig. 5.3).
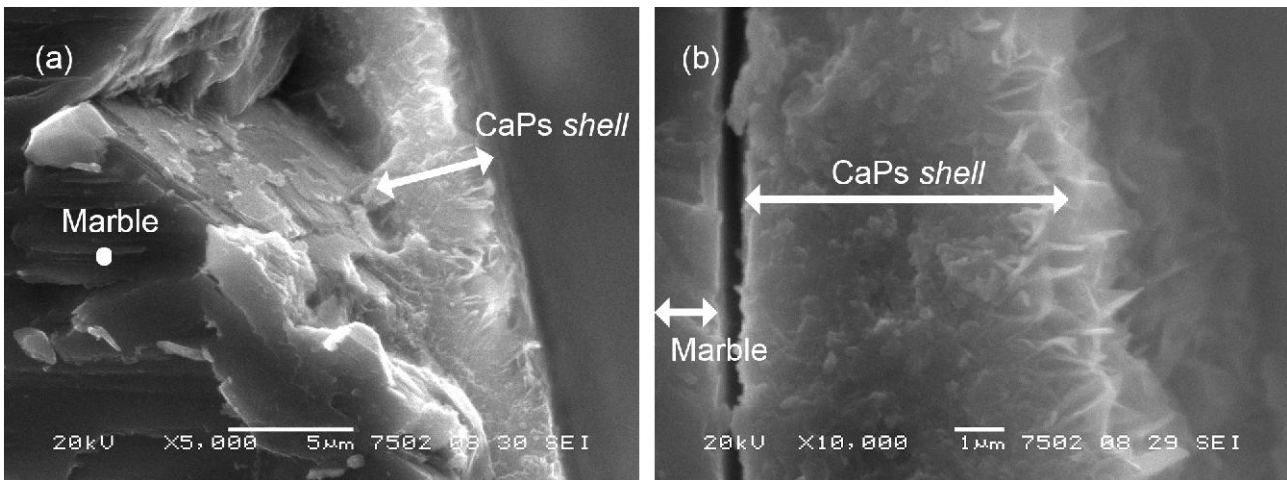
Fig. 5.3 SEM images (cross section) of calcium phosphate *shell* crystallized on quarry Carrara marble (a), (b) after treatments by capillarity with 0.76 M DAP solution. Due to the low porosity, the diffusion of DAP solutions is highly inhibited and, in some cases, the *shell* seems not bonded to the underlying substrate.

The phosphate crystallization occurs more in depth on more porous matrixes, *e.g.,* on artificially decayed Carrara marble and Noto limestone, where the voids act as crystallization spaces and host the crystal growth.

On decayed Carrara marble, the calcium phosphate phases nucleate at boundaries of detached grains down to 40-600 µm, showing the ability of DAP-based treatments to hinder the marble sugaring (Fig. 5.4). In any case, the crystallization on this lithotype remains quite superficial, especially in comparison with the Noto limestone, where the pronounced presence of voids in the matrix promotes the diffusion of the DAP solution and the descending crystallization within the substrate. As showed in Fig. 5.5, on Noto limestone, the newly-formed phases are not confined close to the surface but are widespread in the stone bulk, with a penetration depth of the order of millimetres. The *shell,* evident on Carrara marble, is formed also on Noto limestone in the form of a network growing on the surface of calcite grains in the voids of the matrix.
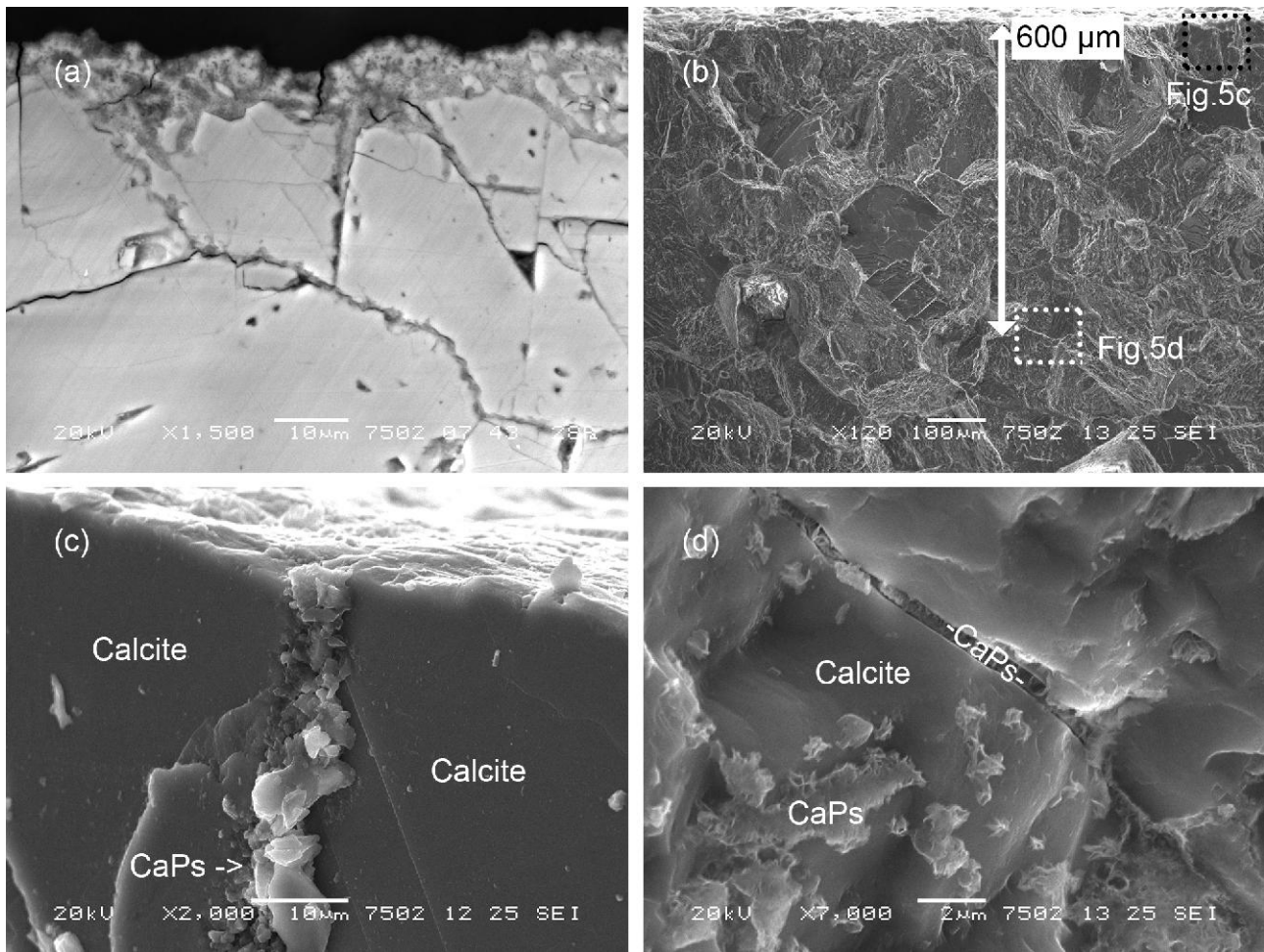
Fig. 5.4 Calcium phosphates *shell* crystallized on artificially-decayed Carrara marble after treatments by poultice, with a 0.76 M DAP solution. Due to the increased porosity, the *shell* nucleates in the cracks (*a*, image collected on polished cross section) and down to 40-600 μm (*b*). The newly-formed calcium phosphates act as effective bonding agent at boundaries of detached grains, as shown in (*c*) and (*d*).
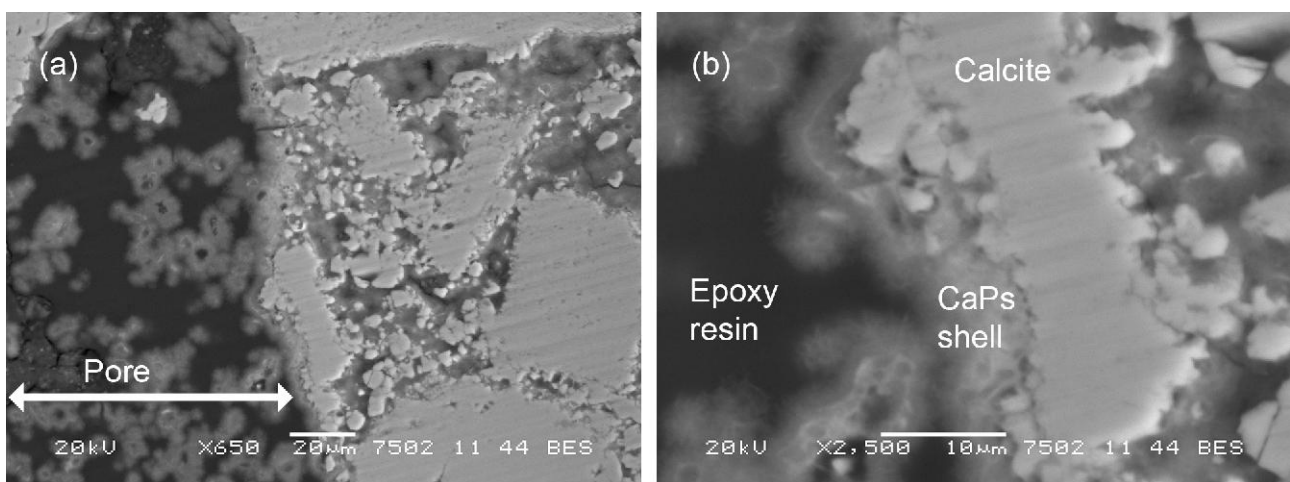
Fig. 5.5 SEM images collected on polished cross sections showing the nucleation of the *shell* of calcium phosphates in a pore within the matrix of Noto limestone (*a*) and detail at higher magnification (*b*) with the crystallization of phases at a depth of 3 mm (treatments by poultice with a 0.76 M DAP solution).

Focusing on the composition, the *shell* is composed of octacalcium phosphate (OCP, $Ca_8(HPO_4)_2 \cdot 5H_2O$) mixed with calcite, as revealed by the XRPD patterns (Fig. 5.6 and Fig. 5.7). The characteristic Bragg peaks of calcite are most likely due to spotty stone grains, detached from the substrate during the reaction and embedded in the newly-formed crystal network during its formation (Fig. 5.2b). The composition of the *shell* does not show variations on specimens treated by capillarity or by poultice.

In the course of crystal growth, OCP is probably formed as sub-micrometric crystals or contains structural defects and vacancies, as its XRPD peaks (detected at 18.56 Å (d_{100}), 9.36 Å, 9.03 Å and 5.49 Å) are broad and weak. The presence of hydroxyapatite (HAP, $Ca_{10}(PO_4)_6(OH)_2$) in the *shell* is actually ambiguous because two peaks, corresponding to inter-planar distances of 3.42 Å and 1.71 Å (indicated in Fig. 5.6 by the dotted lines), could be attributed to HAP but the severe overlapping of OCP and HAP diffraction patterns prevents the unambiguous identification of HAP.
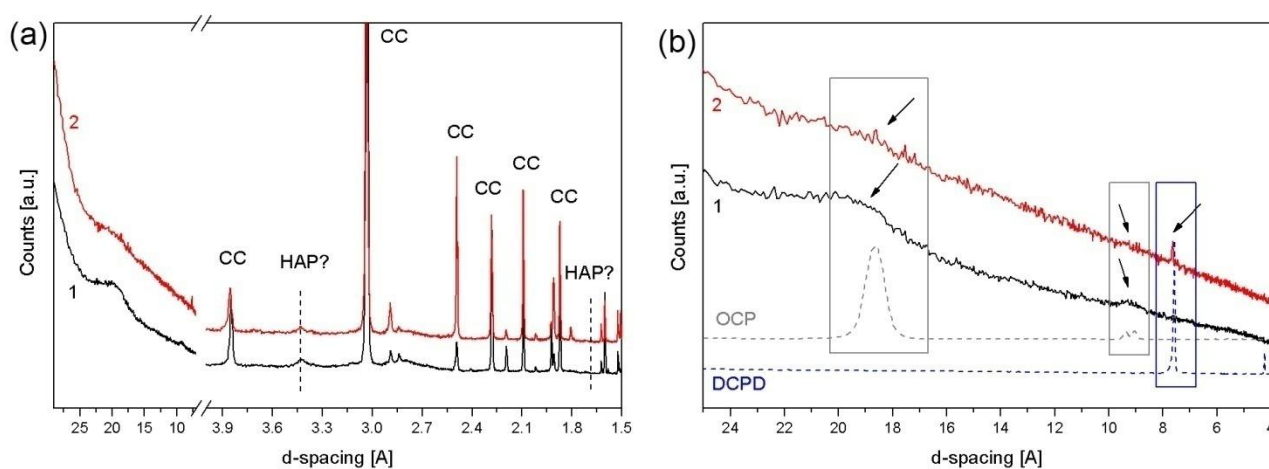
Fig. 5.6 XRPD patterns of calcium phosphates formed on Carrara marble specimens treated by poultice with a 3.00 M (pattern 1) and a 0.76 M (pattern 2) DAP solutions: (a) calcite peaks (CC) embedded in the *shell* and peaks compatible with HAP (dotted lines); (b) formation of OCP and a mixture of OCP and DCPD.
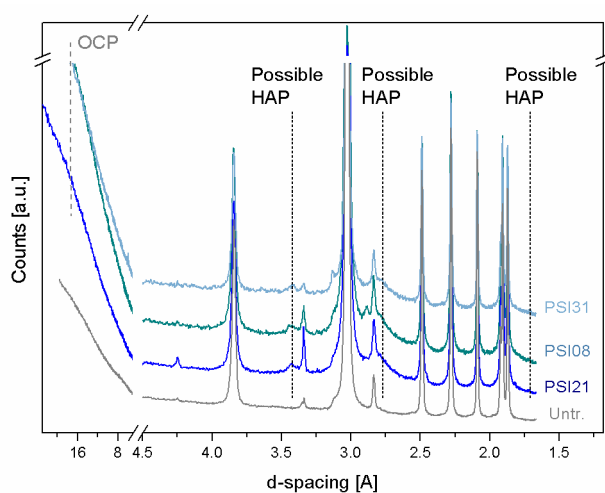
Fig. 5.7 XRPD patterns of three different specimens of Noto limestone (PSI31, PSI08, PSI21), treated by poultice with a 0.76 M DAP solution in comparison with the untreated stone material (Untr.). The powders were scratched from the treated surface. The Bragg peaks of hydroxyapatite (HAP) and octacalcium phosphate (OCP) are broad and weak, due to their nano-crystallinity.

The identification by XRPD of calcium phosphates is more complex on Noto limestone than on Carrara marble, as showed in Fig. 5.8. On some Noto limestone specimens, the peaks of calcium phosphates are weak and in many XRPD patterns their identification is ambiguous. Furthermore, in some cases, the CaPs Bragg peaks are so weak that the XRPD patterns of the untreated lithotype are virtually identical to those of the treated ones. This condition persists even on the surface of the treated specimens, where most likely there is a higher concentration of products, or from the regions were SEM-EDS measurements actually identified Ca-and-P based phases.

This analytical problem can be attributed to a twofold aspects.

The first is the microstructure of Noto limestone, which most likely has a direct role on the crystallization of the new phases. In particular, the micritic texture of calcite grains, characterized by a high specific surface, determines a high reaction rate of the substrate. This implies a high reactivity of the substrate, a quick ion exchange between the DAP solution and calcite and it develops the precipitation of phosphate phases with a low crystallinity.

The second aspect involves the diffusion itself and the XRPD analysis of porous or compact stone materials. As showed from SEM observations and by the scheme of Fig. 5.9, on Noto limestone the phosphate phases form a micro-porous network highly distributed into the matrix. In that case, sampling the treated surface or scratching from inner portions the amount of CaPs is too modest with respect to the calcite of the matrix. On the contrary, in the case of Carrara marble, the crystallization of phosphates is restricted to a superficial portion of material, even on artificially decayed substrates (total open porosity: quarry ~ 1%, artificially decayed ~ 2.5 %). This means that sampling from the treated surface of Carrara marble specimens, the ratio among newly-formed phases and calcite allows the identification of calcium phosphates.
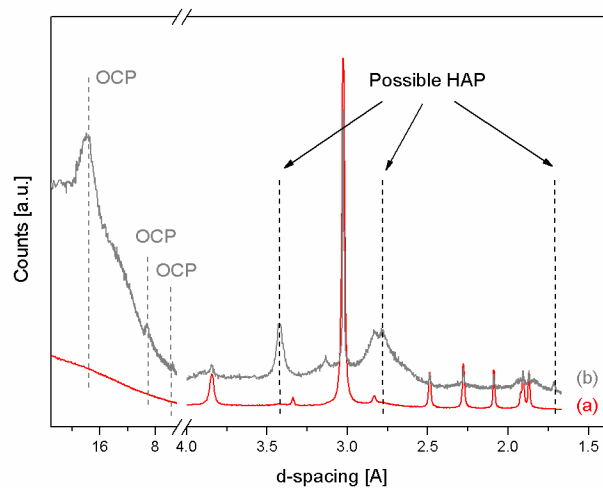
Fig. 5.8 Comparison between XRD patterns of powders scratched from the surface of Noto limestone (a) and Carrara marble (b), both treated by poultice with 0.76 M DAP solutions for 24 h. The low porosity of marble enhances the crystallization of a superficial *shell* of calcium phosphates, while in the porous matrix of Noto limestone, the fraction of calcium phosphates formed on the surface (HAP = hydroxyapatite and OCP = octacalcium phosphate) is modest with respect to calcite. As a result, calcium phosphates are hardly detectable on Noto limestone by XRPD.
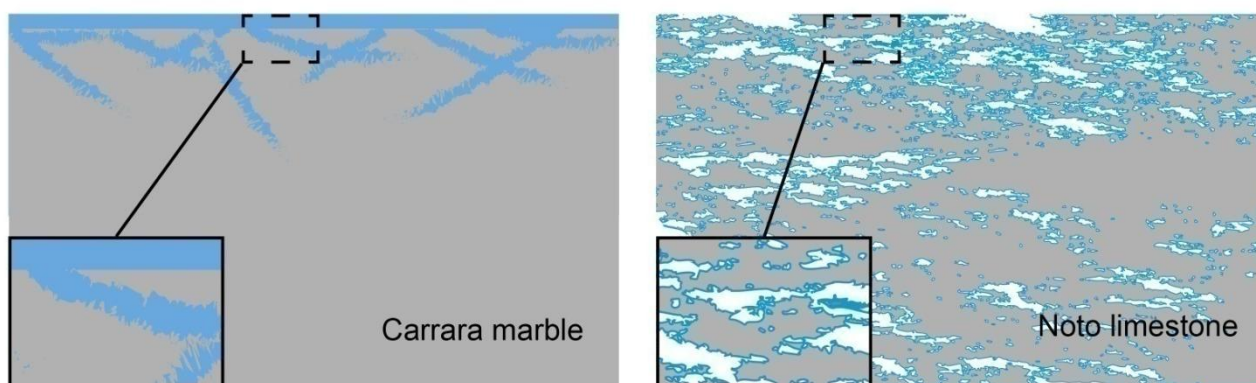
Fig. 5.9 Scheme (not in scale) of the different arrangement of calcium phosphates crystallized on Carrara marble and Noto limestone (grey= calcite, light blue= calcium phosphates, white= voids). The rectangles confine a representative portion scratched for XRPD and show the different ratio calcite/phosphates of different lithotypes, even when treated with the same treatment conditions.

Raman investigations were carried out to study the composition and localization of newly-formed phases with a high lateral resolution (laser spot size of about 1 μm) and two representative Raman spectra, collected on treated Noto limestone and Carrara marble, are shown in Fig. 5.10. Actually, calcium phosphate phases were found to be weak Raman scatterers and their Raman patterns resulted in a sort of convolution of hybrid bands. On Carrara marble (the substrate that better interacted with Raman excitation), the characteristic strong bands of HAP and OCP (respectively located at 961 cm^{-1} and at 958 cm^{-1}, v_1 of PO_4 group), are of low intensity and in many cases centred in a halfway position. The other characteristic Raman bands of HAP, located at 606 cm^{-1}, 591 cm^{-1} and 580–576 cm^{-1} (v_4 of PO_4 group) and at 448 cm^{-1} and 425 cm^{-1} (v_2 of PO_4 group) are definitely weaker, and overlapped to those of OCP. On the other side, as OCP crystallizes in a poorly crystalline structure, its marker bands related to vibration modes of the HPO_4^{2-} group (v_1: 1011 cm^{-1}, 917 cm^{-1} and 883 cm^{-1}; v_3: 1110 cm^{-1} and 1080 cm^{-1}; v_4:556 cm^{-1} and 528 cm^{-1}; v_2: 413 cm^{-1} and 354 cm^{-1}, [67,68,75,158]) resulted poorly resolved from the baseline. Furthermore, the low Raman scattering cross-section of OH$^-$ and H_2O groups prevented their identification in the OH stretching region [67,68,75,159,160].

Raman investigation carried out on Noto limestone, potentially very useful to study the distribution of the phases within the matrix, resulted even more ineffective. In fact, Raman measurements are deeply affected by a strong fluorescence emission, which obscured the marker Raman signal of OCP and HAP.
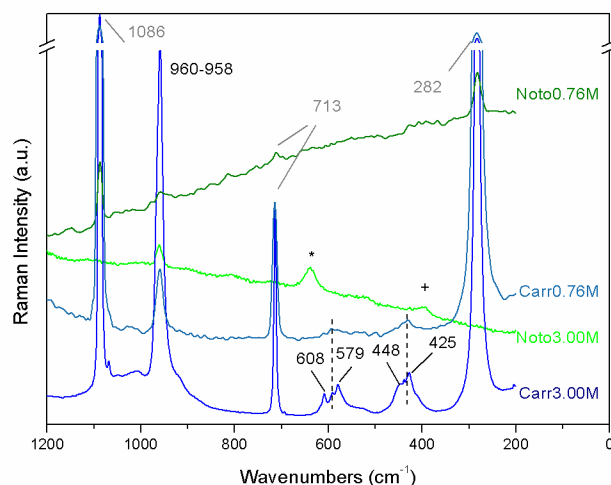
Fig. 5.10 Raman spectra collected on Carrara marble (Carr) and Noto limestone (Noto) specimens treated by poultice with a 0.76 M or a 3.00 M DAP solution. The peaks at 960-958, 608, 579, 448 and 425 cm^{-1} are due to calcium phosphates while the bands at 1086, 713 and 282 cm^{-1} are of calcite. * = anatase, + = goethite. Similar Raman patterns are collected on specimens treated by capillarity.

The FTIR vibrational patterns of treated Noto limestone and Carrara marble are showed in Fig. 5.11. Both of them are dominated by the absorption pattern of calcite, with the typical stretching and bending vibrations of CO_3^{2-} centred around 1428, 873, 713 cm^{-1} [161–163]. Overtone and combination bands of carbonate groups are present as well at 2514 cm^{-1} and 1799 cm^{-1}. FTIR bands of silicates are detectable in the FTIR pattern of Noto limestone, as the lithotype contains low fractions of phyllosilicates and quartz [148]. Therefore, focusing on silicates, SiO_4 tetrahedra stretching vibrations are well detectable by the band at 1033 cm^{-1} and by the shoulder at 1011 cm^{-1}. Other weak bands of silicates are localized at 529 and 469 m^{-1}.

FTIR spectra of treated Noto limestone and Carrara marble display bands owing to calcium phosphates. The main band is centered at ~1038 cm^{-1} with two shoulders around 1107 cm^{-1} and 960 cm^{-1}, while other absorptions are localized at 602 and 563 cm^{-1}. The OH$^-$ stretching region, potentially diagnostic for the identification of OCP and HAP, is not very thorough as the KBr pellets used to collect the spectra are highly hygroscopic and all the spectra show evidence of water molecules absorbed by the pellets. Potentially, OCP and HAP could be distinguished by their FTIR spectra in the fingerprint region: i) strong stretching mode of P-O bond at 1014 cm^{-1} and 1023 cm^{-1}, for HAP and OCP respectively, ii) marker vibrations of PO_4^{2-} groups for crystalline HAP at 1088 cm^{-1}, 1144 cm^{-1} [75], and of HPO_4^{2-} groups at 1294 cm^{-1}, 1195 cm^{-1}, 1114 cm^{-1}, 1074 cm^{-1}, 1034 cm^{-1}, 915 cm^{-1} and 877 cm^{-1} for crystalline OCP [158,164,165]. Actually, the FTIR spectra of the *shell* show that, analogously to Raman spectroscopy, the phases always display an hybrid vibrational patterns between HAP and OCP and the most intense bands in the spectra can be basically considered the convolution of vibrational features of the two phases. The unambiguous detection of HAP in the *shell* it is not achievable even with the high resolution ATR-FTIR microspectroscopy because this ambiguity persists down to the microscale, as demonstrated by the spectra collected on areas of 1x1 μm^2 and by ATR μ-FTIR chemical maps. These findings indicate that OCP and the not well defined apatite phase are most likely formed as a multiphase sub-micrometric mixture, and not as single, crystalline, micrometric individuals. Moreover, the detection of bands at 1460 cm^{-1}, 1399 cm^{-1} and 868 cm^{-1} due to

CO_3^{2-} vibrations suggests the formation of carbonate-substituted non-stoichiometric phases [75,166,167].
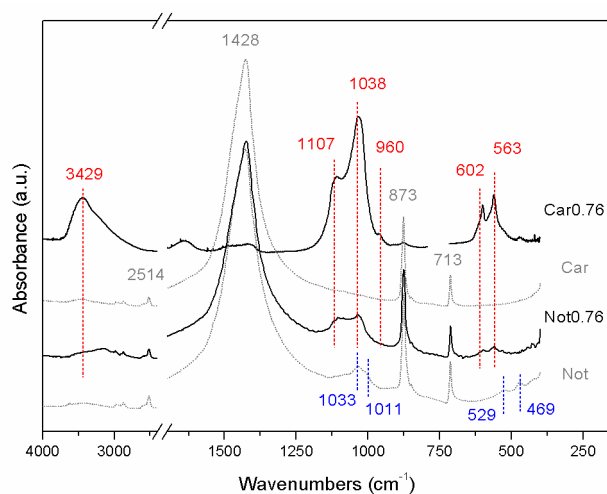
Fig. 5.11 FTIR spectra of Carrara marble (Car) and Noto limestone (Not) specimens untreated and treated by poultice with 0.76 M DAP solutions. The peaks at 3429, 1107, 1038, 960, 602 and 563 cm^{-1} are due to calcium phosphates while the bands at 2514, 1428, 873 and 713 cm^{-1} are of calcite. Silicate bands are visible in Noto limestone's FTIR patterns at 1033, 1011, 529 and 469 cm^{-1}. Very similar vibrational patterns are observed on specimens treated with 3.00 M DAP solutions, either by poultice either by capillarity.

Over the *shell* there is the growth of spotty crystals, as briefly outlines at the beginning of the section and as showed in Fig. 5.12 (*a* and *b*).

SEM and ATR μ-FTIR investigations were carried out on these micrometric crystals in order to investigate their feature and composition with a high lateral resolution and avoiding the compositional interference of the underlying *shell*. The outcomes clearly demonstrated that these aggregates of phases have morphology and composition depending on the molarity of the DAP solution.

In fact, the 3.00 M DAP solutions form over the *shell* spherical aggregates (~ 5 μm diameter) of thin, rose-like blades (Fig. 5.12a) composed of OCP, calcite and ambiguous HAP (Fig. 5.12c, spectrum 1). The spectral feature of these spherical aggregates is very close to the *shell* one (Fig. 5.12c, spectrum 2). On the contrary, the 0.76 M DAP solutions form acicular plate-like crystals (Fig. 5.12b). These spotty crystals are composed only of dicalcium phosphate dihydrate (DCPD, $CaHPO_4 \cdot 2H_2O$), as clearly identified by the marker bands of HPO_4^{2-} groups at 1125 cm^{-1}, 1051 cm^{-1}, 985 cm^{-1}, 874 cm^{-1}, 790 cm^{-1} and of OH vibrations at 3527 cm^{-1}, 3466 cm^{-1}, 3256 cm^{-1}, 3161 cm^{-1} and 1651 cm^{-1} [67,75,168], Fig. 5.12c, spectrum 3). No unreacted reagent is detected in the FTIR spectra.
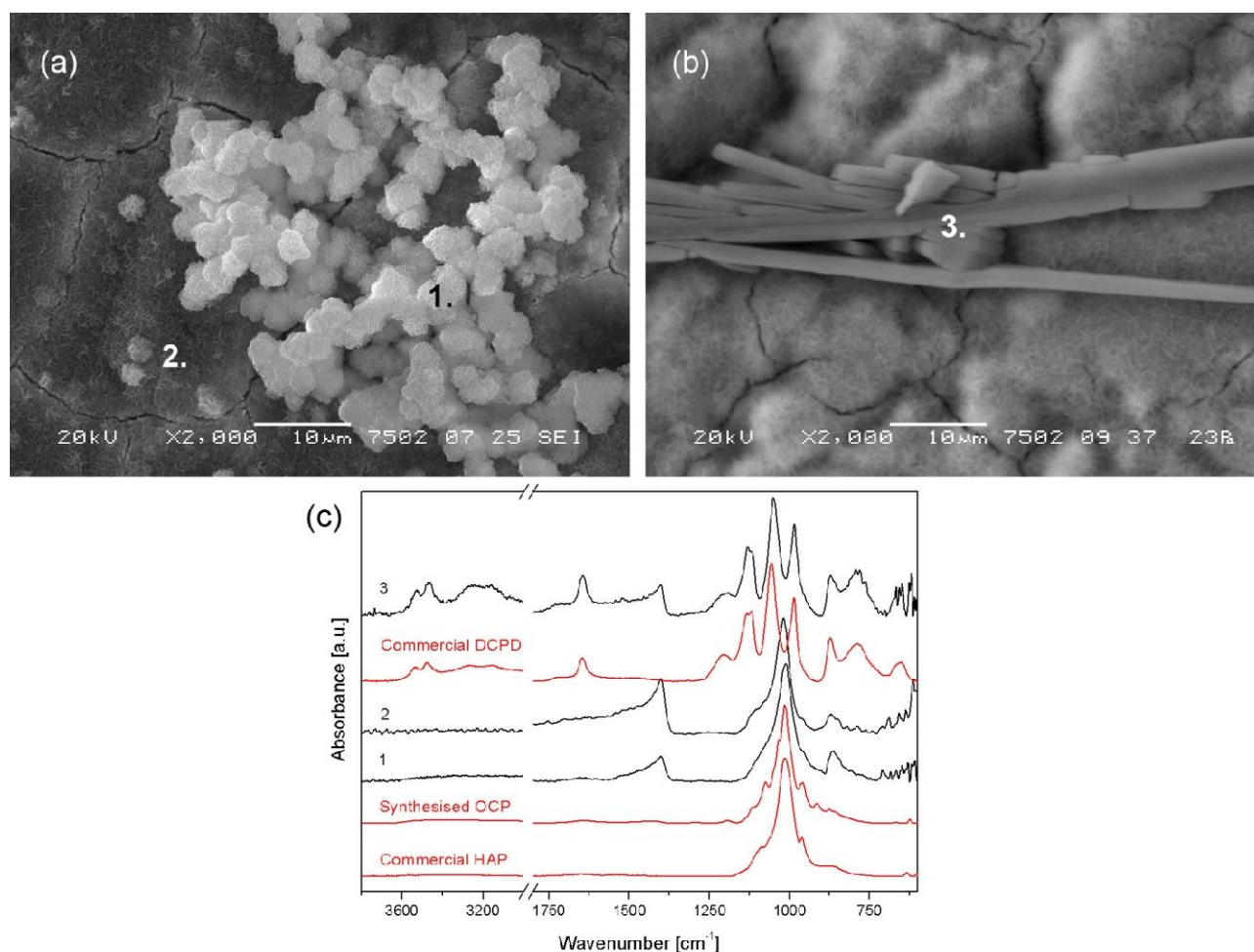
Fig. 5.12 Carrara marble specimens treated by capillarity, showing spotty crystals nucleated over the *shell:* (a) spherical aggregates formed after 3.00 M DAP treatments; (b) acicular plate-like after 0.76 M DAP treatments; and (c) FTIR spectra of the crystals indicated in (a) and (b).

5.2.2 HAP formation demonstrated by thermal treatments

The § 5.2.1 showed that the reaction of DAP solutions with calcite has given rise to complex mixtures of sub-micrometric non-stoichiometric phases. The identification of some of them, such as HAP and carbonate-substituted HAP (C-HAP), is analytically challenging, especially when these phases are non-stoichiometric, nano-crystalline or in mixture with OCP [67]. Moreover, OCP has been described as a precursor in the HAP nucleation [169] and it is highly likely that OCP crystals might act as growth seeds on the calcite grains for the formation of HAP.

To demonstrate the presence of HAP, a set of thermal treatments were carried out, as heating is proved to be an effective approach to discriminate phases which exhibit similar crystalline structure at room-conditions (*i.e.*, temperature induces distinct and univocal phase transformation) [67]. The heating procedure was performed first on reference materials and then on the newly-formed calcium phosphates. To fully understand the transformation induced to calcium phosphates by heating, phase variations were checked by synchrotron radiation (SR) XRPD and by FTIR spectroscopy.

5.2.2.1 Heating of reference materials

Heating of OCP at 250 °C induces a clear variation of the diffraction pattern, due to the first phase transformation. As showed in Fig. 5.13a, the sharp XRPD peaks of OCP peaks disappear and are substituted by broad weaker bands, compatible with the formation of an amorphous phase. FTIR spectra of Fig. 5.13b document the phase transformation as well, with the: i) decrease of the intensity of H_2O molecules vibrational bands located in the ranges 3600-3000 cm^{-1} and 1750-1550cm^{-1} (ν of OH in H-bonded H_2O and HPO_4; δ of H_2O, respectively); ii) disappearance of the OCP marker bands located at 1294 cm^{-1}, 1195 cm^{-1} ($\delta_{in-plane}$ of OH in HPO_4 groups) and 914 cm^{-1} (ν of P-(OH) in HPO_4 groups) [158,164,165,170], iii) shift of the band at 1014cm^{-1} up to 1019 cm^{-1} (ν of PO_4).

The main phase transformation of crystalline OCP occurs after heating at 850 °C, when the amorphous-apatite/collapsed-OCP formed at 250 °C is completely transformed into a mixture of β-tricalcium phosphate (β-TCP, β-$Ca_3(PO_4)_2$) and β-calcium pyrophosphates (β-CPP, β-$Ca_2P_2O_7$) [78,165,171]. The calculated ratio of β-TCP and β-CPP, as resulted from Rietveld refinement, is 66.8 % and 33.2 % respectively, in good agreement with literature data [165]. The satisfying results obtained from the Rietveld refinement of precipitated OCP at room temperature (rT) and of heated OCP at 850 °C basically confirm the high quality purity and crystallinity of synthesized OCP.

Literature indicates that, in some cases, apatite and DCPA might form as transient phases in the heating process of OCP [78,165], but no related peaks were detected in the FTIR or in the XRPD patterns.
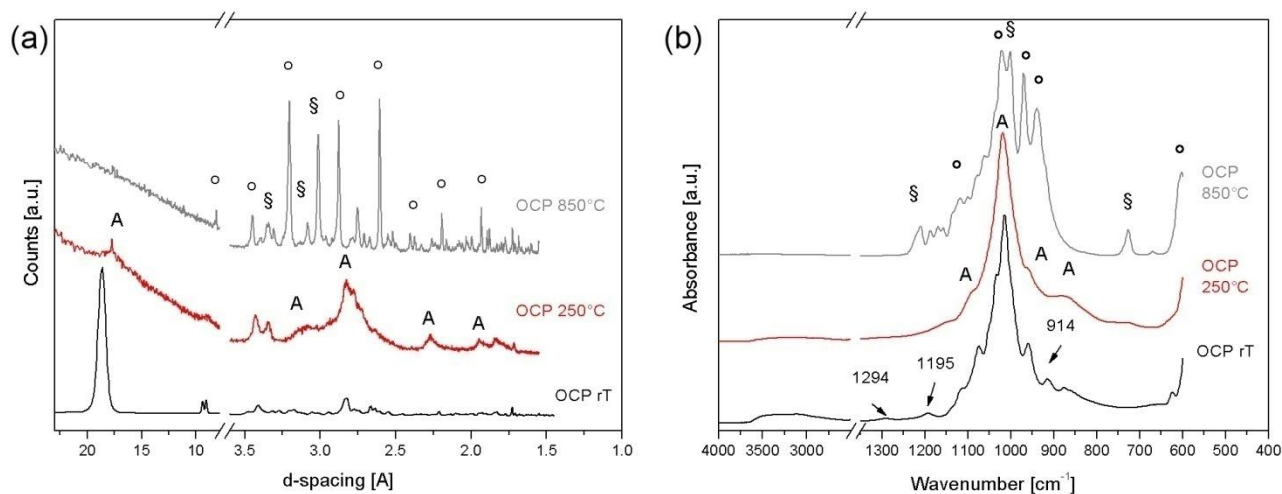
Fig. 5.13 (a) XRPD and (b) FTIR patterns of synthesised OCP at rT and after heating at 250 °C and 850 °C. A = amorphous phase, ° = β-TCP, § = β-CPP.

Moving to commercial HAP, the XRPD pattern displays broad diffraction peaks, ascribable to the presence of a non-stoichiometric calcium-deficient apatite (Fig. 5.14a) in spite of a highly ordered stoichiometric structure. Most likely, this material also contains carbonate groups in the structure, as demonstrated by the broad weak band located at about 876 cm^{-1} occurring in the FTIR spectrum of Fig. 5.14b [166,167]. In general, no detectable phase variations occurred until 750 °C, while a clear parent-to-product phase changes is evident after heating at 850 °C. From this temperature, the XRPD

pattern and the FTIR spectrum reveal the formation of a mixture of β-TCP and crystalline HAP, with β-TCP as a predominant phase [67,83,172].

Focusing on HAP peaks, the transformation of the broad diffraction pattern into a sequence of sharp well-defined peaks is due to the increase, with heating, of the crystallinity degree of the poorly-crystalline commercial phase. On the other side, the growth of β-TCP is a further confirm of the presence of "impurities", such as HPO_4^{2-} or CO_3^{2-}, in the commercial material. In fact, the crystallization of β-TCP is due to a chain reaction involving non-apatitic layers and HPO_4^{2-} ions of HAP, which are transformed into β-CPP between ~400-700 °C; above ~700 °C, β-CPP is commonly transformed into β-TCP [83]. It follows that, the crystallization of a relevant amount of β-TCP unambiguously indicates that commercial HAP is poorly-crystalline and non-stoichiometric compound. Virtually, the heating of stoichiometric poorly-crystalline HAP should not produce any heating by-product (such as β-TCP) but only the reorganization of the structure, with the increase of the crystallinity degree [67,172]. Previous studies, reported in the open literature, describe that stoichiometric crystalline HAP (Ca/P molar ratio higher than 1.667) displays a diffraction pattern with well-defined and sharp peaks even at room temperature [83] and does not undergo to any phase transformation induced by heating up to ~1000-1200 °C [67,83]. Commercial HAP, even if non-stoichiometric and partially substituted, was considered a suitable reference material in order to study the phase transformation of non-stoichiometric calcium phosphates formed after DAP treatments. For the characterization of the *shell*, the Bragg peaks corresponding to the *d* spacing of 2.81 Å, 2.77 Å, 2.71 Å and 2.62 Å were selected as HAP markers, as they do not exhibit significant overlapping with the peaks of other phases.
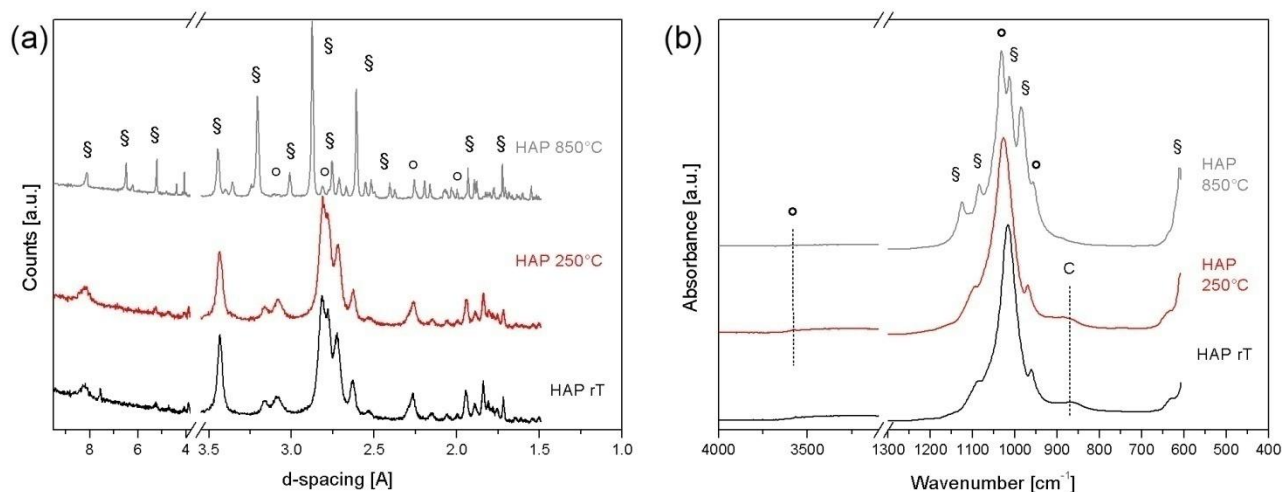
Fig. 5.14 (a) XRPD and (b) FTIR patterns of commercial HAP at rT and after heating at 250 °C and 850 °C. ° = crystalline HAP, § = β-TCP, C = carbonate band.

Calcite is always present in the *shell* in the form of embedded micro-grains, thus the behaviour of calcite to temperature was considered as well. The well-known thermal decomposition of calcite, commonly called calcining or calcination, occurs between ~600 - 850 °C and induces the formation of calcia (calcium oxide, CaO) and carbon dioxide according to the equation [173]:

$$CaCO_3(s) \rightarrow CaO(s) + CO_2(g) \qquad\qquad (5.1)$$

In agreement, calcite powders heated at 850 °C display the typical diffraction pattern of calcia, as product phase of the complete transformation of calcite with high temperature. Furthermore, XRPD patterns also reveal weak peaks due to portlandite (calcium hydroxide, $Ca(OH)_2$), most likely formed after the heating treatment by the quick hydration reaction occurred between calcia and atmospheric moisture:

$$CaO(s) + H_2O(g) \rightarrow Ca(OH)_2(s) \qquad\qquad (5.2)$$
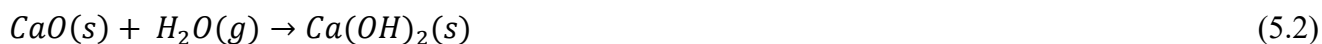
5.2.2.2 Heating of the newly-formed calcium phosphates

The thermal transformation of the *shell* has been investigated with a sequential, continuous, *in-situ* XRPD investigation from room temperature to 900 °C (powders inside a capillary hermetically sealed, synchrotron X-ray source, λ =0.885227(6) Å).

Fig. 5.15 displays the XRPD pattern of the *shell* at rT and at high temperature, showing the principal phase transformations; the results showed in the following are referred to the *shell* formed on Carrara marble treated by capillarity with a 3.00 M DAP solution, but they are representative of all the specimens (Carrara marble or Noto limestone, treated by capillarity or poultice, with a 0.76 M or 3.00 DAP solution).

The first variation is detected at 250 °C, where a decrease of the d_{100} spacing of OCP from 17.51 Å to 14.19 Å suggests that its structure is collapsing, with a transition to an amorphous structure. As long as the temperature increases, calcite and calcium phosphates peaks display a progressive shift of inter-planar distances to higher d values, due to the thermal expansion [83]. Between 250 °C and 750 °C, the intensity of the Bragg peaks corresponding to d values of 3.47 Å, 2.82 Å and 1.73 Å increases, even without any evident phase transformation.

The main transformation occurs from 750 °C to 900°C, where the broad weak band between 2.90 Å and 2.62 Å changes into a sequence of sharper, well-defined peaks centred at 2.84 Å, 2.80 Å, 2.75 Å and 2.65 Å, respectively. These peaks, as well as the sharper peaks at 8.22 Å, 3.47 Å and 2.28 Å, are unambiguously attributed to the crystallinity increase of HAP above 850°C that minimizes the superimposition with the other phases (Fig. 5.15b). This finding definitely confirm the initial presence of nano-crystalline non-stoichiometric HAP in the *shell* of every specimen. From now on, the weak peaks at 3.43 Å and 1.71 Å observed at rT in the XRPD of the *shell* can be attributed without ambiguity to HAP.

β-TCP is documented as well, by its characteristic marker peaks at 3.20 Å, 2.86 Å, 2.33 Å, 2.15 Å and 2.03 Å. It is worth noting that the intensity of β-TCP peaks is quite low. Considering that β-TCP is the heating by-product either of OCP and non-stoichiometric apatite and that β-TCP is rather scarce after heating, it can be concluded that: i) OCP and non-stoichiometric apatite (*e.g.,* carbonate-bearing apatite) were only minor phases; ii) HAP, the main phase after heating, was mainly poorly-crystalline or nano-crystalline but stoichiometric in the *shell*.

No signals of β-CPP (thermal by-product of OCP) are detected after heating, probably due to the formation of this phase in amount below the detection limit. Thus reconfirming the initial low amount of OCP in the *shell*.

Calcite peaks remained visible even after heating at 900 °C, indicating an incomplete calcination, probably due to the presence of a CO_2 overpressure in the sealed capillary. Two weak peaks at 4.23 Å and 3.66 Å can be attributed to periclase (magnesium oxide, MgO) formed by the thermal decomposition of dolomite and/or magnesium calcite [174]. These peaks are most likely due to magnesium-containing grains embedded in the *shell* formed on Carrara marble, as this lithotype contains dolomitic veins.

All the crystalline phases resulted stable after cooling back to rT.
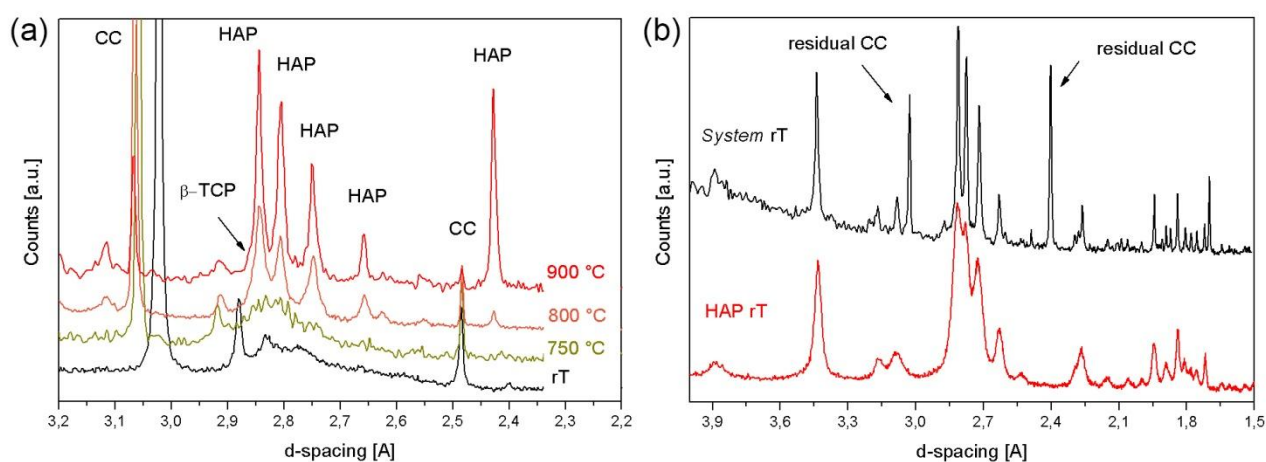
Fig. 5.15 XRPD patterns of the calcium phosphate *shell*: (a) acquired *in-situ* during the thermal treatments, showing the transformation of the broad band between 2.90 Å and 2.62 Å into a sequence of sharper, well-defined peaks of HAP (marker peaks at 2.84 Å, 2.80 Å, 2.75 Å and 2.65 Å). Weak β-TCP peaks and peaks of residual calcite (CC) are also present; (b) comparison of the heated *shell* after cooling to rT and commercial HAP.

This section demonstrated the formation of poorly-crystalline or nano-crystalline stoichiometric HAP after the DAP treatments. The unambiguous investigation of the phases of the *shell* was crucial in this experimental study in order to fully understand which calcium phosphates are formed by the consolidation and which phase assemblage is expected to form in the field on artwork stone surfaces.

The heating protocol here presented is destructive, as thermal treatments gave rise to irreversible phase transformations. In this section, the thermal treatments were carried out on powders, but in case of application to bulk samples, it would induce severe microstructural variations as well. Thus, a similar approach can be successfully translated in conservation science to assess the presence of other crystalline phases whose identification at room temperature and with conventional techniques is challenging, but it should be considered that this investigation is a laboratory procedure, it requires sacrifical specimens and it has not the goal to enhance the performances of the treatment in the field.

5.2.3 Evaluation of the variables (pH, DAP molarity, free ions availability) affecting the crystallization

The investigation of the composition and morphology of the *shell* carried out in § 5.2.1 showed that the crystallization process is influenced by some variables, for example: lithotype, microstructure of the substrate and DAP molarity. It is highly likely that other variables can control the process.

The heating treatments of section § 5.2.2 clearly demonstrated the presence of poorly-crystalline stoichiometric HAP and of low fractions of OCP. Thus, the formation of these phases occurred under reaction condition that prevented the formation of well-ordered crystals. All these data clearly indicate that the stone-treatment system is directly influenced by mutually interfering factors. Therefore, many aspects should be taken into consideration, starting from the kinetic of the reaction. The pH of the DAP solution is basic (pH about 8.8 at 22 °C). When the DAP solution is applied to the carbonatic substrate, namely at the beginning of the reaction, the pH is kept basic and the solution contains a high concentration of HPO_4^{2-} ions. Ideally, a similar pH value is described as suitable for the formation of HAP [64] but not enough calcium ions and OH^- groups are available for a stoichiometric crystallization. As the reaction evolves, the reagent precursor is dissociated into a higher fraction of PO_4^{3-} ions, following the equilibrium reaction [31,56]:

$$HPO_4^{2-} \leftrightarrow H^+ + PO_4^{3-} \qquad K \; = \frac{\{H^+\}\{PO_4^{3-}\}}{\{HPO_4^{2-}\}} = \; 10^{-12.36} \qquad\qquad (5.3)$$
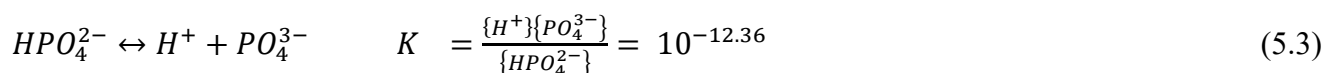
The protons of the reagent react with calcite and induce a slight dissolution of the substrate components (Fig. 5.16). The increasing availability of free Ca^{2+} ions and PO_4^{3-} groups allows the beginning of the crystallization of calcium phosphates, meaning that the reaction is self-powered. At the same time, the dissociation of the precursor implies an acidification of the media, due to the continue release of protons. HAP crystallizes preferentially at basic pH value and needs a supersaturation of Ca^{2+} and PO_4^{3-} ions (Ca/P molar ratio = 1.67) but when the pH is basic, the solution provides a low concentration of PO_4^{3-} and calcium ions. Vice versa, OCP crystallizes at pH values close to the neutrality, needing lower amount of Ca^{2+} and PO_4^{3-} ions (Ca/P molar ratio = 1.33) but requiring also HPO_4^{3-} ions that are progressively consumed by the reaction. In both the cases, the reaction environment is never supersaturated toward the ideal crystallization of one of the two phases. It follows that the carbonate-to-phosphate conversion is essentially based on pH, free Ca^{2+}, PO_4^{3-} and HPO_4^{3-} ions, and the formation of OCP and HAP occurs under not ideal reaction conditions [64]. In this reaction environment, CO_3^{2-} groups are also available and the crystallization of carbonate-substituted apatite, with the typical surface layers hosting groups such as CO_3^{2-}, HPO_4^{2-} instead of PO_4^{3-}, is promoted, as confirmed by FTIR spectroscopy [75,166].

Following that, and considering the data obtained by ATR µ-FTIR of Fig. 5.12, the detection of "hybrid" vibrational pattern between OCP and HAP, down to 1×1 µm^2, strongly suggests a probable interlayering of these two phases in the same individual as intra-crystalline mixtures [93,96]. The interlayering of OCP and HAP is actually a well-known phenomenon, described in literature as *central dark line* [169], and it strengthen the thesis of an initial formation of OCP as growth seed on calcite rims, followed by the predominant development of poorly crystalline HAP.
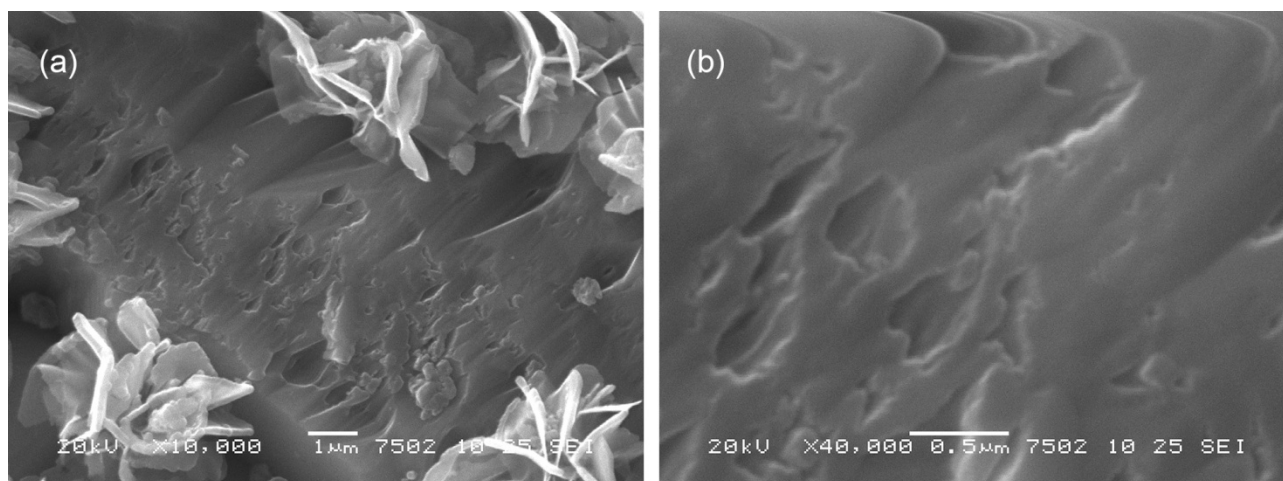
Fig. 5.16 SEM images of the surface of Carrara marble (treatment by poultice, 0.76 M DAP), showing slight dissolution marks induced to calcite during the DAP reaction.

The crystallization of DCPD crystals allows discussing about another aspect of the calcium phosphate crystallization. In fact, DCPD platelets nucleate only on Carrara marble, after treatments performed with 0.76 M DAP solutions and only over the *shell.*

DCPD is an acidic calcium phosphates, it has a Ca/P molar ratio of 1.00 and its growth can be linked to a low Ca/P molar ratio in the solution. Its crystallization requires the availability of HPO_4^{2-} groups and a low Ca^{2+} concentration, a reaction condition not properly suitable for the nucleation of OCP and HAP. Most likely, similar conditions take place in the final steps of the reaction with 0.76 M DAP solutions, when the growth of an almost completed *shell* starts to represents a barrier for the ion exchange and the release of calcium ions from the substrate. Consequently, DCPD crystallizes over the *shell* in an external reaction environment progressively poor of Ca^{2+} but still rich of HPO_4^{3-}.

Furthermore, the crystallization of DCPD depends also on the DAP molarity and on the composition/heterogeneity of the substrate.

Dealing with the molarity, the 0.76 M DAP solutions are found to have a "reduced capability" to dissolve the calcite of the substrate. In fact, the treatments performed with this molarity are less aggressive on the stone substrate and, for this reason, the *shell* is well adherent to the substrate. On the contrary, a DAP solution with a higher molarity releases in water a higher amount of proton. This means that, if from one side the solution can form thicker *shell*, on the other side high molarities dissolves calcite from the substrate efficiently, making available high amounts of Ca^{2+} ions. The consequence is that, *e.g.* for 3.00 M DAP solutions, the release of protons is 3.95 times higher than for 0.76 M ones, the treatment is more aggressive on the substrate and calcite shows deep corrosion marks on the reaction profile. Moreover, the formed *shell* shows evident detachments from the substrate.

The direct influence of the substrate (composition and micro-structural heterogeneity) on the availability of calcium ions during the reaction is particularly evident on the surface of Carrara marble specimens treated with 0.76 M DAP solutions in correspondence of a dolomitic vein (study by grazing incidence X-ray diffraction – GIXRD, results published on Applied Physics A, [175]).

Over the Carrara marble veins, DCPD crystals in addition to OCP are well detectable in the GIXRD patterns (Fig. 5.17), in combination to the minerals of the vein: dolomite, phyllosilicates and quartz. On the contrary, the presence of calcite is ambiguous and the HAP marker peaks at 3.43 Å and 1.71 Å

are never distinguishable from the baseline. This data clearly indicate that, in correspondence of a substrate poor of calcium ions, the newly-formed phases (DCPD and OCP) are characterized by a low Ca/P molar ratio as well.
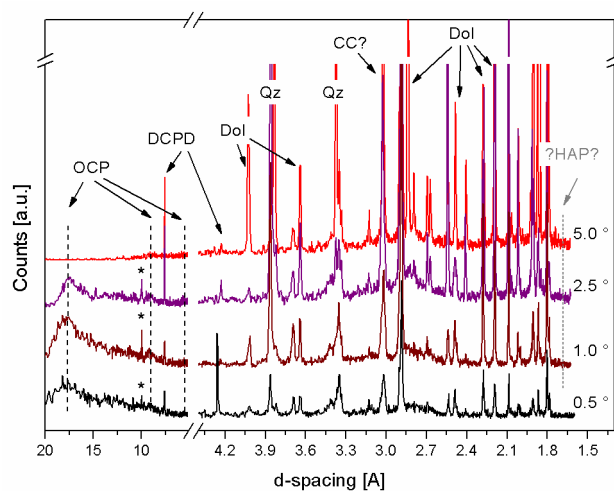
Fig. 5.17 GIXRD patterns of the surface of a treated marble specimen over a dolomitic vein. In this case, DCPD and OCP are the newly-formed phases, while the detection of HAP is ambiguous. *Dol* **dolomite,** *CC* **calcite,** *QZ* **quartz, * phyllosilicates.**

The scheme of Fig. 5.18 summarizes the composition of the calcium phosphate phases nucleated on the studied carbonatic substrates by using DAP solutions with different molarity.
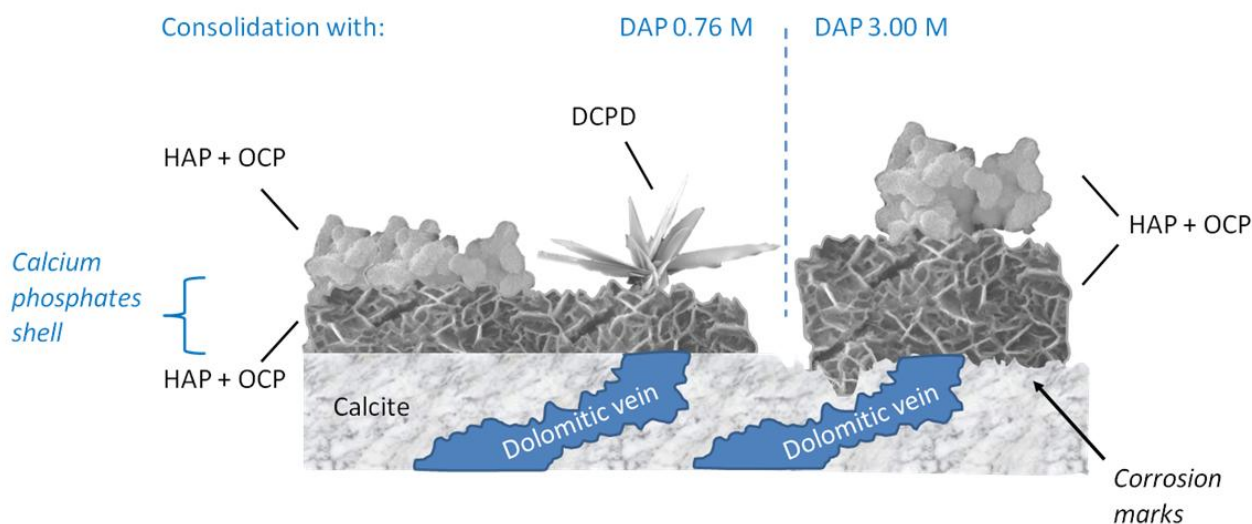
Fig. 5.18 Scheme (not in scale) of the morphology and composition of the calcium phosphates nucleated on the studied lithotypes, after the consolidation with DAP solutions at different molarity.

As final section remark, the phases association which contitutes the *shell* is expected to generate positive performances in the conservation field as: i) HAP is poorly-crystalline but mainly stoichiometric, thus highly insoluble in a wide pH range; ii) OCP, which is slightly more soluble than HAP, is actually a highly insoluble phase as well and it is more insoluble than calcite [23,64,65,71].

Dealing with the stability of the newly-formed phases, HAP is a highly stable phase while some of them are metastable: DCPD and OCP. Noverthless, their formation is positive from the conservation point of view as: i) their formation (especially for DCPD) reflect a minor attack of the stone substrate; ii) these calcium phosphates tends to evolve toward more stable and insoluble crystalline phases. In fact, their transformation in HAP by dissolution and reprecipitation processes or by topotactic mechanism in known in literature and it has already been observerded on calcite-based lithotypes treated with DAP solutions [31,64,68].

In conclusion, considering all the investigated variables influencing the crystallization and the collected results, the DAP-based consolidating treatment and the newly-formed calcium phosphates show premise of an improvement of the substrate features in terms of durability and compatibility, even in acid environment.

5.3 Crystallization of calcium phosphates within Noto limestone

The penetration depth and distribution in the stone substrate are important factors to assess the efficacy of a consolidating product. Focusing on DAP-based treatments, the presence of the consolidant within the stone matrix has previously been evaluated with different methods: *e.g.,* visual observation in fractured prismatic specimens right after the application of the treatment [69], X-ray powder diffraction, Fourier-transform infrared spectroscopy (FTIR) [69], Raman spectroscopy [21,33,50,54,176], ionic chromatography (IC) [69] and scanning electron microscopy (SEM) [24,31,35,47,53,61]. Mercury intrusion porosimetry (MIP) investigations are also performed to investigate the variations induced to the substrate by the diffusion of DAP solutions [44,47,69,177,178]. Recently, preliminary experimental findings reported by neutron tomography and radiography evaluated the penetration depth of inorganic-mineral treatments [177,179,180], by taking advantage of the high neutron attenuation of hydrogen to localize hydrogen-rich substances employed for stone conservation [181].

In many cases the combination of these techniques is frequently not exhaustive, as many of them provide "point information", thus having strong limitations when investigating heterogeneous matrixes.

Therefore, a further step forward aims to optimize the analytical protocols in order to understand: i) the crystal-chemistry origin of the positive effects observed in literature, ii) how these mechanical and physical effects depends on the diffusion mechanisms and crystallization in the core of the stone matrix. Following that, the action of DAP consolidating treatments on Noto limestone has been evaluated as the effects induced to the substrate in terms of micro-structural variations, modification of the porosity (pore size distribution, total open porosity and average of pore radius), penetration depth, crystallization of specific phases and their distribution on the surface and inside the voids.

A group of analytical techniques was used to study the composition and distribution of the newly-formed phases inside the treated stone matrix. Within this group, the techniques are subdivided in interpretative methods and qualitative methods. Scanning electron microscopy coupled with energy-dispersive X-ray spectrometry (SEM-EDS) and wavelength-dispersive X-ray spectrometry (WDS) were used as "interpretative" methods, to localize the newly-formed phases by point analysis. X-ray powder diffraction (XRPD), X-ray diffraction in transmission geometry (T-XRD) and infrared spectroscopy (FTIR) were used as qualitative methods to unambiguously identify the nature of the crystalline phases.

On the other side, synchrotron radiation X-ray micro-computed tomography (SR-μCT), determination of water absorption by capillarity and mercury intrusion porosimetry (MIP), were used to investigate the variations induced by the treatments to the stone. Moreover, these techniques shed light on the diffusion mechanism of DAP solutions inside the voids, because it depends not only on the total porosity but also on textural properties of the pore network, such as the pores shape, tortuosity and connectivity, and the specific surface area of the pores due to the pore size distribution. The limits of this approach, substantially linked to their non-qualitative nature, were integrated by qualitative methods.

In the following discussion, the word *specimen* identifies the 5×5×2 cm parallelepipeds of Noto limestone, while the word *sample* indicates a fragment, a slice or the sampling of a part of the specimen.

The water absorption by capillarity of Noto limestone specimens was investigated before DAP treatments according to the European Standard UNI EN 15801:2010 (Conservation of cultural property – test methods – determination of water absorption by capillarity, [182]), a protocol indicating how to measure the water absorption by capillarity of stone materials, the duration of the measurement (which normally takes up 7-8 days) and how to express the water uptake in terms of absorption curve and capillary absorption coefficient (CA).

The rate of capillarity absorption was screened for 40 specimens and a group of 6 parallelepipeds has been selected for DAP treatments on the basis of similar sorptivity properties (Fig. 5.19). The specimens labelled n° 8, 10, 14, 21, 30 and 31 were selected for investigations. These specimens were selected comparing their absorption curves and their water uptake. Observing Fig. 5.19, it is possible to observe that this set of specimens is in the middle of the values measured for all the specimens. At the same time, three of them show values slightly lower the average (n° 10, 14, 30), while the other three show a water absorption slightly higher of the average (n° 8, 21, 31). This allows that the 6 selected specimens are representative of an "average behaviour" in water absorption but at the same time they shows residual differences, which are representative of the micro-heterogeneities of the microstructure and porosity of Noto limestone. In this way, evaluations on how consolidating treatments modify the porous structure and the sorptivity properties are possible among the 6 specimens and among untreated and treated specimens.

To monitor the absorption curve of untreated parallelepipeds, the measurements have been performed after 10 min, 20 min, 30 min, 60 min, 2 hours, 4 hours, 5 hours and 24 hours. The same intervals and duration of the measurement have been carried out on the specimens after treatments, and the descending results are discussed in the following. Focusing on the 6 untreated Noto limestone specimens, their water absorption curve is shown in Fig. 5.20.

The water absorption curve plots the amount of water absorbed Q (calculated with the formula showed in § 3.2.3.2.) with respect to the absorption time, calculated in $\sqrt{s}$ as indicated by the European Standard [182].

In general, all the untreated Noto limestone specimens show an initial straight stretch, which occurs in the first absorption steps, followed by a dramatic decrease of the slope in the last measurements. At the same time, even if the trend of the six curves is common, different specimens present slight differences in their water absorption curves due to microstructural variations from a specimen to another.

Focusing on the water uptake, Noto limestone presents the most significant weight increase due to water absorption in the first 3-4 measurements, namely, in the first 42-60 $\sqrt{s}$. In this absorption time, the lithotype absorbs about 94-95 % of the total water uptake. After that, the absorption rate of water shows a decrease, even if the water absorption continues constantly.

The six specimens of untreated Noto limestone absorbed between 12.09 g and 13.27 g of water in 294 $\sqrt{s}$, which corresponds to the 13.78-15.52 % of their dry weight.

Considering all the absorbed water, from 85 $\sqrt{s}$ to 120 $\sqrt{s}$ there is an average increase of 0.5 % while from 120 $\sqrt{s}$ to 134 $\sqrt{s}$ there is an increase of 0.36 %. The remaining 4-5 % is absorbed between 134 $\sqrt{s}$

and 294 √s, with a calculated average of about 0.2-0.3 %/hour. Therefore, since there is not a significant increase of the water uptake between 134-294 √s, the sorptivity test of Noto limestone can be considered concluded after 294 √s, as, with a good proxy, the lithotype reaches an equilibrium state after this interval.
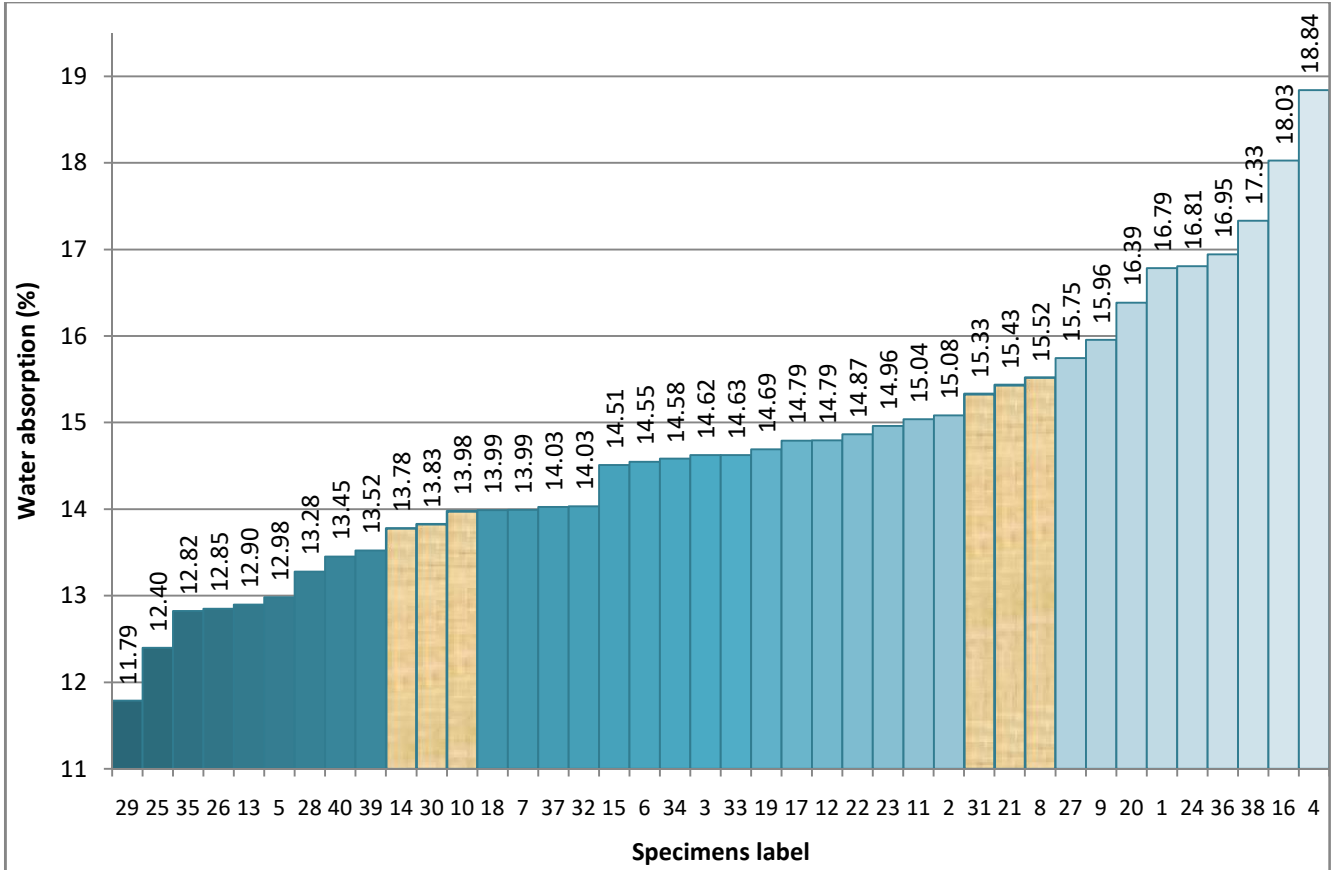
Fig. 5.19 Water uptake by capillarity (plotted as % increase on their dry weight) after 294 √s of 40 different specimens of quarry Noto limestone. The specimens labelled 8, 10, 14, 21, 30 and 31 were selected for DAP treatments by poultice, on the basis of their % increase on the dry weight.

Water absorption curve of untreated specimens
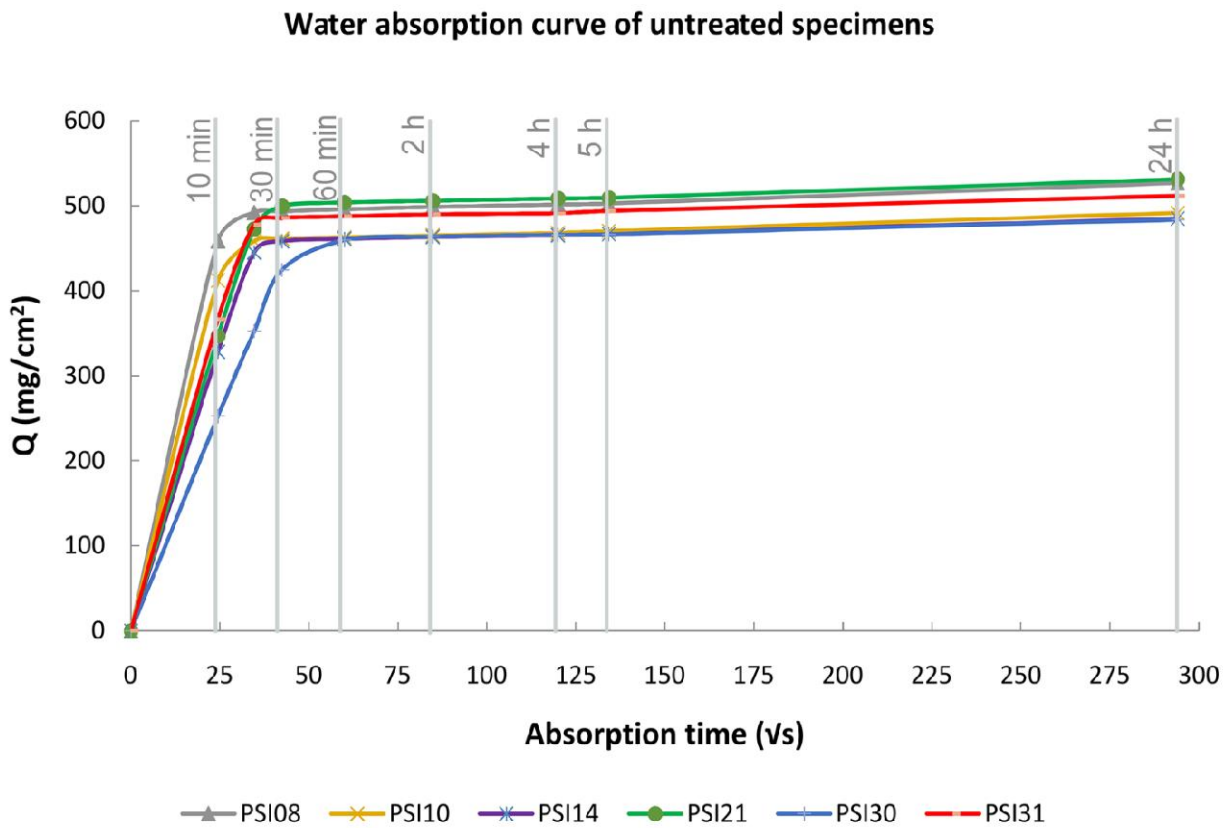
Fig. 5.20 Water absorption curves before the DAP treatment of the 6 quarry Noto limestone specimens selected for investigations.

The capillarity investigations showed that the specimens absorbed about the 94-95 % of the total water uptake between 35-60 √s. The same phenomenon was observed during DAP treatments, where the specimens were found to be optically darker and saturated, due to the impregnation of the porous matrix with the liquid used for the consolidation (§ 3.1.2, Treatment protocol). For this reason, the specimens were treated for 2 h by poultice with a 0.76 M DAP solution. Another set of specimens was treated with the same protocol for 24 h, to compare the effects induced by the treatment time on the crystallization and penetration depth of newly-formed phases. Capillarity measurements after treatment were carried out only on specimens treated for 2 h.

The penetration depth of calcium phosphates inside Noto limestone was investigated by morphological observations and by mapping the crystallization of P-containing phases. In Fig. 5.21, two representative SEM images shows the typical morphology of Noto limestone before and after the reaction with 0.76 M DAP solutions. Calcite of the substrate can be recognised in the portions showing a light grey hue, while calcium phosphates are well distinguishable on the boundaries of calcite grains in the darker area. The grey hue of calcium phosphates is detectable close to the reaction surface of calcite as well as inside the micro-porosity of calcite grains, as showed by the arrows in Fig. 5.21b (localization supported by EDS analyses).

SEM morphological investigations clearly demonstrate that DAP treatments preserve the highly porous nature of the lithotype. In fact, the study of several cross sections showed that, even if the

crystallization of newly-formed phases occurs of pore walls, their formation actually do not fill the entire pores, as showed in Fig. 5.21 and as demonstrated by MIP measurement (discussed in the following). Focusing on the reaction profile, calcite grains show irregular boundaries, demonstrating the occurrence of a topotactic reaction in which the reagent partially dissolves the substrate, while P-containing phases employ the pre-reacted substrate as growth seed for the new crystallization.
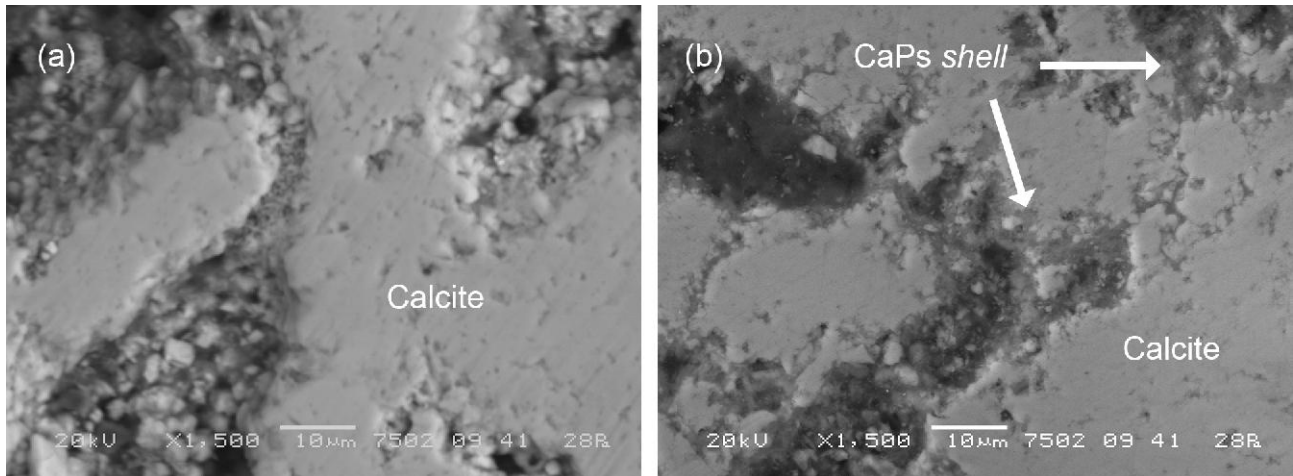
Fig. 5.21 SEM images of untreated (a) and treated (b) Noto limestone embedded in polished cross section at a depth of 700 μm from the surface of the Noto limestone specimen. The (b) image shows the well distinguishable formation of the calcium phosphates *shell* on the boundaries of calcite grains, preserving the voids due to the natural porosity of the stone..

In general, the formation of calcium phosphates is actually quite widespread and permeates the lithotype. SEM-EDS analyses, carried out on transversal cross sections and on longitudinal sections parallel to the treated surface (Fig. 5.22), unambiguously demonstrate the formation of newly-formed phosphorous-based compounds down to several millimetres.
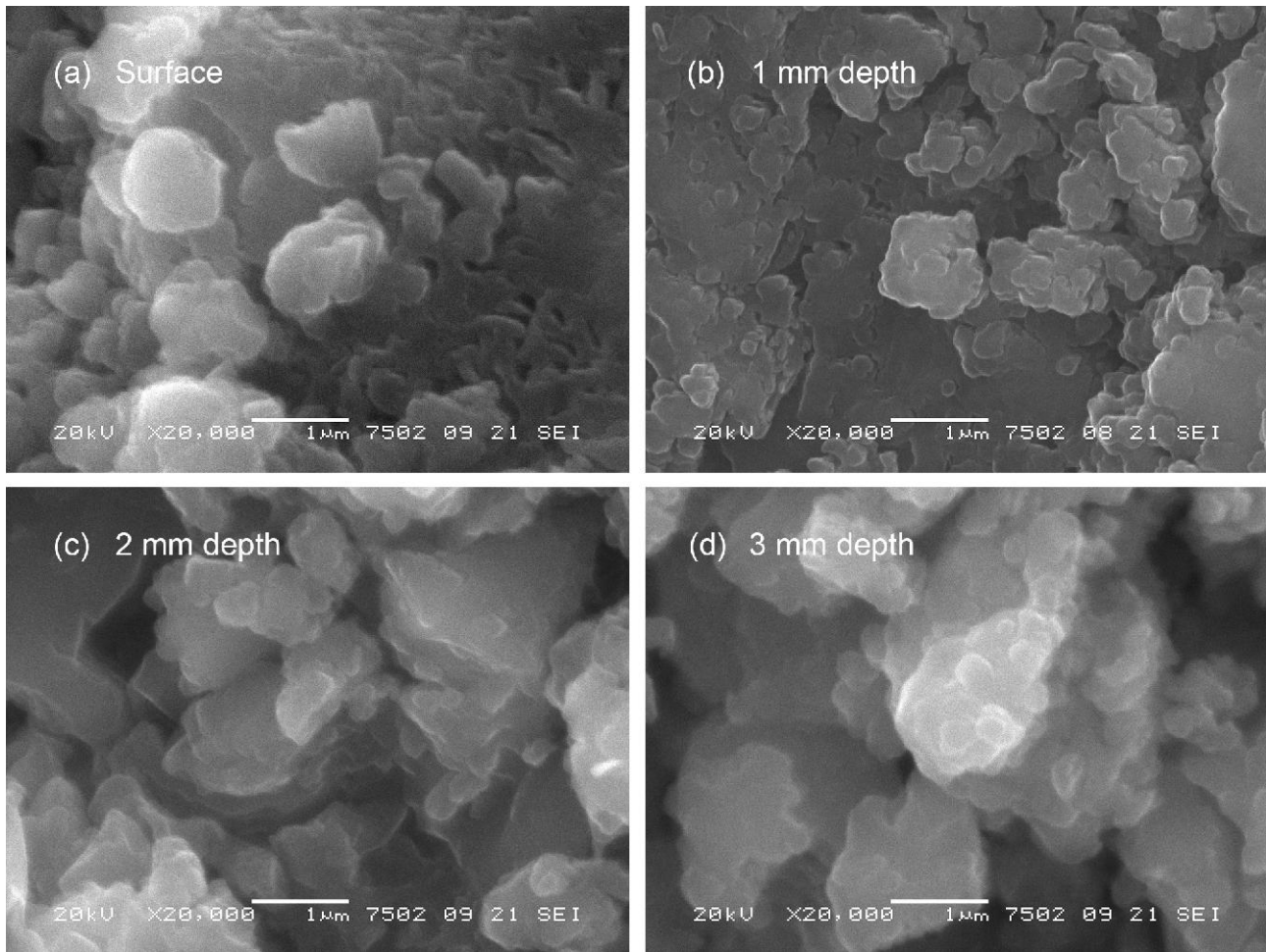
Fig. 5.22 SEM images of treated Noto limestone, showing the typical rounded morphology of calcium phosphates. The images were collected on the surface of the stone matrix (a) and on sections parallel to the treated surface cut at 1 mm (b), 2 mm (c) and at 3 mm (d) depth.

The phosphate phases, detected by EDS spectra of points or 2D maps, are more abundant in the most superficial portion of stone materials, while they undergo to a slight but progressive reduction as long as the measurements are focused toward the inner portions. A sort of accumulation on the surface is somehow expected, as it is the portion of stone materials which is directly in contact with the source of DAP solution, and also because the solution which penetrates through the first millimetres is still rich of reagent. At the same time, it is interesting to observe that the newly-formed phases formed close to the surface do not form an external thick, compact crust, but, on the contrary, they are localized in the voids and generate a network highly interconnected that binds calcite grains. Another aspect issued by SEM-EDS investigations is the detection of a further enrichment of calcium phosphates on the bottom of treated specimens, namely on the opposite side of the treated surface.

No significant morphological and compositional differences are observed comparing the specimens treated for 2 h or for 24 h, confirming that, in both the cases, the DAP solution permeates the stone matrix and reacts with the whole thickness. Previous studies showed that the DAP reaction with calcite takes at least 4 h to form a detectable amount of calcium phosphates [56], and about 24 h to develop a crystal network with consolidating properties [31]. Actually, the detection of calcium phosphates after 2 h of treatment is not in contrast with these findings. In fact, if the treatment time is 2 h, the duration

in which the stone remains wetted by the treatment solution is longer, ranging between 20-24 h. From one side, this "wetting" time allows an effective reaction of the reagent with the stone material. From the other side, the slow but progressive evaporation of the solution determines a sort of reversal of direction of the DAP solution. In fact, if during the treatment the flux is from the surface toward the inner part, during evaporation the flux has the opposite direction, thus shifting the unreacted product from the inner portion, ideally not decayed, toward the most external portion of material, ideally weathered. This change of flux during evaporation might form a further crystallization of CaP phases close to the surface, contributing to the gradient of P-containing compounds observed by SEM-EDS investigations.

Thus, these investigations suggest that even a short treatment time (*e.g.,* 2 h by paper poultice) is able to induce the formation of a detectable and effective amount of newly-formed crystalline phases, as long as the evaporation of the solution, and therefore the interruption of the reaction, is controlled.

SEM-EDS investigations shed light on the localization of calcium phosphates with respect to calcite grains but the collected data are referred only to a general P-containing substance. Furthermore, Noto limestone might naturally contain traces of phosphorous due to its biogenic origin. Thus, these data needs to be integrated with the characterization of the composition of the newly-formed phosphates, as the performances of inorganic-mineral treatments depends also on the nature of the formed crystalline phases. The formation of newly-formed calcium phosphate phases at different depth was then investigated sampling micro-fragment at fixed distances from the treated surface (*e.g.* 1 mm, 2 mm, 3 mm, etc.), and the polycrystalline materials were characterized by FTIR spectroscopy and conventional X-ray powder diffraction (XRPD). Thin sections (400-700 μm) were instead investigated by X-ray diffraction with synchrotron radiation in transmittance geometry (T-XRD). A scheme of the analytical protocol is showed in Fig. 5.23.
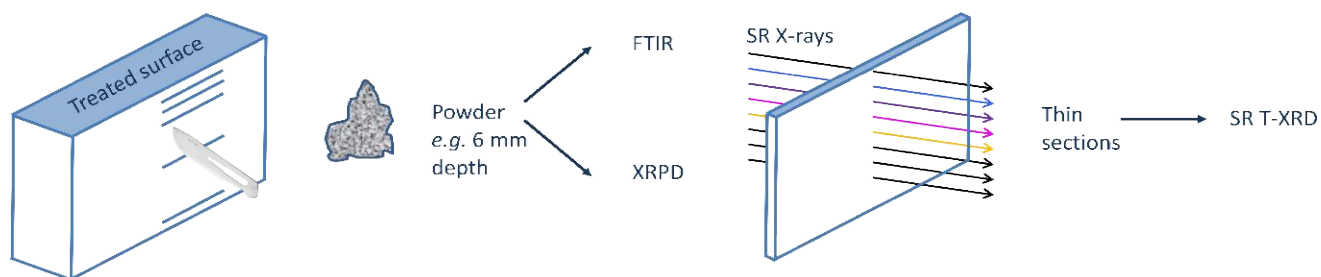
Fig. 5.23 Scheme (not in scale) of the sampling protocol used for FTIR, XRPD and T-XRD investigations.

The FTIR patterns of treated Noto limestone at different depth are shown in Fig. 5.24, in comparison with the FTIR pattern of the quarry lithotype. Calcium phosphates bands are well distinguishable in the spectra collected from the most superficial portions, namely down to 2-3 mm depth. Below this level, the fraction of calcium phosphates progressively decrease and the bands of silicates of the matrix are progressively more visible. Below 4-5 mm depth, the partial overlapping of the PO_4 stretching bands of phosphates at 1038 cm^{-1} with the SiO_4 stretching of silicates at 1033 cm^{-1} prevents the unambiguous identification of calcium phosphates. Therefore, the PO_4 bending vibration at 602 and 563 cm^{-1}, even though weaker than the stretching vibrations, becomes important to discriminate newly-formed phosphates from the stone matrix. In some cases, *e.g.,* for sample PSI08 of Fig. 5.24,

FTIR bands of calcium phosphates were detected down to 7-8 mm of depth, while more commonly they are detected down to 3-5 mm. In all the cases, the intensity of these two bands is so modest that below 7-8 mm of depth these bending vibrations are hardly distinguishable from the background.

As general remark, FTIR spectroscopy resulted sensitive to detect the newly-formed phases in the inner portions of stone materials, but not enough for the discrimination among HAP and OCP.
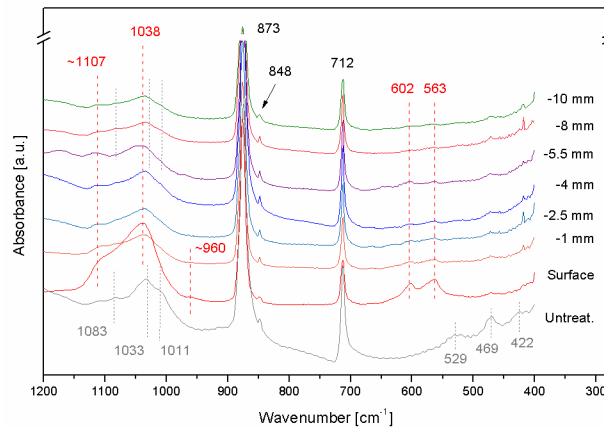
Fig. 5.24 FTIR spectra of the surface and at different depth of Noto limestone treated for 24 h by 0.76 M DAP solution by paper poultice and comparison with the untreated stone. The dashed lines at about 1107, 1038, 602 and 563 cm^{-1} are of calcium phosphates. The dotted lines at 1083, 1033, 1011, 529, 469, 422 cm^{-1} corresponds to silicates of the matrix. Calcite peaks are at 873, 848 and 712 cm^{-1}.

The impossibility to detect the vibrational bands of calcium phosphates below a given penetration depth is due to the FTIR detection limits (in mass percentages) of these phases [67] and it does not mean that the calcium phosphates are not formed at all.

In fact, the SEM-EDS morphological investigations and elemental analysis (*i.e.*, SEM-EDS images of polished cross sections and longitudinal sections, Fig. 5.21 and Fig. 5.22) complement FTIR outcomes as they showed a noteworthy crystallization of Ca- and P-bearing compounds in the matrix of Noto limestone down to 2 cm, namely down to the opposite side of the surface treated with DAP solutions.

The composition of the newly-formed phases and the possible phase variations along the penetration depth was investigated with X-ray diffraction. Initially, the nature of the calcium phosphate phases was explored with conventional XRPD, but the technique resulted poorly exhaustive. In fact, as discussed in § 5.2.1, these phases are poorly-crystalline and in such a low fraction with respect to calcite of the matrix, that their XRPD peaks are hardly detectable below a depth of 1-2 mm from the surface (Fig. 5.25).
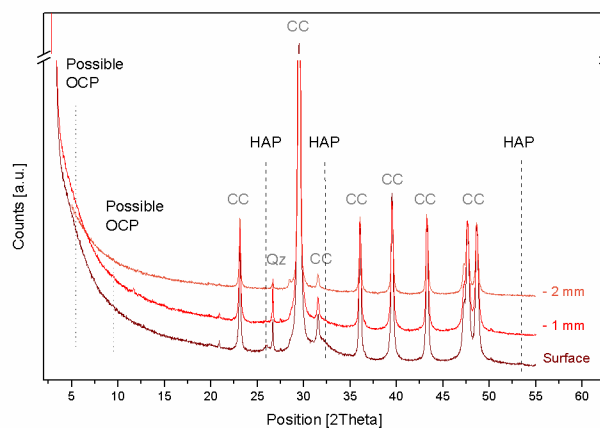
Fig. 5.25 XRPD patterns of DAP treated Noto limestone. The Bragg peaks of calcium phosphates (HAP = hydroxyapatite and possible OCP = octacalcium phosphate) are detectable on the surface of the lithotype and in the most superficial portion of stone matrix. Below 2 mm depth, their detection is very ambiguous. CC = calcite, Qz = quartz.

On the contrary, XRD in transmittance geometry (T-XRD) carried out with synchrotron radiation provided the most exhaustive outcomes. The investigations were performed on this sections (thickness about 400-700 micrometers) of treated stone embedded in epoxy resin and the main representative XRD patterns are showed in Fig. 5.26 and Fig. 5.27.

T-XRD investigation were carried out in two synchrotron facilities with a twofold aim: at ELETTRA (data showed in Fig. 5.26), the measurements were carried at the XRD1 beamline with a beamsize of 40x40 μm to study the penetration depth of calcium phosphates in the whole specimens; at ESRF (data showed in Fig. 5.27), the goal of the investigations was to detect possible phase changes from the surface to the inner portion of stone material. In this last case, the measurements were carried out at the beamline ID15b, with a smaller beamsize (10x10 μm).

All the diffraction patterns show mainly the Bragg peaks of calcite of the matrix, similarly to the conventional XRPD ones. At the same time, thanks to the highly energetic and collimated beam providing high quality data, minor mineral components are also detectable. In fact, in the T-XRD patterns of Fig. 5.26, it is possible to well identify silicates and calcium phosphates.

Focusing on silicates, all the specimens contains kaolinite (main peak at 7.17-7.20 Å), clay minerals such as smectite/montmorillonite (broad peaks at 4.48 Å and 2.57 Å) and quartz (4.25 Å and 3.34 Å). In all the cases, the intensity of their peaks is very low, and their relative abundance is randomised, following the micro-heterogeneities of the matrix. The characteristic peaks of HAP are visible at 3.43 Å, 2.79 Å and 1.71 Å as well. The intensity of these peaks is higher in the most superficial portion while it undergoes a progressive decrease as long as the T-XRD data are collected from the inner portion.

Even though a gradient of the intensity of HAP Bragg peaks exists (the inner, the lower- similarly to what observed by FTIR and SEM-EDS), it is not possible to perform a quantitative evaluation, as the distribution of HAP suffer of the heterogeneity of the stone matrix and spotty thickening might occurs close to the voids, interconnected pores and micro-cracks. In any cases, HAP is detected in the whole thickness of the specimens.

Regarding the possible presence of other calcium phosphate phases, a humped baseline of the initial spectrum portion blinds the region at high interplanar distances, preventing the identification of OCP and other metastable phases. In some T-XRD patterns collected from the sample surface, a weak shoulder at ~ 18.70 Å is compatible with OCP, but the presence of a such high baseline makes ambiguous the identification.
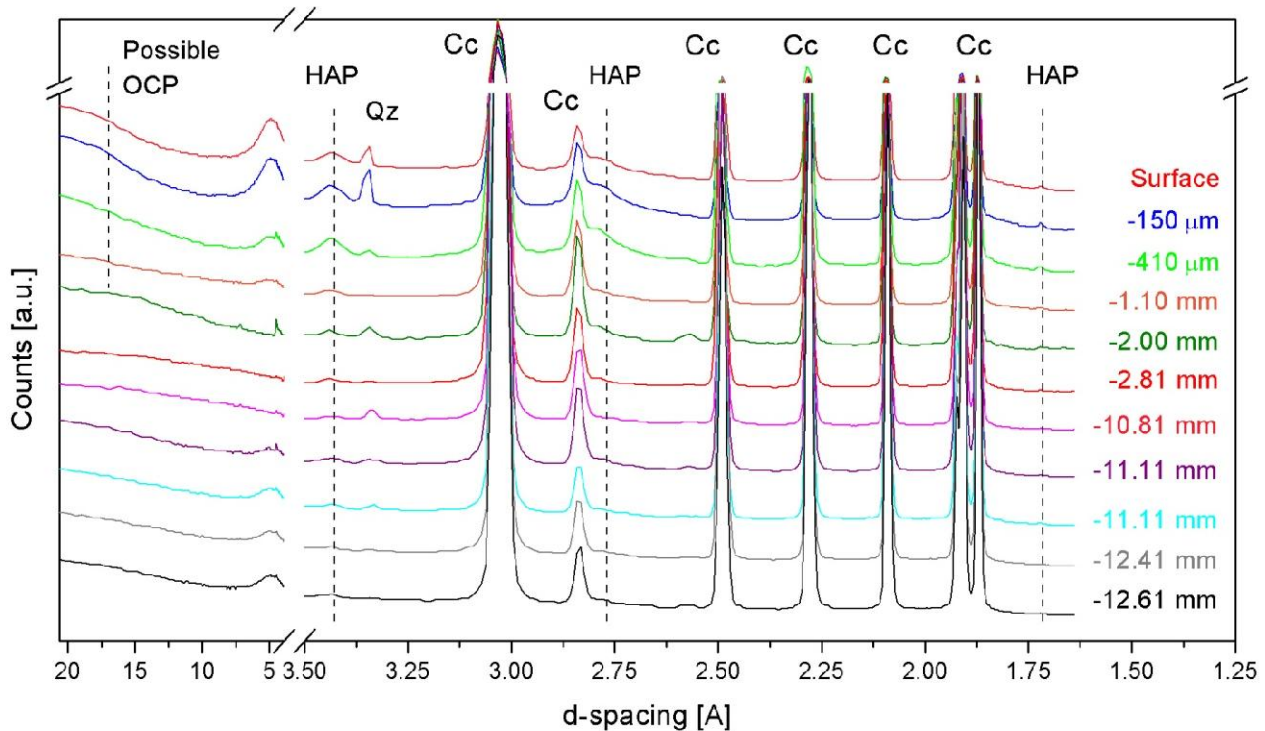
Fig. 5.26 T-XRD patterns of treated Noto limestone from the surface down to 12.61 mm depth, showing the unambiguous presence HAP peaks. Possible peaks due to OCP are showed as well. Qz = quartz, Cc = calcite.

Fig. 5.27 shows the T-XRD patterns collected at ESRF to study the distribution of the newly-formed crystalline phases in the first millimetre of treated Noto limestone. In this case, the baseline is definitely flatter and upgrades the possibility to identify crystallites with high interplanar distances. In these T-XRD patterns, ADP and DAP are detected by their Bragg peaks localised at 5.33 Å, 3.76 Å, 2.37 Å and at 5.59 Å, 5.06 Å, 5.01 Å (shoulder), 4.95 Å, respectively. The identification of the reagent (DAP) and of the acid by-product of the reaction (ADP), in well agreement with the PDF references 37-1479 and 1-70-1461, occurs only in the spectrum referred to the surface.

OCP is detected as well by the peaks at 9.49-9.10 Å and at 5.51 Å, in the patterns collected from 200 µm to 600 µm depth. The weak shoulder at 9.10 Å in the T-XRD pattern collected in the most external portion suggests that OCP might be present also on the surface, even if the secondary peak at 5.51 Å is overlapped with a DAP peak. Below 600-700 µm depth, the identification of OCP becomes ambiguous. The results, in terms of composition and localization of the crystalline phases, are similar between specimens treated for 2 h or for 24 h.
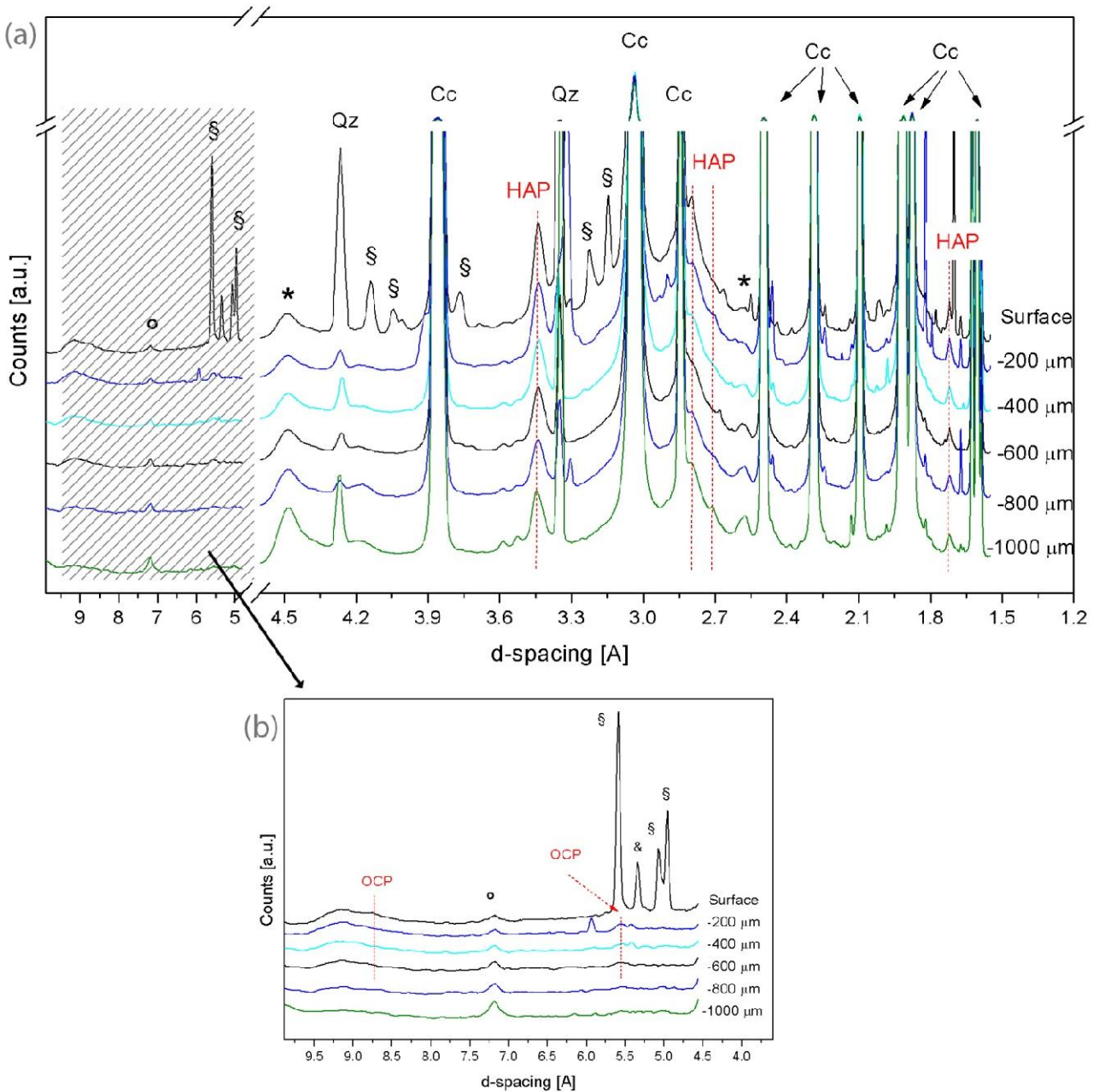
Fig. 5.27 (a) T-XRD patterns at different depth from the surface of treated Noto limestone. (b) zoom of the T-XRD patterns in the region at higher interplanar distances. Cc = calcite, Qz = quartz, HAP = hydroxyapatite, OCP = octacalcium phosphate, * = clay minerals (illite), ° = kaolinite, § = unreacted DAP, & = unreacted ADP. HAP is present in all the spectra, while OCP is present from the surface down to 600 micrometers.

Noto limestone contains small amount of silicates, detectable by a few peaks with a very low intensity in the T-XRD patterns of Fig. 5.27. The most abundant mineral in the sandy–silty fraction of Noto limestone is quartz, followed by low fractions of microcline, albite, hematite and fluorapatite. Phyllosilicates (*e.g.,* illite, kaolinite and smectite/montmorillonite) are present in the clay fraction [148]. Si-Al-containing phases are also visible is WDS chemical maps collected on treated specimens Fig. 5.28. These phases are mainly located into the voids of the stone matrix, which host also the crystallization of P-containing compound after DAP treatments.
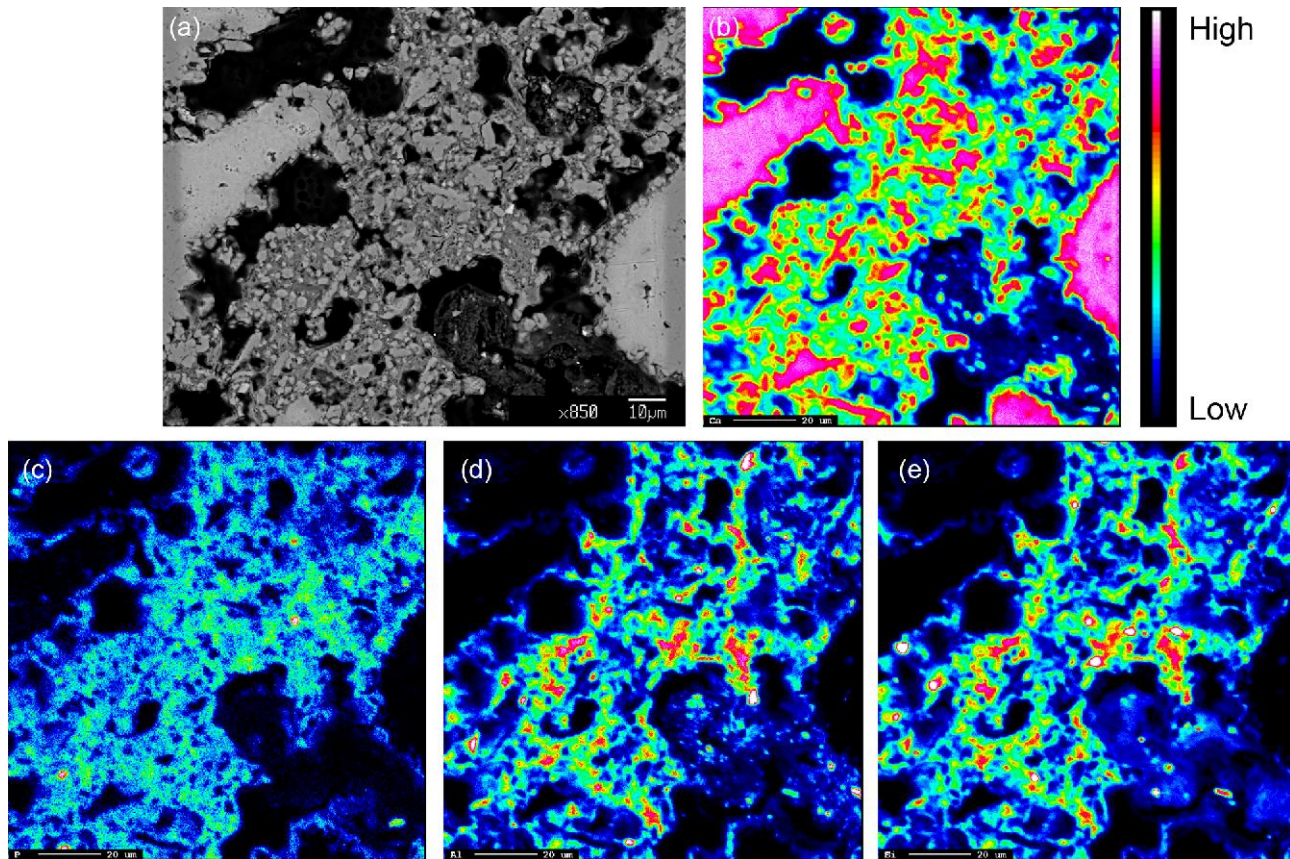
Fig. 5.28 Micro image (a) of treated Noto limestone and chemical maps (WDS) of calcium (b), phosphorous (c), aluminium (d) and silicon (e). The scale bar (on the top) shows the relative concentration.

The determination of water absorption by capillarity uptake was done on the treated specimens and their absorption curves are showed in Fig. 5.29. The variation of the water absorption curves before and after the DAP treatment is showed in Fig. 5.30. All the treated specimens display a common trend, thus, for clarity's sake, Fig. 5.30 displays the feature of a representative specimen (PSI10) to avoid a graphical crowding in the diagram. In order to give some numerical data to the reader, Table 5.1 presents the Q and CA values calculated for PSI10 before and after the treatment.

The capillarity measurements shows that Q values, namely the amount of water absorbed per surface unit, decrease after the DAP treatment and this decrease occurs at each absorption time. Focusing on the absorption curve, the shape of the plot does not show a dramatic variation after the treatment even if the capillary absorption coefficient CA, namely the slope of the curve, shows evidence of variations. Subsequent to the DAP treatment, CA undergo a general decrease in the initial steps of the curve, meaning a decrease of the water uptake in the short term according to the relationship "the lower is the slope, the lower is the water absorption rate of the material".

As showed in Fig. 5.29 and Fig. 5.30, the significant variation of CA occurs about after $\sim 60 \sqrt{s}$, suggesting a drastic different behaviour between treated and untreated materials. After the unambiguous variation of the slope occurring at $\sim 60 \sqrt{s}$, the treated lithotype stands to a trend typical of Noto limestone (*i.e.,* slow absorption but to a total fraction of absorbed water which is slightly lower than in the untreated specimens). Thereby, these data clearly show that the calcium phosphates

nucleated inside the matrix modify the microstructure and the sorptivity speed of the substrate but do not alter the water absorption capability of the lithotype.
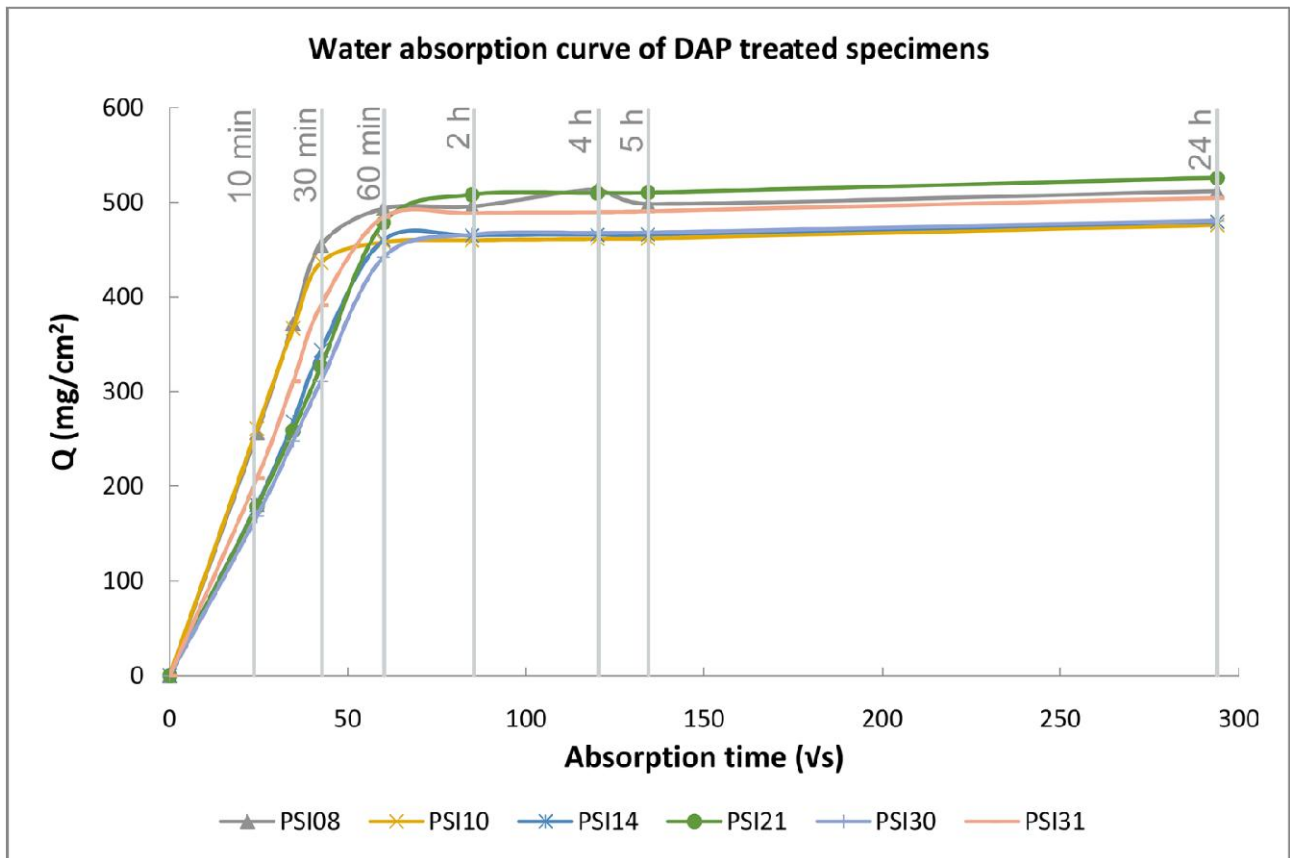
Fig. 5.29 Water absorption curves of the 6 specimens in Noto limestone after the DAP reaction (treatment by capillarity, duration time 2 hours, 0.76 M DAP solution).
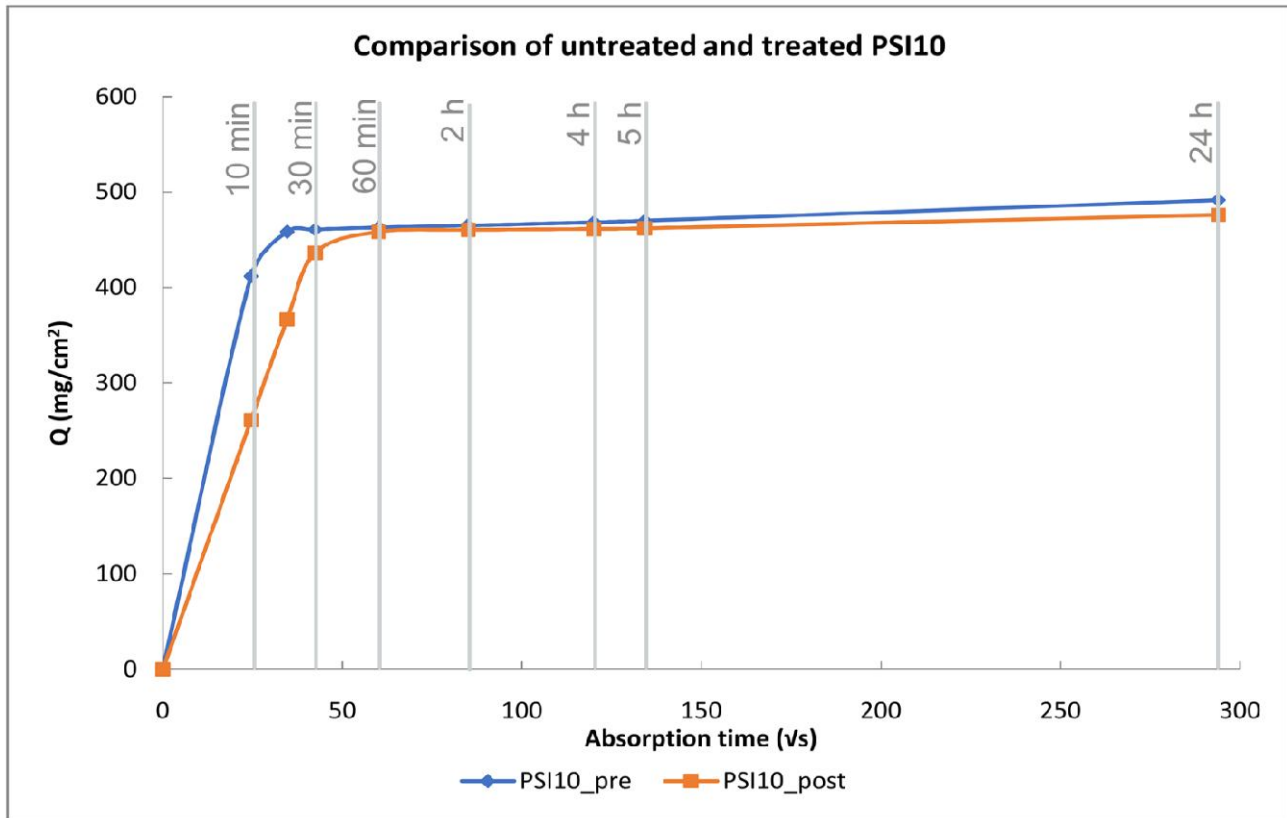
Fig. 5.30 Water absorption curves of a representative specimen of Noto limestone before (PSI10_pre) and after (PSI10_post) the DAP treatment. All the treated specimens undergo a similar trend, namely, the decrease of the suction speed and the fraction of water absorbed in the short term.

Absorption time (√s)	Absorption time (min)	Q before	Q after	CA before	CA after
0	0	0.000	0.000	0.000	0.000
24	10	411.596	261.044	83.164	52.744
35	20	458.276	366.820	7.931	17.972
42	30	460.764	436.364	0.382	10.677
60	60	463.032	458.220	0.293	2.822
85	120	464.856	460.308	0.198	0.227
120	240	468.136	461.436	0.299	0.103
134	300	469.928	462.000	0.155	0.049
294	1440	491.536	476.224	1.260	0.830

Table 5.1 Absorption time and calculated Q and CA values for specimen PSI10 before and after the DAP treatment.

The crystallization of calcium phosphates in the stone matrix occurs with an initial backing of the pore surface (with a slight increase of the pore diameter), and is followed by the growth of new phases in the voids in place of the dissolved original materials (Fig. 5.31). As this mechanism is expected to modify the microstructure and the porous structure of the stone matrix, MIP investigations were

carried out on untreated specimens and on treated ones, in order to investigate the microstructural alterations suggested by capillarity.
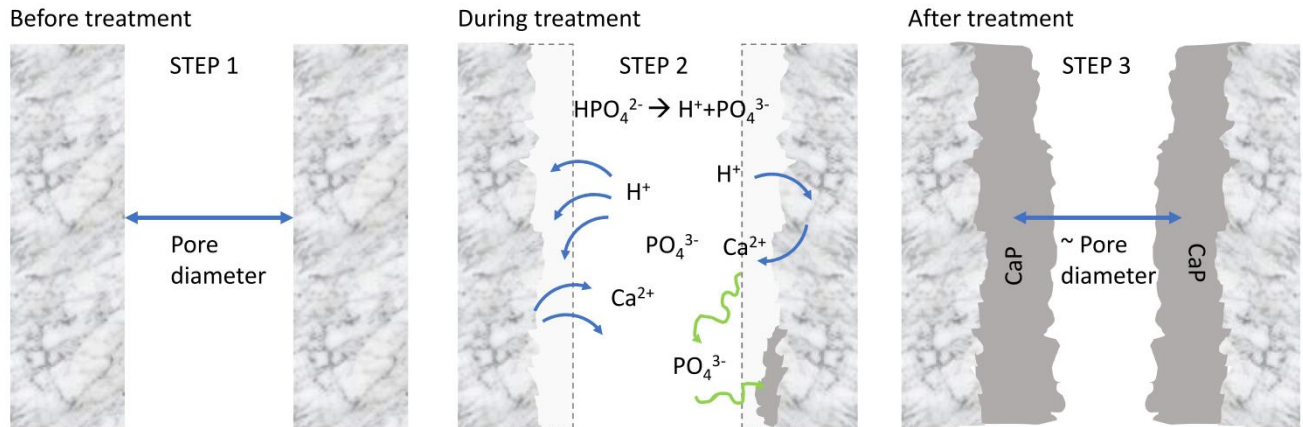
Fig. 5.31 Scheme (not in scale) illustrating the dissolution-recrystallization mechanism of calcium phosphates (CaP) inside the void of a pore, as the reaction product between the substrate and an aqueous solution of DAP salts.

The pores of materials are classified by the IUPAC (International Union of Pure and Applied Chemistry) in four classes: micropores (pores with radius < 0.001 µm), mesopores (0.001 µm < radius < 0.025 µm), macropores (0.025 µm < radius < 3.75 µm) and megapores (radius larger than 3.75 µm) [103,104]. The total open porosity of Noto limestone was analysed investigating the pores having cylindrical pore radii between 0.0037 µm and 50 µm, as experimentally the pressure can be varied 0.02 - 200 MPa. This wide range of pore radii, which comprises from mesopores to megapores, has been further subdivided in 20 pore size classes. The sub-division of pore classes in 20 segments allows evaluating the contribute of smaller classes to the total open porosity, and it has been selected on the basis of the specificity of the instrument and the investigated lithotype [150].

The MIP data collected from the analyzed untreated fragments are plotted in Table 5.2. Fig. 5.32 and Fig. 5.33 show the pore size distribution of quarry Noto limestone, as classified by the IUPAC and by the working protocol defined for this research.

	Noto 1		Noto 2		Noto 3		Average		
	Relative Volume (%)	Relative surface (m²/g)	Relative Volume (%)	Relative surface (m²/g)	Relative Volume (%)	Relative surface (m²/g)	Relative Volume (%)	Relative surface m²/g	Relative surface (%)
Average pore radius (μm)	2.376		2.212		2.903		2.496		
Total porosity (%)	37.32		35.018		35.815		36.051		
Total specific surface area (m²/g)	1.648		2.072		1.897		1.872		
Pore radius ranges (μm)									
50-35	0.2	0	0.39	0	0.55	0	0.38	0	0
35-30	0.1	0	0.19	0	0.23	0	0.173	0	0
30-25	0.15	0	0.19	0	0.37	0	0.237	0	0
25-20	0.29	0	0.39	0	0.37	0	0.35	0	0
20-15	0.34	0	0.44	0	0.64	0	0.473	0	0
15-10	0.69	0	0.73	0	1.92	0.001	1.113	0	0.018
10-7.5	0.59	0	0.73	0	5.67	0.003	2.33	0.001	0.053
7.5-5	2.16	0.002	2.09	0.002	23.26	0.017	9.17	0.007	0.374
5-2.5	42.89	0.054	38.12	0.05	21.25	0.027	34.087	0.044	2.334
2.5-1	28.68	0.075	31.43	0.083	18.78	0.054	26.297	0.071	3.777
1-.75	4.36	0.021	4.41	0.022	4.25	0.022	4.34	0.022	1.158
0.75-0.5	3.87	0.026	4.07	0.029	4.66	0.035	4.2	0.03	1.603
0.5-0.25	3.92	0.046	4.17	0.051	6.49	0.084	4.86	0.06	3.225
0.25-0.1	4.85	0.133	5.14	0.146	5.67	0.157	5.22	0.145	7.768
0.1-0.075	1.23	0.06	1.26	0.063	0.96	0.05	1.15	0.058	3.082
0.075-0.05	1.32	0.091	1.36	0.096	1.14	0.085	1.273	0.091	4.846
0.05-0.025	1.91	0.229	1.89	0.232	1.33	0.168	1.71	0.21	11.206
0.025-0.01	1.72	0.469	1.75	0.474	1.23	0.357	1.567	0.433	23.161
0.01-0.0075	0.34	0.165	0.63	0.31	0.59	0.309	0.52	0.261	13.968
0.0075-0.0037	0.39	0.276	0.63	0.512	0.64	0.527	0.553	0.438	23.428

Table 5.2 Average pore radius, total porosity, total specific surface area and pore size distribution of three different samples of untreated Noto limestone (Noto1, Noto2 and Noto3) and their average.
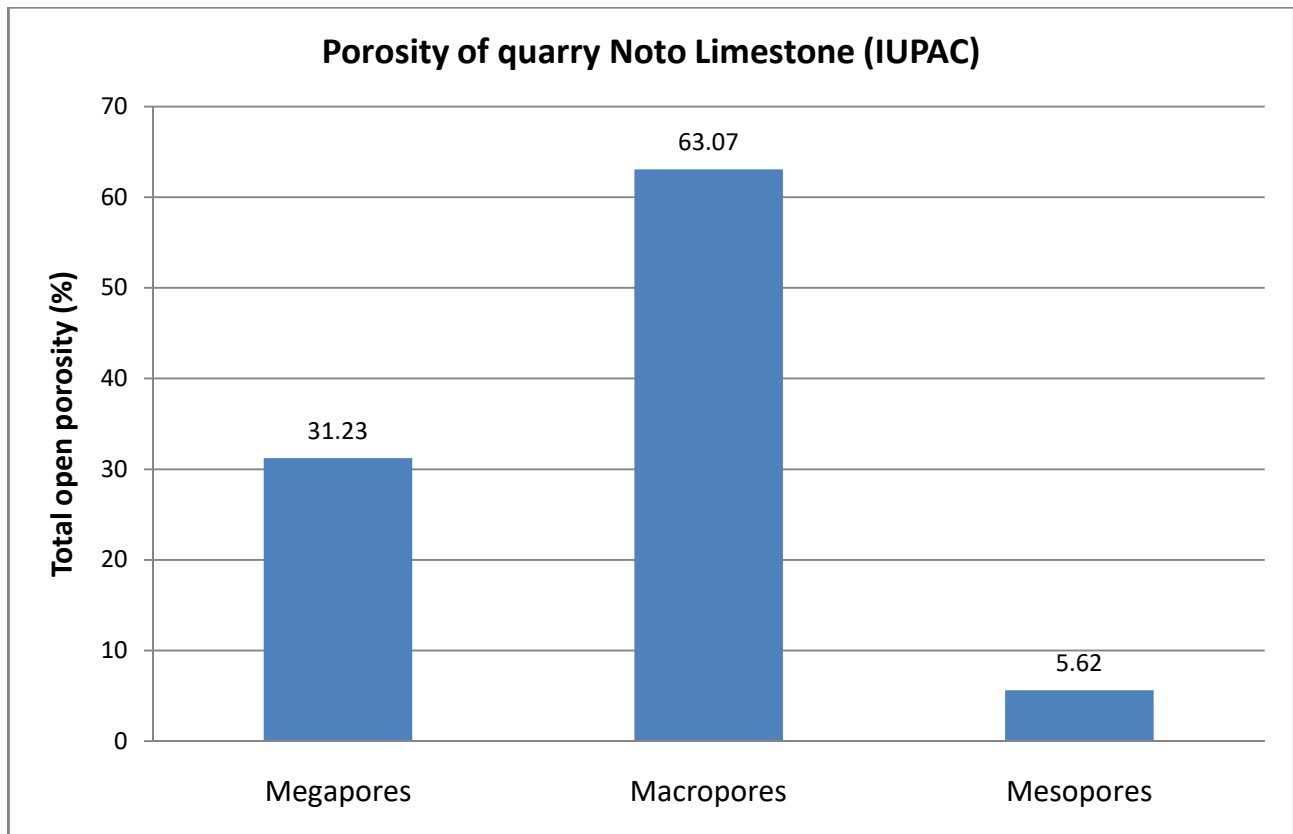
Fig. 5.32 Pore size distribution of three different samples of untreated Noto limestone (average of three samples) according to the IUPAC classification.
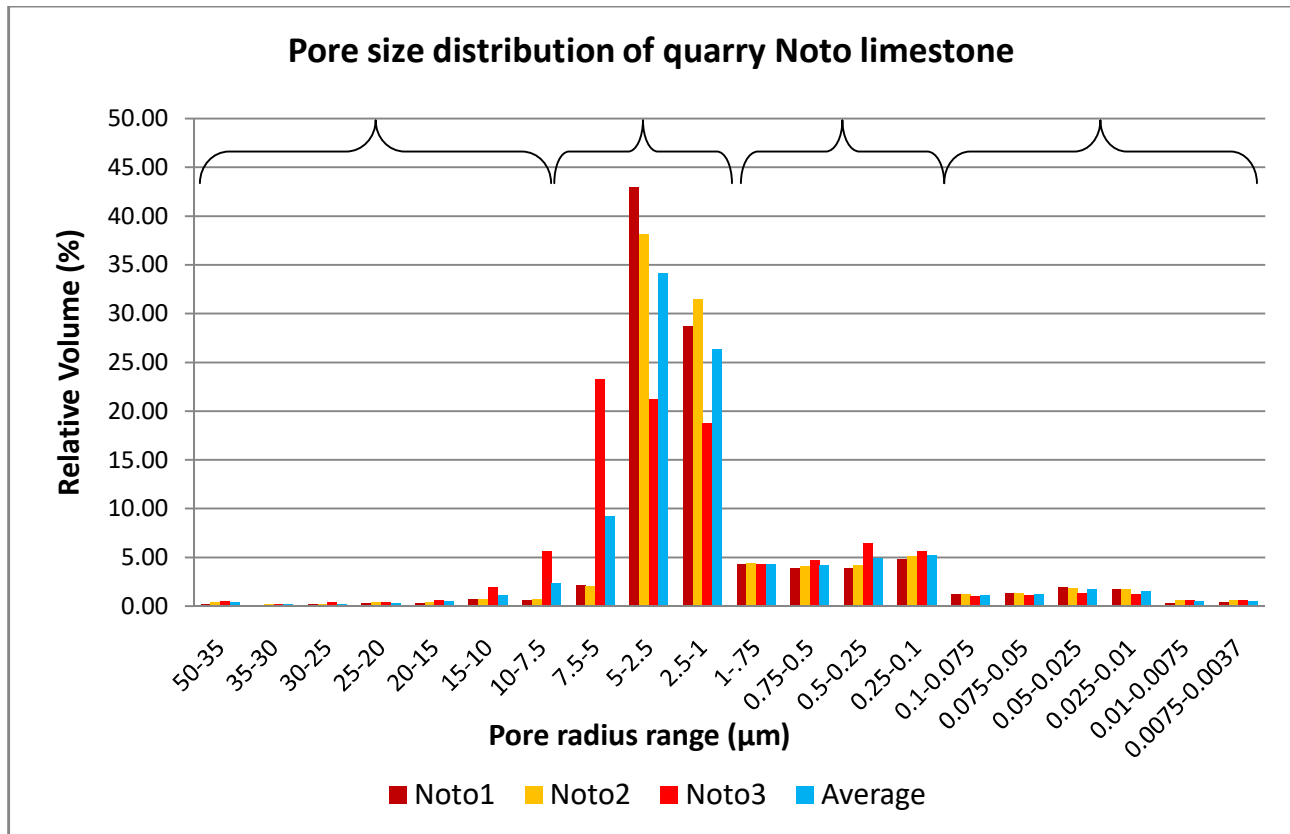
Fig. 5.33 Pore size distribution of three different samples of untreated Noto limestone (Noto1, Noto2 and Noto3) and average of the measurements (Average). Four classes of pores(which are characteristic of the untreated lithotype) are bracketed.

As shown by Table 5.2, quarry Noto limestone has a highly porous matrix, with a measured total open porosity in the range 35-37 % and a peculiar pore size distribution. The values of total open porosity and the pore size distribution measured on these specimens are in line with the values assessed in a previous study carried out on a wide set of quarry specimens [150]. In [150], the total open porosity ranged between 32.60-38.70 % and the specimens were divided in three sub-groups on the basis of their pore size distribution. Thus, taking into account the data reported in [150] and the natural heterogeneity of Noto limestone (which provides occasionally values out of the trend of the lithotype), the porosity values obtained from the three quarry specimens are discussed also as their average and they are considered a reference for the data collected in this study on the six treated specimens. This approximation most likely introduces errors, but, due to destructive nature of MIP measurements (mercury impregnating the sample is not completely removable after the investigation), it is not possible to repeat the measures on the same specimen before and after the treatment. For these reasons, the following discussion aims to make comparisons and to show evidence of a trend. Numerical values are given to guide the reader in the evaluation of the effects induced by the treatment to the stone matrix.

Fig. 5.32 show that macropores and megapores constitute almost the 94 % of the total open porosity of Noto limestone (63.07 % and 31.23 % respectively), while finer pores are only a minority. Fig. 5.33 shows that, observing more in detail the contribute of smaller pore classes, a more accurate evaluation of the porosity is possible. For this reason, in the following, the porosity of Noto limestone and the

pore size variations will be discussed using the 20 pore classes of the ICVBC-CNR protocol. Fig. 5.33 shows that the pore size distribution of quarry Noto limestone can be subdivided in four groups of pore radius. The distribution shows a maximum in the pores with medium radius, with a total open porosity of about 70 % in the range of 7.5-1.0 μm, while the remaining total open porosity is partitioned as following: about the 18-19 % of the pores have a pore radius range between 1-0.1 μm, the 6-7 % have a pore radius lower than 0.1 μm and about the 5-6 % have a pore radius larger than 7.5 μm. The average pore radius on single fragments ranges between 2.21 and 2.90 μm, with an average of the three fragments of 2.49 μm.

Considering that the DAP treatment interacts on the surface of the pores and that each pore class has a specific surface, the total specific surface area and the specific surface of pore classes were considered as well (Table 5.2).

On quarry Noto limestone, the total specific surface area ranges between 1.648 m²/g and 2.072 m²/g, with an average of 1.872 m²/g. Considering the four "classes" of pores of the histogram, it is interesting to highlight that the class pore radius "7.5-1.0 μm", which holds to 70 % of the total open porosity, actually determines only the ~ 6.48 % of the total specific surface area. On the contrary, pore classes with a low impact in terms of total open porosity, *e.g.,* the classes 1.0-0.1 μm and 0.1-0.0037 μm, essentially holds the ~ 13.75 % and the ~ 79.69 % of the total specific surface area, respectively. In other words, the comparison between pore radius ranges, relative volume and relative surface is crucial to fully investigate the porous structure on Noto limestone. An example is shown in Fig. 5.34.
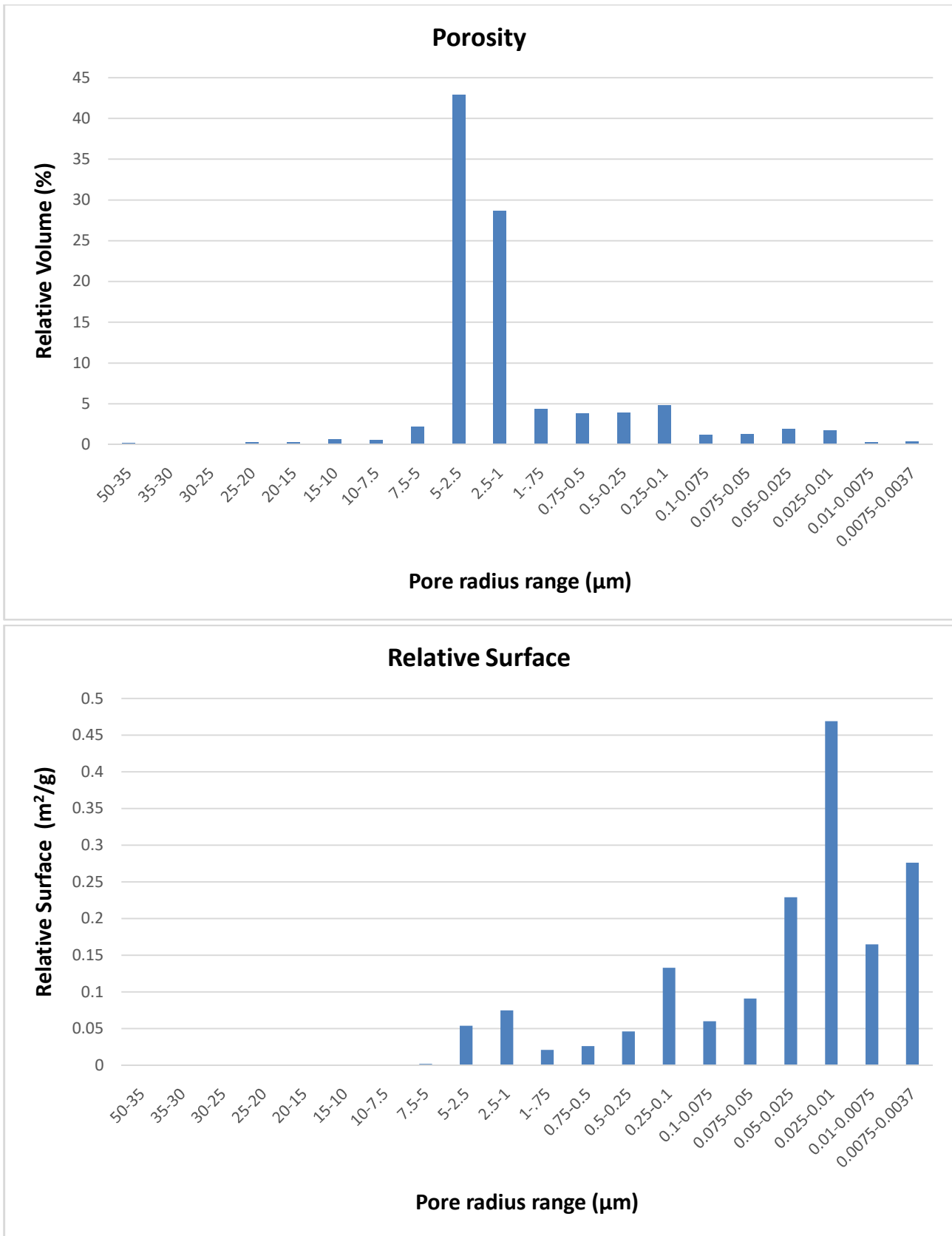
Fig. 5.34 Comparison of the pore size distribution and the relative surface of the pore radius ranges of untreated Noto limestone.

To study how the crystallization of phosphate phases modify the microstructure of the stone matrix from the surface to the bulk, the treated specimens were dissected in slices of ~ 2 mm thick. From each treated specimen, five slices were sampled: three from the treated side (*layer 1* 0-2 mm; *layer 2* 2-4 mm; *layer 3* 4-6 mm, corresponding to a total thickness of about ~ 6 mm), one in the middle of the specimen (*layer 4*, slice from 9 to 11 mm from the surface) and one at the bottom of specimens, from the surface opposite to the application of the treatment (*layer 5*, 18-20 mm). The slices were samples from the core of the 5x5x2 cm specimen, to avoid boundary effects. Each slice was then divided in four different fragments and analysed by MIP. A scheme of the sampling method is shown in Fig. 5.35.
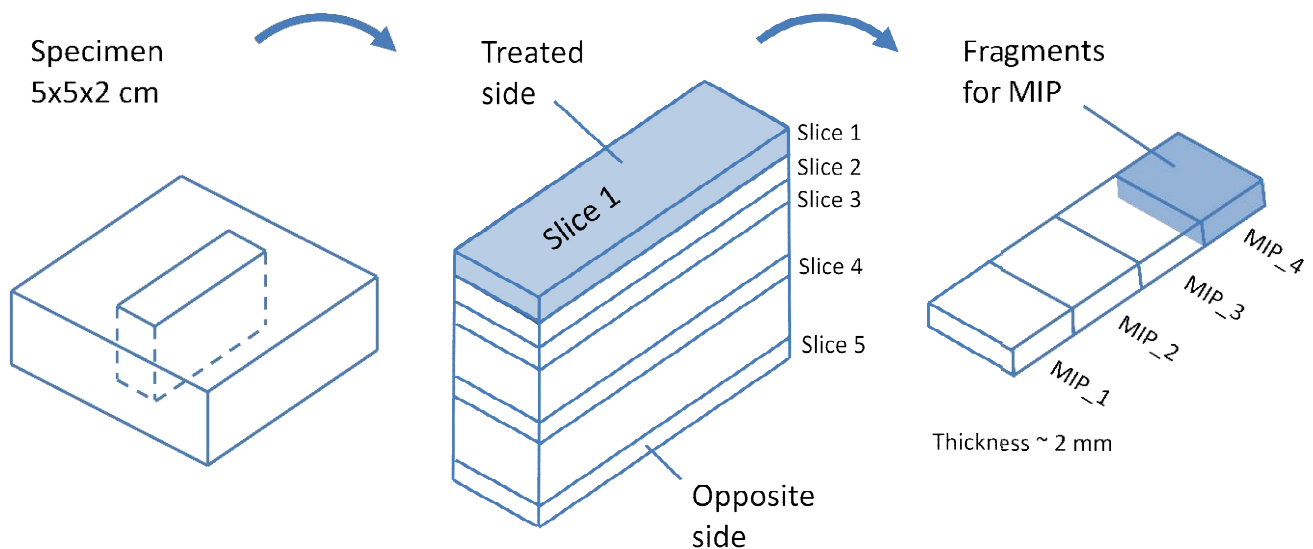
Fig. 5.35 Scheme (not in scale) of the dissected fragments from a treated specimen used for MIP investigations.

In this discussion and in the evaluation of how the treatment modify the porosity, the natural heterogeneity of Noto limestone has been considered as well. The MIP results collected from the four fragments of each slice were then averaged, in order to obtain data which are representative of the slice. This value, which corresponds to a single "diffusion layers" of a specific specimen, was then averaged with the data of the same diffusion layer of the other specimens, obtaining a representative value of the system.

Table 5.3, Fig. 5.36, Fig. 5.37 and Fig. 5.38 compare the total open porosity, the pore size distribution, the average pore radius and the relative surface distribution of the untreated and treated Noto limestone specimens.

Pore radius ranges (µm)	Untr.		Layer 1		Layer 2		Layer 3		Layer 4		Layer 5	
	Rel. vol. (%)	Rel. surf. (m²/g)	Rel. vol. (%)	Rel. surf. (m²/g)	Rel. vol. (%)	Rel. surf. (m²/g)	Rel. vol. (%)	Rel. surf. (m²/g)	Rel. vol. (%)	Rel. surf. (m²/g)	Rel. vol. (%)	Rel. surf. (m²/g)
50-35	0.38	0	0.683	0	0.565	0	0.448	0	3.065	0	0.695	0
35-30	0.173	0	0.355	0	0.375	0	0.303	0	1.325	0	0.41	0
30-25	0.237	0	0.448	0	0.408	0	0.288	0	1.48	0	0.405	0
25-20	0.35	0	0.525	0	0.41	0	0.42	0	1.87	0	0.57	0
20-15	0.473	0	0.918	0	0.823	0	0.773	0	1.83	0	0.903	0
15-10	1.113	0	1.848	0	2.133	0	1.773	0	2.435	0	2.128	0
10-7.5	2.33	0	1.89	0	3.138	0	2.678	0	1.94	0	2.695	0
7.5-5	9.17	0.007	7.893	0.003	10.688	0.004	9.558	0.003	3.245	0.002	9.405	0.004
5-2.5	34.087	0.044	29.658	0.031	28.445	0.028	30.873	0.03	16.26	0.018	27.858	0.036
2.5-1	26.297	0.071	17.175	0.067	17.65	0.066	19.543	0.068	30.83	0.066	19.453	0.063
1-.75	4.34	0.022	4.19	0.02	5.658	0.026	3.998	0.021	6.05	0.024	4.468	0.026
.75-.5	4.2	0.03	3.87	0.027	4.863	0.031	4.805	0.032	4.975	0.03	4.788	0.032
.5-.25	4.86	0.06	4.15	0.046	5.49	0.059	5.21	0.059	5.505	0.058	5.448	0.064
.25-.1	5.22	0.145	3.805	0.088	4.478	0.118	4.35	0.12	4.885	0.118	4.49	0.128
.1-.075	1.15	0.058	1.055	0.044	1.23	0.057	1.103	0.059	1.29	0.056	1.275	0.066
.075-.05	1.273	0.091	1.7	0.119	1.833	0.137	1.748	0.132	2.1	0.13	2.05	0.161
.05-.025	1.71	0.21	5.685	0.694	4.21	0.465	4.028	0.475	3.425	0.364	4.283	0.546
.025-.01	1.567	0.433	10.77	2.844	5.198	1.201	5.34	1.38	4.975	1.158	5.708	1.575
.01-.0075	0.52	0.261	1.585	0.797	1.065	0.405	1.228	0.555	0.775	0.335	1.365	0.613
.0075-.0037	0.553	0.438	1.783	1.542	1.333	1.128	1.528	1.661	1.745	1.314	1.6	1.433

Table 5.3 Pore size distribution with relative volume % (Rel. vol.) and relative surface m²/g (Rel. surf.) of the pore radius ranges of untreated (Untr.) and treated Noto limestone calculated on different diffusion layers (layer 1-layer 5).

In particular, the treated specimens show a slight reduction of the total open porosity, from an average values of ~36 % to 29-34 %, depending on the specimen and the depth from the treated surface. All the diffusion layers record a decrease of the total open porosity even though there is not a linear gradient of the total open porosity reduction, following the somehow expected trend "on the surface the porosity dramatically decreases, below some millimetres the porosity is only slightly reduced", down to "no modifications in the core of the specimens". On the contrary, the variation of the total open porosity seems random, probably more influenced by the local microstructure (preferential penetration paths, cracks) than by the distance from the treated surface.

In any case, ever the layer 5, the diffusion layer opposite to the treated surface, shows a total open porosity minor than those of the untreated Noto limestone, thus indirectly confirming the crystallization of calcium phosphates observed by SEM-EDS investigations down to 20 mm of penetration depth.

A more pronounced effect of the DAP treatment on the Noto limestone microstructure is recorded on the pore radius and on the variation of the pore size distribution. The nucleation of calcium phosphates on the surface of the voids determines a variation of the average pore radius, which shows a decrease from an average value of 2.497 µm for untreated Noto limestone down to 1.674-1.866 µm for treated specimens, corresponding to an average reduction of about 33-26 %. The average pore radius of different slices shows a trend as well: the most external slices, corresponding to the most external portion of stone material, have an average pore radius smaller than the inner ones (Fig. 5.36). This value confirms FTIR, XRD and capillarity data, demonstrating that the phosphate crystallization is more abundant in the superficial portion, and that CaPs are responsible for the decrease of the suction speed. A further interesting data is that the average pore radius undergoes a decrease also in layer 5, namely the diffusion layer on the bottom of the specimen, thus reconfirming the diffusion of DAP solutions through the whole specimen.
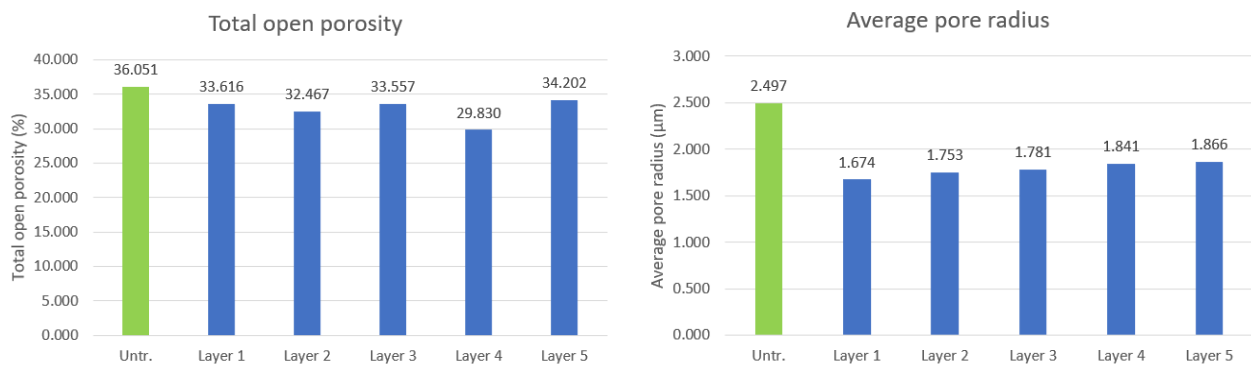
Fig. 5.36 (a) Total open porosity (%) and (b) average pore radius of untreated Noto limestone (Untr.) and treated Noto limestone, sub-divided in five diffusion layers (Layer 1-5).

Dealing with the pore size distribution, the topotactic nucleation of phosphates in the pores determines a decrease in the coarser ones, especially those having radius in the range 15-2.5 microns, while finer pores (void characterized by radius smaller than 1 µm) undergo a clear % increase (Fig. 5.37 and Fig. 5.38). This trend is common to all the investigated "diffusion layers", with a variation particularly evident in layer 1 (the portion directly in contact with the treatment). In general, the pores with a radius between 15-2.5 µm change from 46.70 % in untreated Noto limestone to 36.54-23.89 % in the

treated one. Differences layer by layer are present, and their values are plotted in Table 5.4. Finer pores, namely pores with radius lower that 2.5 µm increase from 51.69 % to an average of 60.84-67.46 %. An interesting subdivision can be performed on finer pores. In fact, the pores having a radius between 2.5-1.0 µm are a class of pores highly present in untreated Noto (initially 26.30 % of the total open porosity), and after the treatment slightly increase (average 28 %). Pores with a radius lower that 1.0 µm, apparently poorly significant (25.39 % of the total open porosity, subdivided in 10 classes of pore radius ranges), rise at a relative volume 37.28 % on the total open porosity, experiencing average increase of the 32.86 % from the original values.
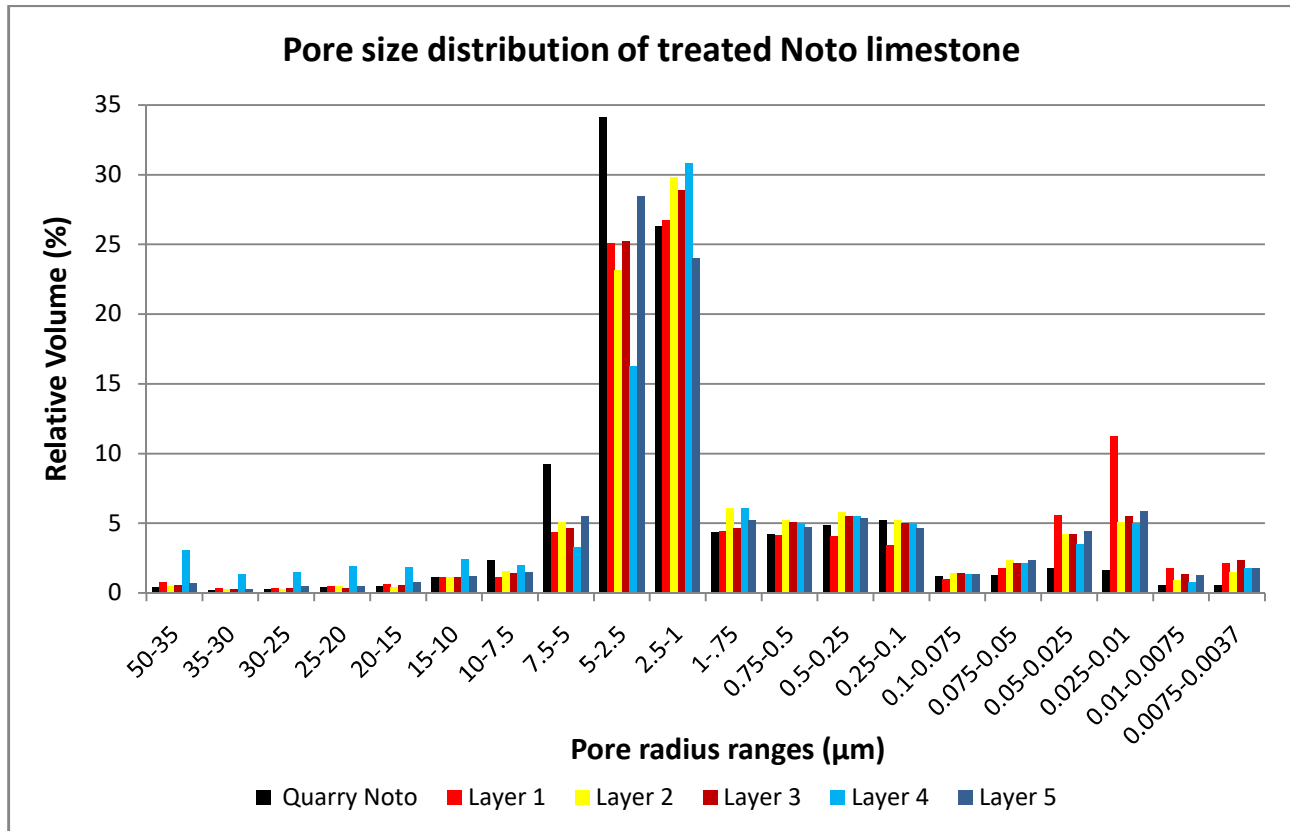
Fig. 5.37 Pore size distribution of untreated (Untr. Noto) and treated Noto limestone in different diffusion layers.
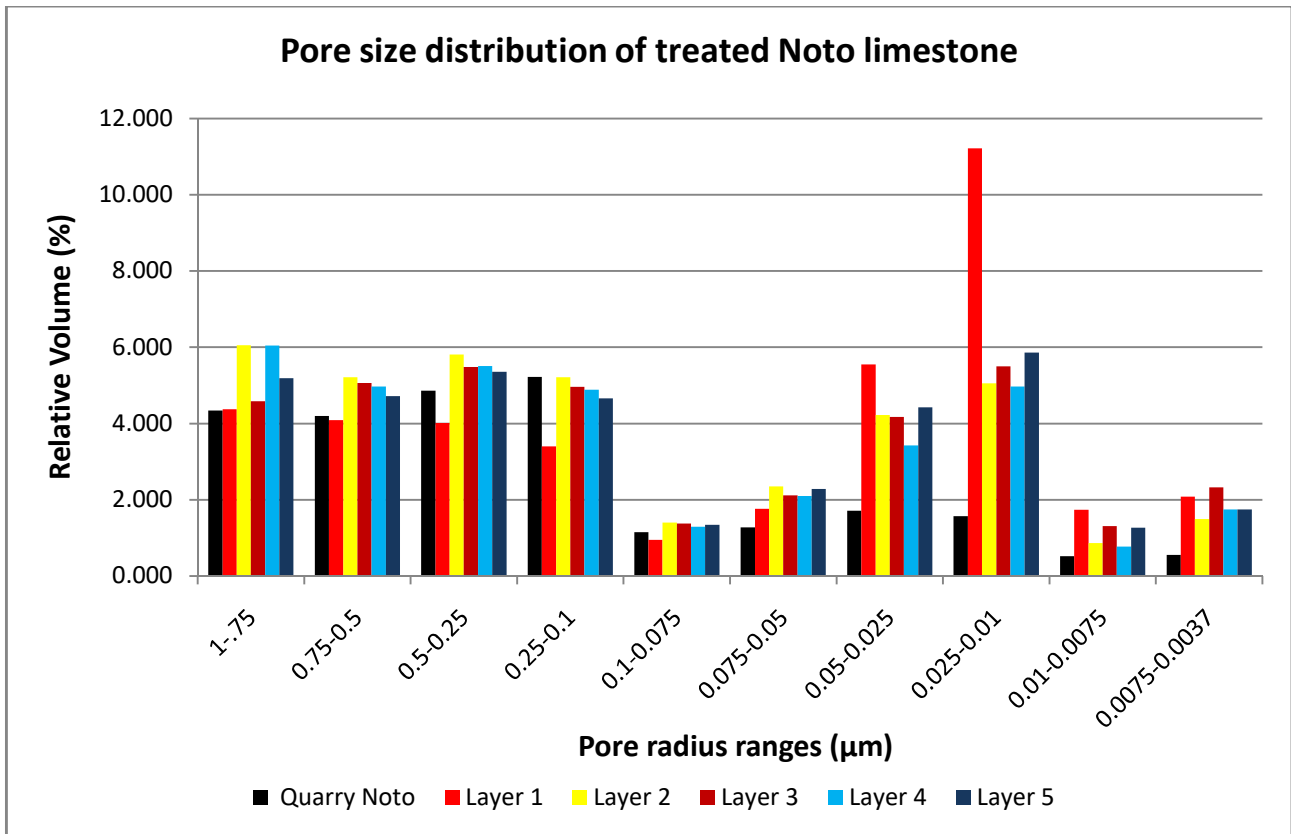
Fig. 5.38 Detail of the pore size distribution of untreated (Untr. Noto) and treated Noto limestone in the 10 ranges of finer pore radius.

Pore radius range (µm)	Relative Volume (%)					
	Untreated	**Layer 1**	**Layer 2**	**Layer 3**	**Layer 4**	**Layer 5**
15-2.5	46.70	31.62	30.77	32.32	23.89	36.54
2.5-0.0037	51.69	65.94	67.46	65.78	66.55	60.84
Of which	26.30	26.76	29.78	28.89	30.83	24.00
2.5-1.0						
< 1.0	25.39	39.19	37.68	36.89	35.73	36.86

Table 5.4 Variation of the pore size distribution, in relative volume (%), between untreated and treated Noto limestone, investigated in 5 different layers.

In general, the smaller is the pore radius, the higher is the increase of the relative volume (%). Significant % increase is observed for very small pore radius, *e.g.,* the interval 0.075-0.050 µm or the 0.025-0.010 µm show increments up to 200-600 % of their starting value. The severe increase of finer pores, and especially of sub-micrometric pores, has a direct consequence on the variation of the specific surface area of the matrix. As showed in Table 5.3 and Table 5.5, the total specific surface area varies dramatically on treated Noto limestone, ranging values from 3.675 m²/g to 6.322 m²/g, with an average of 4.630 m²/g (average on untreated Noto limestone 1.872 m²/g). Considering the pore size distribution, the classes with smaller pore radius are the classes which mostly contribute to the total

specific surface area. In fact, observing the histogram of Fig. 5.39, the contribution of relative surface is positioned toward the micro- and mesopores, with a trend that was existing in quarry Noto limestone as well. The significant difference is the contribute of these classes to the total specific surface area, as all the values with pore radius lower than 0.075 μm undergo a clear growth. On the contrary, almost all the pore ranges with radius > 0.075 μm show to a decrease of their relative surface. Typically, pores with radius > 7.5 μm do not reveal detectable variations, as their contribute to the total specific surface area ranges usually between 0.000-0.003 m²/g.

It is worth noting that differences are detectable among different diffusion layers as well. Layer 1 is the portion of stone material which experienced the most dramatic variations, reaching the highest values of total specific surface area (*e.g.,* 6.202 m²/g for sample PSI08, 5.943 m²/g for PSI21 and 6.822 m²/g for PSI30) and of relative surface of tiniest classes (*e.g.*, in comparison to untreated Noto limestone, pore radius range 0.05-0.025 μm + 230 %, 0.025-0.010 μm + 560 % respectively). Fig. 5.39 displays that the columns of layer 1 stand out above all the others. Layer 2 is in countertrend, showing a clear increase of voids with small radius respect to the quarry stone, but its values are lower than those of layer 3 and 4. On the contrary, layer 3 and 4 reveal a trend very similar to layer 1 and their values are progressively lower, showing evidence of a gradient of calcium phosphates crystallizations, from the surface toward the bulk, as observed with the other techniques.

Sample name	Untr.	Layer 1	Layer 2	Layer 3	Layer 4	Layer 5
Total specific surface area (m²/g)	1.872	6.322	3.772	4.631	3.675	4.749

Table 5.5 Total specific surface area (m²/g) of untreated (Untr.) and of treated Noto limestone, measured on the five diffusion layers described in Fig. 5.35. The values for the layers are the average of the data collected, for each layer, on all the treated specimens.
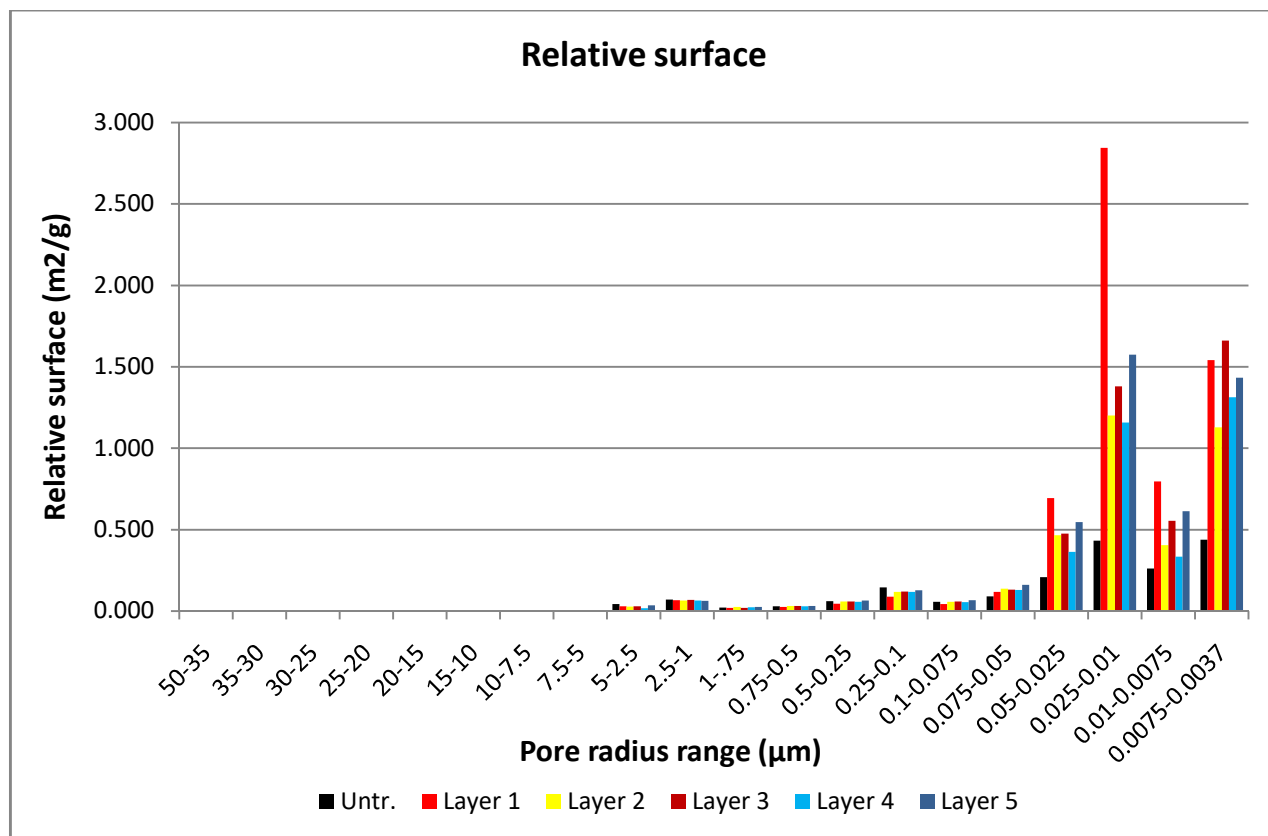
Fig. 5.39 Relative surface of the pore radius ranges of treated Noto limestone, investigated from layer 1 to layer 5. A comparison with untreated Noto limestone (Untr.) is shown as well. The comparison with Fig. 5.37 shed light of the differences existing between the pore size distribution and the contribute of each pore radius range to the total specific surface area.

Synchrotron Radiation X-ray Micro-Computed Tomography (SRμ-CT) was used to investigate the voids and their interconnections. The SRμ-CT investigations were carried out on parallelepiped-shape samples of about 2x2x20 mm obtained from two representative specimens of Noto limestone: an untreated specimen and a treated one (treatment protocol: capillarity, 0.76 M DAP solution, 2 h). As T-XRD demonstrated that the main phase differences occur in the first millimetres from the treated surface, SRμ-CT was carried out in the most superficial portion (though if, due to experimental needs, the collected data are close to the treated surface, but not exactly from the treated surface).

Data reconstruction

The SRμ-CT experiments generated dataset of about 2000 slices of 2048x2048 voxel each (voxel size is ~1 μm^3). These SRμ-CT images were processed with an analysis protocol showed in Fig. 5.40.

A single-distance phase-retrieval algorithm was applied to the sample projections before slice reconstruction, in order to reduce phase-contrast artifacts and improve the differences of materials with similar absorption coefficients [114]. For the investigated samples, a δ/β ratio equal of 6 (with δ = refractive index decrement, proportional to the electron density of a material, and β = extinction coefficient, related to the absorption coefficient and wavelength) was selected for reconstructions. As drawback, the phase-retrieval procedure introduces a certain level of image blurring, which has been

considered in the image processing. Ring artifacts, namely concentric rings in tomographic images rising from inhomogeneities in the pixel response of detector elements [114], were reduced by applying a ring mask. After that, the slices were reconstructed with a conventional filtered back-projection algorithm [183].

Tomographic reconstruction and image quality	3D digital imaging processing	3D image analsysis
Artifacts correction (*e.g.,* algorithms for the compensation of ring artifacts)	VOIs selection	Morphometric analysis →basic analysis
Brightness and contrast correction	Segmentation (binarization)	Connected components analysis → blob analysis
	Thresholding	Skeleton analysis
	Pre- and post-segmentation filters	

Fig. 5.40 Scheme of the image analysis protocol used for the pre- and post-processing of the SRµ-CT images. The boxes with the text in red are referred to analyses ongoing and not inserted in this discussion.

3D Digital imaging processing
The tomographic reconstruction origins a such big file (8 GB data set of 8-bit images) that the elaborations on smaller volumes has been necessary. Therefore, the starting point was the selection of several volume of interest (VOI), assuming that all the characteristic porous distribution is contained in the selected sub-volume and that the VOI is big enough to contain possible variability of the stone matrix (Representative Elementary Volume, REV) [119]. In this study, representative 3D subvolumes of 300x300x300 voxels each (corresponding to a cube of ~300 µm side length) were initially extracted from the original dataset.

The segmentation, or binarization, is a post-processing which aims to create binary images, by the partitioning of a digital image into multiple segments. It allows distinguishing the elements of the stone matrix (voids, calcite of the substrate and newly-formed calcium phosphates), initially discernible by their different grey shades. After segmentation, similar elements are visualised as a set of contiguous voxels (Fig. 5.41). During the process, the use of thresholds isolates voids from the matrix and provides an estimation of the total porosity. The process acts on the VOI, therefore the value of calculated total porosity is referred to the elaborated volume.
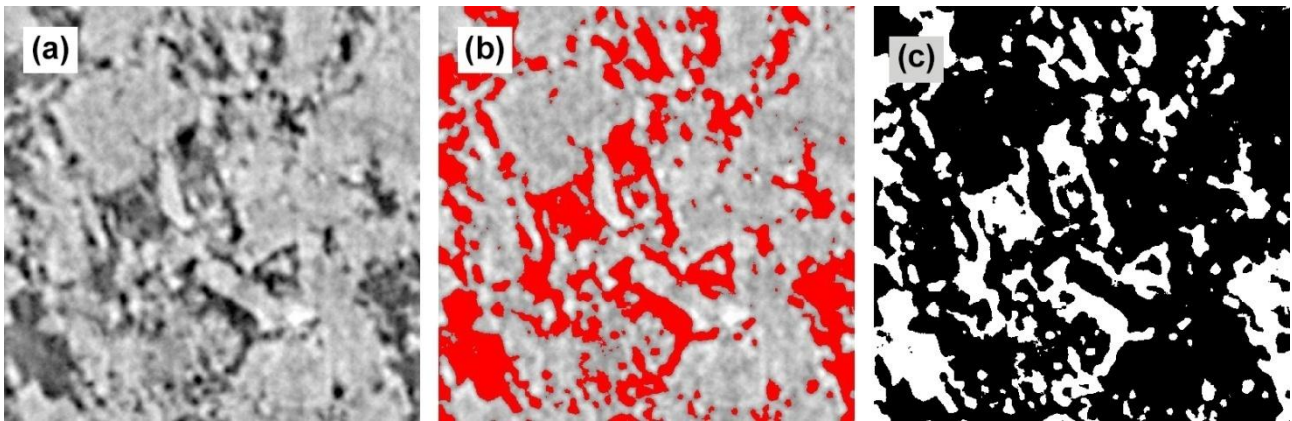
Fig. 5.41 Original image (a), voids, in red, selected by the threshold (b) and segmented X-ray SRμ-CT image (c).

Filtering has been necessary to homogenize the images, to enhance the contrast and to reduce the background noise of the reconstructed slices, which might negatively affect the segmentation process [119,184]. In order to define a protocol for the elaboration of the slices, different image processing tests were carried out. The pros and cons of using *Brightness and Contrast* correction, *Gaussian Blur* filter and *Median* filter were evaluated.

The *Brightness and Contrast* tool modifies the minimum and maximum settings, adjusting the image brightness and the image contrast (Fig. 5.42). The upper and lower limits of the display range can be manually adjusted by the user, by moving the brightness and contrast sliders. For the image processing, only the automatic thresholding, based on the image's histogram, has been used to process all the slices, in order to avoid an arbitrary manipulation of the images. The tool was used only once for each dataset, to avoid the creation of artefacts (*e.g.,* spurious contrast) due to the repetition of the processing. All the VOIs of 300^3 voxels were cropped from the original dataset, after the Brightness and Contrast adjustment.
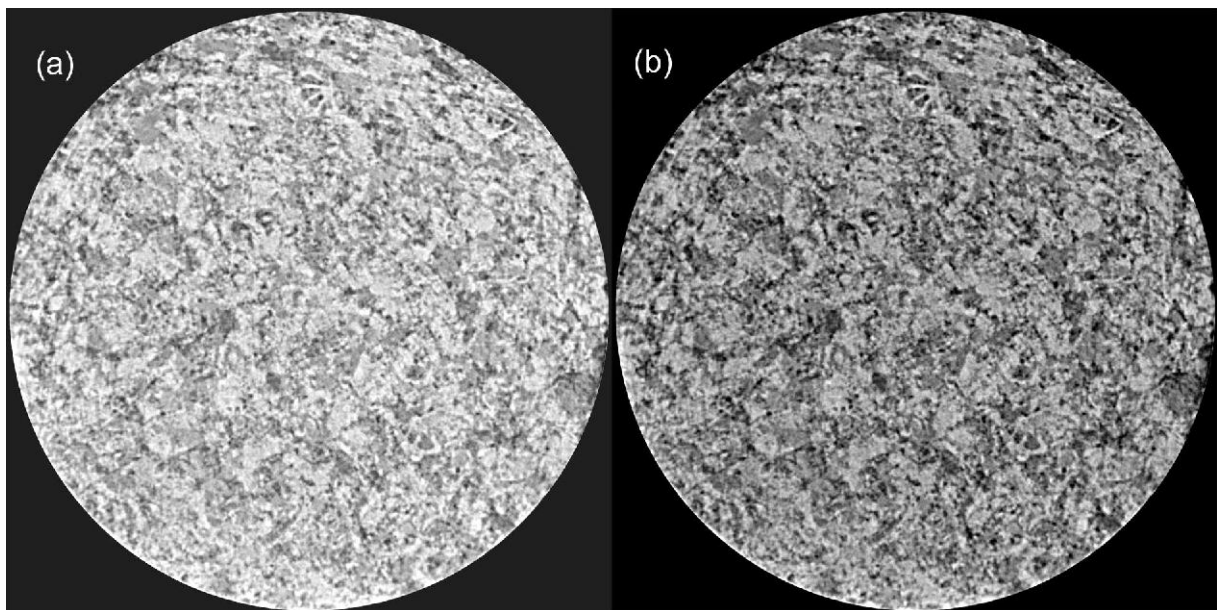
Fig. 5.42 Original image (a) and image obtained after the brightness and contrast adjustment with an automatic thresholding, based on the image's histogram (b).

The *Gaussian Blur*, also known as *Gaussian smoothing*, in an effect of blurring that reduce the noise of the images by a Gaussian function. As shown by Fig. 5.43, the visual effect is a general smoothing of the image and an homogenisation of the grey tones which are inside a void. As a consequence, the voids are characterized by a smoothed range of grey hues, which allows a better selection of the voids in the segmentation due to their filling with smoothed grey hues and less noisy plot profile (Fig. 5.44). At the other side, the Gaussian Blur filter determines a loss of details, which results in a loss of resolution (*e.g.,* worse description of the shape of the pore) and in an underestimation of the porosity. Therefore, the Gaussian Blur filter was used for the image manipulations focused to study the pore distribution, the connections among voids and to skeletonise the porous structure. No Gaussian Blur filter was used to estimate the total porosity, to investigate the boundaries of the voids and to understand how the treatment interacts with the shape and boundary of the pores. The standard deviation of the Gaussian Blur filter selected for the final image processing is 5.
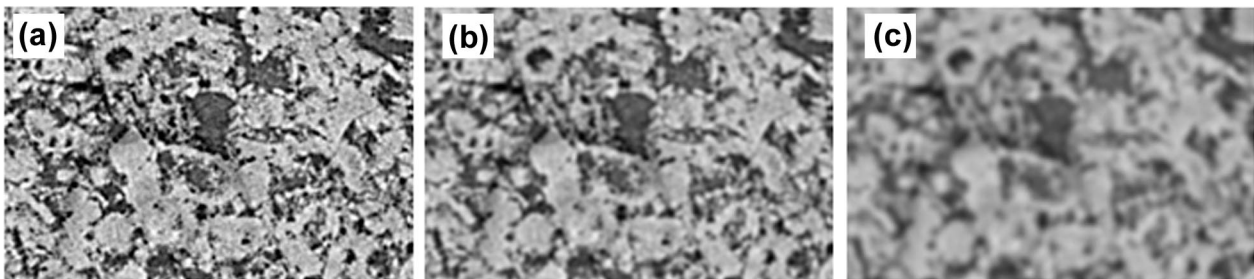
Fig. 5.43 Reconstructed slide of the surface of the untreated Noto limestone (a) and differences induced by the Gaussian Blur filter with StDev = 5 (b), StDev = 10 (c).
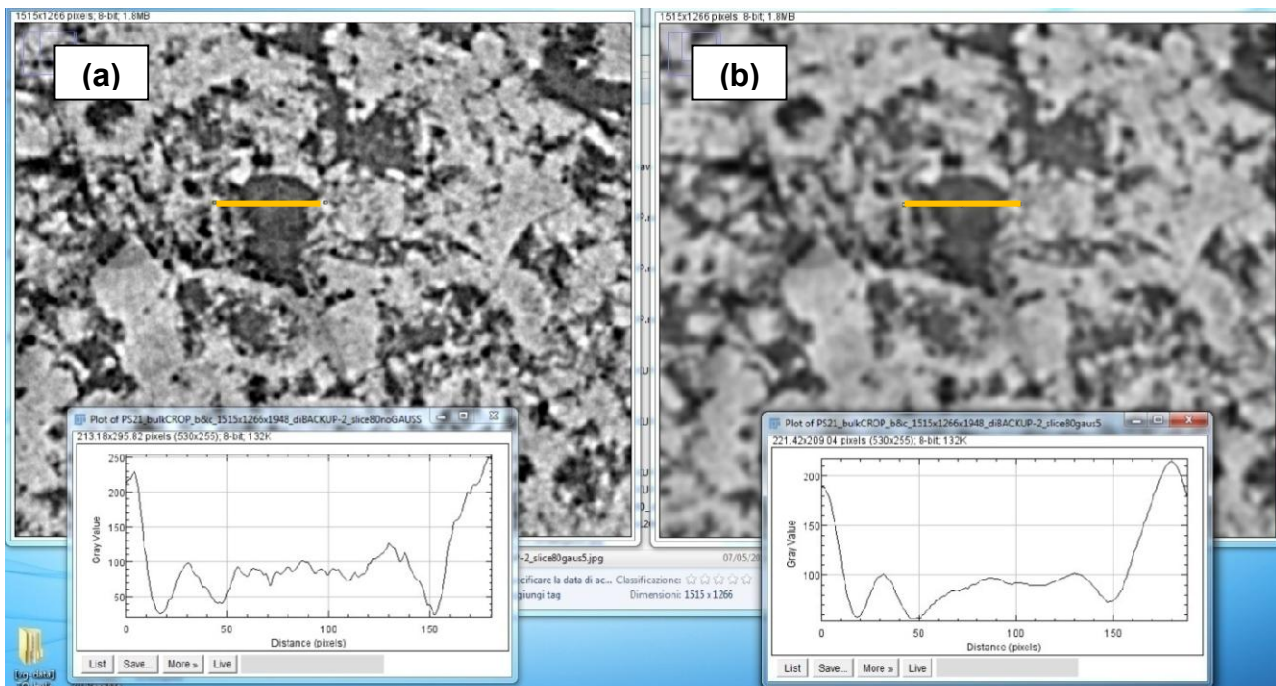
Fig. 5.44 Snapshot of the screen showing the plot profiles of the grey value for the original image (a) and the image processed with the Gaussian Blur filter, StDev = 5 (b).
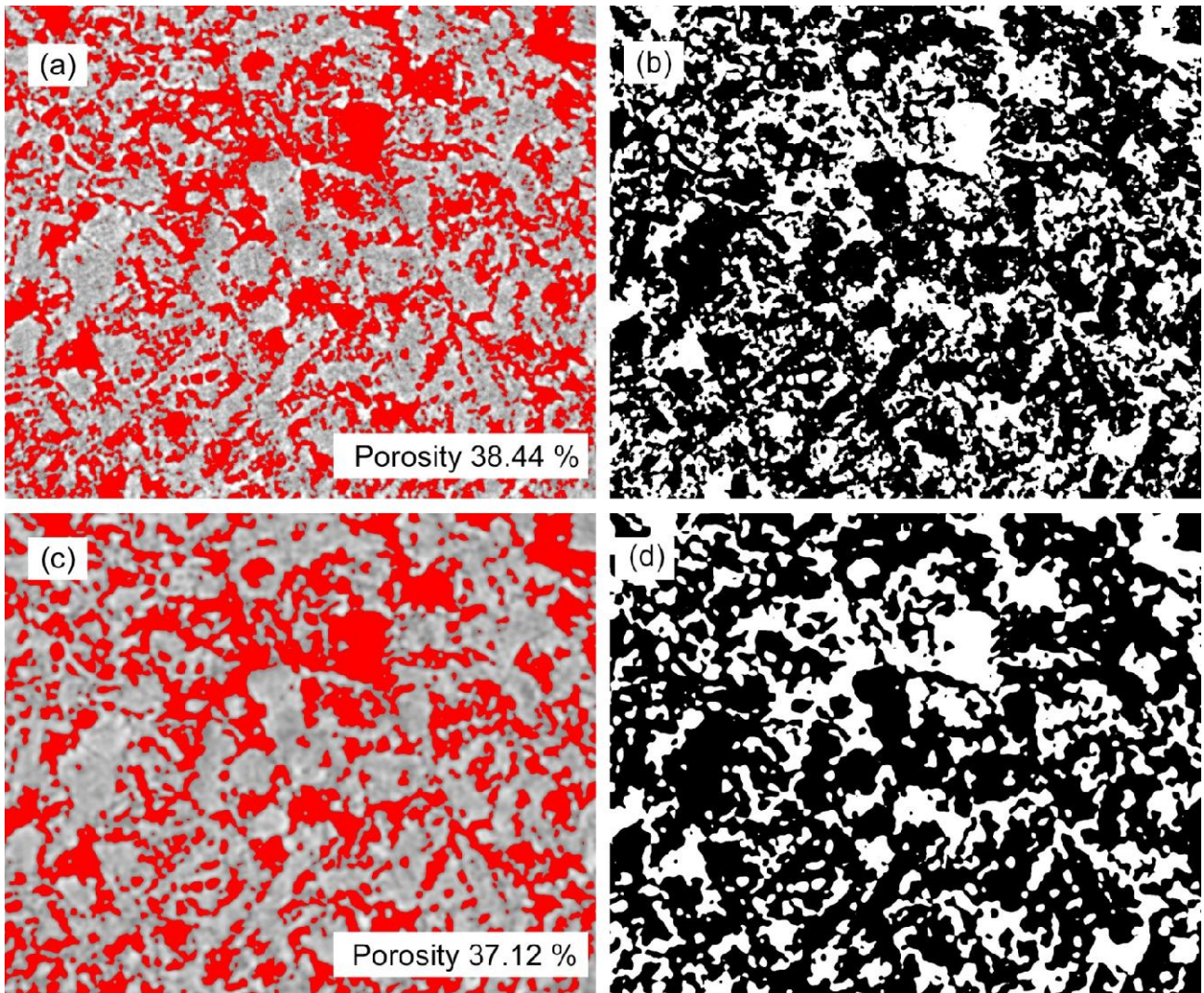
Fig. 5.45 Binarization of the original image, without Gaussian Blur filter (a), (b). Image processed with the Gaussian Blur filter with StDev = 5 (c), (d). The use of Gaussian Blur filter decreases the estimated porosity.

The *Median* filter has been also used to manipulate the porosity. A median filter reduces the noise of an active image by replacing each pixel (or voxel) with the median of the neighbouring pixel values. The higher is the threshold (by selecting specific radius values), the higher is the reduction of the noise.

In this study, this filter has been applied to segmented images mainly to reduce the contribute of isolated voxels or small groups of voxels. In this way, the filter simplifies the dataset deleting details of grain boundaries, of pore profiles and of micro-heterogeneity of the texture and the final outcome is the obtaining of simpler models for the rendering of the 3D pore network. As a drawback, the use of this filter underestimates the total porosity and the inter-connections among pores.
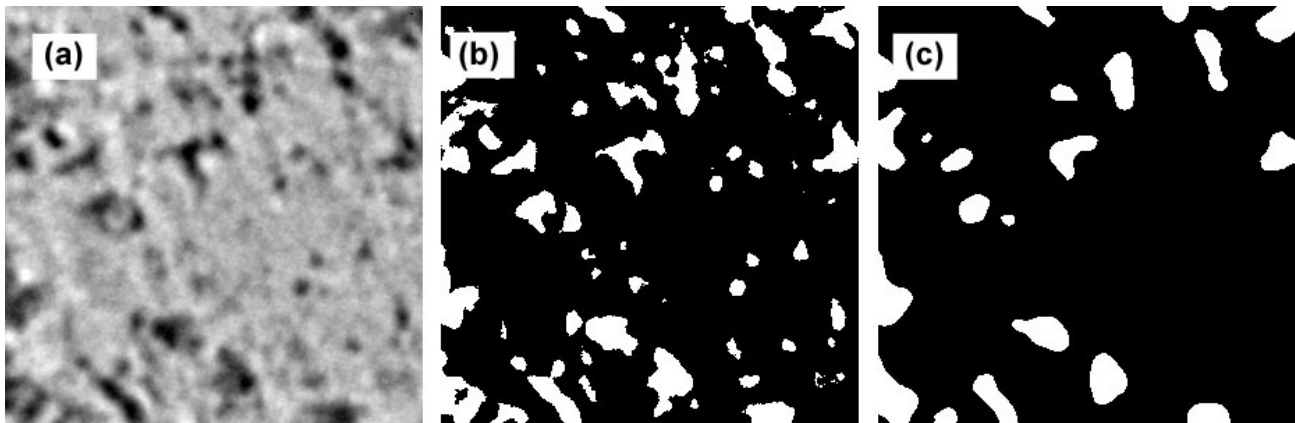
Fig. 5.46 Reconstructed slide of untreated Noto limestone (a), segmented image to isolate the voids (b) and application of the median filter with radius value =10 pixel (c).

Each of the discussed filters and post-processing operations modify the images, conditioning the subsequent operations and basically influencing the interpretation of the images. Therefore, tests were carried out in order to define the best sequence of image manipulations.

Defining A = Brightness and Contrast correction, B = Gaussian Blur Filter, C = Binarization of the images with threshold, D = Median filter, the tested combinations were ABCD, BACD, ACD.

The ACD sequence resulted in datasets highly rich in details, which are too complex to be manipulated for the renderings and poorly significant for the interpretation. The ABCD and BACD alternatives determined an homogenisation of the data and the generation of a simpler dataset. No severe differences were observed among the ABCD and BACD protocols, therefore the ABCD sequence was used for the image processing. The interconnected porosity of the VOI was extracted from the segmented images using the tool "Find connected regions" of the FIJI software. SRμ-CT images allow studying the isolated porosity, providing important data which can not be given by MIP measurements. For this reason, the isolated pores were extracted by the total porosity by subtraction ("Image calculator", operator subtract), and the interconnected pores and isolated ones were then analysed in two separated files.

3D image analysis, renderings and morphometric analysis (basic analysis)
Fig. 5.47 and Fig. 5.48 present two external slices, the selection of a representative VOI and the descending volume rendering on untreated and treated Noto limestone. The reconstructions allow distinguishing interesting differences between the samples. In particular, mainly two grey shades are visible in the slices of the untreated Noto limestone (Fig. 5.47): a dark grey, corresponding to the voids of the sample, and a lighter one, corresponding to calcite of the matrix. In many slices, fossils typical of the biogenic origin of the limestone are evident (indicated by the arrows). The slices of treated Noto limestone (Fig. 5.48) show a texture and microstructure significantly different. In fact, a third halfway grey shade is present and it is localized mainly inside the pores. It is apparently composed by micro-particles, suggesting that this third colour is due to the nucleation of micrometric and sub-micrometric phases inside the voids of the lithotype. These morphologies are very similar to those observed by SEM on an equivalent treated specimen (Fig. 5.49).

The clear presence of this third grey hue in the reconstructed images is more noticeable in the most external slices while this effect wanes as long as the slices are referred to more inner portions. In this way, the halfway grey shade is a further overview of the different arrangement and abundance of calcium phosphates with depth. After 10-15 slices, the presence of the grey hue attributed to phosphates dramatically decreases and it seems to be confined mainly to the pore boundaries.

This feature reverses in the last slices, where the image reconstruction shows a further increase of halfway grey shades attributed to phosphates in the voids. This can be attributed to a more abundant crystallization of new phases, which most likely occurs locally, in correspondence of preferential penetration path. In this light, SRμ-CT highlights the need to combine point analyses (such as μFTIR or T-XRD) to imaging techniques and bulk analyses in the study of the penetration depth of conservation treatments, as heterogeneities at the microscale are very common in stone materials and using only point analyses might lead to misinterpretations of the outcomes. About the new phases, SRμ-CT images demonstrated that the new phases do not fill the voids but form a highly porous network of micrometric crystals nucleated on the pore surfaces. This evaluation is perfectly in agreement to the SEM findings (*e.g.,* of Fig. 5.49) as well as with MIP data, which showed that the DAP treatments modify the porous structure of the stone matrix, reducing the total open porosity and the average pore radius. The crystallization of new phases in the whole thickness of the specimens, as observed by T-XRD measurements and by SRμ-CT images, implies that the entire matrix should be characterized by a system of communicating channels.
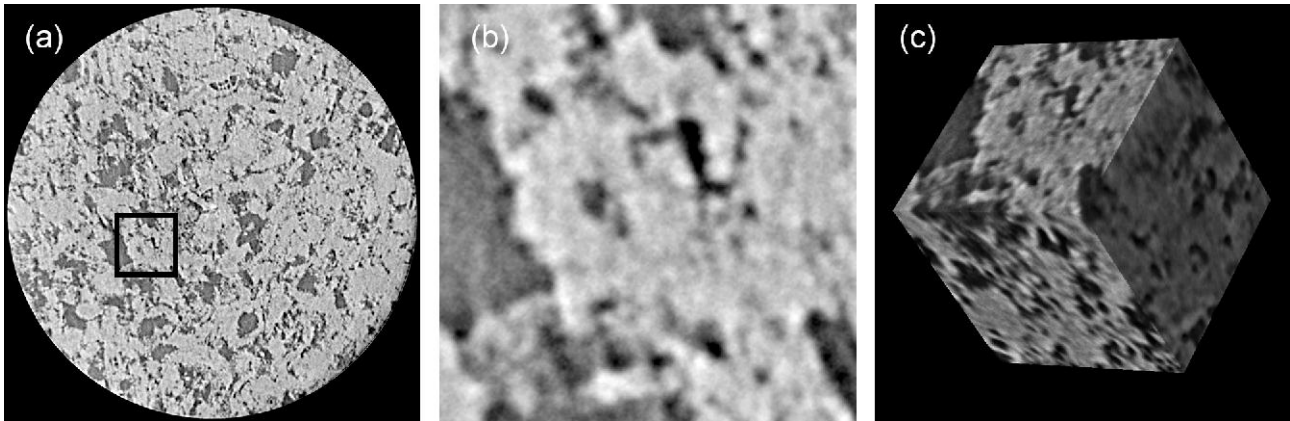
Fig. 5.47 (a) Reconstructed slice of the surface of the untreated Noto limestone. (b) Detail of the slice (a), area of 300x300 voxel^2 indicated by the black square. (c) Volume rendering of (b)
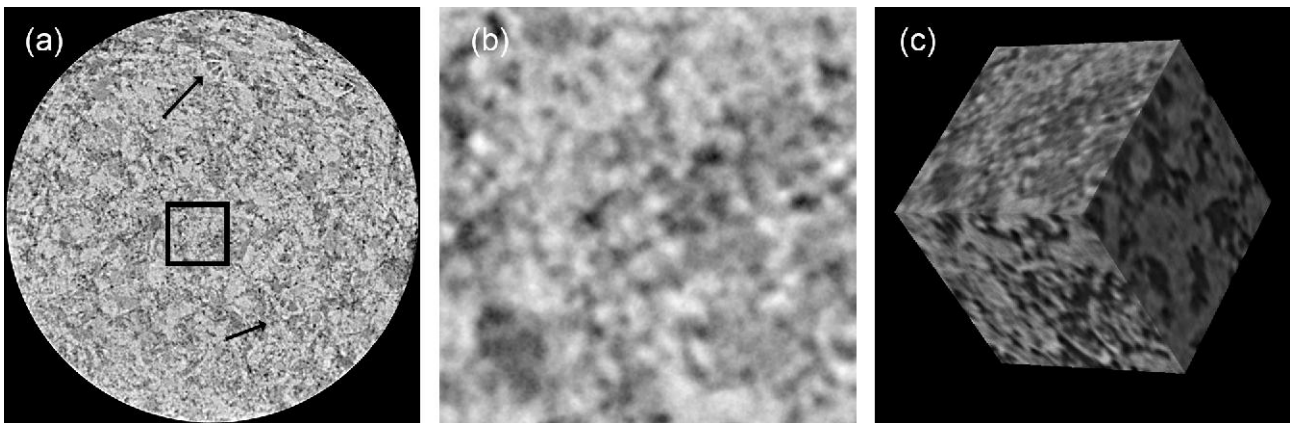
Fig. 5.48 (a) Reconstructed slice of the surface of the treated Noto limestone. In the slice, three different grey shades are well visible, while the arrows indicate two evident fossils. (b) Detail of the slice (a), area of 300x300 voxel^2 indicated by the black square. (c) Volume rendering of (b).
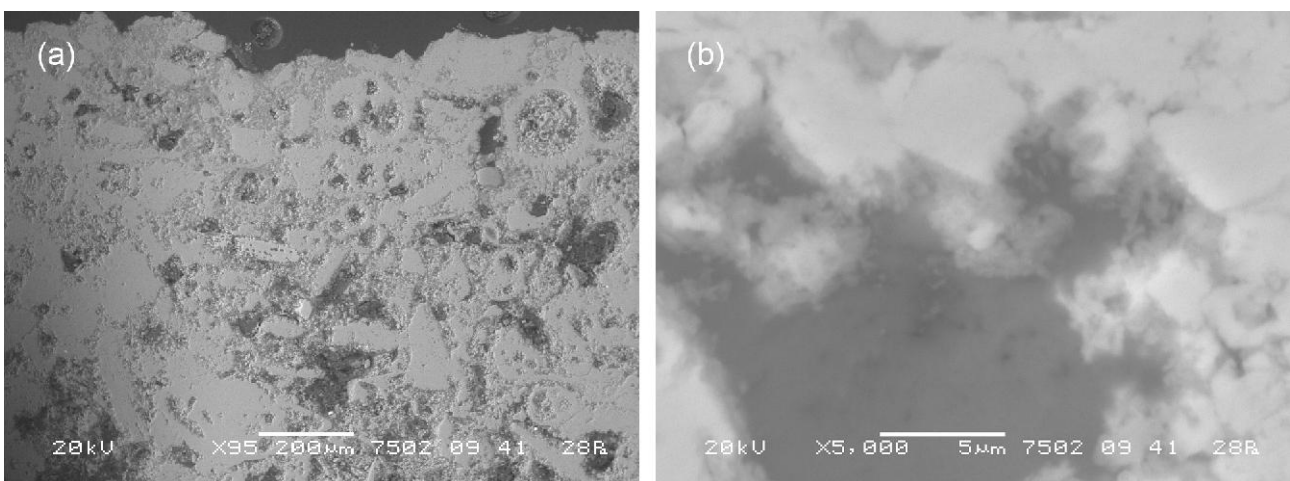
Fig. 5.49 SEM images of treated Noto limestone, showing the widespread presence of fossils (a) (b). Lighter areas are of calcite, dark areas are of voids, intermediate grey shades identify calcium phosphates micro-crystals.

The post-processing elaborations, briefly described, generate datasets which can be visualized by a three-dimensional (3D) rendering. The graphical results of the segmentation of voids are shown in Fig. 5.50 and Fig. 5.51, with the rendering of interconnected pores, isolated pores and their inset in the volume renderings.

The total porosity (connected and isolated) estimated by the software during the segmentation ranges between 21.50-24.50 % for untreated Noto limestone and between 23.11-25.90 % for the treated sample (estimations carried out with Gaussian blur filter -StDev = 5, no median filter, threshold for voids 0-118). The total porosity calculated without the application of Gaussian blur filter is slightly higher (~32-37 %) and actually quite close to the values obtained by MIP.

Typically, both the specimens present a highly porous matrix and the measured values between treated and untreated lithotype can be considered analogous. The stone does not contain detectable micro-cracks, indicating that the penetration depth of DAP treatments is due to the permeation of the natural porosity and not to fractures, which are notoriously preferential penetration paths for fluids. The connected pores are considered the only "objects" that contribute to the fluid flow, and therefore to the consolidant impregnation and redistribution. A closer examination of the 3D reconstructed volumes of pores allows analysing the branching of the voids. The processing revealed that the porous structure is highly interconnected, and that, in general, one or two "objects" (namely, pores) constitute a single highly interconnected void of a determined VOI. In other words, selecting a single, even small pore, its branchings constitute the total open porosity of the investigated volume (Fig. 5.52). This trend is worth for all the representative investigated VOIs, especially considering that the investigations of interconnected pores occurs after the application of median filters, which strongly reduce the contribute of small voids to reciprocal interconnections. Indeed, it is possible to claim that the branching of the pores are quite underestimate, as a strong filtering has been necessary to obtain readable renderings. This means that, in the volume rendering and in quantitative analyses, the small pores (connected and isolated) are particularly underestimate.
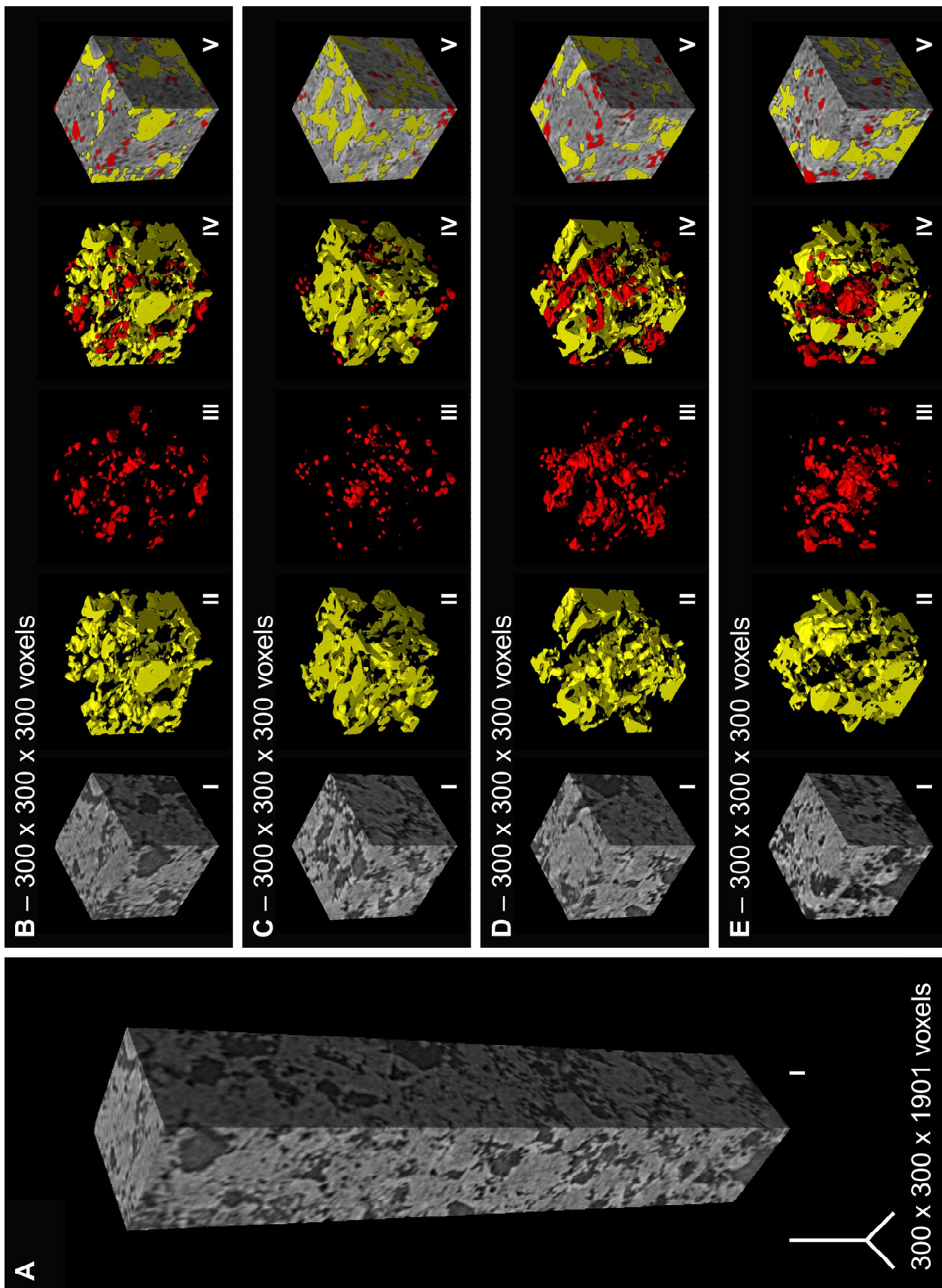
Fig. 5.50 Volume renderings of untreated Noto limestone: parallelepiped cropped from the whole SRμ-CT dataset (A) and VOIs (300 voxel³) close to the surface (B), just below (C), from the middle (D) and close to the bottom (E). The renderings include: X-ray tomographic images (I), connected (II) and isolated (III) segmented pores, combination of connected and isolaterd pores (IV) and their inset in the volume rendering.
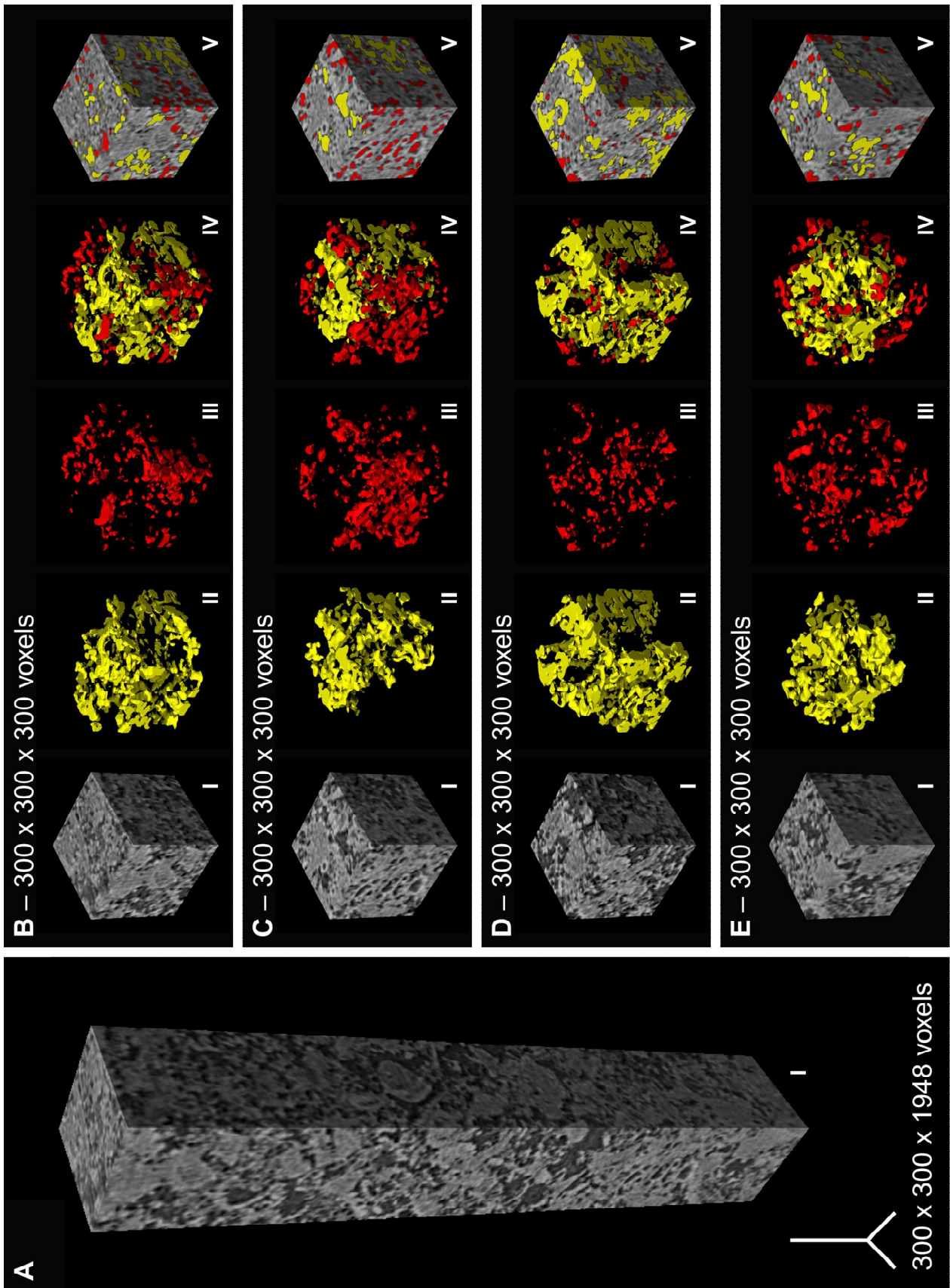
Fig. 5.51 Volume renderings of treated Noto limestone: parallelepiped cropped from the whole SRµ-CT dataset (A) and VOIs (300 voxel³) close to the surface (B), just below (C), from the middle (D) and close to the bottom (E). The renderings include: X-ray tomographic images (I), connected (II) and isolated (III) segmented pores, combination of connected and isolaterd pores (IV) and their inset in the volume rendering
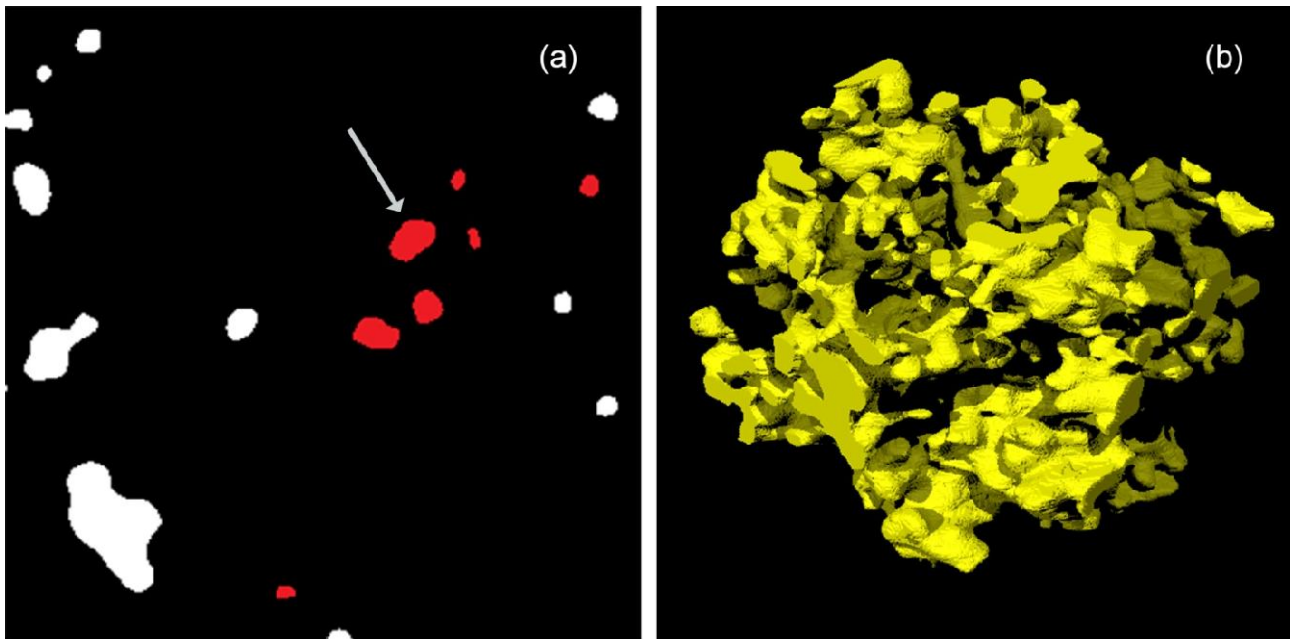
Fig. 5.52 Segmented X-ray SRµ-CT slice (a). By starting the segmentation from the void indicated by the arrow, the tool "Find connected regions" individuates as a single interconnected pore the voids in red. The volume rendering of this "object" is the 3D network shown in (b). A significant part of the VOI results filled by a highly interconnected single pore.

The morphometric analysis was used to provide detailed and quantitative data on the porosity and its connectivity. The quantitative analysis was performed on the pores of the representative VOIs of Fig. 5.50 and Fig. 5.51, obtaining the basic (or first-order) parameters (also called *Minkowski functionals*) [119,185]:

- Volume density (V_v), expressed as the ratio of the number of voxels belonging to the object phase with respect to the total number of voxels in the considered VOI. In this study, the object phase is the pores, thus V_v corresponds to the porosity (total, interconnected or isolated). V_v is a dimensionless parameter ($0 < V_v < 1$).

- Specific surface area (S_v), expressed as the ratio of the interface between the phases (the solid phase and the porous one) to the volume of the total VOI. The S_v is expressed in mm^{-1}.

- Integral of mean curvature (M_v). It is a descriptor index to characterize the presence of concave *vs* convex structures. $M_v > 0$ implies the dominance of convex structures, while $M_v < 0$ occurs in the case of predominance of concave structures. M_v parameters are not considered in this discussion.

- Euler Characteristics (X_v). It is a descriptor index of the connectedness of a 3D complex pore network. It provides a value of connectivity density indicating the number of connections between void structures per unit volume. The X_v is expressed in mm^{-3}. X_v is positive when the number of isolated pores exceeds the number of multiple interconnections between the pores. Whereas, X_v is negative for connected pore networks

Quantitative data resulted from the basic analysis are showed in Table 5.6.

Sample	VOIs		Connected pores			Isolated pores	
	Position	*Reference:*	V_v	S_v (mm^{-1})	X_v (mm^{-3})	V_v	S_v (mm^{-1})
Untr.	Superficial	Volume (i) of Fig. 5.50b	0.17	24.85	-4002.86	0.02	6.21
	Second	Volume (i) of Fig. 5.50c	0.22	32.57	-5087.74	0.01	2.18
	Middle	Volume (i) of Fig. 5.50d	0.21	33.77	-6584.14	0.02	7.60
	Bottom	Volume (i) of Fig. 5.50e	0.24	32.89	-5723.71	0.01	3.30
	Mean		0.21	31.02	-5349.61	0.015	4.82
Treated	Superficial	Volume (i) of Fig. 5.51b	0.15	29.84	-5012.92	0.02	6.08
	Second	Volume (i) of Fig. 5.51c	0.09	20.61	-2730.92	0.04	11.95
	Middle	Volume (i) of Fig. 5.51d	0.17	36.53	-7369.74	0.01	3.86
	Bottom	Volume (i) of Fig. 5.51e	0.15	32.14	-6322.27	0.02	6.58
	Mean		0.14	29.78	-5358.96	0.0225	7.12

Table 5.6 Results of quantitative image analysis of connected and isolated pores performed with the Pore3D software on VOIs of Fig. 5.50 and Fig. 5.51. The results show the volume density (V_v), the specific surface area (S_v) and the Euler Characteristics (X_v) of the pore network.

The investigated VOIs present a connected porosity (from 0.17 to 0.24, average 0.21) higher than the isolated porosity (0.01-0.02, average 0.015), confirming what graphically observed by volume renderings of interconnected and isolated pores. The connected pores, in Table 5.6 expressed as volume density (V_v), decrease after the DAP treatment, either as absolute value (average of the values of all the VOIs) either comparing VOIs corresponding to the same "diffusion layer" (*e.g.,* comparing the VOI (ii) of Fig. 5.50b with the VOI (ii) of Fig. 5.51b).

Focusing on the V_v values of the treated sample, there is a slight gradient of connected porosity from the surface down to the bulk of matrix. Most likely, this difference is due to the nucleation within the matrix of calcium phosphates, in agreement with MIP data on diffusion layers of treated specimens. In this case, the SRµ-CT images allow a further insight on the penetration depth of the treatment, investigating the diffusion layers of the matrix at a different magnification scale and with a higher lateral resolution. As expected, the isolated pores do not show significant variations before and after the treatment (ideally, this fraction of pores is not reached by the DAP solutions).

The data on the specific surface area (S_v) show a trend whose interpretation is more complex than V_v parameters. In fact, S_v values decrease in the treated specimens, from an average of 31.02 mm^{-1} to 29.78 mm^{-1}.

Most likely, the modification of S_v from the surface to the bulk is due to the diffusion, with a gradient, of phosphates crystallization within the matrix and to the deriving modification of the pore size

distribution. At the same time, two factors must be considered: i) the values S_v present a wide variability (*e.g.* from 24.85 to 33.77 mm^{-1} for the untreated Noto limestone, Δ=8.92 mm^{-1}), which is definitely higher than the difference between untreated and treated materials (Δ=1.24 mm^{-1}); ii) measurements are not carried out on the same fragment, before and after the treatment, but on two different fragments. This is an analytical problem when investigating heterogeneous matrixes, and, as discussed evaluating MIP data, it makes the ambiguous the comparisons.

Euler Characteristics (X_v) basically do not vary with the treatment. Thus, even considering also in this case the variability of the X_v data from VOI to VOI, it can be deduced that the crystallization of phosphates does not alter negatively the connectedness of the 3D pore network, which preserves the initial feature of a highly interconnected system.

5.4 DAP consolidating treatments on a pilot case study

Based on the results collected on laboratory specimens and with the aim to scale up the research to worksites, the DAP consolidating performances were investigated in a real conservation task. This case study deals with a burning issue in Milan and in Lombardy, namely the challenging conservation of Angera stone, a lithotype widely used as ornamental stone for architecture façades, columns and decorative carved elements of monuments since the Communal period.

Angera stone is a fine grained dolostone mainly composed by dolomite ($CaMg(CO_3)_2$) with a low fraction of iron oxides (in the form of limonite and hematite) and clay minerals. Angera stone is significantly different from the lithotypes investigated in § 5.2 and§ 5.3, thus the nucleation of the new phases after DAP treatments is expected to be different. However, there are some features similar to the DAP application on Carrara marble and Noto limestone (*e.g.,* the crystallization in presence of Mg ions, the DAP reaction within a porous fine-grained carbonatic matrix), thus the good results obtained on calcite-based lithotypes are used as scientific background to interpret the effects induced by DAP treatments on Angera stone. For these reasons, the analytical-approach optimized in the previous sections is used to carry out, for the first time, a pilot experimental study on the potentiality of DAP - based treatments as consolidating agent for dolomitic substrates.

The conservation worksite identified for the study is the 'Cortile del Richini' or 'Richini courtyard' in Milan, an absolute masterpiece of the Lombard baroque architecture. The courtyard was designed in the seventeenth century by the architect Francesco Maria Richini and, at present, is the main courtyard of the University of Milan, in the Ca' Granda architectural complex [157]. The four internal facades of the courtyard are entirely decorated in Angera stone, including capitals, bas-relief panels, high-relief figures, mouldings and sculpted voussoir. At present, the dolostone of the architectonical elements show severe decay evidences, also due to the complex conservative history of the monument (wide damages during the Second World War bombardment and extensive restorations in the following decades [154,155]). Then, a carved stone element stored in the deposits of the Ca' Granda has been selected to carry out the pilot study on Angera stone decayed in a urban environment.

A set of measurements were initially carried out to investigate the composition and the conservation state of the artefact. Macroscopically, the carved artefact shows detachments, exfoliation and delamination, and granular disintegration with powdering, chalking, sanding and erosion at the microscale (Fig. 5.53). The XRPD and FTIR analyses clearly revealed the presence of dolomite, and low fraction of silicates, iron hydroxides and decay salts: *e.g.,* gypsum, hexahydrite ($MgSO_4 \cdot 6H_2O$), eptahydrite ($MgSO_4 \cdot 7H_2O$), nitratine ($NaNO_3$) and halite ($NaCl$). From compositional analyses, the artefact can be reasonably identified as a white variety or as an intermediate step between the white and the yellow variety. FTIR investigations also showed the minor presence of an organic polymeric product (Fig. 5.54), most likely a residual of previous conservation treatment. To remove the soluble salts, the artefact was exposed to cleanings carried out by poultice (paper fibres and deionised water, weight ratio 1:4, Fig. 5.53b) with the collaboration of the restorer Dr. Fabio Bevilacqua. The matrix resulted highly rich of salts, thus three poultices were necessary to remove the main part of them. At the third poultice application, a migration of chromofores (most likely traces of iron hydroxides of the matrix) was clearly visible, probably due to presence of water in the matrix. Thus, water-based cleanings were interrupted, even though a minor fraction of sodium salts (mainly nitratine, identified by XRPD) remained in the matrix. Sulphates and chlorides were completely removed by cleanings.

The carved artefact was then treated by poultice in two pilot area with 0.76 M and 3.00 M DAP solutions. The application time was 48 h, as the DAP reaction with dolomite is drastically slower if compared to that with calcite (the conversion rate of dolomite is about eight times slower than the conversion rate of calcite [186]).

Fig. 5.53 Detail of the 'Cortile del Richini' in the Ca' Granda architectural complex, XVII century (a). Carved element in Angera stone coming from the 'Cortile del Richini' selected for the pilot study, showing exfoliations on the surface (b,c), and cleanings by poultice with deionised water (d). As the artefact presents exfoliations, Japanese paper was used to preserve the surface, avoiding the sticking at the removal of the cleaning poultice.
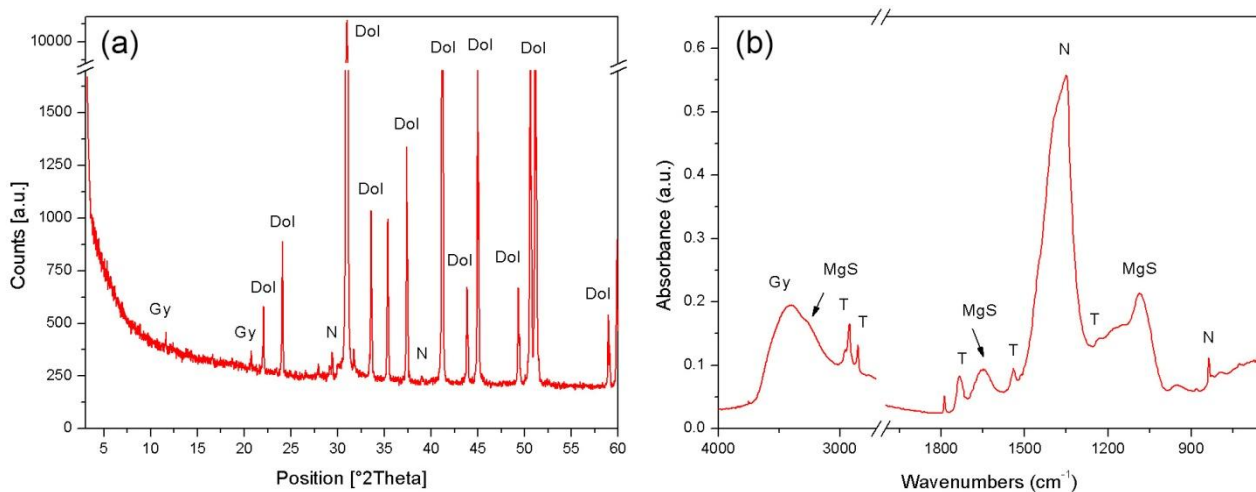
Fig. 5.54 XRPD (a) and FTIR patterns (b) of the surface of the carved artefact in Angera stone before cleanings, showing dolomite (Dol), the presence of decay salts (Gy=gypsum, MgS= hexahydrite and eptahydrite, N= nitratine) and an organic substance, most likely a residual of a previous conservation treatment (T).

Similarly to what observed on Noto limestone and Carrara marble, the DAP reaction with dolomite induces the crystallization of newly-formed phases on the surface of the lithotype and within the stone

matrix. In the first places, the measurements were focused to investigate the effects induced by the treatments on the surface, followed by an insight on the composition and distribution of the reaction products.

After the DAP consolidating treatments, optical micro-images show the presence of a salt crystallization on the surface of Angera stone. Macroscopically, there are no significant differences between areas treated with the 0.76 M or the 3.00 M DAP solution, while at the microscale the crystallization appears slightly more evident on areas treated by the 3.00 M DAP solution.
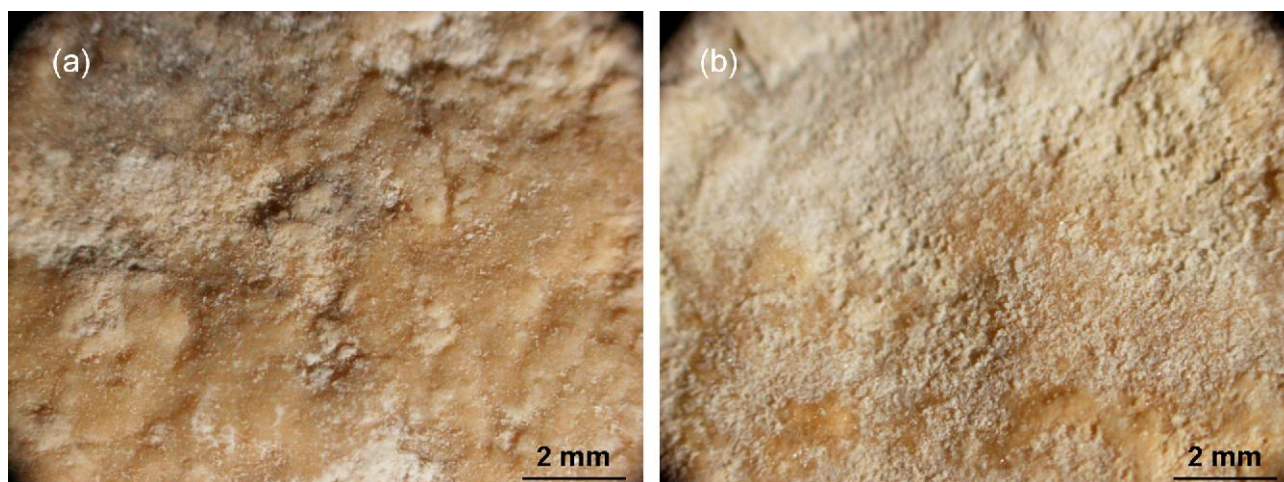
Fig. 5.55 Optical micro images of the surface of Angera stone after 0.76 M (a) and 3.00 M (b) DAP treatments.

Any conservation treatment applied to cultural heritage objects should not significantly modify the aesthetic appearance of the treated material. The formation of crystalline phases on the surface of the artefact might alter the perceived colour of the artefact, thus, colour measurements were carried out following the Italian Recommendation NORMAL 20/85 [187], to monitor possible variations induced by the treatments.

The colour of an object can appear different because of differences in the level of specular reflectance and the chromaticity can be measured considering the Specular Component Included and the Specular Component Excluded mode (SCI/SCE). Measurements carried out with the SCE mode exclude the specular reflectance and only the diffuse reflectance is measured. With this setup, the measured colour is correlated to a "visual evaluation", as it considers the morphology of the surface and the descending effects (*e.g.,* gloss of polished flat surfaces).

On the contrary, the SCI mode measures either the diffuse either the specular reflection of the material. SCI measurements are not affected by the superficial feature of the material, and thus the SCI values reflect the "true" colour of the material. Investigating the colour variations on treated Angera stone, chromaticity values were measured considering the SCI/SCE mode. The SCE mode values resulted slightly higher than SCI mode ones, even though both of them show a common trend. However, to discuss the effects induced by DAP treatments to the carved work of art, only the SCI mode is considered as the goal of this preliminary investigation to evaluate the total appearance independently by the surface conditions. The SCI mode quantitative values are reported in Table 5.7.

The principal colour alteration occurs in terms of L^* parameters (lightness) which decrease after the treatment. The a^* and b^* parameters experiences very limited modifications. In general, a^* values, corresponding to the green-red chromaticity, show an increase (meaning a relocation toward the red component), while the b^* values are almost unvaried or slightly increased (limited relocation toward the yellow component). Only in the case of treatments by 3.00 M DAP solution, b^* values show a very small decrease (meaning a relocation toward the blue component).

Typically, L^*, a^* and b^* variations are more noticeable for areas treated with 3.00 M DAP solutions than those treated with 0.76 M DAP solutions. Generally speaking, the stone surface treated with DAP shows a darkening and a shift toward the yellow and red chromatism, which can be perceived by the human eye as a saturation of the stone colour. Most likely, this variation is due to the migration of iron-based chromofores, which occurs in responce to the chemical and mechanical decay which characterize the carved artefact.

The colour difference (ΔE) between untreated and treated specimens is of 4.76 and of 6.16 for areas treated by 0.76 M and 3.00 M DAP solutions, respectively. In both the cases, the corresponding colour variation is visible by human eye (human eye detection limit, HEDL, $\Delta E \geq 3$, [23]).

Considering the threshold generally considered acceptable for stone consolidants ($\Delta E \geq 5$, [188]), only the 0.76 M DAP treatments can be considered compatible.

	L^*	a^*	b^*	AE
UNTR	82.30	2.74	17.01	
0.76 M DAP	77.61	3.57	17.02	4.76
UNTR	81.59	2.55	16.29	
3.00 M DAP	75.54	3.70	16.19	6.16

Table 5.7 Results of spectrophotometry of untreated (UNTR) and treated Angera stone (0.76 M DAP, 3.00 M DAP). L^* = lightness, a^* = green-red chromatism and b^* =blue-yellow chromatism; ΔE = colour difference. The AE for the human eye detection is 3, while the threshold accepted for stone materials subjected to conservation treatments is 5.

The crystallization of phases after the treatments determines a modification of the sorptivity properties, as showed by water absorption tests with the contact sponge method (European Standard UNI 1142:2011, [121]). The water absorption Wa of the Angera stone artefact (expressed as the mass difference in function of area and time, § 3.2.3.2) was checked on 12 different areas (6 for pilot areas treated by 0.76 M DAP solutions, 6 for 3.00 M ones) before and after the treatments. All the measurements were carried out twice in the same regions to assess the reproducibility, which was found to be very good. In some cases, the values of Wa suffered of the micro-heterogeneities of the stone matrix, along with the presence of differential decay and exfoliations, thus they are not evaluated as absolute values but to show a clear modification after treatments. Untreated Angera stone is characterized by an average Wa of ~ 8.90 g/m^{2}s, which noticeably decreases after treatments, settling to ~ 1.00 g/m^{2}s and to 0.73 g/m^{2}s for area treated by 0.76 M and 3.00 M DAP solutions respectively.

In general, DAP treatments determine a radical reduction of the water absorbed by capillarity, corresponding to a reduction of about ~ -90 %. Comparing the area treated with two different molarity, the portion treated with the highest molarity shows the most relevant decrease (~ -91.38 %). The

portion treated with DAP solution at low molarity experiences a minor decrease of water absorption (~ -89.35 %), even though the measured values are quite close to the 3.00 M ones.

The effects induced by the treatments to the stone are related to a compositional and microstructural modification of the stone matrix. In fact, before the treatments, the Angera stone of the artefact showed evidence of decohesion either close to the surface (Fig. 5.56a) either in the inner portion, down to several millimetres within in the stone matrix (Fig. 5.56b). On the surface, Na- and N-rich compounds are clearly detected by EDS (Fig. 5.56c-Fig. 5.56e). These sodium salts (already present in the carved artefact and not completely removed by the de-salinization procedure) are arranged in rounded aggregates and grow on the crystals of the matrix, while dolomite is well detectable by the combination of Ca and Mg on crystals showing the typical rhombohedral habit.
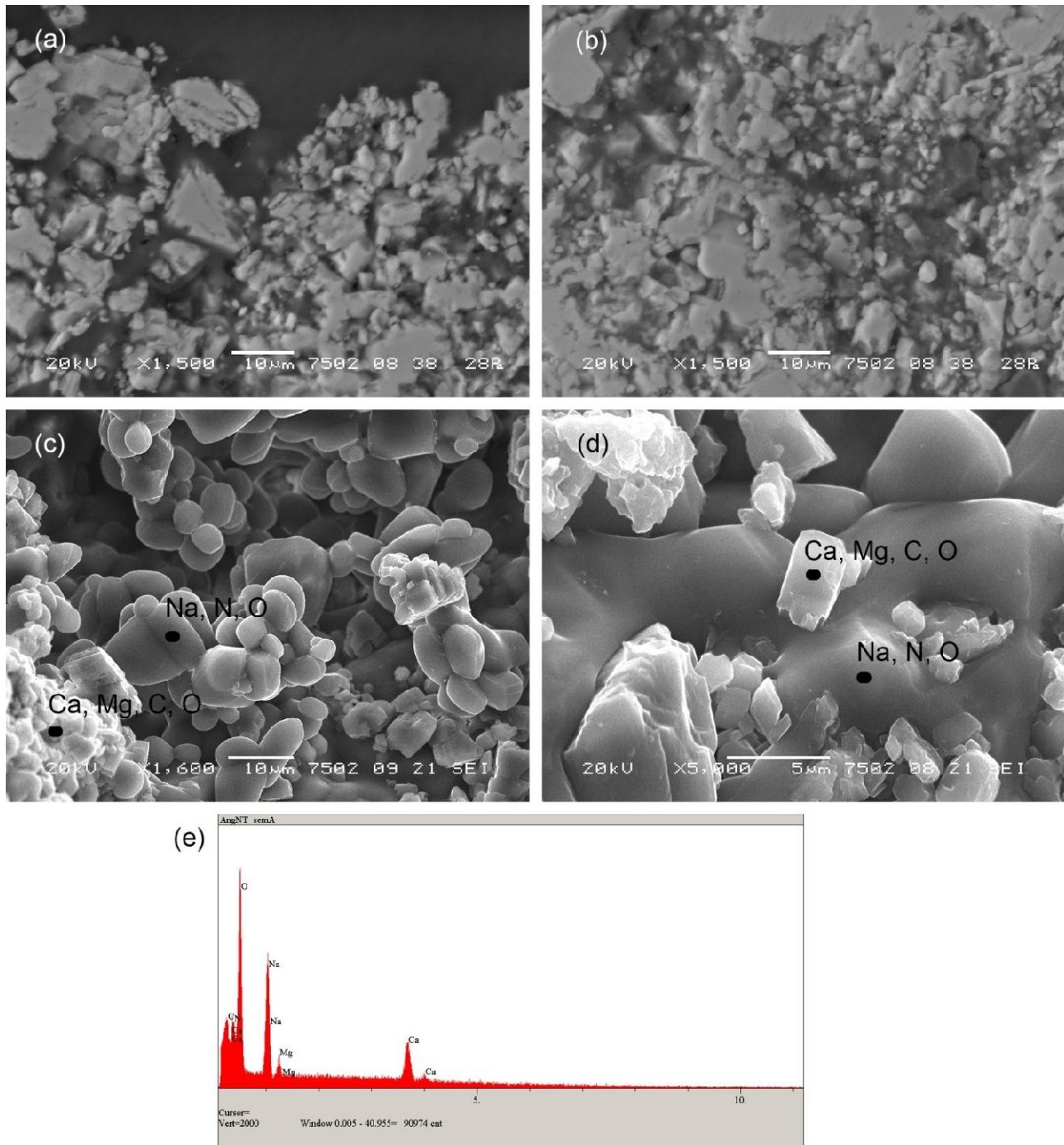
Fig. 5.56 SEM images of untreated Angera stone, showing decohesions on the surface (a) and inside the matrix down to several millimetres (b). The N- and Na-rich compounds (most likely nitratine, identified in XRPD and FTIR patterns of Fig. 5.54), is localised in aggregates (c, d) mainly on the surface of the stone material. Representative EDS spectrum of N- and Na-rich compounds (e). Ca and Mg peaks are due to the dolomite of the substrate.

The DAP reaction with dolomite determine the growth of a *shell* of newly-formed phosphate phases, likewise to what occurs on calcite. Focusing on their morphology, these phases are composed by thin rose-like aggregates and by rounded aggregates, with a feature similar to the phases crystallised on Noto limestone and Carrara marble. In both the cases, the crystal size is very low, being always lower than 1 micron (Fig. 5.57).
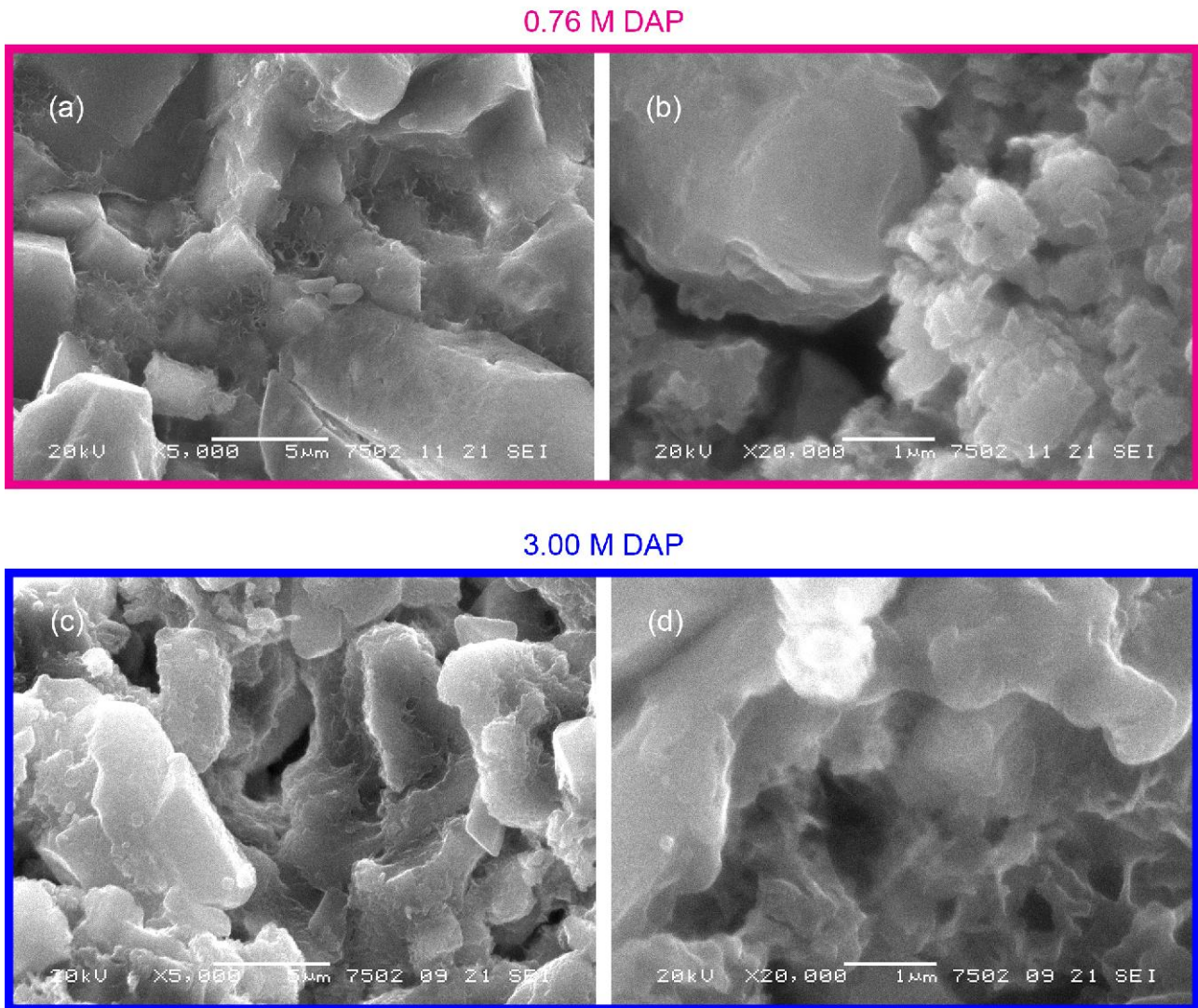
Fig. 5.57 SEM images of Angera stone treated with 0.76 M (a, b) and 3.00 M (c, d) DAP solutions. The newly-formed crystals have a rose-like or rounded morphology. In case of 0.76 M DAP treatments, the P-containing crystals are localized mainly at grain boundaries and dolomite grains are well visible, while 3.00 M DAP treatments determine the covering of the surface with newly-formed P-containing crystals.

The newly-formed crystals nucleate on the boundaries of the stone grains, in cracks and in the pores of the matrix (Fig. 5.58a and Fig. 5.58b). Fig. 5.58c show a representative SEM image of an external portion of consolidated Angera stone by 3.00 M DAP solution. Fig. 5.58d is a re-elaboration of Fig. 5.58c, carried out with the FIJI (ImageJ) software. In the re-elaboration, an *ad hoc* greyscale threshold was used to select the grey shades which morphologically correspond to the newly-formed P-containing crystals. This elaboration, merely graphic, allows appreciating the effect of the consolidation, which is the formation of a phosphorous-based crystal network that nucleates on the reaction profile of dolomite grains and reconnect detached stone grains of the matrix. A similar feature is detected also on pilot areas treated by 0.76 M DAP solution.
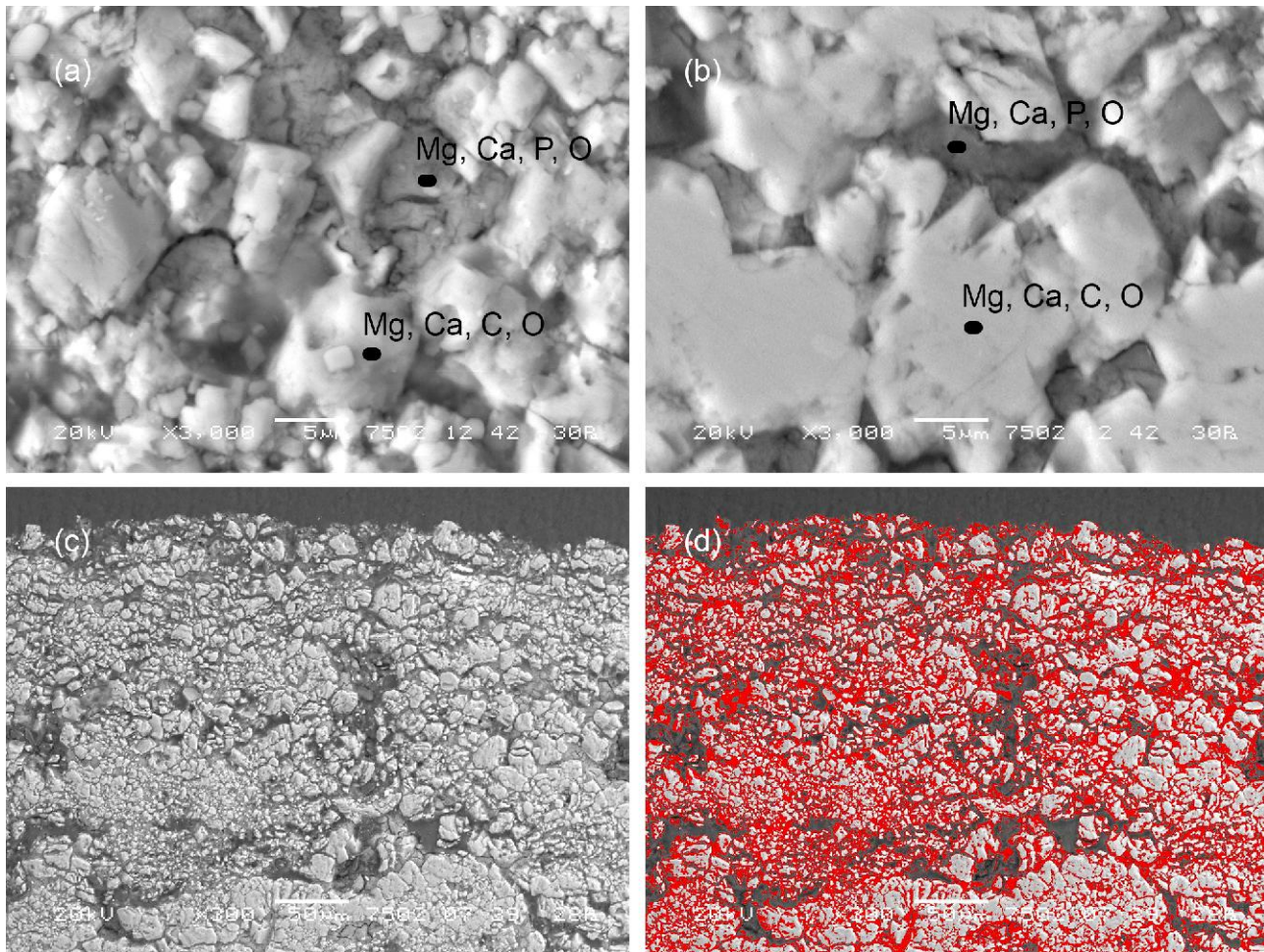
Fig. 5.58 SEM images at different magnification of polished cross sections showing the formation of newly-formed phases in the voids of the matrix (a-c). (d) is a graphical re-elaboration of the SEM image (c) aimed to highlight the arrangement of the new phases in a binding network around the detached grains of the matrix.

P is detected in combination to Mg or to Ca in the voids of the matrix (Fig. 5.59). The reaction profile of dolomite grains is neat and it does not show severe corrosion marks (as, *e.g.,* in Fig. 5.58a and Fig. 5.58b), reconfirming the minor susceptibility of Mg-containing substrates to the acid dissolution of DAP treatments.

Morphologically, the natural silicatic veins of Angera stone are portions showing decohesions and inducing exfoliation. Microanalyses reveal that these veins do not act as preferential paths for the diffusion of DAP solutions, as: i) no phosphorous is present inside the veins or very close to these veins, either in the surface either more in depth; ii) there is no a gradient of phosphorous close to a vein or far from the vein (*e.g.,* 200 μm from the vein). The only detected gradient of phosphorous is due to the penetration depth, according to the relationship "the inner, the lower".

Na- and N-rich compounds detected by EDS and WDS are still visible after DAP treatments and they are localised only close to the surface (penetration depth max. 1 mm). No phosphorous is detected in areas containing nitrogen or sodium, indicating that the matrix impregnated with these soluble salts is not reactive to DAP treatments and it remains incoherent after the consolidation.

The area of the artefact treated with DAP solutions with different molarity do not show dramatic differences, except for the distribution of the new phases. In fact, after 0.76 M DAP treatments, the

reaction products are localized mainly at grain boundaries and dolomite grains on the surface are well visible (Fig. 5.57a and Fig. 5.57b). P-containing phases are detected below the surface down to 2-4 mm, with an irregular presence below 2-3 mm. Focusing on the 3.00 M DAP treatments, the amount of newly-formed phases is higher, and the whole surface is covered by a thin layer of P-bearing compound showing a feature similar to a coating (Fig. 5.57c and Fig. 5.57d). The penetration depth of the phosphates in the bulk is slightly deeper than with 0.76 M DAP treatments, with the localization the P-containing compounds down to 3-5 mm and an intermittent presence below 3 mm.

It should be considered that the presence of a remaining of a previous conservative treatment within the Angera stone matrix might have some effects on the diffusion of the DAP solution and thus locally inhibit the DAP reaction with the substrate and the crystallization of the new phases, similarly to what observed in presence of Na-based salts.
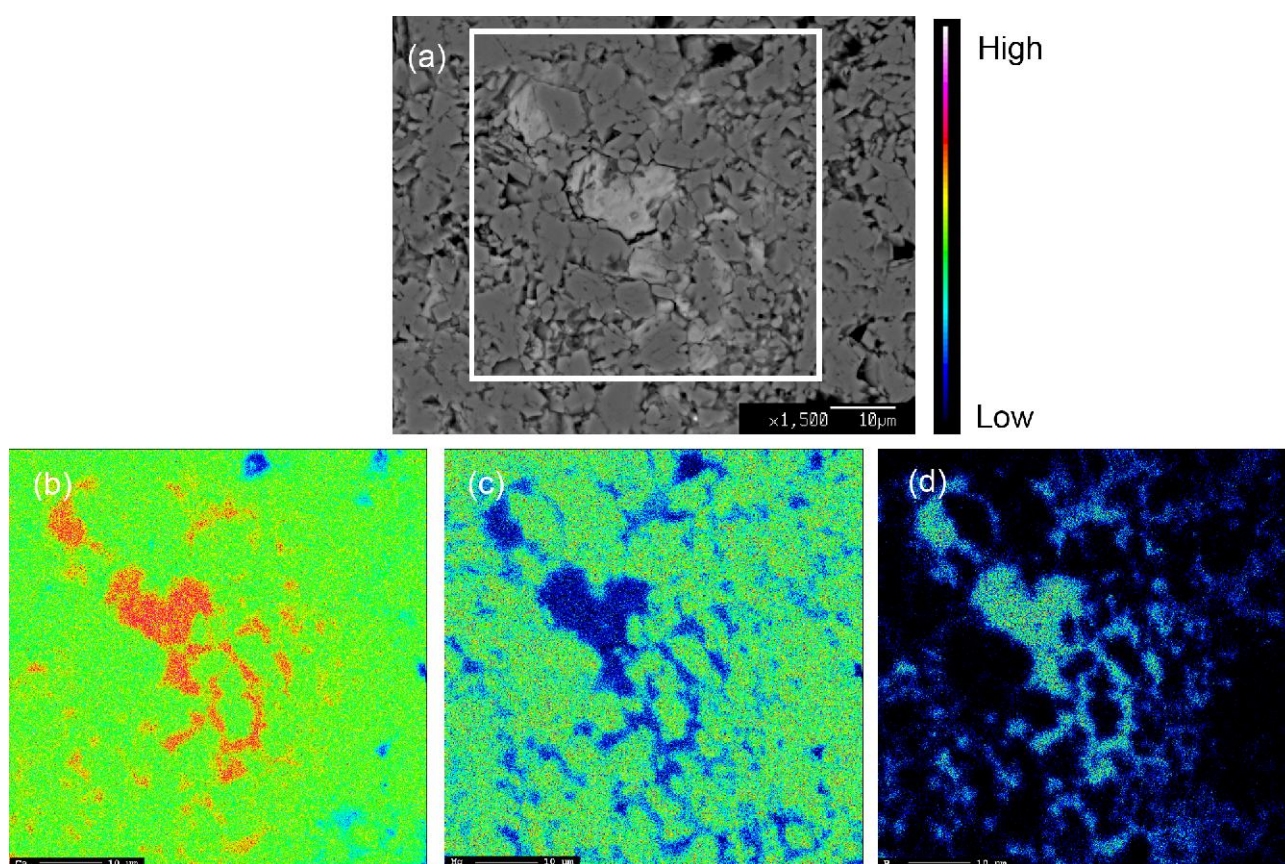
Fig. 5.59 Micro image (a) of treated Angera stone and chemical maps (WDS) of calcium (b), magnesium (c) and phosphorous (d). The scale bar (on the top) shows the relative concentration. The square indicates the area of the WDS maps.

Struvite, a magnesium ammonium phosphate hydrate ($NH_4MgPO_4 \cdot 6H_2O$), is the only newly-formed phase identified by X-ray powder diffraction and FTIR and Raman spectroscopies. No peaks of calcium phosphates are detected in the diffraction patterns. FTIR and Raman vibrational weak broad bands of possible calcium phosphates (compatible with HAP, OCP or ACPs) are detected, but the nature of this phase (or phases) remained ambiguous. Then, it is highly likely that Ca and P identified by EDS and WDS analyses correspond to calcium phosphates formed as amorphous/poorly crystalline

phases (in sub-micrometric crystallites). Further investigations on the nature of these CaPs phases by grazing incidence X-ray diffraction with synchrotron radiation are scheduled. No compositional variations are detected by changing the molarity of the DAP solution.
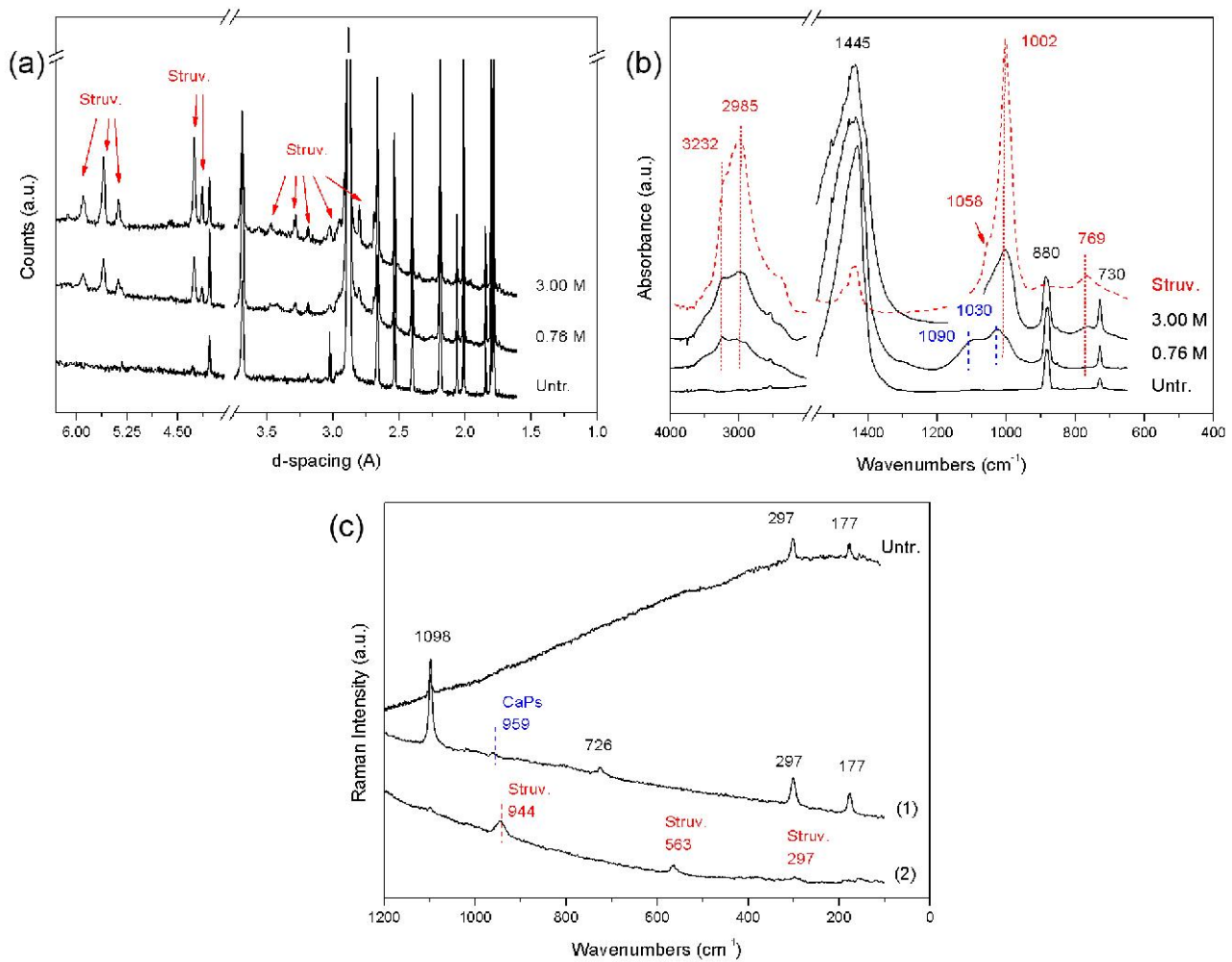
Fig. 5.60 XRPD patterns (a), FTIR spectra (b) and Raman spectra (c) of the untreated (Untr.) and treated Angera stone. In black are reported the peaks of dolomite, in blue the peaks of possible calcium phosphates, while in red the peaks of struvite. In (c), the spectra (1) and (2) refer to different points of Angera stone treated by 0.76 M DAP solution. These spectra are representative also of the phases formed by using 3.00 M DAP solution.

The widespread crystallization of P-containing phases within the matrix modify the microstructure of Angera stone, as showed by the MIP investigations. In detail, on Angera stone of the carved artefact, the DAP treatments determine a variation of the total open porosity, a decrease of the average pore radius and an increase of the total specific surface area. A brief aside, before going in depth in the MIP data. For clarity's sake, in the following, the lithotype will be labelled only "Angera stone", avoiding the repetition "carved artefact, real artwork, etc." but the discussion focuses only on this case study and not the general modifications, as: i) Angera stone is available in several varieties (white, yellow, pink, veined and intermediate steps) and each variety has a proper porosity and microstructure; ii) the porosity and pore size distribution varies being carved and exposed, and these variations depends on the stone variety; iii) the microstructural variations vary also on the basis of the conservative history of single Angera stone elements.

Starting from the total open porosity, the connected pores of the untreated Angera stone correspond to 17.75 % of the volume, which reflects the presence of a decohesion if compared to the 12-13 % of quarry one (experimental data on white Angera stone, from the ICVBC-CNR MIP archive of stone materials). The total open porosity is basically unaltered after 0.76 M DAP treatments (17.78 %) while it decreases after 3.00 M DAP treatments (14.13 %). This suggests that the treatments carried out with the solution at high molarity determines a more relevant phase crystallisation. The average pore radius changes from 0.58 µm for the untreated Angera stone to 0.45 µm and 0.24 µm for the treated ones, for 0.76 M and 3.00 M, respectively. Evaluating these values, it should be considered that the fragments used for MIP investigations were irregular parallelepiped of ~ 7×7×7 mm sampled from the carved surface, thus the MIP data average the porosity values of the more superficial region of the treated matrix (which experienced the most relevant porosity variations, either due to the decay and to the treatment) and of an inner portion (which most likely preserves the porosity features of the sound/untreated lithotype or it is only spotty reached by the decay/treatment). Ideally, the collection of thinner fragments, more similar to "diffusion layers" as carried out in § 5.3, would have provided more punctual information but it was not not possible due to the incoherent matrix of the Angera artefact and to a conservation need, namely keeping the sampling as minimum as possible. For this reason, the modifications induced to the porosity features of Angera stone are expected to be actually more significant than those showed by MIP values, especially in the millimetres closer to the carved surface. Focusing on the pore size distribution, important modifications are detectable as well. The crystallization of Mg and Ca phosphates in the voids determine the redistribution of the pore classes with the decrease of pores with radius between 2.50-0.25 µm and the increase of voids with radius lower than 0.25 µm. This variation is more evident for the area treated with 3.00 M DAP solution. A further variation consists in the actual formation, after treatments, of pore classes initially not existing in the Angera stone, namely pores with radius < of 0.050-0.025 µm. Following this, a noticeable variation consequently occurs on the relative surface. The total specific surface area rises from a starting value of 0.37 m^2/g (untreated matrix) to 1.16 m^2/g (after 0.76 M DAP treatment) and to 1.30 m^2/g (after 3.00 M DAP treatment). As a result of the % increase of tiniest pore classes, the relative surface mutually increases in the same classes. Fig. 5.61 shows the clear raise of the relative surface of the pores with radius lower than 0.25 µm. The growth of these values is particularly important for pores with radius lower than 0.075-0.050 µm. 3.00 M DAP solutions induce in the stone matrix the most evident variations, either in terms of modification of the pore classes distribution either in the relative surfaces of tiny pores. For these reasons, the clear modification of the sorptivity properties occurred after DAP application in the pilot area are due to the micro-structural variations described by MIP investigations.
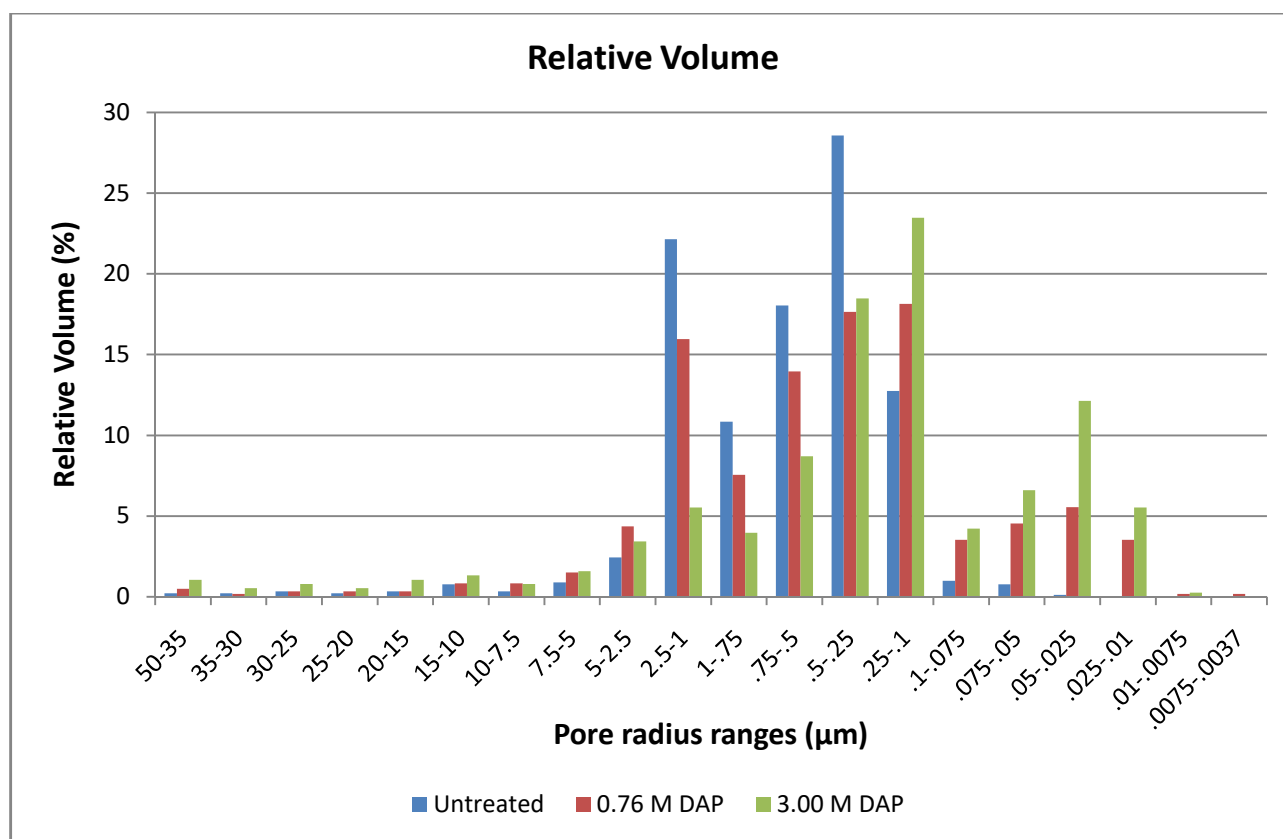
Fig. 5.61 Pore size distribution of untreated and treated Angera stone using 0.76 M or 3.00 M DAP solutions.
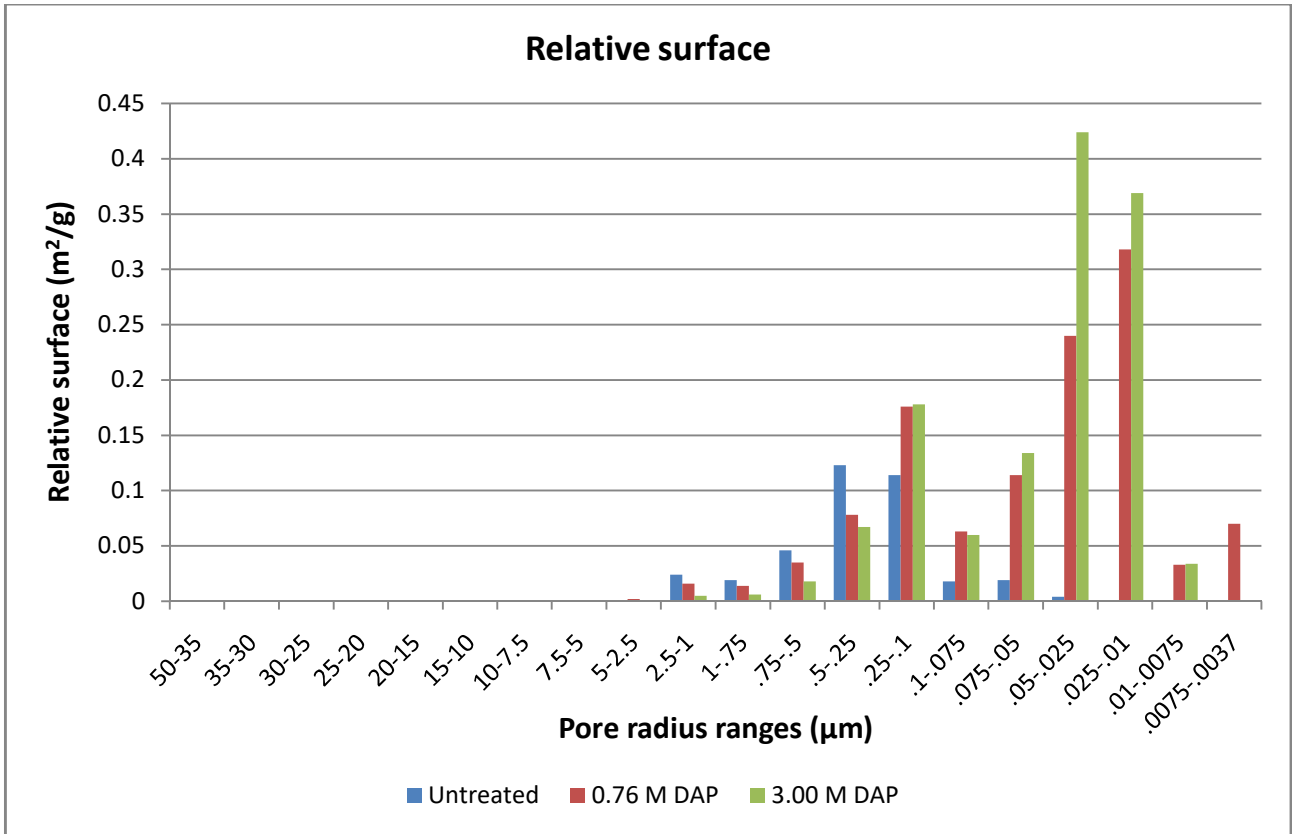
Fig. 5.62 Relative surface of the pore radius ranges of untreated and treated Angera stone using 0.76 M or 3.00 M DAP solutions.

6 Conclusions and future perspectives

6.1 Conclusions

Diammonium hydrogenphosphate (DAP) solutions react with carbonatic substrates and form phosphate phases. This crystallization, occurring in the stone pores and binding detached grains, modifies the microstructure of the lithotype. In this light, the crystal-chemistry of the newly-formed phases and the effects induced to the matrix by their crystallization were both explored.

The formation of the newly-formed phosphate phases depends on the availability of free calcium ions, which, in turn, depends on several variables: the DAP molarity, the lithotype (*e.g*, grain size, microstructure), the treatment protocol (*e.g*, application modality and duration). The initial pH and the pH variations during the reaction influence the calcium availability as well. These mutually interfering factors have twofold consequences: they determine the composition of the new phases and their location.

It is possible to identify three main reaction conditions: i) high availability of free calcium ion; ii) low availability of free calcium ion; iii) presence of free magnesium ions.

The high availability of calcium ions occurs on substrates rich of calcium ions, with a high specific surface area, and in presence of a high DAP molarity (which affects the pH). The presence of a high molar fraction of calcium in the crystallization environment induces the formation of phases with a high Ca/P molar ratio, namely hydroxyapatite (HAP). On the contrary, in reactions with a low DAP molarity and on substrates releasing a low fraction calcium (*e.g*, with compact matrixes, substrates poor of calcium), the minor availability of free calcium ions generates crystals with a low Ca/P molar ratio, as dicalcium phosphate dihydrate (DCPD). Octacalcium phosphate (OCP) is formed in both the cases, as its crystallization occurs in halfway reaction condition.

The availability of free magnesium ions, in equal molar fraction with calcium ions, determines the formation of struvite and amorphous calcium phosphates (ACPs).

The crystalline phases with a low Ca/P molar ratio are confined to areas poorer of free calcium ions, while phases with higher Ca/P molar ratio are widespread within the matrix.

All the new phosphate phases grow in a *shell* on the surface of stone grains. This occurs either on compact substrates either on porous ones. On compact substrates, the phosphate phases mainly form an external layer on the surface of the treated stone. On porous matrixes, the DAP solutions penetrates into the pores and calcium phosphates nucleates mainly inside the voids. This crystallization generates a crystal framework with consolidating properties, as it mutually binds detached stone grains. At the same time, the crystallization of phosphates within the stone induces microstructural modifications, even though these variations do not revolutionize the substrate in its characteristic features.

The nucleation determines the variations of the pore network, which, in turn, modify the capillarity absorption and decreases the sorptivity speed. These variations were detected down to a noticeable

penetration depth, thus demonstrating the penetrating capability of DAP treatments. The crystallization of new phases, which ideally are able to permeate weathered portion of stone matrix down to the sound material, maintains the permeability to water flows and the hydrophilic properties of the lithotype.

The effects induced by the treatments to the stone substrate were documented on lithotypes showing opposite characteristics, *e.g.*, compact/porous, sedimentary/metamorphic, fine-grained/bigger-grains. The selection of these lithotypes, in a sort of "end-members" examples of ornamental stones, actually aimed to study the modifications induced by DAP treatments on simplified systems. Here, the presented results were collected in laboratory and on *ad hoc* specimens. It is conceivable that DAP treatments might act differently on other carbonatic stones. At the same time, dealing with lithotypes showing so different features, the expectation is that some key points raised from this research might be adopted to study the application of the reagent to stones with intermediate characteristics. Clearly, the use of DAP treatments on different lithotypes and in real conservation worksites opens the scenario to a new spectrum of variables. In this case, the conservation picture is more complex, due to the possible introduction of new factors affecting the crystallization, as the presence of decay phenomena, previous conservative treatments, etc.

As showed by the study carried out on Angera stone (a sedimentary porous lithotype with dolomitic composition), the effects induced by the treatments are different than on calcite-rich materials. In fact, the reduced release of calcium ions, the availability of free magnesium ions as well as the presence of a decayed microstructure with soluble salts and a high porosity generate the formation of magnesium phases (struvite) and ACPs, alongside HAP. For these reasons, the collected experimental findings of this research project are expected to serve as guidelines to support the application of DAP consolidating treatments to complex matrixes in conservation field.

6.2 Future perspectives: when a problem drives a new research project

Approaching this last section, I asked to myself "what are the future perspectives of this Ph.D. research? What is the next step?". After that I remembered what Prof. G. Zerbi used to say to me: "any research project rises from a problem. So, what is your problem?". There are still many open issues and many others have been opened by this research activity. However, thinking to the overall path of these three years, some crucial topics became progressively clear.

DAP treatments show positive effects when applied to carbonatic stones. Some have been briefly described and many others are discussed in the open literature. At present, literature on DAP treatment for stone conservation is constantly growing, while studies on the effects of DAP application to other carbonatic materials is at the beginning. Actually, the potential application in this field is wide, considering *e.g.,* the complex scenario of the artificial stone materials, including plasters, mortars, stuccoes, wall paintings and *frescos*. In this view, several are the unexplored issues. "How does interact the DAP solution with matrixes showing an heterogeneous composition? How is it distributed between binders and aggregates? Are the aggregates reactive, in some way? Does the treatment have any effect on carbonatic pigments, when applied to painted layers, *e.g.* on a wall painting? Are non-carbonatic pigments influenced by the modification of the substrate after the DAP reaction? What are

the aesthetic performances when applied to coloured substrates?" And also, if gypsum has been described as a potential further source of calcium ions, "how DAP treatments interacts with materials containing calcium sulphates? When does gypsum act as a booster of the reaction [33,34,36,41] and when, on the contrary, does it apparently inhibit the diffusion of DAP solutions [189]? What can we expect if DAP solutions are applied to substrates decayed by the presence of soluble salts in complex mixture?"

The analytical approaches used in this thesis, based on the combination of conventional and innovative techniques, allowed answering to a question asked frequently during these three years: "how to investigate the composition of a consolidant, its distribution with the matrix and the effects induced by the consolidant to the microstructure in the same measurement?". Furthermore, stated that a conservation product modifies the microstructure of a stone substrate, "is it possible to carry out these investigations on the same sample before and after the treatment, in order to investigate the effects induced in the same region?". Many of the available analytical techniques provided data only on one aspect (*e.g*, composition, position or microstructural variations) or in some cases two. At present, a possible pathway has been identified in combining X-ray microtomography and X-ray diffraction microtomography carried out with synchrotron radiation. These techniques, whose combination is still quite unexplored in conservation field, provide qualitative data and topographic information at the same lateral resolution, overcoming the limitations of more conventional methods. Furthermore, they potentially allow characterizing the same matrix before and after inorganic-mineral conservation treatments, thus making reliable comparisons between untreated and treated matrixes.

These techniques, as well as many techniques used in this research project, usually require the sampling from the object under investigation and, in many cases, an *ad hoc* manipulation. Actually, dealing with artistic materials, avoiding the sampling should be the preferential approach. Thus, an objective of this 3-years research project was to identify possible analytical techniques able to gain the maximum amount of information with the minimum damage for the investigated sample (or object). In this direction, a step forward has been carried out exploring the potentiality of synchrotron radiation grazing incidence X-ray diffraction to study artworks, and two scientific papers have been published on the topic: the characterization of calcium phosphates formed after the DAP consolidation [175] and the crystalline phases in painted layers of real cultural heritage objects (*e.g.,* pigments, fillers, decay products) [190]. These investigations shed light on the feasibility of a depth profile study preserving the whole sample for further analyses but, at the same time, the need to better understand the potentiality and the limits of these technique (*e.g.,* surface topography, irregular layer succession, preferential orientations) when applied to cultural heritage materials.

A question is still open: "how can be quantified the fraction of consolidant formed within the matrix?" and, even more important, "how much consolidant is needed by the stone matrix?". These questions raised frequently during the interpretation of the data and many attempts were carried out to answer these questions, by combining different analytical techniques. There are several possible analytical options, but nevertheless, none of them is still fully exhaustive.

At present, aware that these 3 years were a ring in the wider process of the "research chain", I would like to conclude this manuscript with the hope that this thesis can be a small source of answers but also a source of questions which might provide some starting points for the new rings of the chain.

7 Appendix and references

7.1 Appendix

7.1.1 List of figures

7.1.2 List of tables

7.2 References

[1]   S. Siegesmund, R. Snethlage, eds., Stone in Architecture, 4th ed., Springer Berlin Heidelberg, Berlin, Heidelberg, 2011. doi:10.1007/978-3-642-14475-2.

[2]   G. Torraca, Lectures on Materials Science for Architectural Conservation, 1st ed., the Getty Conservation Institute, Los Angeles, 2009.

[3]   E. Doehne, C.A. Price, Stone Conservation. An overview of current research, 2nd ed., the Getty Conservation Institute, Los Angeles, 2010. http://www.getty.edu/conservation/publications/pdf_publications/stoneconservation.pdf%5Cnht tp://www.getty.edu/conservation/publications_resources/pdf_publications/pdf/stoneconservatio n.pdf%5Cnhttp://www.getty.edu/conservation/publications_resources/books/.

[4]   Charola, I.C. on M. and Sites, Stone Deterioration in Historic Buildings and Monuments, in: 10th, Int. Congr. Deterior. Conserv. Stone, ICOMOS, 2004: pp. 3–14.

[5]   Commisione Tecnica UNI, UNI 11182:2006 Beni culturali - Materiali lapidei naturali ed artificiali - Descrizione della forma di alterazione - Termini e definizioni, (2006) 1–33.

[6]   ICOMOS-ISCS, Illustrated glossary on stone deterioration patterns. English-French version, (2008) 1–78.

[7]   A. Sierra-Fernandez, L.S. Gomez-Villalba, M.E. Rabanal, R. Fort, New nanomaterials for applications in conservation and restoration of stony materials: A review, Mater. Construcción. 67 (2017) 107. doi:10.3989/mc.2017.07616.

[8]   G.G. Amoroso, V. Fassina, Stone Decay and Conservation: Atmospheric Pollution, Cleaning, Consolidation and Protection, Amsterdam, 1983.

[9]   M. Matteini, Inorganic treatments for the consolidation and protection of stone artefacts and mural paintings, Conserv. Sci. Cult. Herit. 8 (2008) 13–27. doi:10.6092/issn.1973-9494/1393.

[10] E. Hansen, E. Doehne, J. Fidler, J. Larson, B. Martin, M. Matteini, C. Rodriguez-Navarro, E.S. Pardo, C. Price, A. de Tagle, J.M. Teutonico, N. Weiss, A review of selected inorganic consolidants and protective treatments for porous calcareous materials, Stud. Conserv. 48 (2003) 13–25. doi:10.1179/sic.2003.48.Supplement-1.13.

[11] G.W. Scherer, G.S. Wheeler, Silicate Consolidants for Stone, Key Eng. Mater. 391 (2009) 1–25. doi:10.4028/www.scientific.net/KEM.391.1.

[12] C.A. Grissom, N. Weiss, Alkoxysilanes in the conservation of art and architecture, 1861-1981, Art Archaeol. Tech. Abstr. 18 (1975).

[13] G. Wheeler, Alkoxysilanes and the Consolidation of Stone, 2005. http://www.jstor.org/stable/40025051.

[14] A.P.F. Pinto, J.D. Rodrigues, Stone consolidation: The role of treatment procedures, J. Cult. Herit. 9 (2008) 38–53. doi:10.1016/j.culher.2007.06.004.

[15] Favaro Monica, F. Ossola, P. Tomasin, P.A. Vigato, G.L. Rossetto, N. El Habra, M. Casarin, A novel approach to compatible and durable consolidation of limestone, in: J.W. Łukascewicz, P. Niemcewicz (Eds.), 11th Int. Congr. Deterior. Conserv. Stone, 15-20 Sept. 2008, Torun, Pol. Proc. Vol. 2, Uniwersytetu Mikołaja Kopernika, 2008: pp. 865–872.

[16] L. Maiore, M.C. Aragoni, G. Carcangiu, O. Cocco, F. Isaia, V. Lippolis, P. Meloni, A. Murru, A.M.Z. Slawin, E. Tuveri, J.D. Woollins, M. Arca, Oxamate salts as novel agents for the restoration of marble and limestone substrates: case study of ammonium N-phenyloxamate, New J. Chem. 40 (2016) 2768–2774. doi:10.1039/C5NJ02505B.

[17] L. Maiore, M.C. Aragoni, G. Carcangiu, O. Cocco, F. Isaia, V. Lippolis, P. Meloni, A. Murru, E. Tuveri, M. Arca, Synthesis, characterization and DFT-modeling of novel agents for the protection and restoration of historical calcareous stone substrates, J. Colloid Interface Sci. 448 (2015) 320–330. doi:10.1016/j.jcis.2015.01.092.

[18]   J. Correia, F. Matero, Calcium Tartrate Tetrahydrate Preconsolidation of Salt-Contaminated Limestone at Mission San José Y San Miguel De Aguayo, J. Am. Inst. Conserv. 47 (2008) 81–95. doi:10.1179/019713608806112160.

[19]   M. Matteini, F. Paccagnella, A. Pinetti, P. Zannini, Study and synthesis of organic precursors for salt treatments developed to protect and strengthen building materials and "frescos," J. Cult. Herit. 6 (2005) 235–243. doi:10.1016/J.CULHER.2005.02.003.

[20]   R.-M. Ion, D. Turcanu-Caruțiu, R.-C. Fierăscu, I. Fierăscu, Chalk Stone restoration with hydroxiapatite-based nanoparticles, Sci. Bull. VALAHIA Univ. – Mater. Mech. 9 (2014) 1–4.

[21]   E. Sassoni, E. D'Amen, N. Roveri, G.W. Scherer, E. Franzoni, Photocatalytic hydroxyapatite-titania nanocomposites for preventive conservation of marble, in: IOP Conf. Ser. Mater. Sci. Eng., 2018: p. 12073. doi:10.1088/1757-899X/364/1/012073.

[22]   E. Sassoni, E. D'Amen, N. Roveri, G.W. Scherer, E. Franzoni, Durable self-cleaning coatings for architectural surfaces by incorporation of TiO2 nano-particles into hydroxyapatite films, Materials (Basel). 11 (2018) 1–16. doi:10.3390/ma11020177.

[23]   M. Matteini, S. Rescic, F. Fratini, G. Botticelli, Ammonium Phosphates as Consolidating Agents for Carbonatic Stone Materials Used in Architecture and Cultural Heritage: Preliminary Research, Int. J. Archit. Herit. Conserv. Anal. Restor. 5 (2011) 717–736. doi:10.1080/15583058.2010.495445.

[24]   E. Sassoni, S. Naidu, G.W. Scherer, The use of hydroxyapatite as a new inorganic consolidant for damaged carbonate stones, J. Cult. Herit. 12 (2011) 346–355. doi:10.1016/j.culher.2011.02.005.

[25]   P. Maravelaki-Kalaitzaki, Black crusts and patinas on Pentelic marble from the Parthenon and Erechtheum (Acropolis, Athens): characterization and origin, Anal. Chim. Acta. 532 (2005) 187–198. doi:10.1016/j.aca.2004.10.065.

[26]   J. Martín-Gil, F.J. Martín-Gil, M. del Carmen Ramos-Sánchez, P. Martín-Ramos, The orange-brown patina of Salisbury Cathedral (West Porch) surfaces: evidence of its man-made origin., Environ. Sci. Pollut. Res. Int. 12 (2005) 285–9. doi:10.1065/espr2005.05.257.

[27]   K. Polikreti, Y. Maniatis, Micromorphology, composition and origin of the orange patina on the marble surfaces of Propylaea (Acropolis, Athens)., Sci. Total Environ. 308 (2003) 111–9. doi:10.1016/S0048-9697(02)00613-7.

[28]   O. Salvadori, M. Realini, Characterization of biogenic oxalate films, in: EDITEAM (Ed.), Int. Symp. Oxalate Film. Conserv. Work. Art, Milan, March 25-27, Milano, 1996: pp. 335–351.

[29]   C. Vázquez-Calvo, M. Álvarez De Buergo, R. Fort, A. De Los Rios, Detection of calcium phosphates in calcium oxalate patinas, Eur. J. Mineral. 24 (2012) 1031–1045. doi:10.1127/0935-1221/2012/0024-2240.

[30]   C. Vazquez-Calvo, M. Alvarez de Buergo, R. Fort, Overview of recent knowledge of patinas on stone monuments: the Spanish experience, Geol. Soc. London, Spec. Publ. 271 (2007) 295–307. doi:10.1144/GSL.SP.2007.271.01.28.

[31]   E. Possenti, C. Colombo, D. Bersani, M. Bertasa, A. Botteon, C. Conti, P.P. Lottici, M. Realini, New insight on the interaction of diammonium hydrogenphosphate conservation treatment with carbonatic substrates: A multi-analytical approach, Microchem. J. 127 (2016) 79–86. doi:10.1016/j.microc.2016.02.008.

[32]   A. Kasioptas, C. Perdikouri, C. V. Putnis, A. Putnis, Pseudomorphic replacement of single calcium carbonate crystals by polycrystalline apatite, Mineral. Mag. 72 (2008) 77–80. doi:10.1180/minmag.2008.072.1.77.

[33]   E. Molina, L. Rueda-Quero, D. Benavente, A. Burgos-Cara, E. Ruiz-Agudo, G. Cultrone, Gypsum crust as a source of calcium for the consolidation of carbonate stones using a calcium phosphate-based consolidant, Constr. Build. Mater. 143 (2017) 298–311. doi:10.1016/j.conbuildmat.2017.03.155.

[34]   E.M. Piernas, L.R. Quero, G. Cultrone, E.R. Agudo, A new use of hydroxyapatite-based

consolidant : cleaning and consolidation of stones in one step by reaction with gypsum crust, in: Geophys. Res. Abstr., 2015.

[35] F. Yang, Y. Liu, G. Zuo, X. Wang, P. Hua, Q. Ma, G. Dong, Y. Yue, B. Zhang, Hydroxyapatite conversion layer for the preservation of surface gypsification marble relics, Corros. Sci. 88 (2014) 6–9. doi:10.1016/j.corsci.2014.07.003.

[36] E. Sassoni, G. Graziani, E. Franzoni, G.W. Scherer, Conservation of marble artifacts by phosphate treatments : influence of gypsum contamination, in: 4th Int. Conf. Salt Weather. Build. Stone Sculpt., Potsdan, 2017: pp. 143–149. doi:10.5165/hawk-hhg/331.

[37] R. Snethlage, C. Gruber, V. Tuci, W. Wendler, Transforming gypsum into calcium phosphate: A better way to preserve lime paint layers on natural stone?, in: J. Delgado, R. and J.M. Mimoso (Eds.), Stone Consol. Cult. Herit. Res. Pract. Proc. Int. Symp. Lisbon, 6–7 May, 2008, Lisbon, 2008: pp. 1–14.

[38] G. Botticelli, D. Carson, G. Chiari, F. Fratini, M. Matteini, Ammonium phosphate based treatment: an innovative mineral-inorganic approach for the consolidation of mural paintings. Pilot tests and scientific investigation, in: Opera Primaziale Pisana (Ed.), ICOM CC Interim Meet., Pisa, 2010.

[39] M. Balonis-Sant, X. Ma, I. Kakoulli, Preliminary Results on Biomimetic Methods Based on Soluble Ammonium Phosphate Precursors for the Consolidation of Archaeological Wall Paintings, in: ACS Symp. Ser., 2013: pp. 419–447. doi:10.1021/bk-2013-1147.ch022.

[40] E. Sassoni, G. Graziani, G.W. Scherer, E. Franzoni, Preliminary study on the use of ammonium phosphate for the conservation of marble-imitating gypsum-stuccoes, in: 4th Hist. Mortars Conf., 2016: pp. 391–398.

[41] E. Sassoni, G. Graziani, E. Franzoni, G.W. Scherer, Conversion of calcium sulfate dihydrate into calcium phosphates as a route for conservation of gypsum stuccoes and sulfated marble, Constr. Build. Mater. 170 (2018) 290–301. doi:10.1016/j.conbuildmat.2018.03.075.

[42] A.E. North, Biomimetic hydroxyapatite as a new consolidating agent for archaeological bone, University of California, 2014.

[43] F. Yang, D. He, Y. Liu, N. Li, Z. Wang, Q. Ma, G. Dong, Conservation of bone relics using hydroxyapatite as protective material, Appl. Phys. A. 122 (2016) 479. doi:10.1007/s00339-016-0015-x.

[44] E. Sassoni, G. Graziani, E. Franzoni, An innovative phosphate-based consolidant for limestone. Part 1: Effectiveness and compatibility in comparison with ethyl silicate, Constr. Build. Mater. 102 (2016) 918–930. doi:10.1016/j.conbuildmat.2015.10.202.

[45] E. Sassoni, G. Graziani, E. Franzoni, An innovative phosphate-based consolidant for limestone. Part 2: Durability in comparison with ethyl silicate, Constr. Build. Mater. 102 (2016) 931–942. doi:10.1016/j.conbuildmat.2015.10.202.

[46] E. Sassoni, E. Franzoni, B. Pigino, G.W. Scherer, S. Naidu, Consolidation of calcareous and siliceous sandstones by hydroxyapatite: Comparison with a TEOS-based consolidant, J. Cult. Herit. 14 (2013) e103–e108. doi:10.1016/j.culher.2012.11.029.

[47] E. Franzoni, E. Sassoni, G. Graziani, Brushing, poultice or immersion? The role of the application technique on the performance of a novel hydroxyapatite-based consolidating treatment for limestone, J. Cult. Herit. 16 (2015) 173–184. doi:10.1016/j.culher.2014.05.009.

[48] G. Graziani, E. Sassoni, E. Franzoni, Consolidation of porous carbonate stones by an innovative phosphate treatment: mechanical strengthening and physical-microstructural compatibility in comparison with TEOS-based treatments, Herit. Sci. 3 (2015) 1. doi:10.1186/s40494-014-0031-0.

[49] E. Sassoni, E. Franzoni, Consolidation of Carrara Marble by Hydroxyapatite and Behaviour After Thermal Ageing, in: L. Toniolo, M. Boriani, G. Guidi (Eds.), Built Herit. Monit. Conserv. Manag., Springer International Publishing, Cham, 2015: pp. 379–389. doi:10.1007/978-3-319-08533-3.

[50] M. Matteini, C. Colombo, G. Botticelli, M. Casati, C. Conti, R. Negrotti, M. Realini, E. Possenti, Ammonium phosphates to consolidate carbonatic stone materials: an inorganic-mineral treatment greatly promising, in: Built Herit. 2013 Monit. Conserv. Manag., 2013: pp. 1278–1286.

[51] G. Graziani, E. Sassoni, G.W. Scherer, E. Franzoni, Phosphate-based treatments for consolidation of salt-bearing Globigerina limestone, in: IOP Conf. Ser. Mater. Sci. Eng., 2018: p. 12082. doi:10.1088/1757-899X/364/1/012082.

[52] E. Molina, C. Fiol, G. Cultrone, Assessment of the efficacy of ethyl silicate and dibasic ammonium phosphate consolidants in improving the durability of two building sandstones from Andalusia (Spain), Environ. Earth Sci. 77 (2018) 302. doi:10.1007/s12665-018-7491-6.

[53] F. Yang, Y. Liu, Artificial hydroxyapatite film for the conservation of outdoor marble artworks, Mater. Lett. 124 (2014) 201–203. doi:10.1016/j.matlet.2014.03.081.

[54] E. Sassoni, G. Graziani, E. Franzoni, Repair of sugaring marble by ammonium phosphate: Comparison with ethyl silicate and ammonium oxalate and pilot application to historic artifact, Mater. Des. 88 (2015) 1145–1157. doi:10.1016/j.matdes.2015.09.101.

[55] G. Graziani, E. Sassoni, E. Franzoni, G.W. Scherer, Hydroxyapatite coatings for marble protection: Optimization of calcite covering and acid resistance, Appl. Surf. Sci. 368 (2016) 241–257. doi:10.1016/j.apsusc.2016.01.202.

[56] S. Naidu, G.W. Scherer, Nucleation, growth and evolution of calcium phosphate films on calcite, J. Colloid Interface Sci. 435 (2014) 128–137. doi:10.1016/j.jcis.2014.08.018.

[57] E. Sassoni, G. Graziani, E. Franzoni, G.W. Scherer, New insights on protective treatments for marble by FIB-SEM, in: IOP Conf. Ser. Mater. Sci. Eng., 2018: p. 12092. doi:10.1088/1757-899X/364/1/012092.

[58] E. Sassoni, G. Graziani, E. Franzoni, G.W. Scherer, Calcium phosphate coatings for marble conservation: Influence of ethanol and isopropanol addition to the precipitation medium on the coating microstructure and performance, Corros. Sci. 136 (2018) 255–267. doi:10.1016/j.corsci.2018.03.019.

[59] E. Sassoni, Phosphate-based treatments for conservation of stone, RILEM Tech. Lett. 2 (2017) 14. doi:10.21809/rilemtechlett.2017.34.

[60] E. Sassoni, Hydroxyapatite and Other Calcium Phosphates for the Conservation of Cultural Heritage: A Review, Materials (Basel). 11 (2018) 557. doi:10.3390/ma11040557.

[61] E. Possenti, C. Colombo, C. Conti, L. Gigli, M. Merlini, J.R. Plaisier, M. Realini, D. Sali, G.D. Gatta, Diammonium hydrogenphosphate for the consolidation of building materials. Investigation of newly-formed calcium phosphates, Constr. Build. Mater. 195 (2019) 557–563. doi:10.1016/j.conbuildmat.2018.11.077.

[62] A.P.F. Pinto, J.D. Rodrigues, Consolidation of carbonate stones: Influence of treatment procedures on the strengthening action of consolidants, J. Cult. Herit. 13 (2012) 154–166. doi:10.1016/j.culher.2011.07.003.

[63] M. Ni, B.D. Ratner, Nacre surface transformation to hydroxyapatite in a phosphate buffer solution., Biomaterials. 24 (2003) 4323–31. doi:10.1016/S0142-9612(03)00236-9.

[64] L. Wang, G.H. Nancollas, Calcium Orthophosphates: Crystallization and Dissolution, Chem. Rev. 108 (2008) 4628–4669. doi:10.1021/cr0782574.Calcium.

[65] S. V. Dorozhkin, Calcium orthophosphates, J. Mater. Sci. 42 (2007) 1061–1095. doi:10.1007/s10853-006-1467-8.

[66] M. Kamiya, J. Hatta, E. Shimada, Y. Ikuma, M. Yoshimura, H. Monma, AFM analysis of initial stage of reaction between calcite and phosphate, Mater. Sci. Eng. B. 111 (2004) 226–231. doi:10.1016/j.mseb.2004.05.007.

[67] I.A. Karampas, C.G. Kontoyannis, Characterization of calcium phosphates mixtures, Vib. Spectrosc. 64 (2013) 126–133. doi:10.1016/j.vibspec.2012.11.003.

[68] C. Drouet, Apatite formation: Why it may not work as planned, and how to conclusively

identify apatite compounds, Biomed Res. Int. 2013 (2013) 1–12. doi:10.1155/2013/490946.

[69] G. Graziani, E. Sassoni, G.W. Scherer, E. Franzoni, Penetration depth and redistribution of an aqueous ammonium phosphate solution used for porous limestone consolidation by brushing and immersion, Constr. Build. Mater. 148 (2017) 571–578. doi:10.1016/j.conbuildmat.2017.05.097.

[70] J.O. Nriagu, P.B. Moore, eds., Photosphate Minerals, Springer Berlin Heidelberg, Berlin, Heidelberg, 1984. doi:10.1007/978-3-642-61736-2.

[71] S. V. Dorozhkin, Calcium Orthophosphates in Nature, Biology and Medicine, Materials (Basel). 2 (2009) 399–498. doi:10.3390/ma2020399.

[72] C. Cipriani, C. Garavelli, Cristallografia chimica e mineralogia speciale, Firenze, 1987.

[73] E. Grill, Minerali industriali e minerali delle rocce, Milano, 1963.

[74] F. Liebau, S. Koritnig, Phosphorous, Part 15A, in: W. KH (Ed.), Handb. Geochemistry, Springer Berlin Heidelberg New York, 1970.

[75] S. Koutsopoulos, Synthesis and characterization of hydroxyapatite crystals: a review study on the analytical methods., J. Biomed. Mater. Res. 62 (2002) 600–12. doi:10.1002/jbm.10280.

[76] S. V. Dorozhkin, Calcium orthophosphates: occurrence, properties, biomineralization, pathological calcification and biomimetic applications., Biomatter. 1 (2011) 121–64. doi:10.4161/biom.18790.

[77] M.S.A. Johnsson, G.H. Nancollas, The role of brushite and octacalcium phosphate in apatite formation., Crit. Rev. Oral Biol. Med. 3 (1992) 61–82. http://www.ncbi.nlm.nih.gov/pubmed/1730071 (accessed January 22, 2018).

[78] J.C. Elliott, General Chemistry of the Calcium Orthophosphates, in: Struct. Chem. Apatites Other Calcium Orthophosphates, 1994: pp. 1–62. doi:10.1016/B978-0-444-81582-8.50006-7.

[79] J.C. Elliott, P.E. Mackie, R.A. Young, Monoclinic Hydroxyapatite, Science (80-.). 180 (1973) 1055–1057. doi:10.1126/science.180.4090.1055.

[80] A.S. Posner, A. Perloff, A.F. Diorio, Refinement of the hydroxyapatite structure, Acta Crystallogr. 11 (1958) 308–309. doi:10.1107/S0365110X58000815.

[81] M.I. Kay, R.A. Young, A.S. Posner, Crystal Structure of Hydroxyapatite, Nature. 204 (1964) 1050–1052. doi:10.1038/2041050a0.

[82] L.M. Rodríguez-Lorenzo, Studies on calcium deficient apatites structure by means of MAS-NMR spectroscopy, J. Mater. Sci. Mater. Med. 16 (2005) 393–398. doi:10.1007/s10856-005-6977-4.

[83] J.C. Elliott, Hydroxyapatite and Nonstoichiometric Apatites, in: Struct. Chem. Apatites Other Calcium Orthophosphates, 1994: pp. 111–189. doi:10.1016/B978-0-444-81582-8.50008-0.

[84] T.I. Ivanova, O. V. Frank-Kamenetskaya, A.B. Kol'tsov, V.L. Ugolkov, Crystal structure of calcium-deficient carbonated hydroxyapatite. Thermal decomposition, J. Solid State Chem. 160 (2001) 340–349. doi:10.1006/jssc.2000.9238.

[85] C. Rey, C. Combes, C. Drouet, H. Sfihi, Chemical Diversity of Apatites, Adv. Sci. Technol. 49 (2006) 27–36. doi:10.4028/www.scientific.net/AST.49.27.

[86] D. Zahn, O. Hochrein, On the composition and atomic arrangement of calcium-deficient hydroxyapatite: An ab-initio analysis, J. Solid State Chem. 181 (2008) 1712–1716. doi:10.1016/j.jssc.2008.03.035.

[87] P.W. Brown, R.I. Martin, An Analysis of Hydroxyapatite Surface Layer Formation, J. Phys. Chem. B. 103 (1999) 1671–1675. doi:10.1021/jp982554i.

[88] H.H. Zhou, H. Li, L.H. Guo, Molecular and Crystal Structure Characterization of Calcium-Deficient Apatite, Key Eng. Mater. 330–332 (2007) 119–122. doi:10.4028/www.scientific.net/KEM.330-332.119.

[89] D.W. Jones, J.A.S. Smith, 268. The structure of brushite, $CaHPO_4, 2H_2O$, J. Chem. Soc. (1962) 1414. doi:10.1039/jr9620001414.

[90] C.A. Beevers, The crystal structure of dicalcium phosphate dihydrate, $CaHPO_4 .2H_2O$, Acta

Crystallogr. 11 (1958) 273–277. doi:10.1107/S0365110X58000670.

[91]   M. Catti, G. Ferraris, A. Filhol, Hydrogen bonding in the crystalline state. CaHPO4 (monetite), P1 or P1? A novel neutron diffraction study, Acta Crystallogr. Sect. B Struct. Crystallogr. Cryst. Chem. 33 (1977) 1223–1229. doi:10.1107/S0567740877005706.

[92]   B. Dickens, J.S. Bowen, W.E. Brown, A refinement of the crystal structure of CaHPO4 (synthetic monetite), Acta Crystallogr. Sect. B Struct. Crystallogr. Cryst. Chem. 28 (1972) 797–806. doi:10.1107/S056774087200322X.

[93]   W.E. Brown, J.P. Smith, J.R. Lehr, W.A. Frazier, Octacalcium Phosphate and Hydroxyapatite: Crystallographic and Chemical Relations between Octacalcium Phosphate and Hydroxyapatite, Nature. 196 (1962) 1050–1055. doi:10.1038/1961050a0.

[94]   M. Mathew, W.E. Brown, L.W. Schroeder, B. Dickens, Crystal structure of octacalcium bis(hydrogenphosphate) tetrakis(phosphate)pentahydrate, Ca8(HP04)2(PO4)4.5H2O, J. Crystallogr. Spectrosc. Res. 18 (1988) 235–250. doi:10.1007/BF01194315.

[95]   W.E. Brown, J.R. Lehr, J.P. Smith, W.A. Frazier, Crystallography of octacalcium phosphate, J. Am. Chem. Soc. 79 (1957) 5318–5319. doi:10.1021/ja01576a068.

[96]   W.E. Brown, L.W. Schroeder, J.S. Ferris, Interlayering of crystalline octacalcium phosphate and hydroxylapatite, J. Phys. Chem. 83 (1979) 1385–1388. doi:10.1021/j100474a006.

[97]   G.H. Nancollas, ed., Biological Mineralization and Demineralization, Springer Berlin Heidelberg, Berlin, Heidelberg, 1982. doi:10.1007/978-3-642-68574-3.

[98]   W.E. Brown, N. Eidelman, B. Tomazic, Octacalcium phosphate as a precursor in biomineral formation., Adv. Dent. Res. 1 (1987) 306–313. doi:10.1177/08959374870010022201.

[99]   B. Dickens, L.W. Schroeder, W.E. Brown, Crystallographic studies of the role of Mg as a stabilizing impurity in β-Ca3(PO4)2. The crystal structure of pure β-Ca3(PO4)2, J. Solid State Chem. 10 (1974) 232–248. doi:10.1016/0022-4596(74)90030-9.

[100]   S. V. Dorozhkin, Amorphous calcium (ortho)phosphates, Acta Biomater. 6 (2010) 4457–4475. doi:10.1016/j.actbio.2010.06.031.

[101]   R.Z. LeGeros, Preparation of octacalcium phosphate (OCP): A direct fast method, Calcif. Tissue Int. 37 (1985) 194–197. doi:10.1007/BF02554841.

[102]   D. Pittaluga, F. Fratini, A. Nielsen, S. Rescic, Industrial archaeological sites and architectonic remains: the problem of consolidation in humid areas, in: Arcadia Ricerche (Ed.), Sci. E Beni Cult. XXVIII, 2012: pp. 303–312.

[103]   J. Rouquerol, D. Avnir, C.W. Fairbridge, D.H. Everett, J.M. Haynes, N. Pernicone, J.D.F. Ramsay, K.S.W. Sing, K.K. Unger, Recommendations for the characterization of porous solids (Technical Report), Pure Appl. Chem. 66 (1994) 1739–1758. doi:10.1351/pac199466081739.

[104]   K.S.W. et al. Sing, Reporting physisorption data for gas/solid systems with special reference to the determination of surface area and porosity (Recommendations 1984), Pure Appl. Chem. 57 (1985) 603–619. doi:10.1351/pac198557040603.

[105]   H.M. Rietveld, A profile refinement method for nuclear and magnetic structures, J. Appl. Crystallogr. 2 (1969) 65–71. doi:10.1107/S0021889869006558.

[106]   H.M. Rietveld, The Rietveld method, Phys. Scr. 89 (2014) 98002. doi:10.1088/0031-8949/89/9/098002.

[107]   A. Lausi, M. Polentarutti, S. Onesti, J.R. Plaisier, E. Busetto, G. Bais, L. Barba, A. Cassetta, G. Campi, D. Lamba, A. Pifferi, S.C. Mande, D.D. Sarma, S.M. Sharma, G. Paolucci, Status of the crystallography beamlines at Elettra, Eur. Phys. J. Plus. 130 (2015) 43. doi:10.1140/epjp/i2015-15043-3.

[108]   L. Rebuffi, J.R. Plaisier, M. Abdellatief, A. Lausi, P. Scardi, MCX: a Synchrotron Radiation Beamline for X-ray Diffraction Line Profile Analysis, Zeitschrift Für Anorg. Und Allg. Chemie. 640 (2014) 3100–3106. doi:10.1002/zaac.201400163.

[109]   J.R. Plaisier, L. Nodari, L. Gigli, E. Paz, R. San, R. Bertoncello, A. Lausi, The X-ray diffraction beamline MCX at Elettra : a case study of non-destructive analysis on stained glass, ACTA

IMEKO. 6 (2017) 71–75.

[110] M. Merlini, M. Hanfland, Single-crystal diffraction at megabar conditions by synchrotron radiation, High Press. Res. 33 (2013) 511–522. doi:10.1080/08957959.2013.831088.

[111] A. Abrami, F. Arfelli, R.C. Barroso, A. Bergamaschi, F. Billé, P. Bregant, F. Brizzi, K. Casarin, E. Castelli, V. Chenda, L. Dalla Palma, D. Dreossi, C. Fava, R. Longo, L. Mancini, R.H. Menk, F. Montanari, A. Olivo, S. Pani, A. Pillon, E. Quai, S. Ren Kaiser, L. Rigon, T. Rokvic, M. Tonutti, G. Tromba, A. Vascotto, C. Venanzi, F. Zanconati, A. Zanetti, F. Zanini, Medical applications of synchrotron radiation at the SYRMEP beamline of ELETTRA, Nucl. Instruments Methods Phys. Res. Sect. A Accel. Spectrometers, Detect. Assoc. Equip. 548 (2005) 221–227. doi:10.1016/j.nima.2005.03.093.

[112] G. Tromba, R. Longo, A. Abrami, F. Arfelli, A. Astolfo, P. Bregant, F. Brun, K. Casarin, V. Chenda, D. Dreossi, M. Hola, J. Kaiser, L. Mancini, R.H. Menk, E. Quai, E. Quaia, L. Rigon, T. Rokvic, N. Sodini, D. Sanabor, E. Schultke, M. Tonutti, A. Vascotto, F. Zanconati, M. Cova, E. Castelli, K.K.W. Siu, The SYRMEP Beamline of Elettra: Clinical Mammography and Bio-medical Applications, in: K.K.W.Siu (Ed.), 6th Int. Conf. Med. Appl. Synchrotron Radiat., 2010: pp. 18–23. doi:10.1063/1.3478190.

[113] E. Larsson, Quantitative Analysis of Bone Tissue Engineering Scaffolds and Skull Bones by means of Synchrotron and Conventional X-ray Computed Microtomography Quantitative Analysis of Bone Tissue Engineering Scaffolds and Skull Bones by means of Synchrotron and Conve, Link¨oping University, 2010.

[114] M. Parisatto, A. Turina, G. Cruciani, L. Mancini, L. Peruzzo, B. Cesare, Three-dimensional distribution of primary melt inclusions in garnets by X-ray microtomography, Am. Mineral. 103 (2018) 911–926. doi:10.2138/am-2018-6216CCBYNCND.

[115] N. Marinoni, M. Voltolini, M.A.T.M. Broekmans, L. Mancini, P.J.M. Monteiro, N. Rotiroti, E. Ferrari, A. Bernasconi, A combined synchrotron radiation micro computed tomography and micro X-ray diffraction study on deleterious alkali-silica reaction, J. Mater. Sci. 50 (2015) 7985–7997. doi:10.1007/s10853-015-9364-7.

[116] F. Brun, L. Massimi, M. Fratini, D. Dreossi, F. Billé, A. Accardo, R. Pugliese, A. Cedola, SYRMEP Tomo Project: a graphical user interface for customizing CT reconstruction workflows, Adv. Struct. Chem. Imaging. 3 (2017) 4. doi:10.1186/s40679-016-0036-8.

[117] M.D. Abramoff, P.J. Magalhães, S.J. Ram, Image processing with ImageJ, Biophotonics Int. 11 (2004) 36–42.

[118] J. Schindelin, I. Arganda-Carreras, E. Frise, V. Kaynig, M. Longair, T. Pietzsch, S. Preibisch, C. Rueden, S. Saalfeld, B. Schmid, J.-Y. Tinevez, D.J. White, V. Hartenstein, K. Eliceiri, P. Tomancak, A. Cardona, Fiji: an open-source platform for biological-image analysis, Nat. Methods. 9 (2012) 676–682. doi:10.1038/nmeth.2019.

[119] F. Brun, L. Mancini, P. Kasae, S. Favretto, D. Dreossi, G. Tromba, Pore3D: A software library for quantitative analysis of porous media, Nucl. Instruments Methods Phys. Res. Sect. A Accel. Spectrometers, Detect. Assoc. Equip. 615 (2010) 326–332. doi:10.1016/j.nima.2010.02.063.

[120] UNE-EN 15886:2011 Conservation of cultural property - Test methods - Colour measurement of surfaces, (2011).

[121] Commisione Tecnica UNI, UNI 11432:2011. Beni culturali Materiali lapidei naturali ed artificiali - Misura della capacita di assorbimento di acqua mediante spugna di contatto., (2011).

[122] D. Vandevoorde, M. Pamplona, O. Schalm, Y. Vanhellemont, V. Cnudde, E. Verhaeven, Contact sponge method: Performance of a promising tool for measuring the initial water absorption, J. Cult. Herit. 10 (2009) 41–47. doi:10.1016/j.culher.2008.10.002.

[123] Commisione Tecnica UNI, UNI EN 15801:2010 Conservation of cultural property – test methods – determination of water absorption by capillarity, (2010).

[124] R. Peruzzi, T. Poli, L. Toniolo, The experimental test for the evaluation of protective treatments: a critical survey of the "capillary absorption index," J. Cult. Herit. 4 (2003) 251–

254. doi:10.1016/S1296-2074(03)00050-5.

[125] D.B. Honeyborne, Weathering and decay of masonry, in: J. Ashurst, F.G. Dimes (Eds.), Conserv. Build. Decor. Stone, Vol. 1, Butterworth-Heinemann, London, 1990: pp. 153–184.

[126] B.M. Feilden, Conservation of Historic Buildings, 3rd ed., Architectural Press, Oxford, 2003.

[127] G. Grassegger, Decay mechanisms of natural building stones on monuments: A review of the latest theories, in: C.U. Große (Ed.), Werkstoffe Und Werkstoffprüfung Im Bauwes. Festschrift Zum, 1999: pp. 54–81.

[128] B.J. Smith, M. Gómez-Heras, S. McCabe, Understanding the decay of stone-built cultural heritage, Prog. Phys. Geogr. Earth Environ. 32 (2008) 439–461.

[129] A.E. Charola, R. Ware, Acid deposition and the deterioration of stone: a brief review of a broad topic, in: S. Siegesmund, T. Weiss, A. Vollbrecht (Eds.), Nat. Stone, Weather. Phenomena, Conserv. Strateg. Case Stud., Geological Society Special Publication, 2002: pp. 395–406. doi:10.1144/GSL.SP.2002.205.01.28.

[130] P.A. Baedecker, M.M. Reddy, The Erosion of Carbonate Stone by Acid Rain: Laboratory and Field Investigations, J. Chem. Educ. 70 (1993) 104–108. doi:10.1021/ed070p104.

[131] G. Barone, V. Crupi, F. Longo, D. Majolino, P. Mazzoleni, S. Raneri, J. Teixeira, V. Venuti, Neutron radiography for the characterization of porous structure in degraded building stones, J. Instrum. 9 (2014). doi:10.1088/1748-0221/9/05/C05024.

[132] A. Miquel, P. Bromblet, V. Vergès-Belmin, L. Binda, G. Baronio, E. De Witte, H. De Clercq, R. Van Hees, H. Brocken, Experimental study on the compatibility of a polysiloxane treatment with substrates loaded with sodium sulphate: Influence of the physical properties of the substrates on the salt content limit., Restor. Build. Monum. An Int. J. 8 (2002) 271–291.

[133] R. Carlos, E. Doehne, Salt weathering: Influence of evaporation rate, supersaturation and crystallization pattern, Earth Surf. Process. Landforms. 24 (1999) 191–209.

[134] E. Cantisani, F. Fratini, P. Malesani, G. Molli, Mineralogical and petrophysical characterisation of white Apuan marble, Period. Di Mineral. 74 (2005) 117–140.

[135] C. Baroni, A. Ribolini, G. Bruschi, P. Mannucci, Geomorphological map and raised-relief model of the Carrara marble basins, Tuscany, Italy, Geogr. Fis. E Din. Quat. 33 (2010) 233–243.

[136] M. Coli, G. Grandini, L. Matteini, Il bacino marmifero di Orto di Donna - Alpi Apuane, Firenze, 1988.

[137] S. Siegesmund, K. Ullemeyer, T. Weiss, E.K. Tschegg, Physical weathering of marbles caused by anisotropic thermal expansion, Int. J. Earth Sci. 89 (2000) 170–182. doi:10.1007/s005310050324.

[138] A. Luque, E. Ruiz-Agudo, G. Cultrone, E. Sebastián, S. Siegesmund, Direct observation of microcrack development in marble caused by thermal weathering, Environ. Earth Sci. 62 (2011) 1375–1386. doi:10.1007/s12665-010-0624-1.

[139] E. Sassoni, E. Franzoni, Influence of porosity on artificial deterioration of marble and limestone by heating, Appl. Phys. A. 115 (2014) 809–816. doi:10.1007/s00339-013-7863-4.

[140] E. Franzoni, E. Sassoni, Comparison Between Different Methodologies for Artificial Deterioration of Stone Aimed at Consolidation Testing, in: 12th Int. Congr. Deterior. Conserv. Stone, New York, 2012: pp. 1–10. http://iscs.icomos.org/pdf-files/NewYorkConf/fransass.pdf.

[141] E. Sassoni, E. Franzoni, Evaluation of hydroxyapatite effects in marble consolidation and behaviour towards thermal weathering, in: Built Herit. 2013 Monit. Conserv. Manag., 2013: pp. 1287–1295.

[142] E. Franzoni, E. Sassoni, G.W. Scherer, S. Naidu, Artificial weathering of stone by heating, J. Cult. Herit. 14 (2013) e85–e93. doi:10.1016/j.culher.2012.11.026.

[143] M.F. La Russa, G. Barone, C.M. Belfiore, P. Mazzoleni, A. Pezzino, Application of protective products to "Noto" calcarenite (south-eastern Sicily): a case study for the conservation of stone materials, Environ. Earth Sci. 62 (2011) 1263–1272. doi:10.1007/s12665-010-0614-3.

[144] M. Rigo, F. Barbieri, Stratigrafia pratica applicata in Sicilia, Boll. Serv. Geol. d'Italia. 80 (1959) 351–441.

[145] A. Di Grande, M. Romeo, W. Raimondo, Il Membro di Gaetanì ed il Membro di Buscemi della Formazione Palazzolo: Facies, distribuzione ed età, Boll. Della Soc. Geol. Ital. 101 (1982) 343–372.

[146] S. Carbone, M. Grasso, F. Lentini, Lineamenti geologici del plateau Ibleo (Sicilia S.E.): presentazione delle carte geologiche della Sicilia Sud-Orientale, Mem. Della Soc. Geol. Ital. 38 (1987) 127–135.

[147] M. Romeo, F. Sciuto, Stratigrafia micropaleontologica delle successioni mioceniche dell'Alta Valle dei Fiume Tellaro (Sicilia Sud-orientale), Mem. Della Soc. Geol. Ital. 38 (1987) 137–154.

[148] L. Anania, A. Badalà, G. Barone, C.M. Belfiore, C. Calabrò, M.F. La Russa, P. Mazzoleni, A. Pezzino, The stones in monumental masonry buildings of the "Val di Noto" area: New data on the relationships between petrographic characters and physical–mechanical properties, Constr. Build. Mater. 33 (2012) 122–132. doi:10.1016/j.conbuildmat.2011.12.076.

[149] G. Barbera, G. Barone, V. Crupi, F. Longo, G. Maisano, D. Majolino, P. Mazzoleni, S. Raneri, J. Teixeira, V. Venuti, A multi-technique approach for the determination of the porous structure of building stone, Eur. J. Mineral. 26 (2014) 189–198. doi:10.1127/0935-1221/2014/0026-2355.

[150] G. Alessandrini, A. Bocci, R. Bugini, D. Emmi, R. Peruzzi, M. Realini, Stone materials of Noto (Siracusa) and their decay, in: 7th Int. Congr. Deterior. Conserv. Stone, 1993: pp. 11–20.

[151] C. Urzì, M. Realini, Colour changes of Notos calcareous sandstone as related to its colonisation by microorganisms, Int. Biodeterior. Biodegradation. 42 (1998) 45–54. doi:10.1016/S0964-8305(98)00045-6.

[152] A. Cavallo, B. Bigioggero, A. Colombo, A. Tunesi, The Verbano Cusio Ossola province: A land of quarries in northern Italy (Piedmont), Period. Di Mineral. 73 (2004) 197–210.

[153] G. Alessandrini, R. Bugini, R. Peruzzi, I materiali lapidei impiegati nei monumenti lombardi e i loro problemi di conservazione, in: Mater. Lapidei, 1987: pp. 145–156.

[154] G. Alessandrini, Le pietre del monumento, in: A. Pizzi (Ed.), La Ca' Gd. Di Milano. L'intervento Conserv. Sul Cortile Richiniano, Milano, 1993: pp. 173–203.

[155] G. Alessandrini, Lo stato di conservazione dei materiali lapidei: morfologia e cause di degrado, in: A. Pizzi (Ed.), La Ca' Gd. Di Milano. L'intervento Conserv. Sul Cortile Richiniano, 1993: pp. 219–239.

[156] V. Riganti, R. Rosetti, F. Soggetti, F. Veniale, U. Zezza, Alterazione e protezione delle pietre dei monumenti storici dell'Università di Pavia, Pavia, 1978.

[157] D. Gulotta, M. Bertoldi, S. Bortolotto, P. Fermo, A. Piazzalunga, L. Toniolo, The Angera stone. A challenging conservation issue in the polluted environment of Milan (Italy), Environ. Earth Sci. 69 (2013) 1085–1094. doi:10.1007/s12665-012-2165-2.

[158] B.O. Fowler, M. Markovic, W.E. Brown, Octacalcium phosphate. 3. Infrared and Raman vibrational spectra, Chem. Mater. 5 (1993) 1417–1423. doi:10.1021/cm00034a009.

[159] G. Penel, G. Leroy, C. Rey, B. Sombret, J.P. Huvenne, E. Bres, Infrared and Raman microspectrometry study of fluor-fluor-hydroxy and hydroxy-apatite powders., J. Mater. Sci. Mater. Med. 8 (1997) 271–6. doi:10.1023/A:1018504126866.

[160] P.N. de Aza, F. Guitián, C. Santos, S. de Aza, R. Cuscó, L. Artús, Vibrational Properties of Calcium Phosphate Compounds. 2. Comparison between Hydroxyapatite and β-Tricalcium Phosphate, Chem. Mater. 9 (1997) 916–922. doi:10.1021/cm9604266.

[161] H.H. Adler, P.F. Kerr, Infrared study of aragonite and calcite, Am. Mineral. 47 (1962) 700–717.

[162] I.A. Gracia, Applicazioni della spettrofotometria IR allo studio dei beni culturali, 2001.

[163] M.R. Derrick, D. Stulik, J.M. Landry, Infrared spectroscopy in Conservation Science, the Getty Conservation Institute, Los Angeles, 1999.

[164] E.E. Berry, C.B. Baddiel, Some assignments in the infra-red spectrum of octacalcium phosphate, Spectrochim. Acta. 23A (1967) 1781–1792. doi:10.1016/0584-8539(67)80061-8.

[165] B.O. Fowler, E.C. Moreno, W.E. Brown, Infra-red spectra of hydroxyapatite, octacalcium phosphate and pyrolysed octacalcium phosphate, Arch. Oral Biol. 11 (1966) 477–492. doi:10.1016/0003-9969(66)90154-3.

[166] Y. Lee, Y.M. Hahm, S. Matsuya, M. Nakagawa, K. Ishikawa, Characterization of macroporous carbonate-substituted hydroxyapatite bodies prepared in different phosphate solutions, J. Mater. Sci. 42 (2007) 7843–7849. doi:10.1007/s10853-007-1629-3.

[167] M.E. Fleet, Infrared spectra of carbonate apatites: v2-Region bands., Biomaterials. 30 (2009) 1473–81. doi:10.1016/j.biomaterials.2008.12.007.

[168] J. Xu, I.S. Butler, D.F.R. Gilson, FT-Raman and high-pressure infrared spectroscopic studies of dicalcium phosphate dihydrate (CaHPO42H2O) and anhydrous dicalcium phosphate (CaHPO4), Spectrochim. Acta Part A Mol. Biomol. Spectrosc. 55 (1999) 2801–2809. doi:10.1016/S1386-1425(99)00090-6.

[169] Y.-H. Tseng, C.-Y. Mou, J.C.C. Chan, Solid-state NMR study of the transformation of octacalcium phosphate to hydroxyapatite: a mechanistic model for central dark line formation., J. Am. Chem. Soc. 128 (2006) 6909–18. doi:10.1021/ja060336u.

[170] B.C. Cornilsen, R.A. Condrate, The vibratonal spectra of β-Ca2P2O7 and γ-Ca2P2O7, J. Inorg. Nucl. Chem. 41 (1978) 602–605.

[171] A. Massita, A. El Yacoubi, B.C. El Idrissi, K. Yamni, Synthesis and characterization of nano-sized β-Tricalcium phosphate: Effects of the aging time, J. Appl. Chem. 7 (2014) 57–61. http://www.iosrjournals.org/iosr-jac/papers/vol7-issue7/Version-1/J07715761.pdf.

[172] S.N. Danilchenko, A. V. Koropov, I.Y. Protsenko, B. Sulkio-Cleff, L.F. Sukhodub, Thermal behavior of biogenic apatite crystals in bone: An X-ray diffraction study, Cryst. Res. Technol. 41 (2006) 268–275. doi:10.1002/crat.200510572.

[173] C. Rodriguez-Navarro, E. Ruiz-Agudo, A. Luque, A.B. Rodriguez-Navarro, M. Ortega-Huertas, Thermal decomposition of calcite: Mechanisms of formation and textural evolution of CaO nanocrystals, Am. Mineral. 94 (2009) 578–593. doi:10.2138/am.2009.3021.

[174] É. Kristóf-Makó, A. Juhász, The effect of mechanical treatment on the crystal structure and thermal decomposition of dolomite, Thermochim. Acta. 342 (1999) 105–114. doi:10.1016/S0040-6031(99)00290-7.

[175] E. Possenti, C. Colombo, C. Conti, L. Gigli, M. Merlini, J.R. Plaisier, M. Realini, G.D. Gatta, Grazing incidence synchrotron X-ray diffraction of marbles consolidated with diammonium hydrogen phosphate treatments: non-destructive probing of buried minerals, Appl. Phys. A. 124 (2018) 383. doi:10.1007/s00339-018-1798-8.

[176] B.C. Barriuso, G. Botticelli, O.A. Cuzman, I. Osticioli, P. Tiano, M. Matteini, Conservation of calcareous stone monuments: Screening different diammonium phosphate based formulations for countering phototrophic colonization, J. Cult. Herit. 27 (2017) 97–106. doi:10.1016/j.culher.2017.03.002.

[177] G. Graziani, C. Colombo, C. Conti, E. Possenti, E. Perelli Cippo, M. Realini, E. Sassoni, Neutron radiography as a tool for assessing penetration depth and distribution of a phosphate consolidant for limestone, Constr. Build. Mater. 187 (2018) 238–247. doi:10.1016/j.conbuildmat.2018.07.173.

[178] I. Osticioli, G. Botticelli, P. Matteini, S. Siano, R. Pini, M. Matteini, Micro-Raman analysis on the combined use of ammonium oxalate and ammonium phosphate for the consolidation and protection of carbonate stone artifacts, J. Raman Spectrosc. 48 (2017) 966–971. doi:10.1002/jrs.5150.

[179] C. Conti, C. Colombo, G. Festa, J. Hovind, E.P. Cippo, E. Possenti, M. Realini, Investigation of ammonium oxalate diffusion in carbonatic substrates by neutron tomography, J. Cult. Herit. 19 (2016) 463–466. doi:10.1016/j.culher.2015.12.005.

[180] M. Realini, C. Colombo, C. Conti, F. Grazzi, E. Perelli Cippo, J. Hovind, Development of neutron imaging quantitative data treatment to assess conservation products in cultural heritage,

Anal. Bioanal. Chem. 409 (2017) 6133–6139. doi:10.1007/s00216-017-0550-0.

[181] F. Hameed, B. Schillinger, A. Rohatsch, M. Zawisky, H. Rauch, Investigations of stone consolidants by neutron imaging, Nucl. Instruments Methods Phys. Res. Sect. A Accel. Spectrometers, Detect. Assoc. Equip. 605 (2009) 150–153. doi:10.1016/j.nima.2009.01.139.

[182] European Standard EN 15801, Conservation of cultural property – test methods – determination of water absorption by capillarity, (2010).

[183] M. Voltolini, N. Taş, S. Wang, E.L. Brodie, J.B. Ajo-Franklin, Quantitative characterization of soil micro-aggregates: New opportunities from sub-micron resolution synchrotron X-ray microtomography, Geoderma. 305 (2017) 382–393. doi:10.1016/j.geoderma.2017.06.005.

[184] M. Voltolini, D. Zandomeneghi, L. Mancini, M. Polacci, Texture analysis of volcanic rock samples: Quantitative study of crystals and vesicles shape preferred orientation from X-ray microtomography data, J. Volcanol. Geotherm. Res. 202 (2011) 83–95. doi:10.1016/J.JVOLGEORES.2011.02.003.

[185] F. Brun, Development of algorithms and methods for three-dimensional image analysis and biomedical applications, Universit` a degli Studi di Trieste, 2011.

[186] S. Schultheiss, I. Sethmann, M. Schlosser, H.-J. Kleebe, Pseudomorphic transformation of Ca/Mg carbonates into phosphates with focus on dolomite conversion, Mineral. Mag. 77 (2013) 2725–2737. doi:10.1180/minmag.2013.077.6.03.

[187] Istituto Centrale per il Restauro (ICR), Italian Recommendation NORMAL 20/85. Conservazione dei materiali lapidei: Manutenzione ordinaria e straordinaria, (1985).

[188] C. Miliani, M.L. Velo-Simpson, G.W. Scherer, Particle-modified consolidants: A study on the effect of particles on sol–gel properties and consolidation effectiveness, J. Cult. Herit. 8 (2007) 1–6. doi:10.1016/j.culher.2006.10.002.

[189] G. Cacudi, A. Di Marzo, M. Matteini, D. Melica, F. Vescera, 34° convegno internazionale Scienza e Beni Culturali, in: 34° Convegno Internazionale Sci. E Beni Cult. Bressanone, 3-6 July 2018, 2018: pp. 213–224.

[190] E. Possenti, C. Colombo, C. Conti, L. Gigli, M. Merlini, J.R. Plaisier, M. Realini, G.D. Gatta, What's underneath? A non-destructive depth profile of painted stratigraphies by synchrotron grazing incidence X-ray diffraction, Analyst. 143 (2018) 4290–4297. doi:10.1039/C8AN00901E.

Aknowledgements

È con gli occhi un po' lucidi che penso a tutte le persone che mi hanno accompagnato in questo entusiasmante percorso di crescita professionale e personale. Senza ognuna di queste persone, non sarei qui adesso, arricchita di un bagaglio e consapevolezze che prima non avevo.

Voglio innanzitutto ringraziare il mio tutor, Prof. Diego Gatta, per avermi dato l'opportunità di lavorare insieme in questo percorso che si è rivelato fonte di grandi soddisfazioni. Grazie per avermi accompagnato nella ricerca, per la sua disponibilità al confronto, per essere sempre stato di supporto in tutte le fasi del lavoro e per essersi prodigato affinché io facessi nuove esperienze utili alla mia crescita professionale. Grazie anche al Prof. Marco Merlini, per avermi affiancato nella ricerca sperimentale con entusiasmo e disponibilità, offrendo sempre la sua competenza e curiosità allo sviluppo della mia ricerca. Grazie di cuore alla Dott.ssa Nicoletta Marinoni per aver avuto voglia di affiancarmi in questo percorso, per tutto il tempo che mi ha dedicato e per suo modo gentile ed entusiasta di mettersi sempre in ascolto. Voglio ringraziare i miei colleghi dottorandi per avermi accompagnato in questi tre anni nei momenti di incontro, lezione e confronto. Un grazie speciale a Davide e Gianluca: mi mancheranno le nostre chiacchierate di aggiornamento, lavorativo e non, tutti e tre nello stesso ufficio! Ringrazio inoltre tutto il Dipartimento di Scienze della Terra che si è sempre dimostrato interessato alla mia ricerca e disponibile ad offrirmi supporto nell'uso delle strumentazioni del dipartimento.

Un grazie profondamente riconoscente alla mia tutor Dott.ssa Chiara Colombo, per aver creduto in me ed aver continuato a farlo ogni giorno di questo viaggio, un cammino articolato di cui non cambierei un singolo passo. Grazie per avermi guidato con fermezza e dolcezza, per esserci stata sempre ai miei "Chiara mi sono persa", in ascolto e con le idee chiare. Grazie per aver saputo premere i tasti giusti e per aver puntato sempre al massimo di quello che potevo dare. Grazie a tutto questo, mi ri-innamoro ogni giorno di quello che faccio.

Grazie al Dott. Marco Realini per avermi guidato in tutti questi anni di collaborazione e per aver creduto nelle mie potenzialità. Grazie per tutto il tempo che mi ha dedicato nella formazione, per i pomeriggi di confronto in cui le ore volano ragionando sui dati e sul significato delle parole, per le sue (ahimè sempre fondate) frecciatine "te lo boccio io l'articolo o te lo boccia dopo il referee?" e soprattutto per il profondo rispetto che ha sempre dimostrato per la libertà di scelta individuale.

Grazie a Claudia, che mi ha sempre accolto con un sorriso aperto e la massima disponibilità lavorativa e umana, anche quando era sommersa di scadenze, sotto stress e non aveva tempo neanche per respirare. Grazie per le sue riflessioni, per l'essere molto focalizzata ("non scatterata", direbbe una nostra affettuosa conoscenza) e attenta a beccare sempre il nocciolo della questione con i suoi "ok, i

dati sono buoni, ma qual è l'obbiettivo? Il goal? La domanda è la parte più importante". Grazie per la sua passione contagiosa per la ricerca e soprattutto per le risate di pancia che ti alleggeriscono i sentimenti.

Grazie al Prof. G. Zerbi per i suoi insegnamenti, la passione tangibile e la curiosità viva che mette in ogni cosa. Soprattutto grazie alle sue indimenticabili lezioni di spettroscopia vibrazionale e per avermi fatto uscire dalla bocca tanti "Wow", scoprendo quanto è incredibile e affascinante la materia (che abbia dipolo o non).

Un grazie speciale va ad Antonio, per avermi fatto innamorare per la prima volta di questo lavoro, per avermi indirizzato su questa strada e per essere una persona su cui poter contare sempre, scientificamente e non. Grazie a Roberto per le sue preziose "consulenze lapidee" e per essere un galantuomo di altri tempi, uno che ti apre la porta per farti passare e ti chiede come stai, intendendolo davvero. Ringrazio poi Chiara Romoli, Valentina Brunello, Luisa Folli e tutto il gruppo dell'ICVBC-CNR che in questi anni mi hanno accompagnato nel lavoro e nei momenti di relax. Un ringraziamento speciale alle ragazze dell'ICPVB, Ale e Momo, colleghe e amiche preziose. Grazie per avere sempre tempo per me, per ridere, per incoraggiarsi o consolarsi, portando di volta in volta le nostre diversità caratteriali verso qualcosa di costruttivo che ci lega un pezzetto di più. Spero di non perdervi mai.

Grazie ad Irene Aliatis, per il suo sostegno incondizionato e per le nostre chiacchierate mattutine che ci uniscono a dispetto della distanza che ci separa.

Un grazie speciale alla mia famiglia. Ognuno di voi mi ha dato un insegnamento diverso. Mamma e papà, con il loro saldo motto "non importa che problema hai, vedrai che adesso troviamo una soluzione per risolverlo". La mia sorellina, esempio di grande forza, determinazione e infinita dolcezza "se vuoi qualcosa, rimboccati le maniche e datti la fare. Lo otterrai". La zia Pinu, coi suoi aneddoti e il suo insegnamento che "l'importante, nella vita, è sapere qual è la pallottola". La zia Susi, con il suo tenero affetto e il suo "Elenuccia cara" che mi porta indietro negli anni. I miei nonni, col loro forte insegnamento che "se c'è la famiglia, c'è tutto quello che serve" e il loro immancabile "ma non hai ancora smesso di studiare? Che cosa c'è ancora da sapere?!?". Silvia, praticamente una sorellina "acquisita", che si rimbocca le maniche dalla Germania e con animo e forza cura il meraviglioso Federico e la sua famiglia.

E poi tu, Alberto. Grazie per avermi insegnato a credere che ogni obbiettivo è raggiungibile, se lo desideri. Il tuo motto, passato dalla nostra Gio, "basta iniziare, poi un modo lo si trova". Quello che ora è diventato anche il mio motto.

Se puoi sognarlo, puoi farlo.

Elena
30-09-2018